The prediction of stone stability by a three-dimensional eddy resolving simulation technique

Master thesis

at the Delft University of Technology

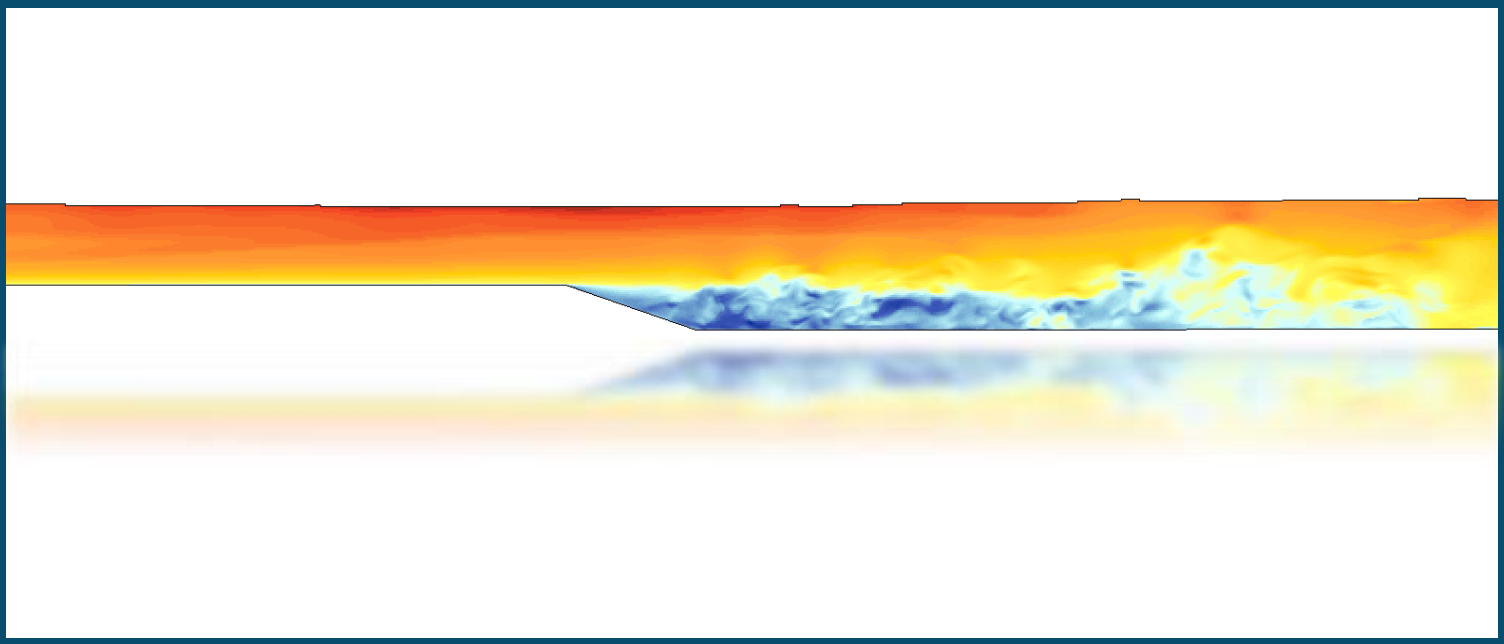

by

Thieu Stevens

TU Delft

Deltares
Enabling Delta Life

The prediction of stone stability by a three-dimensional eddy resolving simulation technique

Master thesis

by

Thieu Stevens

in partial fulfilment of the requirements for the degree of

Master of Science
in Civil Engineering

at the Delft University of Technology,
to be defended publicly on Tuesday 3 July 2018 at 15:30.

Student number:	4315464	
Project duration:	August 1, 2017 – July 3, 2018	
Thesis committee:	Prof. dr. ir. W.S.J. Uijttewaal	TU Delft
	Dr. ir. B. Hofland	TU Delft
	Ir. J.P. Van den Bos	TU Delft
	Ir. A. De Fockert	Deltares
	Dr. ir. T. O'Mahoney	Deltares
	Ir. A. Capel	Deltares

An electronic version of this thesis is available at http://repository.tudelft.nl/.

TU Delft

Deltares
Enabling Delta Life

Preface

After many years of studying, hereby I proudly present my thesis report. The years at the TU Delft definitely have cost a lot of time, discipline and money (sorry dad). However, I can honestly say, not one day has passed that I regretted the choice to obtain a master's degree, after I finished the university of applied sciences. I'm sure I'll benefit the rest of my life from the awful lot I've learned in- and outside the walls of the university during the past few years.

I want to thank all members of my graduation committee for their contribution to this research. Thank you Tom O'Mahoney and Bas Hofland, for sharing your in-depth knowledge and technical enthusiasm, which brought this research to a higher level with each meeting. Thank you Anton de Fockert, for being a great help in guiding the graduation process from start to end, and by reflecting on my general skills and products. Thank you Wim Uijttewaal, Jeroen van den Bos, and Alex Capel, for your sharp remarks and valuable advice during the fewer meetings we have had.

I'm glad I could conduct my thesis research at Deltares. Before I started, I knew nothing about computational modelling or turbulence. Deltares has been the perfect learning environment to master these topics. Deltares, as well as the TU Delft, have been inspiring places for me. Furthermore, Toontje and Sjoerdje deserve a special thanks. Our coffee breaks contributed a lot to the joy I've had in the rather lonely process of writing a thesis report.

Just like the flow I've simulated for this research, my graduation process has been quite turbulent. Lots of love goes to the people I've lost, and to the people that are still always there for me. My sisters, my girlfriend, my family, my friends, and Plurkje, I'm grateful for having your great personalities bringing colour into my life. And last but not least... liefste oudertjesch, bedankt voor dit diploma! Jullie onvoorwaardelijke steun, in werkelijk alle opzichten, is alles wat een jonge ingenieur zich kan wensen.

Thieu Stevens
Delft, July 2018

"One might ask, is it justified to simulate the flow past a car, when the wiper and door handle are not well resolved? The answer depends on the purpose of the simulation."
- Philippe R. Spalart (from: Detached-Eddy Simulation, 2009)

Abstract

In this thesis, it is studied if the stability of a stone in a granular bed protection, can be predicted by the local output of a three-dimensional (3D) eddy resolving simulation technique.

In earlier studies regarding stone stability, Reynolds-Averaged Navier-Stokes (RANS) models are used to determine the loads on the bed. In the resulting stability formulas, depth-averaged flow parameters are used, and the loads caused by turbulent fluctuations are taken into account by the modelled turbulent kinetic energy k. A load caused by turbulent wall pressures is never explicitly taken into account before. With the use of a 3D eddy resolving modelling technique, turbulence can be resolved to a certain extent, by which local parameters can be used to determine the load on the bed. This may result in a more accurate prediction of stone stability, and a more economical design method for granular bed protections.

Due to the computational requirements needed for the most detailed eddy resolving modelling techniques, it is concluded that for the aim of assessing stone stability, Improved Delayed Detached Eddy Simulation (IDDES) is the most appropriate 3D eddy resolving modelling technique for now and the nearby future. This modelling technique is also applied in a study regarding the influence of tidal energy turbines in one of the gates of the Eastern Scheldt barrier. In this thesis, special attention is paid to develop a stability formula, which can be used to assess the stone stability in the highly turbulent flow region behind the Eastern Scheldt barrier, based on the output of these simulations (hereafter "Eastern Scheldt case").

In order to derive a new stability formula, IDDESs are made of the two long sill experiments of Jongeling et al. (2003). In these experiments, an accelerating flow region is present above the sill. At its downstream end, the flow is separating, causing a highly turbulent flow region behind the sill. Thereby, the dominant flow characteristics are similar to those at the Eastern Scheldt barrier. In both regions of the experiments, on top of the sill and in the area downstream of the sill, damages to the granular bed protection are measured.

A new stability formula (equation 4.3) is proposed, based on the assumptions listed below. To avoid the new stability formula to be grid dependent, the wall shear stress τ_x and the pressure gradient $\frac{\partial p}{\partial x}$ are used to represent the loads by drag and inertia respectively.

- The predominant forces for stone stability are:
  1. The mean wall shear stress $\bar{\tau_x}$ - Force due to the near-bed flow velocity
  2. The wall shear stress fluctuations τ'_x - Force due to large-scale energy containing eddies
  3. The mean pressure gradient $\frac{\bar{\partial p}}{\partial x}$ - Force due to spatial accelerations (e.g. geometry) and waves
  4. The pressure gradient fluctuations $\frac{\partial p'}{\partial x}$ - Force caused by turbulent wall pressures. Fluctuations $\geq d_{n50}$ are of importance for stone stability
- Stone movement is caused by the occurrence of an extreme lift force, which increases the exposed area of a stone, followed by an extreme drag force that moves the stone in the near-bottom flow direction.
- Absolute values of τ_x and $\frac{\partial p}{\partial x}$ can be used, as stone stability is not dependent on the direction of the near-bed flow velocity, and both negative, as positive pressure gradients, can result in an extreme lift force.

It appeared, that the proposed stability formula does not predict the number of measured stone movements well, for the entire modelled domain of the long sill experiments. Nevertheless, it is hypothesised, that the assumed pre-dominant load terms are right, but that the ratio between those load terms on top of the sill differs from the ratio between the load terms in the downstream area. Two different entrainment mechanisms are described, that may not be predicted accurately by the same stability formula.

With regard to the Eastern Scheldt case, the choice is made to derive a stability formula that is only valid for the entrainment mechanism in a highly turbulent flow region behind a sill of backward-facing step. The data, behind the point of separation in the long sill simulations, is used to derive this stability relation. It appeared that the best results are obtained for a stability formula that is similar to equation 4.3, with a $C_{m:b}$-value of 1. This is in agreement with the hypothesised entrainment mechanisms for this region.

Finally, the proposed stability formula is applied to the Eastern Scheldt case. A firm conclusion about the exact influence of the tidal energy turbines on the granular bed protection, cannot be drawn based on this study. However, it can be concluded, that the influence on the stability of the stones seems to be insignificant. At the analysed locations, the loads on the bed even seem to be slightly reduced in the simulation with turbines, compared to the simulation without turbines.

At least as important, is the conclusion that IDDES potentially is an appropriate modelling technique to assess the stability of stones in a granular bed protection. For the long sill experiments, the measured flow characteristics are clearly reproduced more accurately when using IDDES, than by applying a RANS model with the same boundary conditions. The computational effort needed for the Eastern Scheldt case is comparable to the computational requirements of the long sill simulations. Nevertheless, in both cases, the effective grid resolution was not yet sufficient to resolve all fluctuations towards the size of $1d_{n50}$. Despite the given that the desired resolution is not yet reached in this thesis, the simulated velocity signals of the long sill experiments are in good agreement with the measured ones. The choice between the use of IDDES or a RANS model should depend on the available computational power, time and required accuracy.

Contents

Nomenclature

Symbol	Unit	Meaning
a	m/s^2	Acceleration
C_b	–	Combined drag and lift coefficient
C_d	–	Drag coefficient
C_l	–	Lift coefficient
C_m	–	Added mass coefficient
d	m	Stone diameter
d_{n50}	m	Nominal stone diameter
f	Hz	Frequency
h	m	Water depth
k	$(m/s)^2$	Turbulent kinetic energy (TKE)
k_s	m	Equivalent sand-grain roughness
L	m	Length
$\frac{\partial p}{\partial x}$	$N/m^2/m$	Pressure gradient in streamwise direction (PG)
Q	l/s	Discharge
r	–	Turbulence intensity
R^2	–	Correlation factor
Re	–	Reynolds number
Re_*	–	Roughness Reynolds number
u	m/s	Flow velocity
u^+	–	Dimensionless velocity
u_*	m/s	Shear / Friction velocity
W	kg	Weight
x	(m)	(Distance in) Streamwise direction
y	(m)	(Distance in) Normal to flow direction in the horizontal plane
z	(m)	(Distance in) Vertical direction
z^+	–	Dimensionless wall distance
z_0	m	Roughness length
z_{mbl}	m	Mean Bed Level
Greek		
Δ	–	Relative submerged density of a stone in water
ε	m^2/s^3	Turbulence dissipation rate
Φ_E	–	Dimensionless entrainment rate
κ	–	Von Karman constant ≈ 0.41
μ_t	$kg/(m*s)$	Eddy viscosity
μ_w	$kg/(m*s)$	Viscosity water
ν	m^2	Kinematic viscosity water
ν_t	m^2	Kinematic eddy viscosity
ρ_s	kg/m^3	Density stone
ρ_w	kg/m^3	Density water
τ	N/m^2	Wall shear stress (WSS)
Ψ	–	Stability parameter
ω	$1/s$	Specific dissipation rate

Symbol	Meaning
Math	
$\bar{..}$ / μ	Mean value
$..'$ / σ	Fluctuating part, Standard deviation
∇	Partial derivative vector in x, y and z-direction
∂	Partial derivative

Abbreviations	Meaning
3D	three-Dimensional
CDF	Cumulative Density Function
CFD	Computational Fluid Dynamics
CFX	Name of modelling tool of ANSYS
DES	Detached Eddy Simulation
DNS	Direct Numerical Simulation
EMF	Electro-Magnetic Flowmeter
ESB	Eastern Scheldt Barrier
IDDES	Improved Delayed Detached Eddy Simulation
LDV	Laser Doppler Velocimeter
LES	Large Eddy Simulation
meas	measured
NAP	Normaal Amsterdams Peil (Dutch reference height)
PDF	Probability Density Function
PG	Pressure Gradient
RANS	Reynolds-Averaged Navier-Stokes
sim	simulated
SST	Shear Stress Transport
TKE	Turbulent Kinetic Energy
WMLES	Wall Modelled Large Eddy Simulation
WSS	Wall Shear Stress

1 Introduction

In this chapter, first some background information will be given about the origin of this research. Problems considering the state of the art of this thesis topic are discussed, followed by the objectives of this study. Consequently the research approach is given, together with the outline of this report.

This research is part of the DMEC project - task 3.7, which is led by Deltares. Dutch Marine Energy Centre (DMEC) is a consortium of 15 partners researching topics that are related to: *energy from water*. Research task 3.7 aims to use and develop tools to investigate the near field and far field hydrodynamic behaviour near the Tidal Power Plant that is located in the Eastern Scheldt Storm Surge barrier.

1.1. Background

This section will provide some background information about the project from which the research question of this thesis is originated.

1.1.1. The Eastern Scheldt Barrier

At the fourth of October 1986, the Dutch queen Beatrix officially opened the Eastern Scheldt Barrier. A three kilometres long open connection between the North Sea and the Eastern Scheldt estuary is realized by sixty five huge concrete pillars, with sixty two steal gates in between that will be closed if the expected sea level is higher than +3 m relative to NAP (the Dutch reference height). The structure is designed for a lifespan of 200 years, where Rijkswaterstaat is responsible for the management and maintenance. To get an impression of the barrier, two pictures are shown below.

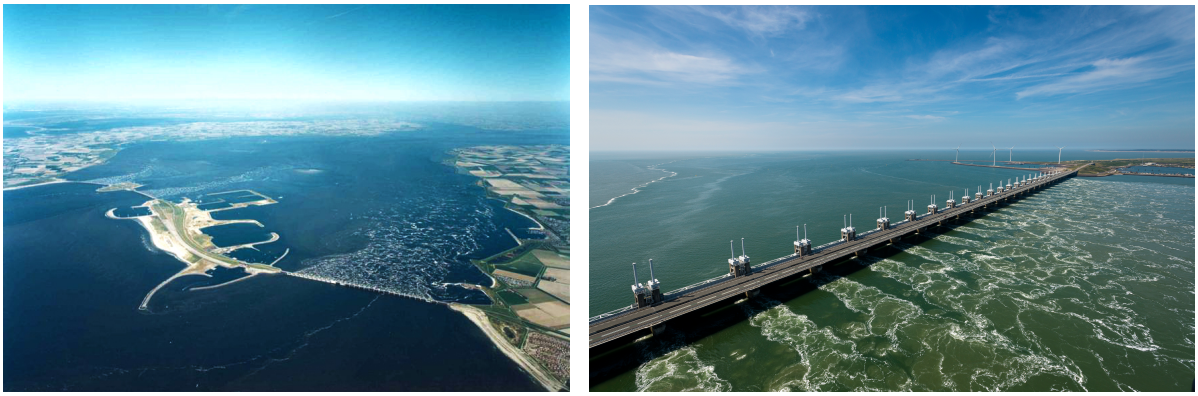

(a) Total overview (b) During flood

Figure 1.1: Impression pictures of the Eastern Scheldt Barrier (Biesboer, 2011)

On these pictures, white foam is visible at the water surface over large areas behind the barrier. This is caused by the high flow velocities through the barrier and the highly turbulent character of this flow. Both pictures are taken during flood, as the white foam is visible at the Eastern Scheldt side. During ebb, the large turbulent eddies will be present at the sea side of the barrier.

1.1.2. Tidal energy turbines

The Eastern Scheldt Barrier can close off the three main channels of the Eastern Scheldt estuary called Hammen, Schaar van Roggenplaat (abbreviated as Schaar) and Roompot. At this moment, research is done if tidal energy can be generated from the high flow velocities through the barrier without negatively influencing the Eastern Scheldt estuary too much. As a test case, five energy turbines are placed in the eighth gate of the Roompot channel (Roompot 8), as indicated in figure 1.2.

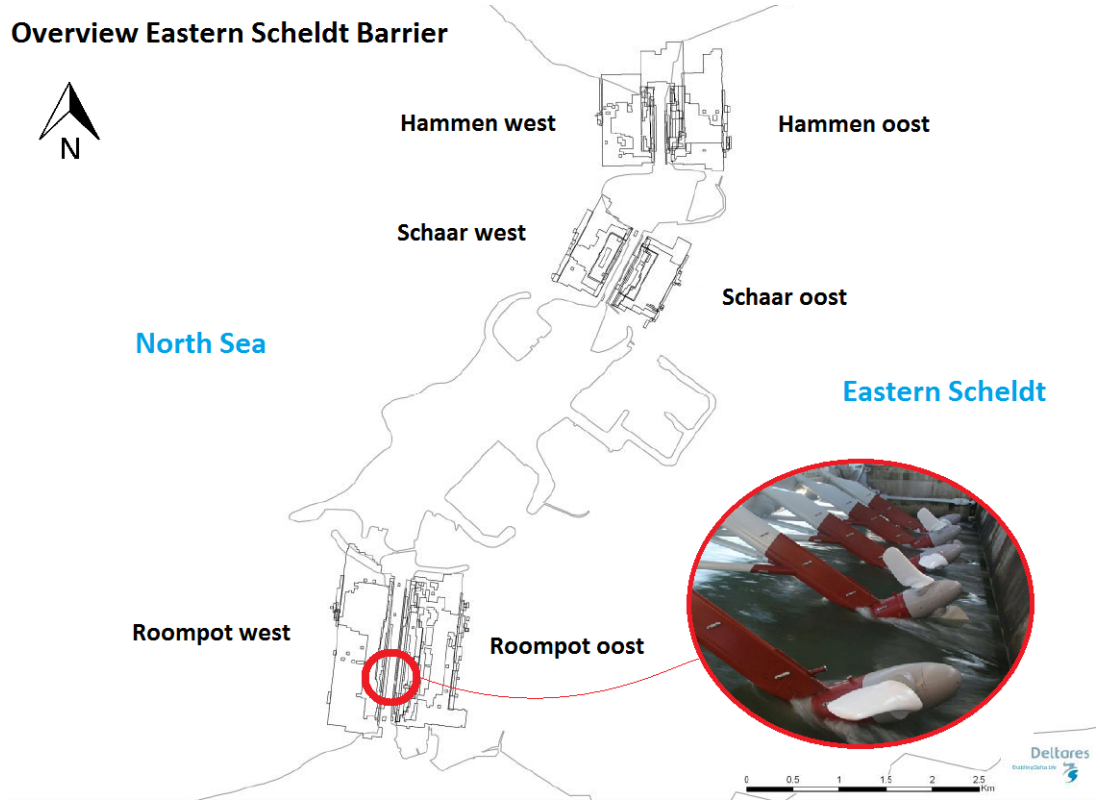

Figure 1.2: Channel sections of Eastern Scheldt Barrier (adjusted from Stoutjesdijk et al., 2012)

The main concerns of Rijkswaterstaat are if the tidal energy turbines could endanger the stability of the Eastern Scheldt barrier or damage the ecosystem of the Eastern Scheldt estuary. Tocardo is the producer and administrator of the tidal energy turbines. They have to prove to Rijkswaterstaat that the side effects of the turbines are within acceptable limits. The test installation at Roompot 8 fulfils an important role in this process. In the long term, Tocardo would like to get a permit to increase the amount of energy turbines installed and to expand the frame in which they are allowed to generate tidal power. Currently the power generation is restricted to a maximum hydraulic head difference of 60 cm during ebb and 80 cm during flood.

This thesis will be part of the more extensive study to the overall effects of the tidal energy turbines at the Eastern Scheldt barrier. In this report, the influence of the energy turbines on bed protection around the Eastern Scheldt Barrier will be assessed. The emphasis will lay on the granular part of the bed protection, as further elaborated in the next section. Throughout this report, the above will be referred to as the "Eastern Scheldt case".

1.1.3. Zooming in: Roompot 8

Recently for several projects in the Netherlands like Stuw Hagestein, Stuw Grave and the Eastern Scheldt case, large computational fluid dynamics (CFD) models are made to study the hydrodynamics. Questions are raised if these models can be used to asses the stability of the granular bed protection at those locations. Compared to the CFD models of Stuw Hagestein and Stuw Grave, the Roompot 8 simulations contain a lot more detailed flow characteristics. Therefore, using the output of this model might allow for a more detailed assessment of the stone stability in the granular bed protection.

In figure 1.3 a cross-section is shown of the Roompot 8 simulation in which the tidal energy turbines are included. The figure is a screenshot of the velocity field during flood flow. It gives an impression of the flow phenomena that play significant role in this thesis.

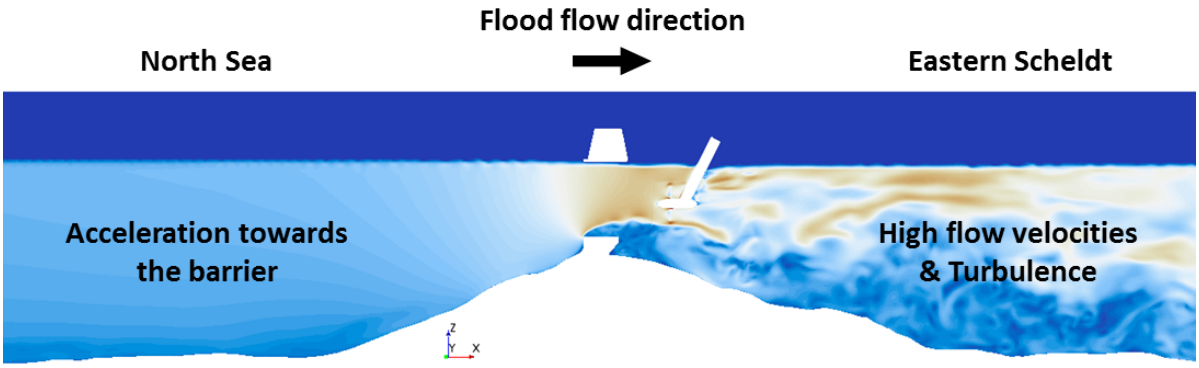

Figure 1.3: Flow characteristic at Roompot 8 in a cross-section over the Eastern Scheldt Barrier during flood

In figure 1.3, a lot of turbulence is visible at the right side of the barrier. Such turbulent fluctuations are not simulated in the CFD models of Stuw Hagestein and Stuw Grave. This might give an idea about what is meant by a higher level of detail for the Roompot 8 simulations. The detailed CFD model used for the Roompot 8 simulations falls into the group of "three-dimensional (3D) eddy resolving techniques". The models used for Stuw Hagestein and Stuw Grave does not.

In the cross-section of figure 1.3, also the large sill of the Eastern Scheldt barrier is visible on which the gates will close during certain extreme conditions. The flow will accelerate towards the sill and separation occurs at its downstream end. Left and right of the barrier an extensive bed protection is present, consisting of several layers and materials. Figure 1.4 shows a drawing of the original design of the bed protection around the Eastern Scheldt barrier at the Roompot channel.

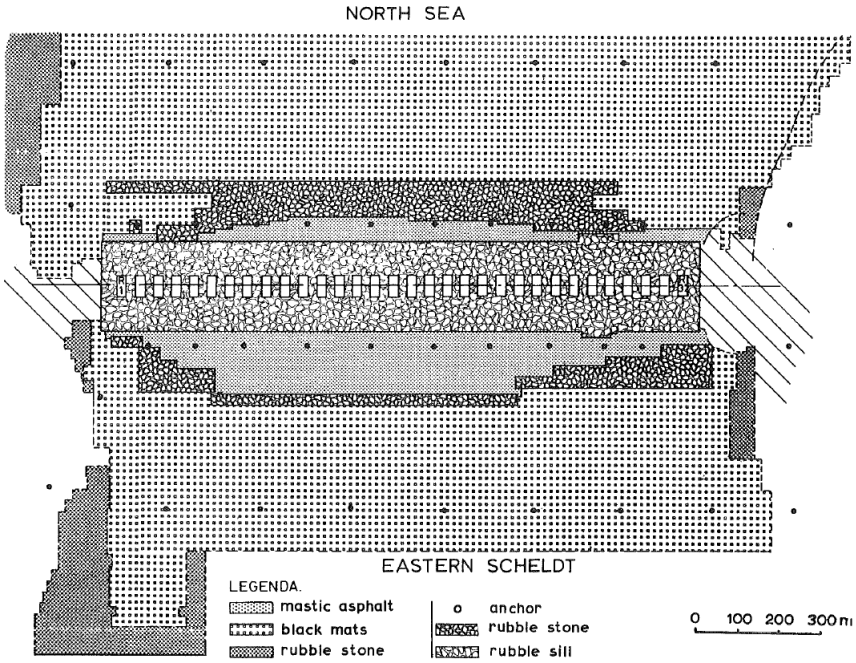

Figure 1.4: The original design of the bottom protection of the Roompot channel

Currently, the largest part of the top layer of this bed protection consists of granular material, partly because of extra stone deposits for repair or reinforcement (Raaijmakers et al., 2012). The tidal energy turbines are expected to increase the turbulent intensities, which might have a negative influence on the stability of the granular bed protection. Furthermore, the flow accelerations towards the barrier can also negatively influence the stone stability, as proved by earlier studies of (Dessens, 2004) and (Huijsmans, 2006). In this report, these flow phenomena will be taken into account for the assessment of stone stability.

In this thesis, it will be studied how the Roompot 8 simulations can be used to determine the influence of the tidal energy turbines on the stability of the granular bed protection at the Eastern Scheldt barrier. Because of the complexity of the flow characteristics through the Eastern Scheldt barrier, first a new design method will be develop based on the results of simulated laboratory experiments.

The expectation is that the use of a 3D eddy resolving technique can improve the prediction of the start of stone movement. In contrast to the models used in earlier studies, a 3D eddy resolving technique might allow for the use of local load parameters of which also the extreme values are reproduced. As such, the developed stability formula could potentially be generally applicable for many other flow configurations.

1.2. Problem description

Recent studies have shown that the stability of a stone in a granular bed protection is dependent on the flow velocities, the velocity fluctuations (turbulence), and a force caused by accelerations (inertia). Currently, often Pilarczyk or an adapted Shields formula are used to determine the required stone size in a granular bed protection around a hydraulic structure. These stability formulas take the load by the velocity fluctuations into account by an empirical turbulence factor or the turbulent kinetic energy k. The load caused by the flow acceleration is not taken into account at all. In a stability formula proposed more recently by Steenstra (2014), a force due to inertia included. A satisfying relation between the damages and the proposed stability parameter was obtained for several distinct laboratory experiments.

Nevertheless, this formula, as well as the Pilarczyk formula and the Shields formula, uses depth averaged flow parameters instead of the flow characteristics near the bed. Furthermore, in Hofland (2005) it is shown that a force due to turbulent wall pressures can be of importance for stone stability as well. It is expected that with a new design method, that includes the turbulent wall pressures, and uses local load parameters, it should be possible to predict the start of stone movement more accurately.

With the modelling technique used in earlier studies concerning stone stability, it is not possible to resolve turbulence. Turbulence is taken into account by special transport equations, and therefore this modelling technique cannot reproduce the real-life velocity fluctuations. With a three-dimensional eddy resolving modelling technique it is possible to reproduce the turbulent fluctuations to a certain extent. Therefore it is expected, that the prediction of real-life flow characteristics can be improved by using a three-dimensional eddy resolving technique.

Besides this, often real-life scale models are built to investigate (the effects of) the hydrodynamic conditions for the design of a large hydraulic structure. A disadvantage of these experiments is that only a limited amount of flow characteristics can be measured at a limited amount of spacial points. The use of 3D eddy resolving techniques seems to offer more possibilities and flexibility on this, as all flow characteristics will be calculated for the entire modelled domain. The amount of information available in a well-validated 3D eddy resolving model seems endless, which also makes it interesting from a financial point of view. With all this extra information, new design formulas are required to exploit the additional possibilities these numerical models offer.

It should be noted that the development of a new method to asses the stability of a stone in a non-uniform flow is not straight forward. Some fundamental problems that will not be solved within this thesis are listed below.

- Stone movement is a stochastic phenomenon. Deriving a physically based formula for the real "start of stone movement" seems to be impossible, among others by the infinite amount of possible local load combinations to put a stone into motion.
- The exact causes of stone movements are very difficult to measure. Therefore, also the derivation of general load combinations that put a stone into motion are not yet part of common knowledge.
- The available computational power is not yet sufficient to completely resolve a large turbulent flow field. This forms an important limitation to the capabilities of CFD modelling.

1.3. Objectives

From the problem description, the need for a new methodology to predict the start of stone movement can be deduced. The stability formula should be based on local load parameters extracted from a 3D eddy resolving model that includes all non-uniform flow phenomena that are known to be relevant. Thereby a more accurate and physically based design formula will be created, that might be generally applicable. Nevertheless, in this thesis special attention is paid to determine the influence of the tidal energy turbines on the granular bed protection at the Eastern Scheldt barrier.

The above can be wrapped up in the following research question:

How to determine the stone stability in the top layer of a granular bed protection located in a non-uniform flow, with the use of local parameters extracted from a three-dimensional eddy resolving simulation, in order to determine the influence of tidal energy turbines on the stability of the granular bed protection of the Eastern Scheldt barrier?

To answer this extensive research question, in this thesis the first three sub-questions are studied. The fourth sub-question is thought to provide some valuable insight in the use of a 3D eddy resolving technique for the intended purpose.

1. Which 3D eddy resolving modelling technique is most appropriate to determine the stone stability in a granular bed protection around a hydraulic structure?
2. How to include the predominant physical forces into a stability formula that uses the output of a 3D eddy resolving technique?
3. What is the influence of the tidal energy turbines on the stability of the granular bed protection at the Eastern Scheldt barrier?
4. Does the use of a 3D eddy resolving technique add value to the assessment of stone stability in a granular bed protection, compared to methods that rely the output of a RANS model?

1.4. Research approach

The abbreviations (RANS & DES) used below are elaborated in the literature study.

In the scheme of figure 1.5 the main components of this thesis research are listed. First, more information about the different topics of this thesis is gathered from literature. At the same time, a start is made to get familiar with the modelling software "Star CCM+" and numerical modelling itself. An attempt is made to obtain accurate RANS models of the flat bed experiments of Jongeling et al. (2003). Eventually, the obtained results are considered irrelevant for the objectives of this thesis. Therefore, nothing of the modelled flat bed experiments is added to this report.

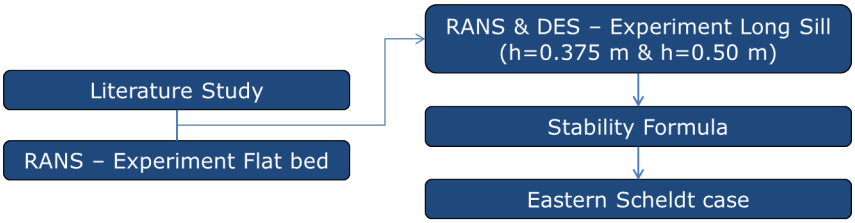

Figure 1.5: Scheme research approach

Based on literature and the first modelling experiences with Star CCM+, the first sub-question of the objectives is answered. The choice is made which 3D eddy resolving modelling technique to use, whereafter RANS models and DESs are made of the long sill experiments of Jongeling et al. (2003) with h = 0.375 m and h = 0.50 m. The DESs are validated and the output is used to derive a formula by which the stone stability can be assessed based on local load parameters. Thereby, the second sub-question of the objectives is answered. To answer the third sub-question, the proposed stability formula is applied to the output of the Roompot 8 simulations to determine the influence of the tidal energy turbines on the stability of the granular bed protection. Finally, the fourth sub-question and the main research question can be answered when evaluating the results of this study.

1.5. Outline

In figure 1.6 the outline of this thesis is given. It does not exactly follow the research approach, but the basic elements are quite similar.

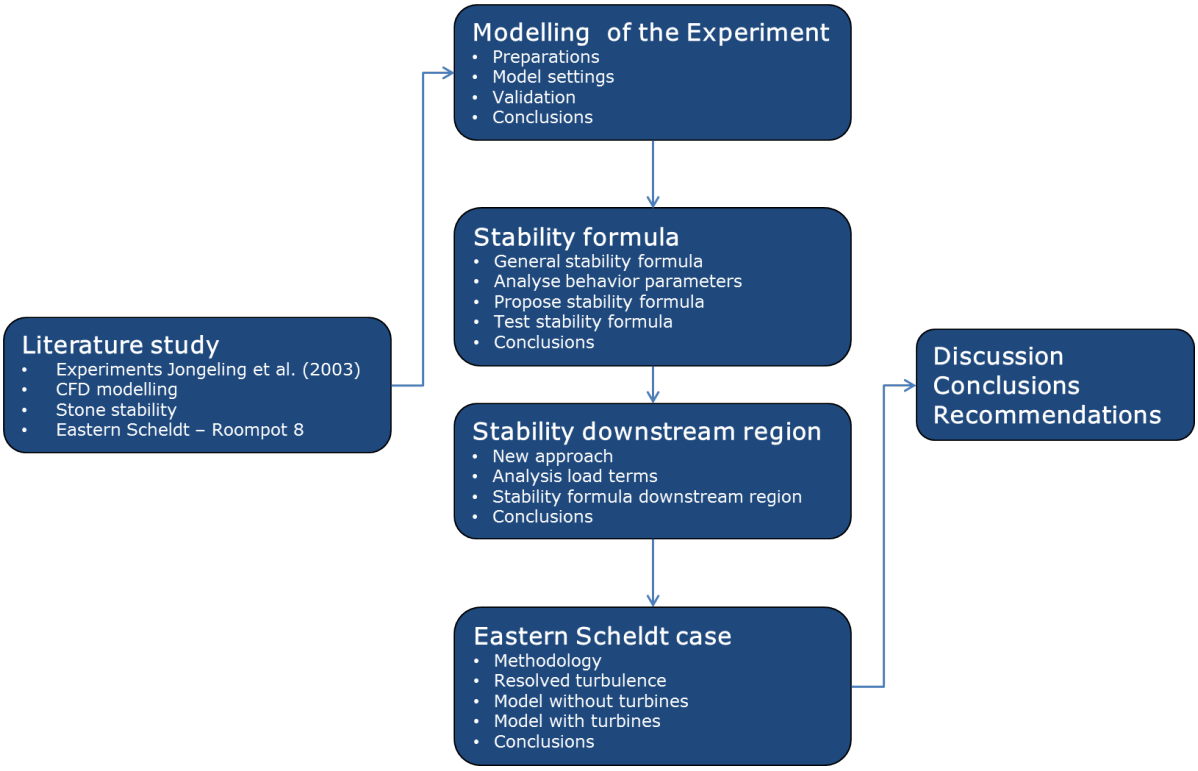

Figure 1.6: Scheme thesis outline

In the next chapter, the results of the literature study are written down. In this part of the report the first sub-question of the objectives is answered. By far the largest part of this report is about answering the second sub-question. In chapter 3 the long sill experiments of Jongeling et al. (2003) are modelled and validated. In chapter 4 and 5 the output of these simulations is used to derive the desired stability formula, whereby the second sub-question of the objectives is answered. In chapter 6 this stability formula is applied to the Eastern Scheldt case to answer the third sub-question. The fourth sub-question and the main research question are answered by the evaluation of this study, written down in chapter 7, 8 and 9.

2

Literature study

In this chapter information will be given about the different main topics of this thesis. This literature study is used to support and declare the approach, observations and results of this research.

2.1. Stone stability

In this section a description is given of the physics involved in the stability of a stone in a granular bed protection. In general the stability is expressed by the balance between the loads and the resistance. The ratio between them is represented by the stability parameter Ψ. In this thesis an effort is made to improve the representation of the loads that act on a stone. Those are expected to contain larger inaccuracies than the resistance part of the available stability formulas. The load parameters will therefore be treated more extensively in this section.

2.1.1. Two consecutive extreme forces

Based on Hofland (2005), it is assumed that stone movement in a bed protection is caused by two consecutive phenomena. First the stone is lifted whereby the exposed area of the stone is increased. Secondly, this increased exposed area is attacked by an increased drag force that is able to transport the stone. The governing lift force is largely caused by inertia. It can be represented by the horizontal pressure difference over the stone, mainly caused by local accelerations, waves and turbulent wall pressures. Fluctuations with a length scale approximately equal to the diameter of the bed material appeared to be effective in lifting a stone out of the bed Hofland (2005). Smaller fluctuations are considered unimportant for stone stability. Also the flow velocity over a bed element causes a lift force because of streamline contraction whereby, even without flow accelerations or small scale turbulence, stone movement can take place. The drag force is caused by the local flow velocity at the bottom. Governing are the peak values of this velocity caused by large scale turbulent motions.

2.1.2. Basic equation

The phenomena mentioned in the previous subsection are captured by Hofland (2005) in the general stability equation given below:

$$\Psi_{tot} \equiv \frac{(C_B(\tilde{\bar{u}} + \tilde{u}')^2 + (C_m(\tilde{\bar{a}} + \tilde{a}')d)_{\max}}{\Delta g d} \tag{2.1}$$

in which:

- Ψ_{tot} is the stability parameter $[-]$
- C_B is a combined drag and lift coefficient $[-]$
- $\tilde{}$ means projection on the bed ($\tilde{u}^2 = u^2 + w^2$ for a horizontal bed)
- $\bar{u}$ is the averaged flow velocity $[m/s]$
- u' are the velocity fluctuations $[m/s]$
- C_m is the added mass coefficient $[-]$
- $\bar{a}$ is the averaged flow acceleration $[m/s^2]$
- a' are the acceleration fluctuations $[m/s^2]$
- d is the stone diameter $[m]$
- max refers to the use of an extreme value for the occurring forces
- $\Delta g d$ is what after some math remains as the resistance part of the stability formula $[m/s]$

The equation above will be the starting point of the stability formula proposed in this thesis. In the remainder of this section the flow phenomena captured by this formula will be elaborated. This is done mainly by referring to earlier studies, which showed that the stability of a stone in a bed protection depends on these loads.

Resistance

The resistance against movement of a stone is in practice mainly attributed to the submerged weight of an averaged-sized stone within a batch. Aspects as interlocking forces, orientation and packing characteristics are generally not explicitly taken into account. Therefore it can be seen as a safe assumption to represent the resistance only by the submerged weight of the used material. In case the stones are located on a slope, the submerged weight can be corrected by a slope factor K_s, but further elaboration of this factor is outside the scope of this thesis. Similar to many other stone stability formulas, in this study the resistance is assumed to be proportional to $(\rho_s - \rho_w) g d^3$.

Load

The main load forces that are predominant for stone stability are the drag force and a force due to inertia. The force due to inertia is most often linked to the lift force on a stone. For most hydraulic engineering purposes the influence of the viscosity of water is negligible compared to the forces due to inertia. The drag and lift forces then will be proportional to the stagnation pressure and accordingly the drag coefficient C_d and the lift coefficient C_l are more or less constant (Hofland, 2000). It can be concluded that for hydraulic engineering purposes the drag and lift force both are proportional to $\rho_w u^2 d^2$ (Schiereck and Verhagen, 2012).

With regard to equation 2.1, the velocity terms are representative for the drag force and the acceleration terms are representative for the force due to inertia. Basically the velocity terms together form an extreme velocity, and therefore an extreme drag force. Similar the mean acceleration and the acceleration fluctuations together can be interpreted as an extreme lift force. Splitting a time dependent quantity into a mean and a fluctuating component is called Reynolds decomposition. Below each load term is elaborated briefly.

Mean flow velocity
The stability formula of Shields (1936) is based on a momentum balance approach on an area considerably larger than one grain. By relating the dimensionless shear stress to the particle Reynolds number, a value of the Shields stability parameter is determined (Schiereck and Verhagen, 2012). The Shields formula is often used in practice, because it enables the use of the depth-averaged flow velocity. This is easier to determine than the velocity at the bottom of a channel. For uniform flows, the start of stone movement can be predicted quite well by the mean flow velocity. Nevertheless in non-uniform flow cases, other flow forces need to be taken into account to determine the stability of a stone. Therefore the Shields formula is not appropriate to assess the stability of a granular bed protection around a hydraulic structure. To enlarge the area of applicability of the Shields formula to non-uniform flow conditions, throughout the years some empirical correction factors are developed.

Velocity fluctuations
The velocity fluctuations generally are caused by large scale turbulence, of which especially the sweep events are important (Hofland, 2005). The influence of turbulence on stone stability is amongst others studied by Jongeling et al. (2003), Hoan (2008), Hoffmans (2006) and De Gunst (1999). All concluded that turbulence has a significant influence on the stone stability, but derived different terms to take the effect of the velocity fluctuations into account. The velocity fluctuations can directly be linked to the turbulent kinetic energy k by $k = 0.5\left({\sigma_{u_x}}^2 + {\sigma_{u_y}}^2 + {\sigma_{u_z}}^2\right)$. In recent studies to stone stability, k is often used to take the load by large-scale turbulence into account.

Mean flow acceleration
The mean acceleration term, also referred to as steady spacial accelerations, represents a force due to inertia. Physically phenomena that can be linked to this force are accelerations due to geometry as for example a steepening slope or a contraction. Also the effect of a jet flow on a bottom protection can be considered as a mean flow acceleration (Hofland, 2005). The influence of the averaged acceleration on stone stability is amongst others studied by Dessens (2004), Huijsmans (2006) and Steenstra (2014). Furthermore also waves can attribute to this load term. This is amongst others studied by Tromp (2004) and Peters (2014). All studies concluded that the force due to inertia should be included in the assessment of stone stability. This force can be represented by the mean flow acceleration as done in equation 2.1, or by a mean horizontal pressure gradient over the stone.

Acceleration fluctuations
The acceleration fluctuations can be used to represent the load caused by turbulent wall pressures (Hofland, 2005). The effects of turbulent wall pressures are studied by Hofland (2005) and implicitly taken into account in his stability formula. The turbulent wall pressures mainly contribute to the extreme lift force on a stone, thereby initiating stone movement. The acceleration fluctuations can be seen as the fluctuations of the force due to inertia. As such, this term can also be represented by horizontal pressure gradient fluctuations.

Max
As described in the intro of this section, it is assumed that the stone stability is governed by the occurrence of an extreme lift force, directly followed by an extreme drag force.

2.1.3. Other stability formulas

Isbash
Isbash (1932) derived his stability formula by describing the force balance of one single stone. He used the local flow velocity at the stone as a load parameter in his stability formula. Unfortunately no clear description was given on which height this velocity should be determined and also the determination of the stone diameter was not clearly defined (Schiereck and Verhagen, 2012). In practise the Isbash formula therefore is used for relatively large rocks with a known flow velocity at the stone, as for example in case of the flow of a bow thruster on a granular slope protection.

Notable is the fact that both Shields as Isbash came to a same proportionality for the load part of their formula, described earlier as the proportionality to the stagnation pressure $\rho_w u^2 d^2$ (Schiereck and Verhagen, 2012). As Isbash (1932) uses local load parameters, his approach might be interesting for this thesis.

Steenstra

In this thesis, special reference is made to the stability formula proposed in Steenstra (2014) (hereafter: Steenstra formula). The Steenstra formula is the first stability formula in which the forces due to flow velocity, large-scale turbulence and inertia are explicitly taken into account. Compared to equation 2.1, in the Steenstra formula only the force by the turbulent wall pressures (acceleration fluctuations) is not taken into account. Steenstra (2014) uses depth-averaged flow parameters to represent the force on the bed. For convenience, the Steenstra formula is given below.

$$\Psi_{RS} = \frac{\left(\max\left[\left\langle \bar{u} + \alpha\sqrt{k}\right\rangle_{L_m} \frac{L_m}{z}\right]^2\right) + C_{m:b}\left(\bar{u}\frac{\partial \bar{u}}{\partial x}\right)_{h_a} d}{K(\beta)\Delta g d}$$

With his stability relation, Steenstra (2014) obtained a good fit for an extended data set of different experiments from several different studies. The power relation between the entrainment rate Φ_E and the stability parameter Ψ_{RS} is shown in figure 2.1. The use of the entrainment rate will be shortly explained in section 2.1.5.

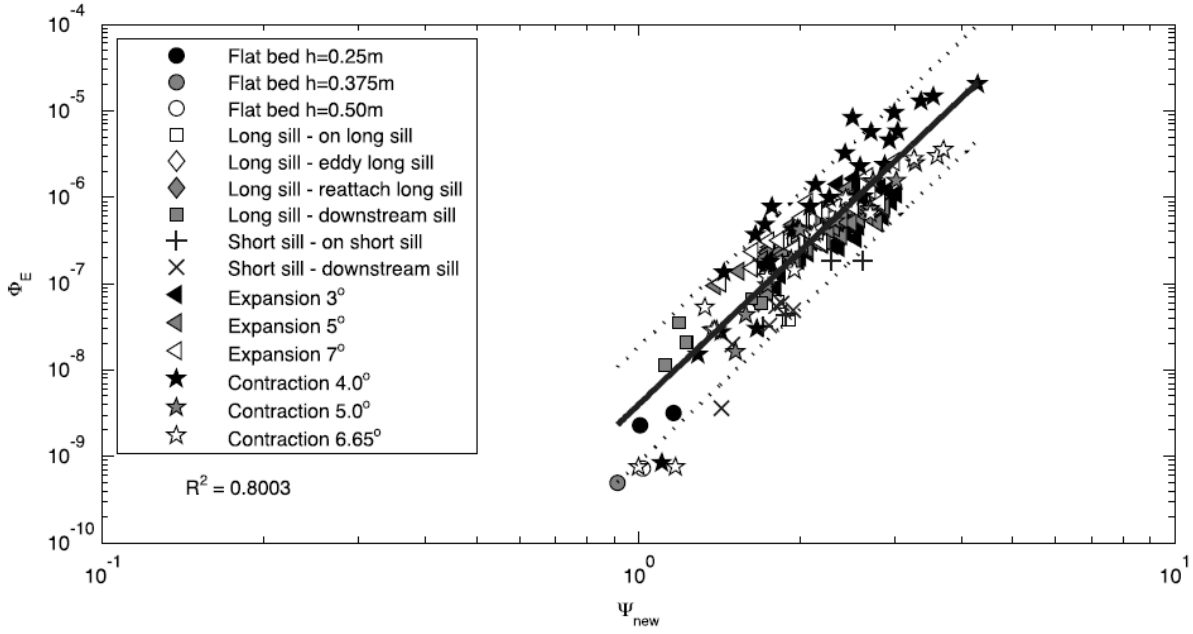

Figure 2.1: Power relation between Φ_E and Ψ_{RS} plotted on log-log scale (Steenstra et al., 2016)

2.1.4. Hydraulically rough boundary

The roughness Reynolds number Re_*, which is defined as $Re_* = \frac{u_* k_s}{\nu}$ can give an indication if a surface is hydraulically smooth or rough. The granular bottom material dealt within this thesis is an clear example of a hydraulically rough surface as the roughness Reynolds number is about 120 or higher. More information about the boundary layer and the differences between a rough and smooth boundary is given in section P.1.

In Nikora et al. (2001) an approach for open-channel flows over a hydraulically rough bottom is proposed. In this approach amongst others a form-induced sublayer is described, which in this paper is assumed to be absent as a first approximation. For flow situations with a water depth h considerably larger than the roughness height k_s, the velocity profile is then subdivided into three regions, as depicted in figure 2.2. From the bottom to the water surface these are:

1. $z_{mbl} < z < z_r$: Interfacial sublayer. The flow in this layer can be described by a linear distribution.
   In which:
   z_{mbl} is the mean bed level, defined as :
   z_r is the upper limit of the roughness layer
2. $z_r < z < z_L$: Logarithmic layer. In this layer the flow can be described by:

$$\frac{\langle \bar{u} \rangle}{u_*} = \frac{1}{\kappa} \ln \frac{z}{z_r} + C \tag{2.2}$$

   In which:
   z_L is the upper limit of the logarithmic layer
3. $z_L < z < z_{ws}$: Outer layer. This is the main flow of which the velocity profile generally follows a parabolic distribution.
   In which:
   z_{ws} is the level of the water surface

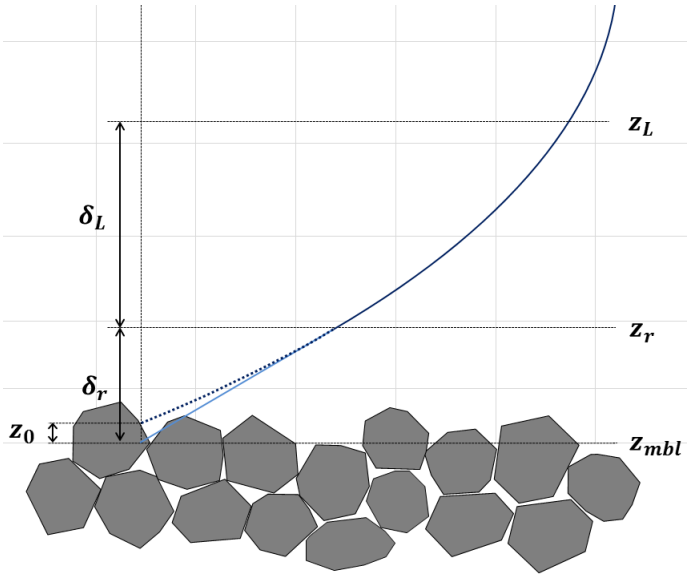

Figure 2.2: Velocity profile above a rough bed according to Nikora et al. (2001)

In figure 2.2 also the roughness length z_0 is indicated. This height is used in the wall functions that are generally used for rough boundaries. More about this is explained in section P.1.3.

2.1.5. Dimensionless entrainment rate Φ_E

The dimensionless entrainment rate Φ_E is a dimensionless form of the volume entrainment rate E. In Hofland (2005), a methodology is proposed to use the dimensionless entrainment rate for experiments in which damages to a coarse granular bed are measured. Similar to the volume entrainment rate E, the dimensionless entrainment rate Φ_E represents the number of stones that are transported out of a certain measuring area during a certain measuring time. In contradiction to the bed load transport, Φ_E is a local damage parameter, just like a stability parameter Ψ is a local stability parameter (Hoan, 2008). As the relation between Φ_E and Ψ depends on local parameters only, it should also be valid in non-uniform flow cases (Hofland, 2005). Moreover, because both parameters are dimensionless, the relation can be scaled easily. After Hofland (2005), the dimensionless entrainment rate is amongst others used in Hoan (2008) and Steenstra (2014). Because in this thesis, a direct comparison is made with the results of Steenstra (2014), and because the relation between Φ_E and Ψ is scalable, in this research also use is made of the dimensionless entrainment rate Φ_E.

The volume entrainment rate E is for rough granular material defined as:

$$E = \frac{nd^3}{AT} \tag{2.3}$$

in which:

- n = the number of stones that moved out of a certain measuring area, during a certain measuring time
- d = the stone diameter (d^3 represents the volume of the stone)
- A = the measuring area
- T = the measured time

The dimensionless entrainment rate Φ_E can be derived from the volume entrainment rate E by formula 2.4.

$$\Phi_E = \frac{E}{\sqrt{\Delta g d}} \tag{2.4}$$

in which:

- Δ = the relative submerged density of a stone in water, defined as $\frac{\rho_s - \rho_w}{\rho_w}$

Compared to sediment transport, stone movement in a granular bed protection should happen sporadic (no continuous transport). The stability parameter Ψ will generally be close to the critical stability parameter Ψ_c. According to Mosselman and Akkerman (1998), the relation between Φ_E and Ψ then should have the form of equation 2.5.

$$\Phi_E = a\Psi^b \tag{2.5}$$

The relation between Φ_E and Ψ is often presented in plots like figure 2.1 of Steenstra et al. (2016). Reading such graphs, one should be aware that Φ_E depends on the stone diameter, the relative submerged density of stone in water, the measured area and the measured time. A Φ_E-value of for example 10^{-8} will therefore represent a different amount of damage for different cases. This is shown by the example in appendix A.

It can be concluded that, to determine if a certain Φ_E-value represents many or less damage, it should be related to a certain time and area, that are in line with the analysed case. Φ_E can therefore be seen as a relative damage parameter.

Based on the example of appendix A, and the presented results of Steenstra et al. (2016) and Hofland (2005), an indication of different damage regions in a Ψ-Φ_E plot, is given in figure 2.3. These regions are just indicative, as an example to show how a Ψ-Φ_E plot can be interpreted. The figure is based on the results of Steenstra et al. (2016), shown earlier in figure 2.1.

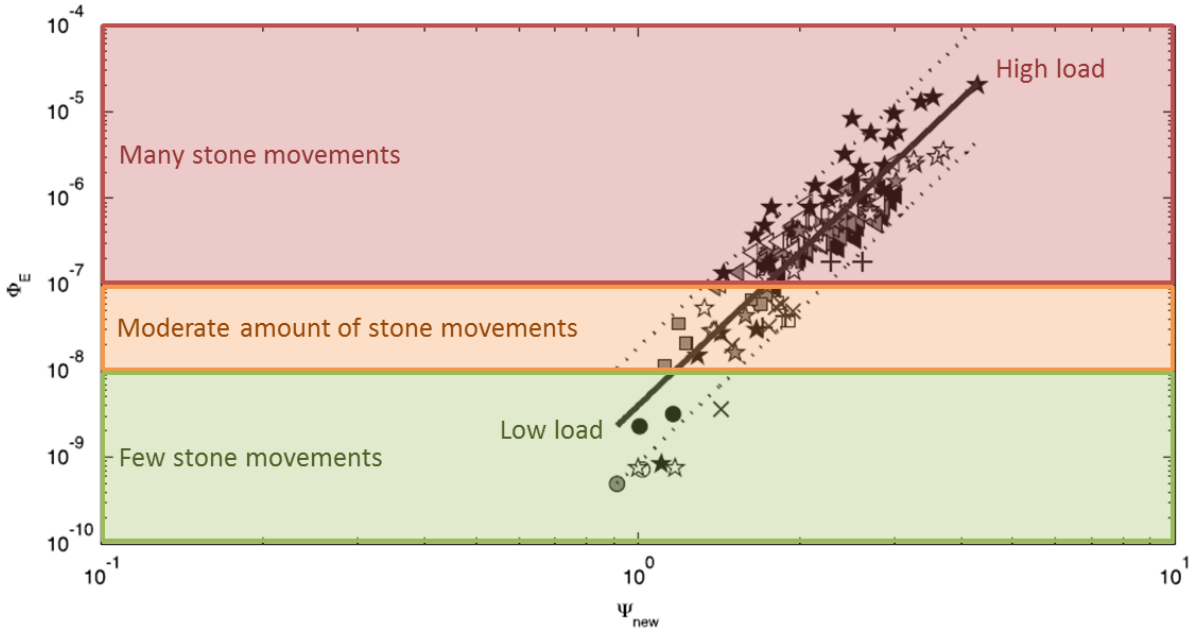

Figure 2.3: Indication how a Ψ-Φ_E plot can be interpreted (adjusted from Steenstra et al. (2016))

In Steenstra et al. (2016), it is mentioned that for uniform flow, a value of $\Phi_E = 10^{-8}$ is corresponding to the critical Shields value of 0.03. This value of the Shields parameter is often used as an indication for the "start of stone movement" of granular material. Graphs presented in Hofland (2005), as well as the example in appendix A, seem to subscribe that $\Phi_E = 10^{-8}$ is a reasonable assumption for the start of stone movement.

2.2. Computational Fluid Dynamics Models

In CFD modelling the Navier-Stokes equation are solved. To do this, one has to choose a method to deal with the closure problem. This can be done in several ways, for which different modelling methods are available. These modelling methods will be elaborated briefly in this section. More information about the Navier-Stokes equation and the closure problem can be found in section P.2.2.

In this section, the terms "modelling" and "resolving" are used frequently. It is important to understand the difference, as this is essential for the interpretation of simulated turbulence and boundary layers. When something is modelled, it is not "physically" present in the model. Only the physical consequences of the modelled phenomenon are taken into account by certain parameter or function. When something is resolved, an attempt is made to represent the resolved phenomenon as accurate as possible.

2.2.1. Modelling method

In section P.3.1, the considered modelling methods for this thesis are described. They can be classified as indicated below:

Turbulence fully modelled

1) RANS

Eddy resolving modelling techniques (Scale-Resolving Simulations)

2) DES
3) LES
4) DNS

Combining the statements in the problem definition (section 1.2) with the information from the literature study section P.3.1, in this thesis the choice is made to explore the possibilities of DES in order to determine the stone stability. The reasons for this choice are summarized on the next page.

- In RANS the effect of turbulence is modelled, whereby the velocity fluctuations that occur in reality are not simulated. Stability formulas based on RANS-output are therefore based on time-averaged quantities. The study of Hofland (2005) showed that the start of stone movement is governed by a combination of extreme forces. In contrast to RANS models, time-dependent simulation methods as the eddy resolving techniques should be able to reproduce these extreme values of the governing load situation.
- Resolving the turbulent eddies enables the use of local flow parameters instead of depth-averaged flow characteristics, because the extreme forces on the bed can be determined.
- It should be able to reproduce the turbulent kinetic energy profile better with a DES than a RANS model, as the large anisotropic turbulent scales are resolved instead of modelled. Exactly those eddies cause the largest inaccuracies for a RANS model, as for RANS implicitly an isotropic eddy viscosity is assumed. By resolving the large energy containing turbulent scales, the energy should be distributed better throughout the simulated domain.
- Not yet all eddy resolving simulations are appropriate for hydraulic engineering purposes. In a LES as well as in a DNS, the boundary layer needs to be resolved. This requires a lot of computational time and power, because the grid cells and the corresponding time steps need to be very small.

A disadvantage of a DES is that for the stone stability at the place of interest i.e. near the bottom, the turbulent quantities are modelled instead of resolved. Nevertheless a DES is expected to predict the turbulent quantities better than a RANS model, as exactly those large anisotropic turbulent eddies that cause the largest inaccuracies in a RANS model, are resolved in a DES. So in flow cases dominated by the effects of large anisotropic turbulent eddies, a DES should perform significantly better than a RANS model. In hydraulic engineering these cases are numerous, especially near hydraulic structures were stone stability relations are be applied for the design a of granular bed protection. This makes it interesting to explore the potential of a DES for the assessment of stone stability.

2.2.2. Detached Eddy Simulation

In this section some improved versions of the original DES formulations are discussed. In this thesis, use is made of the default settings in the used modelling software Star CCM+, which are the IDDES formulations of the chosen turbulence model.

The DES tries to combine RANS and LES formulations in such a way that accurate results can be obtained without the need of an excessively amount of computational time and power. In a DES the switch between the RANS region and the LES region is determined by the turbulent length scale. In a RANS model this length scale will be derived from the calculated turbulent model quantities, but for a LES the turbulent length scale is equal to the grid size. The border between the RANS and LES region is visualised in figure 2.4.

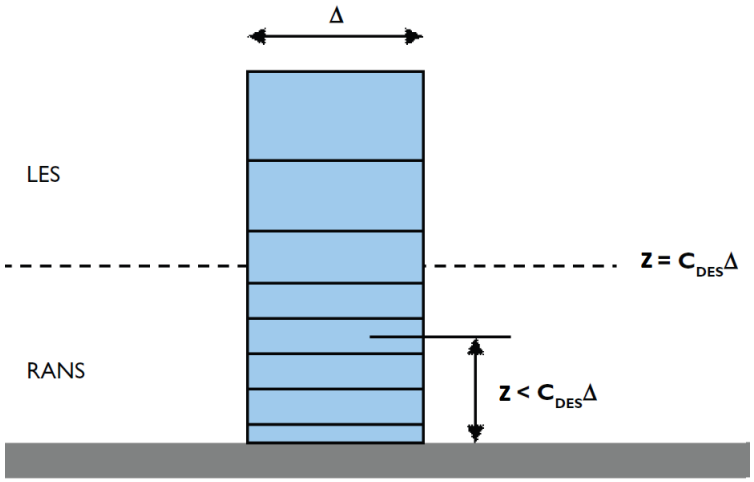

Figure 2.4: Criterion between RANS and LES-mode visualised (adjusted from Rodi et al. (2013))

The criterion for which length scales the switch between LES and RANS is made, is stated in the IDDES formulations. These are partly explained and written down in appendix C. For the complete set of model equations and coefficients is referred to the Star CCM+ (2018).

Due to the LES region in a DES, the solution is very sensitive to the grid resolution. Throughout the years some improvements has been proposed to overcome some of the drawbacks encountered for the original DES. These enlarged the area of applicability for the DES and thereby turned it into a promising modelling method for hydraulic engineering purposes. Two popular improvements are treated below.

1. Delayed Detached Eddy Simulation (DDES)
   By adding an extra term to the limit function for the turbulent length scale, the switch to the LES mode is forced to be outside the boundary layer, even in case of LES grid (Spalart, 2009). Inside the boundary layer the RANS and LES mode will produce significantly different turbulent quantities, as with RANS only the effect of turbulence is modelled while LES really tries to resolve turbulence. An early switch to the LES mode will cause a log-law mismatch and therefore should be prevented.
2. Improved Delayed Detached Eddy Simulation (IDDES)
   The most important difference with the DDES is that the definition of the LES subgrid length scale is made dependent on the wall distance. Practically this improvement means that a DES now also should be applicable to attached boundary layer flows, as the log-layer mismatch between the RANS and LES region will be resolved (Spalart, 2009). Also the switch to the LES formulations can now take place inside the boundary layer without introducing large inaccuracies.

A drawback of DDES as well as IDDES is that the solution might depend on the initial conditions (Spalart, 2009). Nevertheless IDDES will probably be the default formulation for hydraulic engineering applications. Successful applications of IDDES in aerodynamics are reported in Mockett and Thiele (2007) and Shur et al. (2008), among which flow over a backward facing step.

A side note must be placed, as it is hard to pose a clear distinction between some versions of LES and DES. For example, the only differences between an Improved Delayed DES (IDDES) with LES-grid and a Wall-Modelled LES (WMLES) seems to be that IDDES uses an existing RANS model at the solid boundary, where WMLES uses a RANS-like formulation at the solid boundary. Some versions of what in literature is called LES, therefore might be appropriate for hydraulic engineering purposes.

2.2.3. Turbulence models

In this section will be elaborated on the approach that is used to model the effect of turbulence. As mentioned in paragraph P.2.2, this choice determines which assumptions are used to resolve the Navier-Stokes equation. A first choice can be made between turbulence models that use the eddy viscosity (Boussinesq) approach and Reynolds Stress Transport Models. Based on the computational expenses needed for Reynolds Stress Transport Models and because the eddy viscosity based models perform well enough for most cases, the use of eddy viscosity based turbulence models is far more popular. Moreover, for the available DES formulations, eddy viscosity based turbulence models are used for the closure of the RANS model. For this thesis therefore the choice is made to only look into the eddy viscosity based turbulence models. The Reynolds Stress Transport Models are not elaborated further.

With eddy viscosity based turbulence models, reference is made to turbulence models that obey the Boussinesq hypothesis. The Boussinesq hypothesis states that the transfer caused by turbulent eddies can be modelled by the introduction of an artificial eddy viscosity, often denoted as μ_t. Over time several eddy viscosity turbulence models are developed that mainly differentiate in their complexity and their performance for important flow phenomena like separations and wall boundary layers. The most popular eddy viscosity turbulence models are the:

- Spalart-Allmaras model: Only one additional transport equation for the turbulent viscosity
- k-ε model: Two additional transport equations. One for the turbulent kinetic energy k and one for the turbulent dissipation rate ε.
- k-ω model: Two additional transport equations. One for the turbulent kinetic energy k and one for the specific dissipation rate ω.

Of these three basic models, again some different versions exist that are expected to perform better for certain specific flow conditions. One of these customized models will be elaborated in the next section.

2.2.4. SST k-ω turbulence model

According to several studies (e.g. Menter et al. (2003) and Zhang (2017)), the SST k-ω model performs better than other turbulence models for separating flows. Also in the already existing model of the Roompot 8 of the Eastern Scheldt Barrier, the SST k-ω model is used. Therefore this turbulence model will also be used for the modelling of the long sill experiments.

The Shear Stress Transport (SST) k-ω model, developed by Menter (1994), is a mixture of the original k-ω model and the high-Reynolds-number version of the k-ε model, as depicted in figure 2.5. It uses a blending function to switch from the k-ω model near a solid boundary, to the k-ε model away from the wall and in free-shear layers. For this purpose the k-ε formulations are rewritten to a k-ω format.

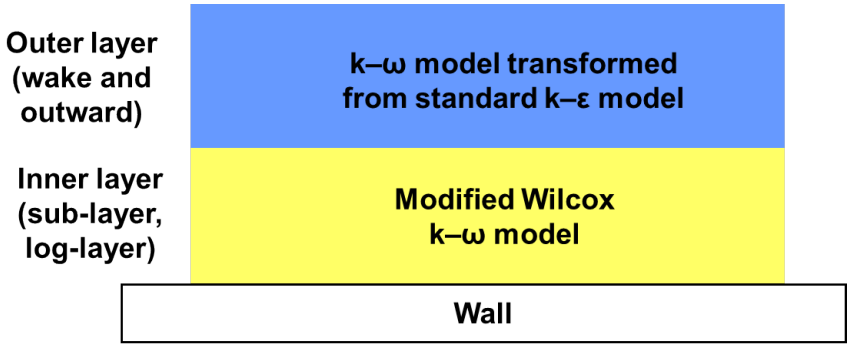

Figure 2.5: Principle of SST k-ω model (Saadati, 2009)

Just as the original k-ω and k-ε model, the SST k-ω model is based on the Boussinesq hypothesis. This means that the closure problem mentioned in paragraph P.2.2 is solved by representing the unknown Reynolds stresses and velocity gradients by the eddy viscosity μ_t. SST k-ω is a two-equation model, which means that the eddy viscosity μ_t is determined by the results of two transport equations. For the SST k-ω RANS model these two equations are:

1. The transport equation for the turbulent kinetic energy k

$$\frac{\partial}{\partial t}(\rho k) + \nabla \cdot (\rho k \bar{\boldsymbol{v}}) = \nabla \cdot [(\mu_w + \sigma_k \mu_t) \nabla k] + G_k + G_{nl} + G_b - 0.09 \rho f_{\beta^*} (\omega k - \omega_0 k_0) + S_k$$

2. The transport equation for the specific dissipation rate ω (dissipation rate per unit turbulent kinetic energy)

$$\frac{\partial}{\partial t}(\rho \omega) + \nabla \cdot (\rho \omega \bar{\boldsymbol{v}}) = \nabla \cdot [(\mu_w + \sigma_\omega \mu_t) \nabla \omega] + G_\omega + D_\omega - \rho \beta f_\beta (\omega^2 - \omega_0^2) + S_\omega$$

Of these equations the meaning of the different terms can be described from left to right as:

- **First term = Transient term**
  Accumulation of the transported quantity in a control volume over a certain time
- **Second term = Convection term**
  Transport due to the presence of the velocity field
- **Third term = Diffusivity term**
  Transport due to molecular diffusion caused by turbulent eddies
- **Fourth term = Production term**
  Production of transported quantity. For example in case of the turbulent kinetic energy k, the production of k due to mean velocity gradients
- **Fifth term = Dissipation term**
  Dissipation of the transported quantity. For example due the natural dampening of turbulent eddies.
- **Sixth term = User defined source term**
- **Seventh term of the ω-equation = Cross-diffusion term**
  Extra term because the k-ε model is rewritten to a k-ω formulation to enable the blending of these two models

Further elaboration of the equations and model coefficients can be found in appendix C. For the complete set of model equations and coefficients is referred to the Star CCM+ (2018). A more reader-friendly description of the IDDES SST k-ω formulations can be found in Gritskevich et al. (2012).

2.2.5. Wall treatment

As explained in 2.2.2, an IDDES seems to be similar to a Wall Modelled LES. Compared to a pure LES, the difference is that in an IDDES the boundary layer is modelled instead of resolved. When the boundary layer is modelled, it means a wall function is assumed to model the effects of (part of) the boundary layer. Use is made of the law of the wall (explained in section P.1.3).

In a pure LES, the boundary layer is resolved. As a general rule, at least 10 to 15 cells are required over the height of the inner boundary layer to simulate the physics in this region (Saadati, 2009). For high-Reynolds-number flows, grid sizes in the order of 0.1 mm or even 0.01 mm are therefore not unimaginable. Considering the fact that most hydraulic engineering problems have a domain of at least several meters, one can image that resolving the boundary layer is practically impossible for most hydraulic engineering purposes.

The difference between modelling and resolving the boundary layer is visualised in figure 2.6.

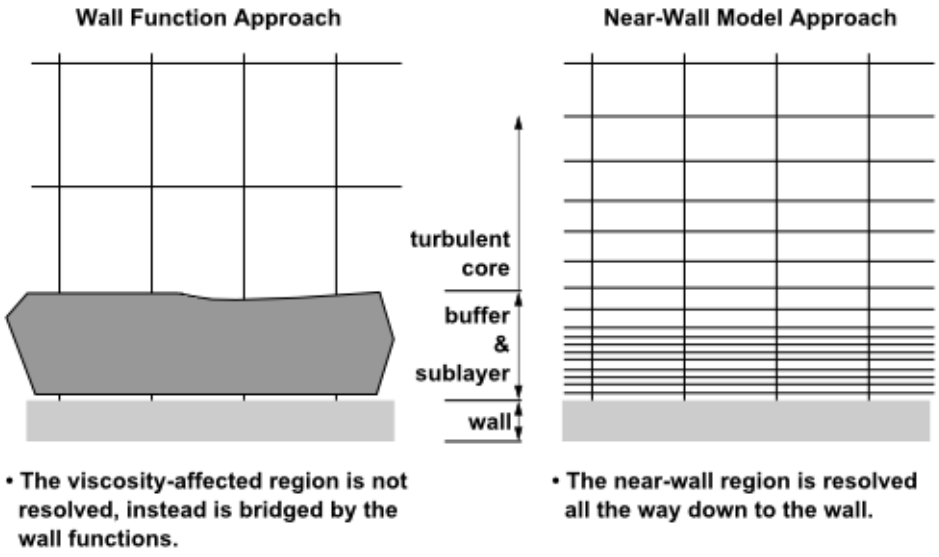

Figure 2.6: Left: Modelling the boundary layer (high z^+ wall treatment)
Right: Resolving the boundary layer (low z^+ wall treatment) (Saadati, 2009)

The chosen wall treatment (modelling or resolving) should correspond to the way the wall roughness is included in the model and to the size of the grid cell at the boundary (hereafter called wall cell).

In numerical modelling there are two options to account for a hydraulically rough bottom.

1. A measured bottom profile is included in the geometry of the simulation. The surface roughness then will be the roughness of the surface of a stone, which might be hydraulically smooth. In this case resolving the boundary layer could result in an accurate representation of the velocity profile. It is also possible to model the boundary layer, which will save a lot of required computational time and power, as explained earlier in this paragraph.
2. A flat bottom with a general surface roughness (e.g. k_s). In this case the boundary layer has to be modelled by a wall function. Resolving the boundary layer cannot result in an accurate representation of the velocity profile, as the numerical software does not know the shape of the modelled bed. Besides that, no algorithms are available to resolve the inertial sublayer present between the roughness elements. A solution for this is described in Stoesser (2010), in which the introduction of an extra momentum sink to the transport equation is proposed. This will create an imaginary rough bed in the numerical software.

The appropriate size of the wall cell is indicated by the z^+ values. For rough surfaces, z^+ is determined as:

$$z^+ = \frac{z}{z_0}$$

In which z is the distance from the wall and z_0 is the roughness length indicated in figure 2.2.

In Star CCM+, the boundary layer is modelled when the high z+ wall treatment is selected. The z^+ values then should approximately be in between the range $30 < z^+ < 150$. The upper limit depends on the Reynolds number of the simulated flow. In literature several divergent values can be found for this, in general within the range of 60 to 300.

In this thesis the all z^+ wall treatment of Star CCM+ is used, because strictly speaking not all wall z^+ values are in the high z^+ range. Therefore this is the default wall treatment in Star CCM+. However the blending function used in this wall treatment is defined as:

$$g = e^{-\frac{Re_z}{11}} \text{ with: } Re_z = \frac{\sqrt{k}z}{\nu}$$

A fast estimate for the value of this blending function gives:
$k \sim 0.01[m^2/s^2]; z \sim 0.003[m]; \nu = 1 * 10^{-6}[m^2/s]$
$\rightarrow Re_z \sim 300[-]$
$\rightarrow g \sim 1.43 * 10^{-12}[-]$

The blending function g being nearly zero reveals that in the largest part of the modelled domain the model specified wall boundary conditions can be assumed equal to the high z^+ values. Therefore the wall boundary conditions belonging to the SST k-ω model with a high z^+ wall treatment are listed below.

Shear velocity /Reference velocity /Friction velocity

$$u_* = \sqrt{\beta^{*0.5} k}$$

Wall-cell production

$$G_k = \frac{1}{\mu_w}\left(\rho u_* \frac{u}{u^+}\right)^2 \frac{\partial u^+}{\partial z^+}$$

Wall-cell specific dissipation

$$\omega = \frac{u_*}{\sqrt{\beta^*}\kappa z}$$

2.2.6. Mesh and Courant number

In an IDDES, the largest part of the modelled domain will be solved according to the LES formulations. The resolved turbulent scales, and thereby the accuracy of the simulation, therefore are directly dependent on the size of the applied numerical grid. At least two grid cells are needed to resolve one eddy (Star CCM+, 2018).

To resolve as many turbulent scales as possible, one could strive to apply very small grid cells. Nevertheless, as the grid size is decreasing, the number of grid cells needs to be increased, whereby also the required computational power will increase. As a general rule it can be stated that, the more turbulent scales one wants to resolve, the smaller the required grid sizes, the higher the required amount of grid cells, and the larger the computational time and costs will be.

In modelling with an eddy resolving technique, smart use can be made of the inertial sub-range of the turbulent energy spectrum. As explained in section P.2.1, the inertial sub-range is reached when the eddies are isotropic, and their breakdown into smaller scales follows a fixed pattern. It is desired to resolve turbulence to the length scales were this inertial sub-range is reached. In the turbulent energy spectrum this region can be recognised as the part with a slope of $k^{-\frac{5}{3}}$. Because the breakdown towards heat from this point on is predictable, it can be modelled without introducing large uncertainties or inaccuracies. Often the Taylor micro-scale is used as an indication for the turbulent scale for which the inertial sub-range is reached. It can be estimated by $Re^{-\frac{1}{2}}$.

In figure 2.7, an idealized double-logarithmic turbulent energy spectrum is shown. Three different regions of turbulent scales are visible, together with an indication to what extend these turbulent scales generally are resolved for the different modelling methods. For the DES, this is not yet known. In this thesis, it will be checked what the effective resolution of the used DESs is.

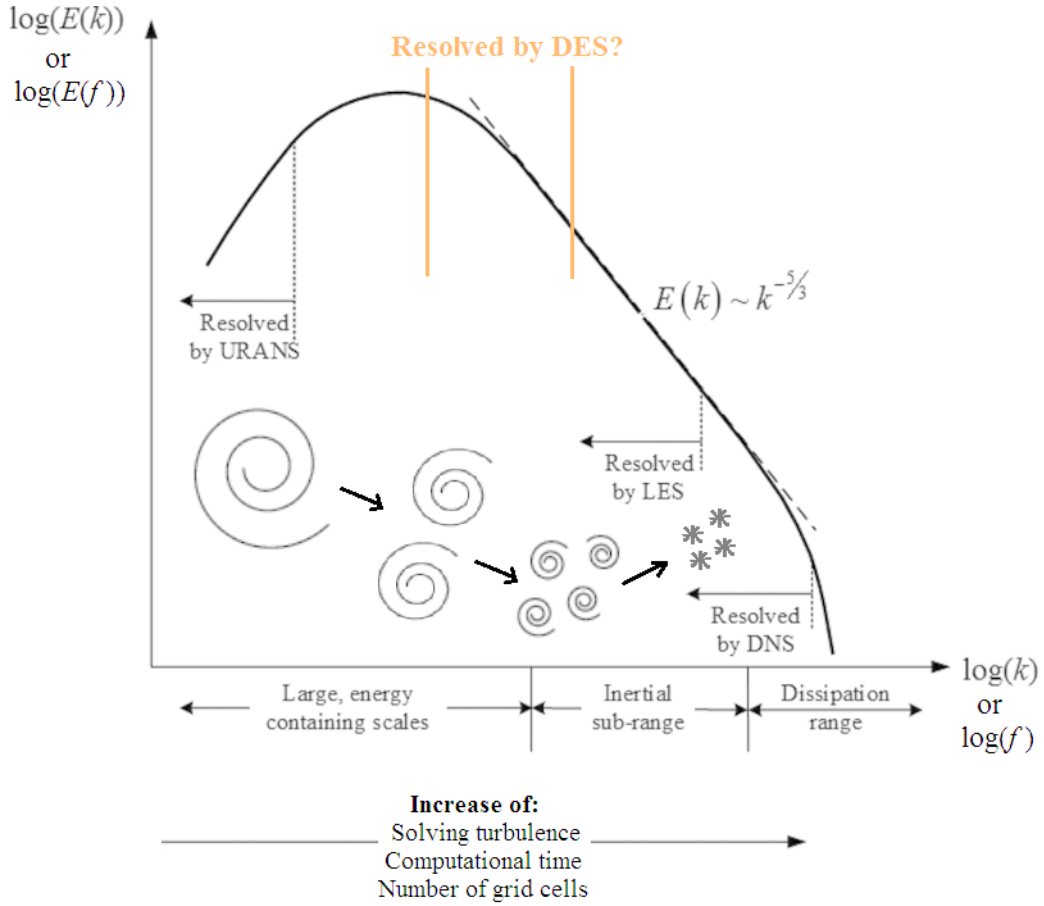

Figure 2.7: Energy density spectrum including an indication of the energy cascade and the turbulent scales that are resolved for the different modelling methods (adjusted from Thompson et al. (2015))

Courant number

The Courant number (CFL number) is a dimensionless ratio between the distance a particle travels during a certain time interval and the applied grid size, defined as: $CFL = \frac{u\Delta t}{\Delta x}$. To limit the numerical error made in an eddy resolving technique, one should try to keep the CFL number smaller or equal to 1. Therefore, when refining the mesh in a numerical simulation, it is advised to adjust the time step such that $CFL = 1$ for the smallest grid cell at the region with the highest flow velocities.

2.3. Experiment Jongeling

The experiments chosen for this study are described extensively in Jongeling et al. (2003). First the general objectives of these experiments will be given, and a choice will be made which experiments will be simulated. Next the research method will be described, together with a the properties of the experiment that are considered most relevant for the correct modelling of the flow.

2.3.1. Aim of the experiments

The experiments of Jongeling et al. (2003) are part of a study towards the improvement of the design of granular bed protections. An extensive experimental series was executed, in which flow characteristic and damages to a granular bed protection were measured. Of each experiment, two-dimensional CFX models were made, in order to develop a stone stability formula that can rely on the output of this modelling method. The aim of the study of Jongeling et al. (2003) was similar to the aim of this thesis, only in Jongeling et al. (2003) RANS models were used instead of a 3D eddy resolving technique.

2.3.2. Long sill experiment to Eastern Scheldt barrier

In figure 1.3 a velocity field of the flood flow at the Eastern Scheldt barrier is visualised. As indicated, different flow regions can be distinguished. Towards the gates, the flow is accelerating. Separation occurs at the sill, and after the sill the flow is decelerating again, creating a highly turbulent flow region. These and more flow regions are schematized in figure 2.8, on which a comparable flow configuration is depicted.

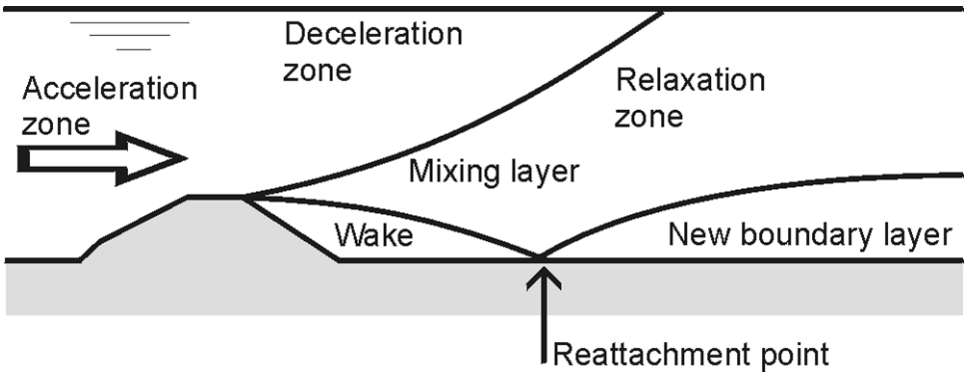

Figure 2.8: Flow regions over a sill or back-ward facing step were seperation occurs (Verhagen, 2017)

In this thesis, the choice is made to model the long sill experiments of Jongeling et al. (2003), because here the same flow regions were present as at the Eastern Scheldt barrier and figure 2.8. The geometry of these experiments are given in the next subsection, but as the name of the experiments already reveals, the geometry is similar to a stretched version of the sill at figure 2.8. The flow velocities over the long sill were high enough to induce flow separation at the downstream edge. Both long sill experiments are modelled, one with a water depth of $h = 0.375$ m and one with a water depth $h = 0.50$ m.

2.3.3. Geometry experiment

The dimensions of the flume and the long sill are given in figure 2.9.

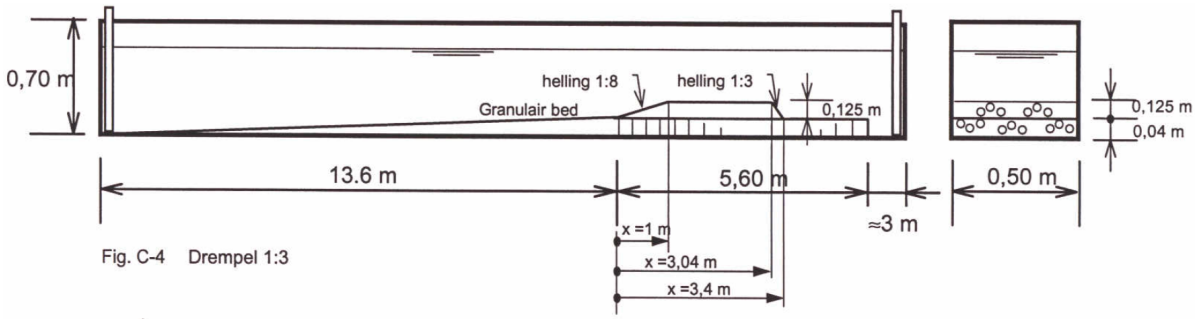

Figure 2.9: Experimental set-up of the experiment "long sill" Jongeling et al. (2003)

The laboratory flume had a length of more than 20 m, of which the first 19.2 m were fully covered by stones with a nominal diameter d_{n50} of 6.2 mm. Of these 19.2 m, the first 13.6 m had a gradual slope from the bottom of the flume towards a layer thickness of 40 mm at the start of the measuring area. This large approach length towards the measuring area was applied to obtain flow characteristics that are adapted to the rough bottom. For the long sill experiment with $h = 0.375$ m, this approach length is approximately 36 times the water depth. For the experiment with $h = 0.50$ m this is equal to approximately 27 times the water depth.

In the measuring area, coloured stones were placed in strips that covered the entire width of the flume, and had a width of 0.10 m in the flow direction. In total eight sequences of strips in seven different colours were applied, to enable the tracking of damages to the bed. An impression of the measuring area with the coloured strips is given in figure 2.10.

Figure 2.10: Impression sketch of the experiment "long sill" described in Jongeling et al. (2003) (not to scale)

At the end of the flume, the water was flowing into a return pipe in which the discharge was measured. At the beginning of the flume, this water was pumped back the through the bottom of the flume, causing a significant amount of turbulence.

2.3.4. Measuring equipment

The velocities were measured in x-, y- and z-direction, respectively streamwise direction, perpendicular to the flow direction in the horizontal plane and perpendicular to the flow direction in the vertical plane. A Laser Doppler Velocimeter (LDV) was used for the velocities in the x- and z-direction and an Electro Magnetic Flowmeter (EMF) was used for the velocities in the x- and y-direction. Because the LDV is able to measure the velocities more accurately, the data of the EMF was corrected via the measurements in the x-direction. With this correction, also was accounted for the fact that the LDV and the EMF cannot measure at the same position. The EMF was located 6 cm downstream of the LDV. The used sample frequency of 100 Hz was assumed to be sufficient, as the bulk of the total turbulent kinetic energy was expected to be present in the lower frequency range under 20 Hz. The discharge was measured by a discharge meter in the return pipe of the closed water circuit.

The measuring accuracy of the LDV is estimated to be about 0.01 m/s. The results of the EMF are considered to include a slightly larger measuring error. The measurements near the bed are expected to contain are larger measuring error, as near the bed the velocity gradients are relatively large. A slight discrepancy between the intended measuring height and the actual measuring height, can have a significant influence on the measured velocities.

2.3.5. Execution

At the beginning of each test, the flume was filled to a certain height and the still-standing water level was noted as the water depth of that specific experiment. After this, the discharge was slowly increased until at the certain point the state "start of stone movement" was observed. The state "start of movement" in the used experiments was defined as the movement of five to ten stones in a time span of five minutes inside the total measuring area.

When this initial state of stone movement was detected, the flow velocities in all directions were measured at several locations. At every location the velocities were sampled for three minutes in the centre of the flume at multiple heights above the bed. At the end of each experiment, the number of stones that moved out of their strip, was counted to map the amount of damage that occurred during the time span of the test.

The cross-sections for which the velocity signals are measured, are indicated in figure 3.8. For convenience, in this thesis the same numbering is used.

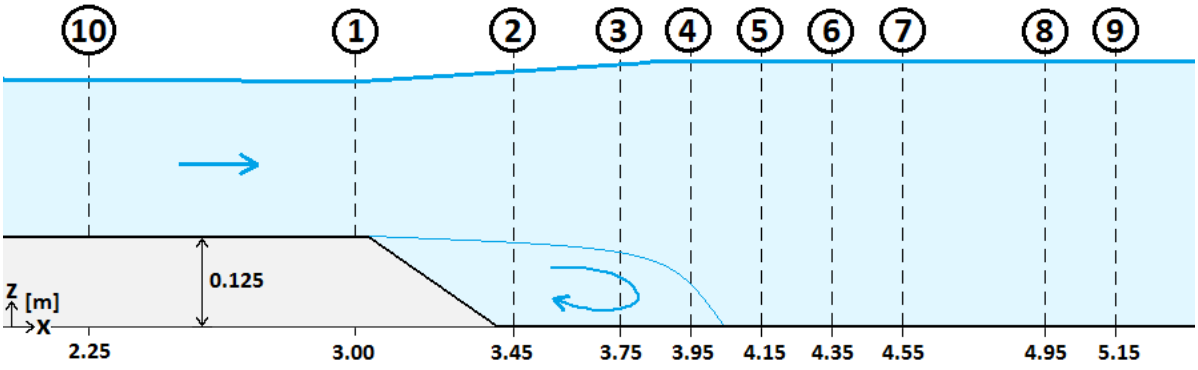

Figure 2.11: Measured cross-sections, numbered in accordance with Jongeling et al. (2003)

2.3.6. Measured damage

In figure 2.12, the measured damages of long sill experiment with $h = 0.375$ m of Jongeling et al. (2003) are shown.

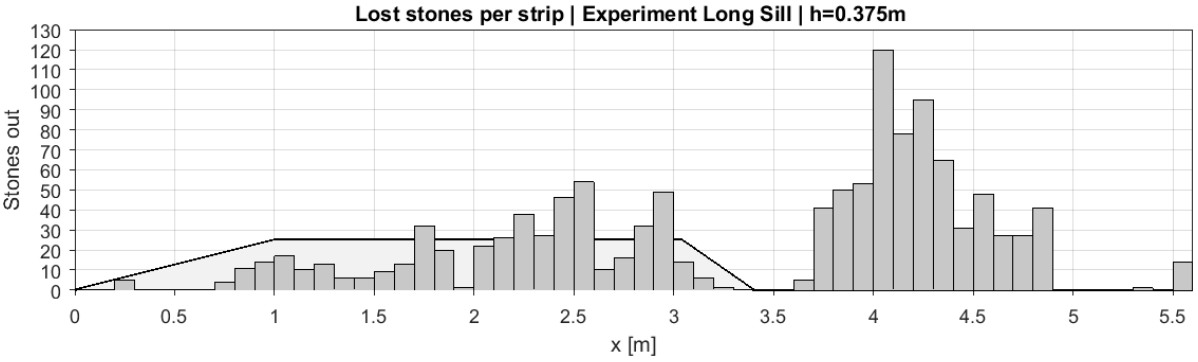

Figure 2.12: Stones that left their strip at the end of the long sill experiment with $h = 0.375$ m

Most damage is observed between $x = 4.00$ m and $x = 4.30$ m. This is about 8 to 10 step heights away from the point of separation at the downstream edge of the sill, and just after the location were the reattachment point was set for this experiment. The reattachment point was determined to fluctuate around cross-section 4 at $x = 3.95$ m, which is about 7 or 8 step heights downstream of the point of separation. Thereby the locations of the reattachment point and the largest damages are in agreement with many other experimental studies like Nezu and Nakagawa (1989) and De Gunst (1999).

Nevertheless, the total amount of measured stone movements are considered too low to obtain a statistically converged damage field. A few stone movements less or more in a certain strip, can change the image 5.3 significantly. Moreover, a difference of about 90 stone movements is present between two graphs about the counted stone movements for one and the same experiment from Jongeling et al. (2003). This is a significant deviation on a total amount of about 1200 counted stone movements.

Dimensionless entrainment rates

In section 2.1.5, the use of the dimensionless entrainment rate is explained. To obtain similar plots as shown in figure 2.1, the damages presented above will be converted into dimensionless entrainment rates. Similar as derived in Hofland (2005), a correction factor of 2.83 is used to determine the volume entrainment rates. This factor is applied to account for the stone movements within a strip, or to a strip of the same colour.

The equation used to determine the dimensionless entrainment rates Φ_E for the damages of the long sill experiments of Jongeling et al. (2003) is given below.

$$\Phi_E = \frac{1}{\sqrt{\left(\frac{\rho_s - \rho_w}{\rho_w}\right) g d_{n50}}} * 2.83 \frac{n d_{n50}^3}{AT} \tag{2.6}$$

In which the following values are used for the long sill experiments of Jongeling et al. (2003):

- $\rho_s = 2.716$ [kg/m^3]
- $\rho_w = 1.000$ [kg/m^3]
- $g = 9.81$ [m/s^2]
- $d_{n50} = 0.0062$ [m]
- $A = 0.1 * 0.5 = 0.05$ [m^2]
- Long sill $h = 0.50$ m: $T = 31320$ [s]
  Long sill $h = 0.375$ m: $T = 31800$ [s]

In table 2.1, some common values of the dimensionless entrainment rate Φ_E are translated back into damage rates. In the second column the number of stone movements n is given per strip per hour. In the third column the Φ_E-values are converted to the number of stone movements n per m^2 per hour.

Φ_E	n per hour per strip	n per hour per m^2
10^{-6}	86	1724
10^{-7}	8.6	172
10^{-8}	0.9	17.2
10^{-9}	0.1	1.7

Table 2.1: Φ_E linked to the damages per hour per strip and per m^2 respectively

Start of stone movement

In Jongeling et al. (2003), the start of stone movement was defined as 5 stone movements over the entire measuring area in 5 minutes. Thereby, the number of stone movements for the strip with the highest damage, and the corresponding Φ_E, are belonging to the state "start of stone movement".

Nevertheless, taking the n-values of 2.1 into account, a Φ_E-value of 10^{-8} seems a safe assumption for the start of stone movement. Using this value as the start of stone movement for the long sill experiments of Jongeling et al. (2003), one can expect that each 70 minutes, one stone will move out of the analysed strip.

2.3.7. CFX modelling of the experiment

In table 2.2, some general information is given about the experiments that are modelled in this thesis, to ease the traceability of the used data. For the long sill experiment with h = 0.50 m, two CFX calculations are made. The second calculation, coded as "herh 17", is an improved version of the original simulation. In this improved calculation the discharge was increased and the turbulence model was changed, as explained further after table 2.2.

Case in this thesis	Experiment number in Jongeling et al.	Number CFX calculation in Jongeling et al.	Water depth stagnant water h [m]	Average discharge Q_{gem} [l/s]	Average velocity $\bar{u}$ [m/s]
LongSill-h = 0.375 m	11	16	0.375	99.7	0.55
LongSill-h = 0.50 m	12	17 & herh 17	0.50	166.1	0.68

Table 2.2: General information about the experiments of Jongeling et al. (2003)

The properties of the CFX models that are believed to be most relevant for this project, are listed below.

- The bottom is modelled flat with an general surface roughness of $2d_{n50}$. Compared to a roughness of d_{n50} and $3d_{n50}$, a bottom roughness of $2d_{n50}$ appeared to give the best results
- A surface roughness of 0.005 m is used for the glass side walls of the flume. Generally glass walls are modelled smooth in numerical modelling. In Jongeling et al. (2003), the surface roughness of 0.005 m was justified by the observation, that the connections between two glass sheets, caused some visible disturbances in the flow
- A free water surface approach was used to model the water surface of the long sill experiments. This appeared to give better results than a rigid lid approach
- The geometry of the model was adjusted such that the water was entering the flume through the bottom under an angle of 45°. Hereby some turbulence is created in the simulation, that in reality also was present at the upstream end of the flume
- First the standard k-ε turbulence model was used. For some tuned recalculations the RNG k-ε model was applied, which gave slightly better results
- For the long sill simulation with h = 0.50 m, better results were obtained when the discharge was increased by 5%

From the CFX modelling was concluded, that satisfying RANS results can be obtained, but that three-dimensional effects could not be neglected. The two-dimensional model needed to be adjusted ("tuned") to obtain a satisfying agreement between the simulation and the measurements.

2.3.8. Results of the CFX modelling

In figure 2.13 and 2.14 the simulated and measured velocity and turbulent kinetic energy profiles are given. For a more clear and complete overview is referred to the extended data and results given in the appendices of Jongeling et al. (2003).

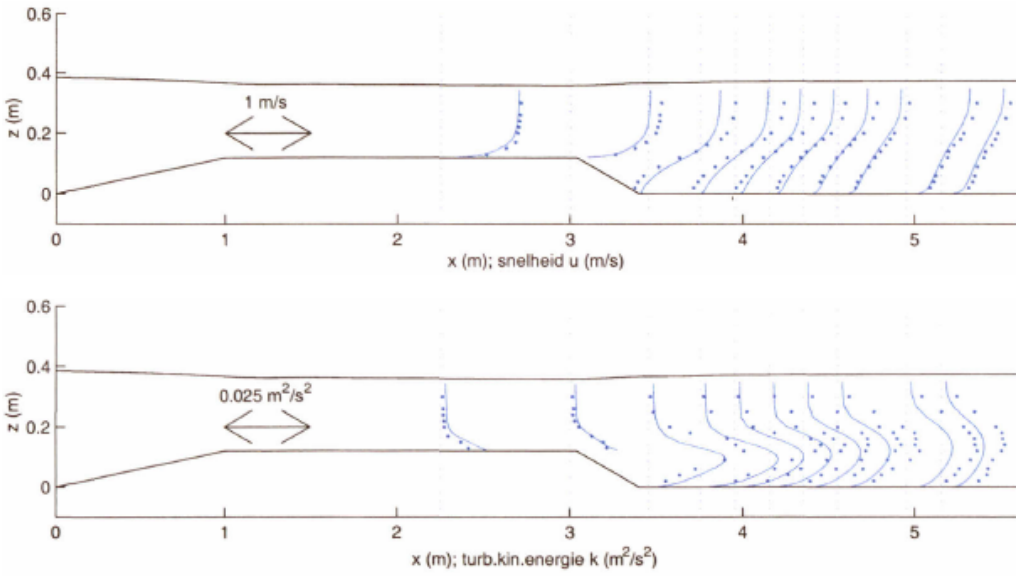

Figure 2.13: Validation of the velocity and TKE profiles of the long sill experiment with $h = 0.375$ m, obtained with CFX (Jongeling et al., 2003)

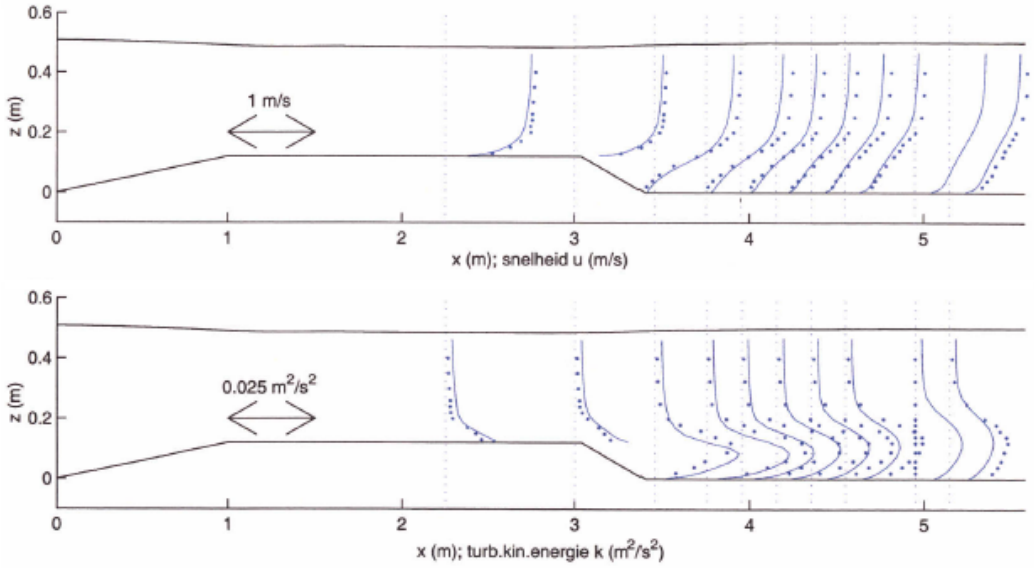

Figure 2.14: Validation of the velocity and TKE profiles of the long sill experiment with $h = 0.50$ m, obtained with CFX (Jongeling et al., 2003)

2.4. Eastern Scheldt case

In this section more information is given about the Eastern Scheldt case, described in section 1.1. First, the aim and some properties of the Roompot 8 simulations are elaborated. Second, the granular bed protection at the east side of the barrier at the Roompot 8 channel is discussed.

2.4.1. Roompot 8 simulations

Originally the Roompot 8 simulations are built to determine the influence of the tidal energy turbines on the discharge through the barrier. To include the rotating tidal energy turbines as accurate as possible, the choice is made to build a three-dimensional IDDES. The SST k-ω model is used as the underlying turbulence model for the RANS regions. Thereby the numerical scheme is similar to what is chosen for the long sill simulations.

The length of the modelled domain covers about 200 m at both the North Sea side, as the Eastern Scheldt side of the barrier. Over the width, gate 8 of the Roompot channel is modelled, together with half of gate 7 and 9. Multiple models are made for flood and ebb flows, caused by a certain water level difference over the barrier. The models used in this thesis are simulating a flood flow for a water level difference of 0.54 m over the barrier. In one of the used simulations the tidal energy turbines are included, in the other one they are absent. Below the boundary conditions are given.

- Downstream (Eastern Scheldt side) the water level is fixed by a pressure outlet
- Upstream (North Sea side) a velocity profile is implemented. During a few iteration steps, the velocity profile is adjusted such that the upstream water level was within plus and minus 1 cm of the intended upstream water level. No artificial initial disturbances are added to the implemented velocity profile
- The water surface is modelled according to the free water surface approach. A short elaboration of this boundary condition is given in section 3.2.3
- For the geometry of the bed, a three-dimensional sonar image, obtained from multibeam measurements, is implemented in the model. Thereby the bed roughness is included in the geometry of the model. The surface roughness of the implemented granular bed is modelled smooth
- At both sides, symmetry boundaries are applied

Both simulations (with and without turbines) are validated based on vertical Acoustic Doppler Current Profiler (ADCP) measurement of the flow through Roompot 8. The simulation with turbines is also validated to horizontal velocity measurements of ADCPs that are fastened to some of the tidal energy turbines. For both simulations, a good agreement is found between the measured and simulated velocities.

2.4.2. Granular bed protection at the Eastern Scheldt barrier

Figure 2.15 shows the original design of the bed protection at the Eastern Scheldt barrier. In the right upper corner also the allowed critical damages are mentioned.

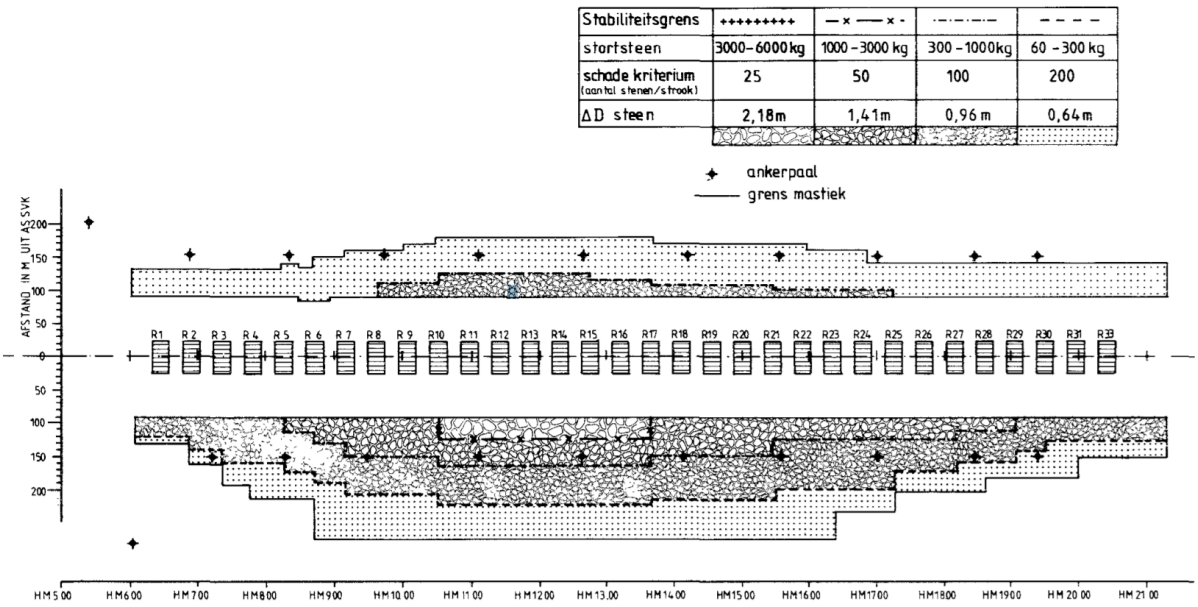

Figure 2.15: Original design of the bed protection at the Roompot channel of the Eastern Scheldt barrier, with in the right upper corner a table with the design damage criteria (Ministerie van Verkeer en Waterstaat, 1991)

As one can see, officially the granular bed protection starts at a distance of approximately 90 m of the Eastern Scheldt barrier. The area closer to the barrier is considered part of the sill construction. Nevertheless, throughout the years, extra stone deposits took place to reinforce or repair the bed protection, also in the area close to the barrier. In table 3.4 of Raaijmakers et al. (2012), the stone deposits at the Eastern Scheldt side of the barrier in the Roompot channel are listed (in Dutch).

The exact locations of these stone deposits cannot be derived from this table. However, the exact locations are not known, as in reality the bed protection will always look different than intended. Data of the intended locations of the listed stone deposits is available from a AutoCAD drawing of Rijkswaterstaat (2017). In this thesis, this AutoCAD drawing is assumed to represent the present state of the granular bed protection.

3

Modelling of the experiment

This chapter will be about the modelling of the long sill experiments of Jongeling et al. (2003). In section 2.2 the choice is made to make a Improved Delayed Detached Eddy Simulation (IDDES) of these experiments. The steps taken to built the long sill simulations, are explained by the long sill simulation with $h = 0.375$ m. For the model with $h = 0.50$ m exactly the same methodology is applied.

In the first section of this chapter, some extra preparations are elaborated that ease (the interpretation of) the modelling. After that, the most important settings for the IDDES are discussed, to note the mesh and the boundary conditions. Subsequently the long sill simulations are validated against the measurements of Jongeling et al. (2003). An extensive validation is done for the long sill simulation with $h = 0.375$ m, followed by a concise validation of the long sill simulation with $h = 0.50$ m. The chapter will conclude with remarks about the general agreement between the simulations and the measurements. Also a side note is placed, based on a movie made of the simulated results.

The terms "modelling" and "resolving" will be used frequently in this chapter. One should be aware of the difference between the two while reading this chapter, as this is essential for the correct interpretation of the results of a DES. This and more is explained in section 2.2 of the literature study.

3.1. Preparations

In this section, first a distinction is made between different flow regions. This is done to be able to derive different load characteristics for each region that can be linked to the measured damages later on. Secondly, the data of the measurements is used to obtain more information about the turbulent scales of the experiment. This information is important for the set-up of the numerical grid, on which the accuracy of a IDDES is highly dependent.

3.1.1. Dividing the domain

For the aim of this thesis, the choice is made to model the experiment "long sill" of Jongeling et al. (2003) because it has several interesting flow regions that each have their own flow characteristics that form the load on the granular bed. The flow over sill is accelerating and separation occurs at its downstream edge. After the sill a recirculation area is present, as well as a reattachment "point" and the recovery area where a new boundary layer is built up. In agreement with the paper of Steenstra et al. (2016), the measuring area of the experiment can be split up into four regions:

1. Top of the sill
2. Recirculation area
3. Reattachment area
4. Flow recovery area

These areas are indicated in figure 3.1. The names of first two regions are self-evident and do not need any further explanation. Region 3 and 4 might be less trivial, and therefore will be briefly elucidated.

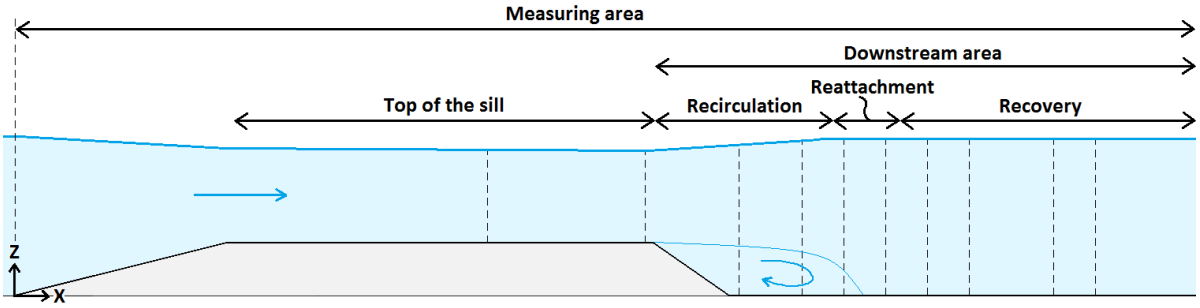

Figure 3.1: Flow regions in the measuring area of the experiment "long sill" of Jongeling et al. (2003)

The definition of the reattachment point is the location were mixing layer is touching the bottom or, to put it in other words, the location were the main flow gets reattached to the bed. In literature this point is often characterised by the location were the mean bottom flow velocity is zero and changing sign at both sides of the point. Nevertheless in reality the reattachment point is fluctuating over a certain area. For the experiments described in Nezu and Nakagawa (1989), it was found that the instantaneous reattachment point was fluctuating over an area of approximately six times the step height. Therefore when observing the flow in detail, it is considered to be more convenient to talk about a reattachment region.

In this thesis, a first characterisation of the reattachment area is used that is in agreement with many other studies, namely the region were the mean velocity is approximately zero and having different signs at both sides of the area. To make it specific, in this thesis the reattachment area will be defined as the region with an absolute wall shear stress $|\tau| \leq 0.1[N/m^2]$. Thereby the reattachment area will be small, but some movement of the reattachment point is taken into account to enable the evaluation of this interesting flow region.

The region downstream of the reattachment area is called the "recovery area". In this region the mean bottom flow velocities are positive again and a new boundary layer starts to build up. The flow is recovering towards a uniform flow state again. Nevertheless this state will not be reached, as this is a slow process that takes a downstream distance of about 75 times the water depth Uijttewaal (2002).

For some applications, it will suffice to make a distinction between the top of the sill and the area downstream of the separation point. The recirculation, reattachment and recovery area then together will form the "downstream area".

3.1.2. Turbulent scales

Before building the numerical model, the order of magnitude of the large energy containing eddies and the Taylor micro-scale are estimated. The smallest Kolmogorov scale is of less importance for a DES and therefore not determined in this section.

Energy containing eddies
For a steady uniform flow the size of the large energy containing eddies is generally assumed to be equal to the water depth, denoted as $L_{ece} \approx h$. The size of the largest eddies above the sill are therefore expected to be in the order of the water depth above the sill, which is about 0.22 m. After the sill, the size of the large eddies might be disturbed by the presence of the expanding mixing layer. Eventually their size will grow again towards the magnitude of the water depth, so in the downstream area the energy containing eddies will have a size in the order of 0.22 m to 0.36 m.

Taylor micro-scale
The size of the Taylor micro-scale is proportional to $Re^{-\frac{1}{2}}$. For this experiment, the Reynolds number is about: $Re = \frac{uL}{\nu} \approx 220000$. Therefore the Taylor micro-scale will be in the order of $L_{tms} \approx 220000^{-\frac{1}{2}} \approx 0.00213$ m = 2.13 mm. At the Taylor micro-scale, turbulence "forgot its origin" and can be assumed isotropic. This also means that L_{tms} is constant throughout the domain.

3.2. Model settings

This section is meant to give insight in the set-up of the long sill simulations. The most important settings will be discussed to ease the reproducibility of modelling others experiment according to the applied methodology. Furthermore the assumptions made to obtain credible results are shown.

3.2.1. Geometry model

The main difference between the RANS models made in earlier studies and the DES made for this thesis, is that a DES is able to resolve turbulence to a certain extend. Turbulence is a three-dimensional (3D) phenomenon and therefore, as the title of this thesis already reveals, a 3D-model is made of the chosen experiment. The numerical model encloses the full size of the laboratory flume, accompanied by some adjustment explained below.

In CFD-modelling, the geometry of a model consists of the total volume of flowing matter. For this experiment this is the volume of water plus a certain amount of air above the water, as a "free water surface"-approach is used to model the water surface. The geometry of the model therefore is higher than the water level of the experiment. Also the downstream end of the flume is extended in the model, to prevent that the downstream boundary condition can influence the results at the area of interest.

Apart from these adjustment, all the dimensions are equal to those of the real-life experiment listed in subsection 2.3.3. For convenience the base sketch of the geometry of the model is given in figure 3.2. This base sketch is used to make the 3D model, by extruding it 0.50 m in y-direction. In figure 3.3 the measuring area is enlarged. Some coordinates are given to indicate the dimensions in the measuring area, as this is the area of interest for this thesis.

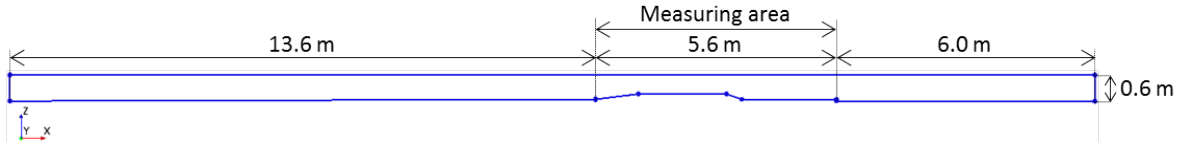

Figure 3.2: Main dimensions of the full model

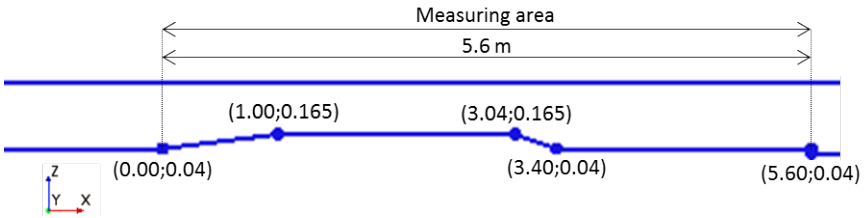

Figure 3.3: Dimensions of the measuring area

3.2.2. Mesh model

For a DES the desired grid size is approximately equal to the Taylor micro-scale, as explained in subsection 2.2.6 of the literature study. The Taylor micro-scale of this experiment is approximated in the previous section to be about 2.13 mm. Unfortunately for this study it was impossible to reach this level of refinement due to limitations in computational power and time. Local grid refinements are used to limit the computational effort needed, but a grid size of 0.005 m in the area of interest appeared to be the minimum achievable size.

To speed up convergence of the model to a certain solution, the numerical grid is refined in several steps. For each refinement step, the time step is adjusted such that the Courant number of the smallest grid cell with the highest flow velocity is approximately 1. Therefore in the entire model, the Courant number $C \leq 1$. In this thesis the following steps of mesh refinement are taken:

- 0.04 m grid with a time step of 0.04 s. Whole domain.
- 0.02 m grid with a time step of 0.02 s. Whole domain.
- 0.01 m grid with a time step of 0.01 s. Local refinement around the measuring area.
- 0.005 m grid with a time step of 0.005 s. Local refinement around the measuring area.

During each refinement step, first 50 s are simulated to let the model converge towards a new solution. Subsequently some monitors are enabled to register the solution during the next 100 s. In this way the solutions corresponding to different grid sizes can be compared afterwards.

Parts of the final mesh are visualised in figure 3.4. The final mesh consists of approximately 10 million grid cells. Using ten nodes with four cores each, it takes one week to simulate approximately 40 s of real-time flow.

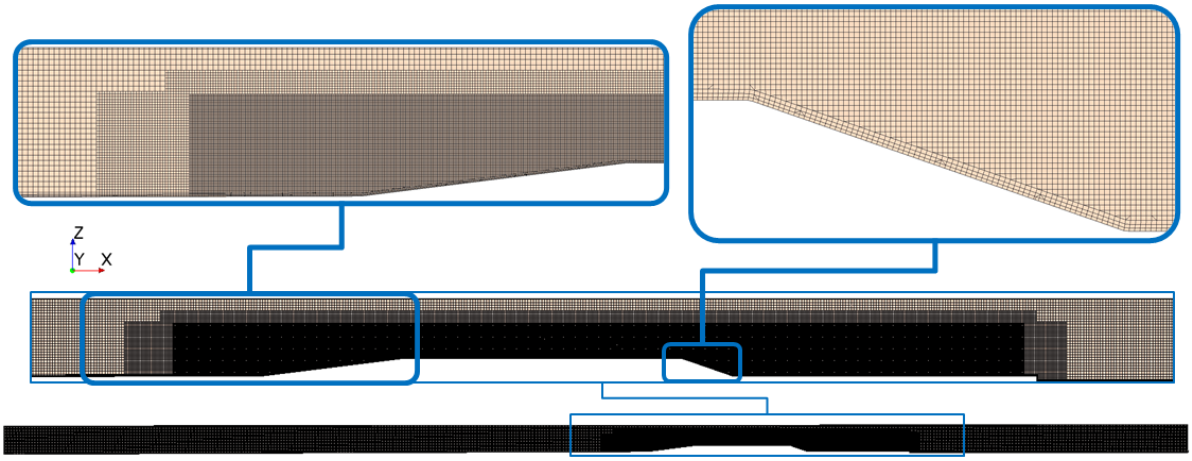

Figure 3.4: Impression of the final mesh

RANS-region | LES-region
As explained in section 2.2.2, the ratio between the turbulent scales and the grid size is decisive for the model to solve the Navier-Stokes equation in RANS-mode or LES-mode. As the size of the turbulent fluctuations are time dependent, so the boundary between the RANS-region and the LES-region is, which is shown in de snapshot of figure 3.5.

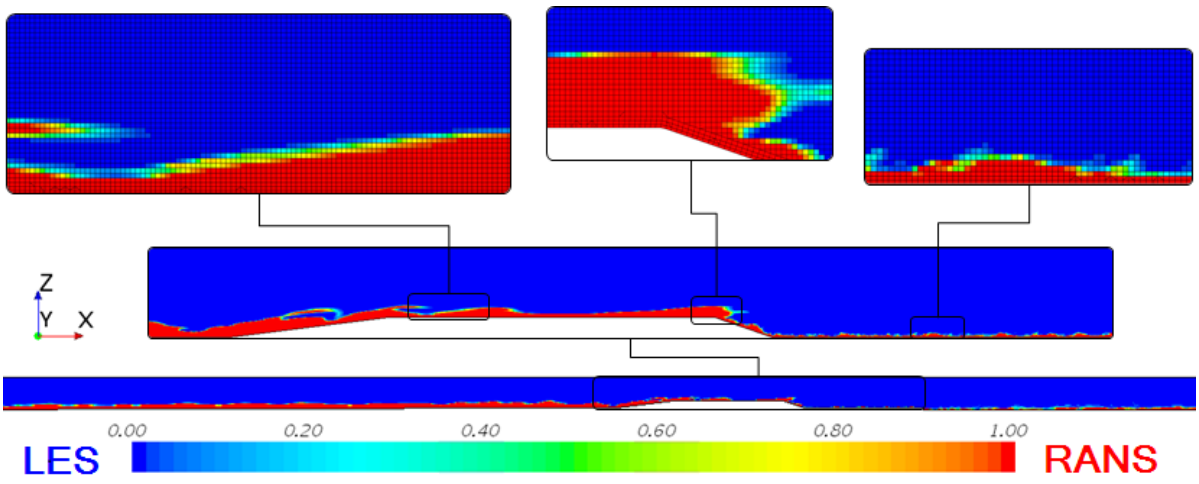

Figure 3.5: Instantaneous distribution of the RANS- and LES-region over the modelled domain

To evaluate the differences between the flow regions mentioned in section 3.1.1, a mean value of the RANS- and LES-region is monitored during the simulating activities. Those are visualised in figure 3.6.

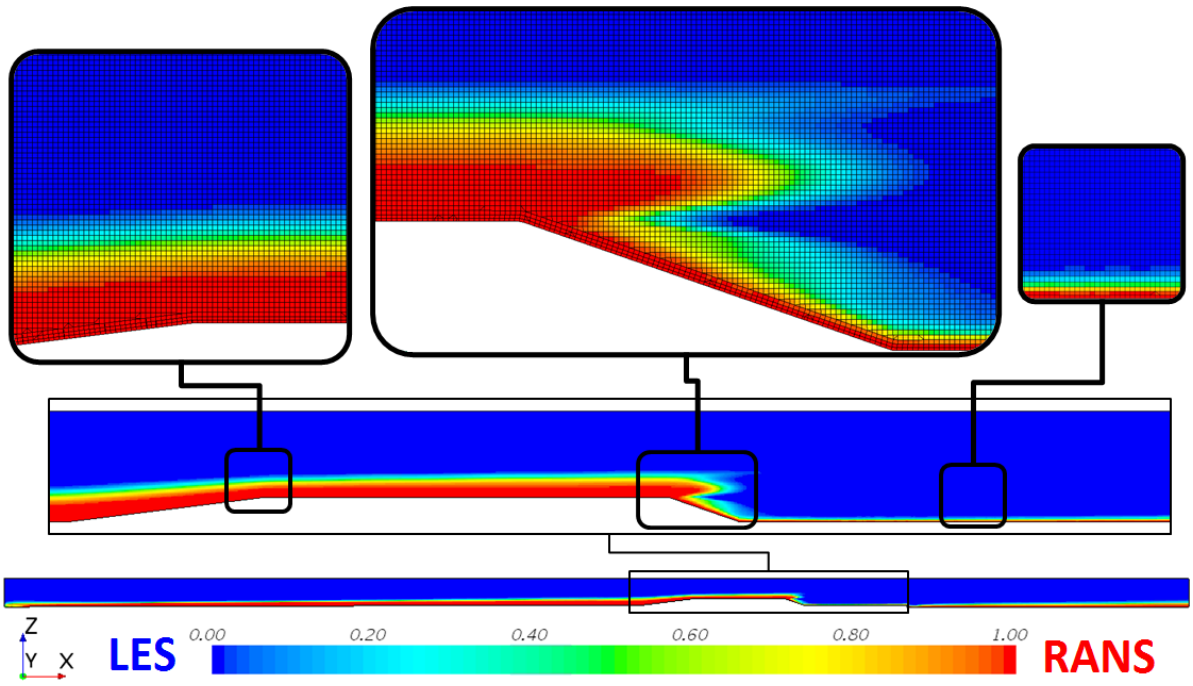

Figure 3.6: Averaged distribution of the RANS- and LES-region over the modelled domain

As expected, the RANS-region is the largest where the turbulence intensity is relatively small and vice versa. Therefore, before the sill the RANS-region is relatively high with a thickness of about 0.09 m. On top of the sill the height RANS-region is very variable. The averaged height is about 0.06 m. In the downstream area the RANS-region is very thin because many large turbulent fluctuations reach the bed in this area. The RANS-region only covers the first two cells of the prism layer here, which is about 0.007 m.

Remind that the choice for performing a DES instead of RANS-model in the first place is made because the turbulent quantities, originating from the flow separation at the downstream end of the sill, are not represented well in a RANS-model. One can see that in the downstream area, the LES-region covers almost the entire water depth. Depending on the grid size, the flow field in the downstream area therefore should be reproduced more accurately than in a RANS-model, as now part of the turbulence will be resolved instead of modelled. The region where most damage to the granular bed occurs also falls inside the downstream area. Therefore it is expected that also the stone stability can be predicted more accurately with the output of a DES.

Prism layer | Wall z^+-values
A prism layer is a further refinement of the grid towards a boundary. In general a flow is characterised by its boundaries but unfortunately these are also the hardest to model. Applying a proper prism layer therefore is essential to obtain an accurate numerical solution. The size of the grid cell at the boundary (hereafter called "wall cell") determines the wall z^+-value. As explained in section 2.2.5, the size of the wall cell should correspond to the chosen wall treatment. The rest of the prism layer should provide a smooth transition from the wall cell to the general grid size of the model. In the zoom at the right-upper part of figure 3.4 the prism layer is visible.

In this thesis use is made of wall functions to model the effects of the boundary layer. In Star CCM+ this is called the high z^+ wall treatment, for which z^+-values between 30 and 150 are desired. To meet this requirement, in the model a constant height of 3 mm is applied for the wall cell. The top view of figure 3.7 shows this results in z^+-values that are within the desired limits for the largest part of the domain. The locations were the z^+-values fall outside the range of 30 to 150 are deliberately left blank in this figure.

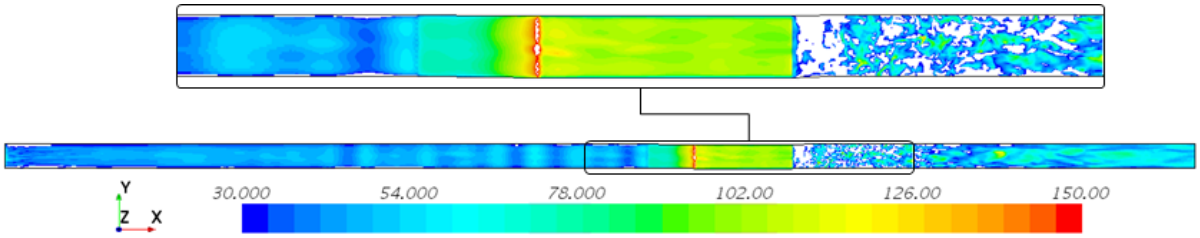

Figure 3.7: Overview of the obtained wall z^+ values (top view)

3.2.3. User specified boundary conditions

The user specified boundary conditions determine how the software interprets the geometry and physics inside the modelled area. Every surface of the model is listed below, together with the selected surface type and a concise description. A short explanation of some of these boundaries is given in the remainder of this subsection.

Surface	Type	Description
Inlet	Velocity inlet	Velocity profile from pre-simulation Synthetic turbulence is added
Outlet	Pressure outlet	Hydrostatic water pressure at the downstream end of the flume
Glass side walls	Wall	No slip - Smooth surface
Bottom of the flow ($\neq$ Bottom of the flume!)	Wall	No slip - Rough surface with a roughness height $k_s = 2d_{n50}$
Top of the model	Wall	Slip
Water surface	-	Free water surface

Table 3.1: Resume of the user specified boundary conditions

Velocity profile from pre-simulation
In CFD-modelling it is common practise to introduce a flow region in which the flow can already adjust to the basic geometry of the model of interest. For this thesis a separated simulation is built to serve this purpose. This pre-simulation is a rectangular box with the same cross-section as the water area at the beginning of the flume. Periodic boundaries and a rigid lid approach are used to obtain a velocity profile that is adjusted to boundaries of the main model, being a certain water height flowing over a bottom with a certain roughness and bounded by two smooth walls over a certain width. The measured discharge is given as an input value for this pre-simulation.

Synthetic turbulence
This is a special boundary conditions required to enable (accurate) LES results. As the modelling method applied in this study (i.e. IDDES) is solving the largest part of the domain by the LES-formulations, synthetic turbulence appeared to be essential to perform a good IDDES as well. Synthetic turbulence is put in the model as a substitute for the original turbulence boundary condition. In Star CCM+ a method is implemented that creates turbulent eddies based on the input of a turbulence intensity and length scale. The eddies created by this method will develop to the turbulent scales that are in accordance with the flow characteristics. For channel flows a distance of at least ten times half the water depth should be taken into account for this development, before the area of interest is reached (Star CCM+, 2018).

A turbulence intensity of 10% and a turbulent length scale of 0.02 m are chosen as input values for the simulation of this thesis, based on information from Star CCM+ (2018). In the model at least fifty times half the water depth is present before the area of interest is reached, which is sufficient for the synthetic turbulence to develop into more realistic turbulence characteristics.

To emphasise the importance of this boundary condition, it should be noted that no separation occurred in simulations where the synthetic turbulence boundary condition was not applied. Using the turbulence characteristics of the pre-simulation as an upstream turbulence boundary condition was not sufficient for the development of turbulence eddies in the main model.

Slip | No slip
A slip boundary means that no restrictions are posed to the near wall flow velocity. A slip boundary therefore just limits the modelled area without further physical meaning. A no slip boundary means that the flow velocity at the wall is forced to be zero, like what in general is assumed for solid surfaces. This is further elaborated in section P.1 about the boundary layer.

Glass side walls - Smooth surface
Glass sheets should normally be modelled as physically smooth. In the CFX-models of Jongeling et al. (2003) a roughness of 0.005 m was assumed for the glass walls , because the connections between the glass sheets caused little disturbances in the flow. Nevertheless the real roughness of the side walls of the flume is not known, and therefore smooth side walls are assumed in the simulations of this thesis.

Granular bottom - Rough surface
Just as in reality, in literature a lot of different justified values can be found for taking the roughness of a granular bottom into account. In Jongeling et al. (2003) best results were obtained with a bottom roughness of $2d_{n50}$. During this thesis a simple test confirmed that better results are obtained for a bottom roughness of $2d_{n50}$, than for a bottom roughness of d_{n50} or $3d_{n50}$. For the bottom roughness therefore a value of $2d_{n50}$ is assumed, which is a commonly used value for a relatively narrow-graded, well-placed granular bottom Schiereck and Verhagen (2012).

Using Star CCM+ as a modelling tool, it is important to note that the option called "Roughness Limiter" should be deactivated for the correct modelling of the entered roughness height. In Star CCM+ this option is enabled by default, which automatically lowers the roughness height to the height of the wall cell centre if the requirement $z >> z_0$ is not met. This is further elaborated in appendix B.

Free water surface
In CFD-modelling the water surface can be modelled as a rigid-lid or as a free water surface. With the rigid-lid approach, the water surface is modelled as a frictionless plate. Therefore no perturbations occur at the water surface and it cannot follow deformations of the water level as for example caused by local accelerations. The rigid-lid approach therefore appeared unsuitable for the modelling of this experiment. Applying the rigid-lid approach resulted in too low flow velocities above the sill, as the water level is kept too high artificially.

The water surface therefore is modelled as a free water surface. A disadvantage of this approach is that it is harder to control the discharge through the domain. After the general conclusions about the modelling results, a side note is placed in section 3.5 considering this subject.

3.2.4. Cross-sections

For convenience, the cross-sections taken in the model are similar to those of Jongeling et al. (2003). In figure 3.8 the numbered cross-sections are shown again. In the next section, the model is validated based on the measurements done in these cross-sections. All cross-sections are taken in the centreline of the flume.

Also the mean bed level z_{mbl} is indicated in figure 3.8. Similar to Jongeling et al. (2003), this is chosen to be the reference height in this study.

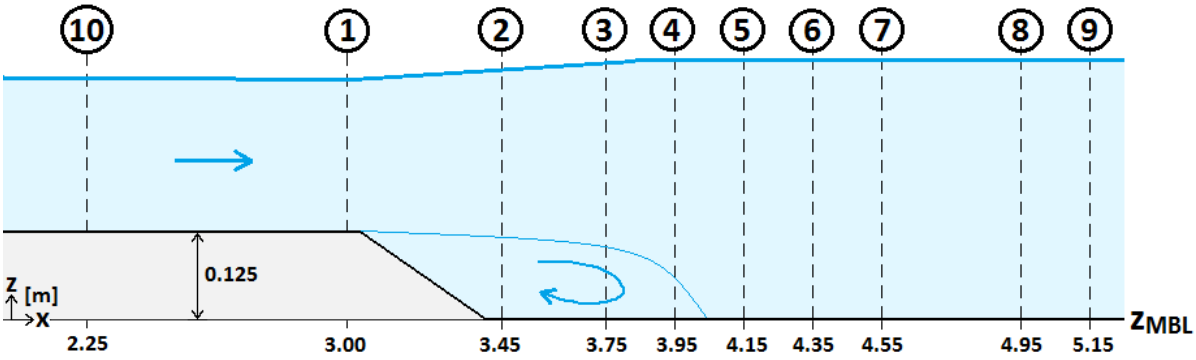

Figure 3.8: Measured cross-sections, numbered in accordance with Jongeling et al. (2003)

3.3. Validation long sill simulations

In this section, first the long sill simulation with $h = 0.375$ m is validated extensively. The model is validated by comparing the simulated velocities in x-direction with the measured velocities in x-direction from Jongeling et al. (2003). After that, also the simulated and measured turbulent kinetic energy profiles are compared. As the turbulent kinetic energy k is directly linked to the velocity fluctuations, the validation of u_x and k together should give an idea about how accurately the real, time dependent flow velocities are reproduced by the simulation. In formula form this can be expressed as $u(t) = \bar{u} + u'(t)$, better known as the Reynolds decomposition mentioned in the literature study. $\bar{u}$ is validated by the comparison of the velocity profiles and $u'(t)$ is validated by the comparison of the turbulent kinetic energy profiles.

The long sill simulation with $h = 0.50$ m is validated less extensive, because an exactly similar methodology is applied to set-up this model. The results presented in this section are obtained with a local mesh size of 0.005 m, as described in 3.2.2.

3.3.1. Velocity profiles - Long Sill $h = 0.375$ m

An general impression of the simulated flow field can be obtained by the longitudinal cross-section of figure 3.9, which is a screenshot of the instantaneous flow velocities in streamwise direction. For convenience, the different flow regions are indicated similarly to figure 3.1.

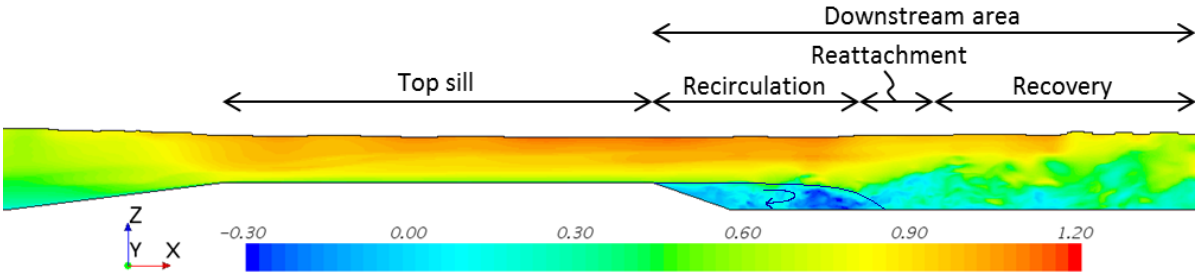

Figure 3.9: Snapshot of the instantaneous velocity field in x-direction [m/s]

The colour plot shows the flow acceleration over the sill and separation at the downstream end. A recirculation area with negative flow velocities can be observed, which is bounded by the sill and the reattachment area. The increased turbulence intensity behind the sill depicts the process of the redistribution of energy over the expanded flow area. As the indication of the flow regions already reveals, these flow characteristics are in accordance with the observations done during the experiment.

Another longitudinal cross-section is given in figure 3.10. It shows the averaged velocity profiles at some of the measured cross-sections. To keep the overview clear, not all measured cross-sections are depicted in this figure.

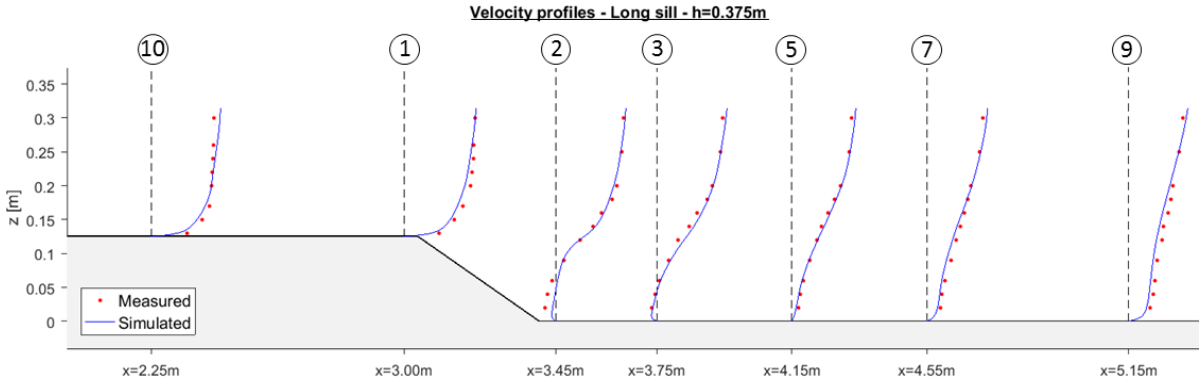

Figure 3.10: Averaged measured and simulated profiles of the velocity in x-direction u_x

It can be concluded that the general velocity field is simulated well by the numerical model. Throughout the entire measured domain, the averaged simulated velocities are in good agreement with the measured flow velocities. The largest deviation between the measured and the simulated flow velocity can be found near the bottom at x = 3.45 m. The model here clearly underestimates the magnitude of the negative flow velocity in the recirculation area.

A more in-depth comparison between the measured and simulated velocities in x-direction is done in appendix D with help of figure D.1 to D.7. The velocity profiles for the 0.005m-grid are used as the final results for this thesis. The averaged simulated velocity profiles shown in this detailed comparison, clearly improve for each step of mesh refinement. This means that not yet all relevant energy containing eddies are resolved for a mesh of 0.005 m.

From this analysis, it can be concluded that another mesh refinement is likely to improve the simulated results even further. This is in agreement with the statement made earlier, that a grid size approximately equal to the Taylor micro-scale is desirable for a IDDES. Nevertheless this is considered unfeasible regarding the required computational time and power, as already mentioned in 3.2.2.

In appendix F a quantitative comparison is made between the measured and simulated velocities obtained with the 0.005m-mesh. The difference between the two streamwise velocities is calculated as: $\Delta_{u_x} = u_{x,sim} - u_{x,mean}$. A percentage difference is not given, as this will give a distorted view for the near-zero flow velocities.

The quantitative comparison shows that all simulated values differ less than 0.1 m/s with the measured flow velocities, except for the two measuring points that are just 0.005 m above the bottom of cross-section 10 and 1. The averaged absolute difference between the simulated and measured velocities is about 0.04 m/s. To put this in perspective, the laser Doppler velocity meter (LDV) used to measure the streamwise velocities has an accuracy of about 0.01 m/s. Nevertheless a larger inaccuracy in the measurements might be present due to inaccuracies in the exact measuring height. Especially near the bottom, were the largest deviations between the simulation and the measurements are found, this measuring height has a large influence on the results as explained earlier in section 2.3.4.

In general it can be concluded that the averaged simulated velocity profiles are a good reproduction of the averaged measured velocities.

3.3.2. Turbulent kinetic energy profiles - Long Sill $h = 0.375$ m

The simulated turbulent kinetic energy (TKE) profiles will be compared visually to the measurement, in a similar way as the velocity profiles are treated in the previous subsection. For the experiment, the values of the TKE (denoted as k) are determined by the standard deviations of the measured velocities as: $k = 0.5\left({\sigma_{u_x}}^2 + {\sigma_{u_y}}^2 + {\sigma_{u_z}}^2\right)$. It should be noted that these velocity fluctuations are not all measured at the same position, nor with the same measuring device, as described in section 2.3.4. In the numerical simulation, two values of the TKE must be distinguished:

1. The modelled k_{RANS}. The value of k is determined by one of the transport equations (section 2.2.4).
2. The resolved k_{LES}. In the LES-region of the modelled domain, the value of k can be determined by manually adding a field-function equal to the one used for the measurements. In Star CCM+, field-variance-monitors of the flow velocity should be added for all three directions to deliver the required input for this calculation. As explained in section 2.2.6, in the LES-region the amount of resolved TKE is directly dependent on the mesh size. At least two grid cells are needed to resolve one eddy, so the resolved turbulent scales are expected to be approximately equal to two times the longest side of a grid cell, denoted as $2\Delta_{LES}$.

Figure 3.11 gives an overview of several averaged TKE profiles throughout the measuring area. The lines represent the total averaged TKE (k_{tot}) determined by the summation of the averaged modelled k_{RANS} and the averaged resolved k_{LES}. To keep the overview clear, not all measured cross-sections are depicted in this figure.

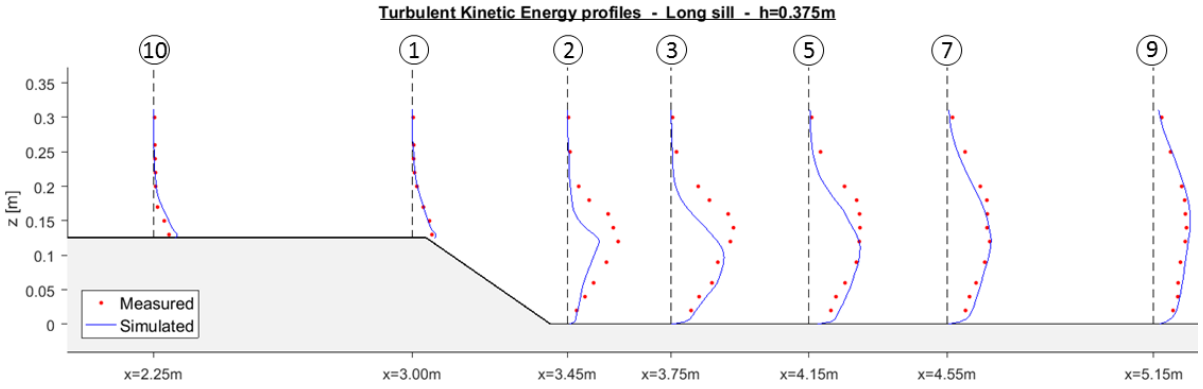

Figure 3.11: Averaged measured and simulated profiles of the total TKE k_{tot}

In general the averaged simulated TKE profiles have the same shape as the measured ones. On top of the sill, the measured and simulated profiles are in good agreement. For cross-section 2 a clear under prediction of the total TKE can be observed over the full water depth. At the height of the sill and above, the simulated k-values are smaller than what was measured for cross-sections 3 and 5. The further downstream of the separation point, the better the agreement between the measured and simulated TKE profiles becomes. This makes sense, as the important turbulent scales just after the separation point are smaller then those further downstream. Clearly the grid size is fine enough to resolve the important scales further downstream, but not yet fine enough to resolve all important scales just after the point of separation.

A detailed comparison of the averaged TKE profiles can be found in appendix E. For convenience the averaged modelled TKE (k_{RANS}) is visualised separately from the averaged resolved TKE (k_{LES}) in figure E.1 to E.14. Especially in the figures for k_{LES}, a huge improvement can be seen between the results of the different refined meshes. This indicates that with every mesh refinement step, more and more important energy containing turbulent scales are resolved. As explained earlier, this is in agreement with the expectations.

In resolving more important turbulent scales, a trend can be observed for the k_{LES} profiles. When the mesh is too coarse, no important turbulent scales are resolved yet and therefore k_{LES} will be small. After the mesh is refined and some turbulent scales are resolved, k_{LES} will increase. Important to note for the interpretation of the results is that a further mesh refinement and resolving even more turbulent scales, at a certain point will result in an overestimation of the TKE. This phenomenon is also observed for relatively coarse LES-grids in other studies, like for example Addad et al. (2008). Further grid refinements will eventually result in a decrease of the overestimation and in a k_{LES} that approaches the measured values.

Overall the results for the averaged total TKE energy are satisfactory. The velocity fluctuations are considered to be predicted well enough for the aim of this thesis. The overall shapes and observed trends are explicable and promising in case the available computational power would increase and further mesh refinements can be applied.

3.3.3. Validation Long Sill $h = 0.50$ m

In the experiment series of Jongeling et al. (2003), the experiment treated before is also executed with an initial water depth h of 0.50 m. Also for this experiment a simulation is made. This is done in a similar way as the simulation of the experiment long sill with a water depth h of 0.375 m. Therefore this model is only validated qualitatively, based on figure 3.12 and 3.13.

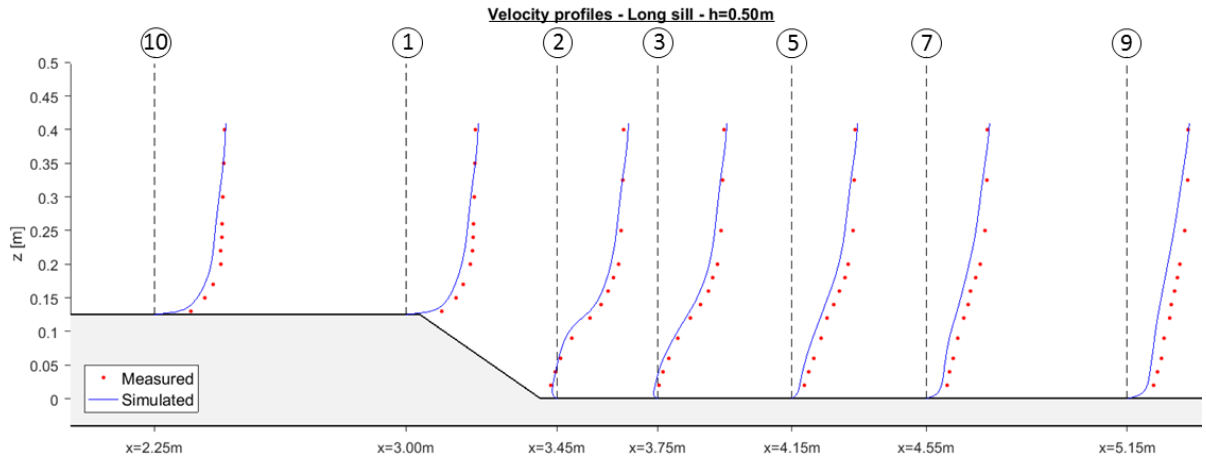

Figure 3.12: Averaged measured and simulated profiles of the velocity in x-direction u_x

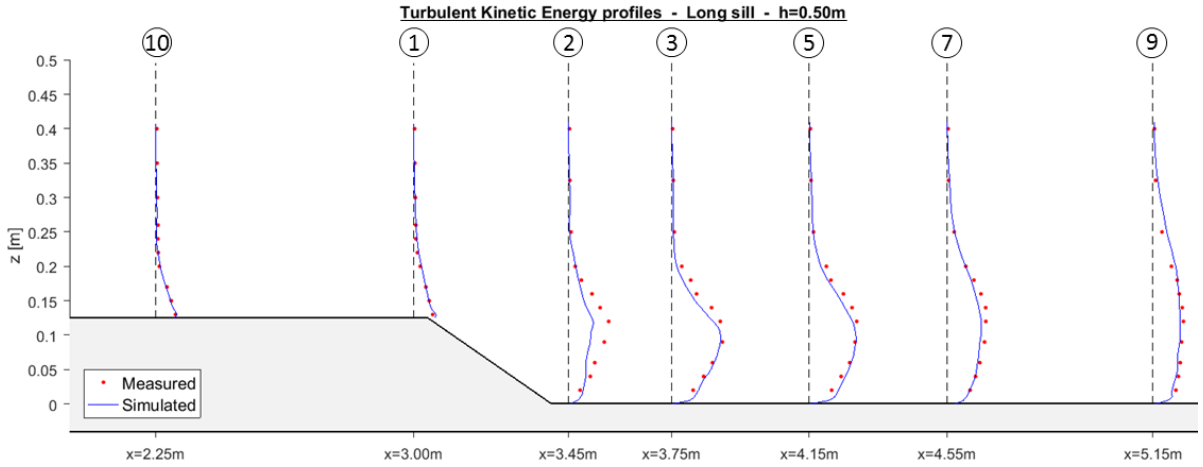

Figure 3.13: Averaged measured and simulated profiles of the total TKE k_{tot}

Figure 3.12 and 3.13 show a similar image of the simulated results as figure 3.10 and 3.11 do for the experiment with $h = 0.375m$. The discharge of the long sill simulation with $h = 0.50m$ seems a bit too low, as the simulated velocities are at the left of the measured velocities. Nevertheless the shapes of the simulated velocity profiles are in good agreement with the measurements. The simulated TKE-profiles look very satisfying. They show the same behaviour as discussed in the in-depth analysis of section 3.3.2, but the general agreement with the measurements is even better. By this qualitative comparison, the simulated results for the experiment long sill with $h = 0.50m$ are considered good enough for the aim of this thesis.

3.4. 3D eddy resolving technique

In this section, the use of a 3D eddy resolving simulation technique for the purpose of this thesis, is evaluated. First, spectra of the measured and simulated velocity signal are compared, to determine to what extend the energy containing eddies are resolved. Besides that, the effective resolution is compared to the stone diameter, to see if the applied grid is fine enough to resolve the eddies with a size of $1d_{n50}$. Second, the obtained velocity and TKE profiles are compared to the results of a RANS model. With these two analysis, an opinion can be formed about the use of IDDES, for the purpose of assessing the stone stability in a granular bed protection.

3.4.1. Resolved turbulent scales

The analysis in this section is based on the velocity signal obtained in cross-section 5 of the long sill simulation with $h = 0.375$ m, at a height $z = 2$ cm above the bed. The expected resolution at this position can be determined with help of the Taylor's hypothesis. Below the frequency is calculated, to which the turbulent fluctuations are expected to be resolved.

- It is assumed that at least two grid cells are needed to resolve an eddy. The grid cells at the chosen location are cubes with sides of 0.005 m.
- The mean velocity u_x 2 cm above the bed at cross-section 5 is about 0.25 m/s.
- The time scale of the eddies that are expected to be resolved, is calculated as: $T_{grid} = \frac{2*L_{grid}}{\bar{u}_x} \approx 0.04$ s. The time step of the numerical calculation is 0.005 s. Because this is smaller than T_{grid}, the grid size is governing for the resolution of the simulation.
- The expected resolution $f_{g,exp} = \frac{1}{T_{grid}} \approx 25$ Hz.

The resolution of the measured velocity signal is 50 Hz. In figure 3.14, first the pre-multiplied energy density spectrum is given, to determine how much turbulent kinetic energy is resolved in the simulation compared to the measurements, and in which turbulent scales this energy is present.

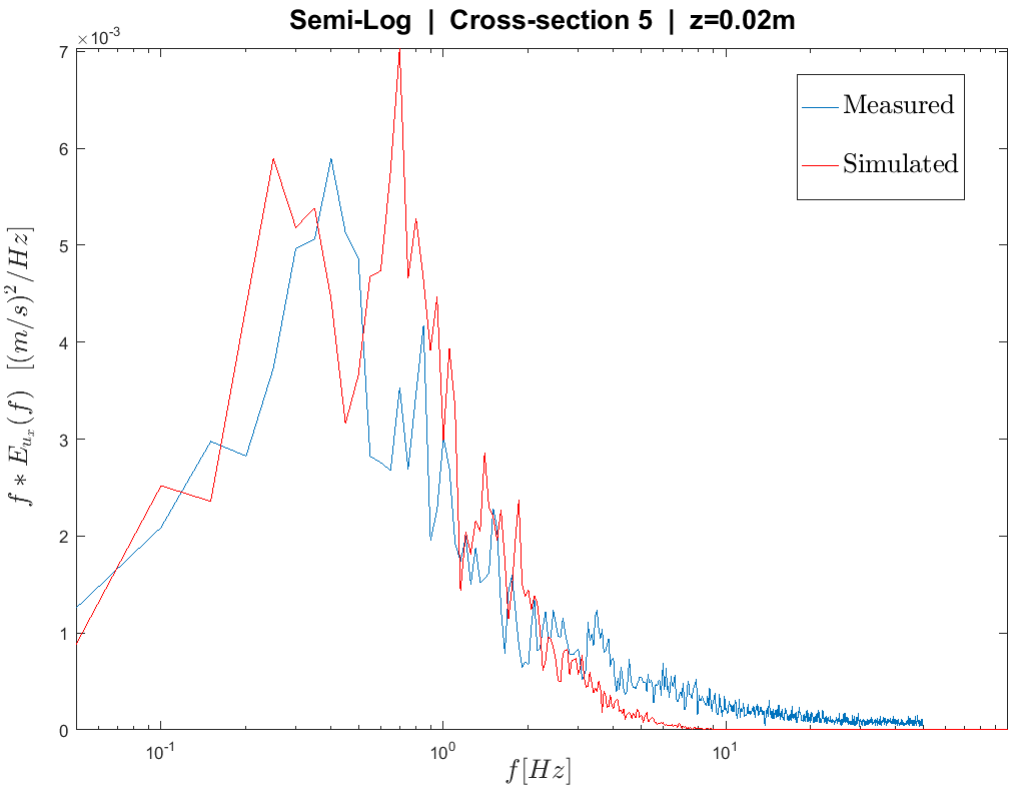

Figure 3.14: Pre-multiplied energy density spectrum of u_x on semi-logarithmic scale, at cross-section 5, 2 cm above the bed of the long sill simulation with $h = 0.375$ m

In figure 3.14, the surface underneath the measured (blue) and simulated (red) graph is approximately equal. This indicates that the total amount of simulated turbulent kinetic energy (TKE) is nearly equal to the measured TKE. In the simulated velocity signal, slightly more fluctuations seem to be present in the lower frequencies between 0.2 and 1 Hz, than in the measured signal. In the frequencies above 3 Hz, the simulated TKE is clearly underestimated. It seems that the effective resolution of the simulation velocity fluctuations is smaller than the expected grid resolution $f_{g,exp}$ of 25 Hz.

Extra information about the resolved turbulent scales and the effective grid resolution, can be obtained from the double-logarithmic variance density spectrum of the measured and simulated velocity signal, given in figure 3.15. In this figure, also a reference line with a slope of $-\frac{5}{3}$ is plotted for the identification of the inertial sub-range (elaborated in section 2.2.6). Furthermore, the frequency to resolve eddies with a size of $1d_{n50}$ is indicated in green. This frequency is calculated as: $f_{stone} = \frac{1}{T_{stone}} = \frac{\bar{u}_x}{d_{n50}} \approx 16$ Hz.

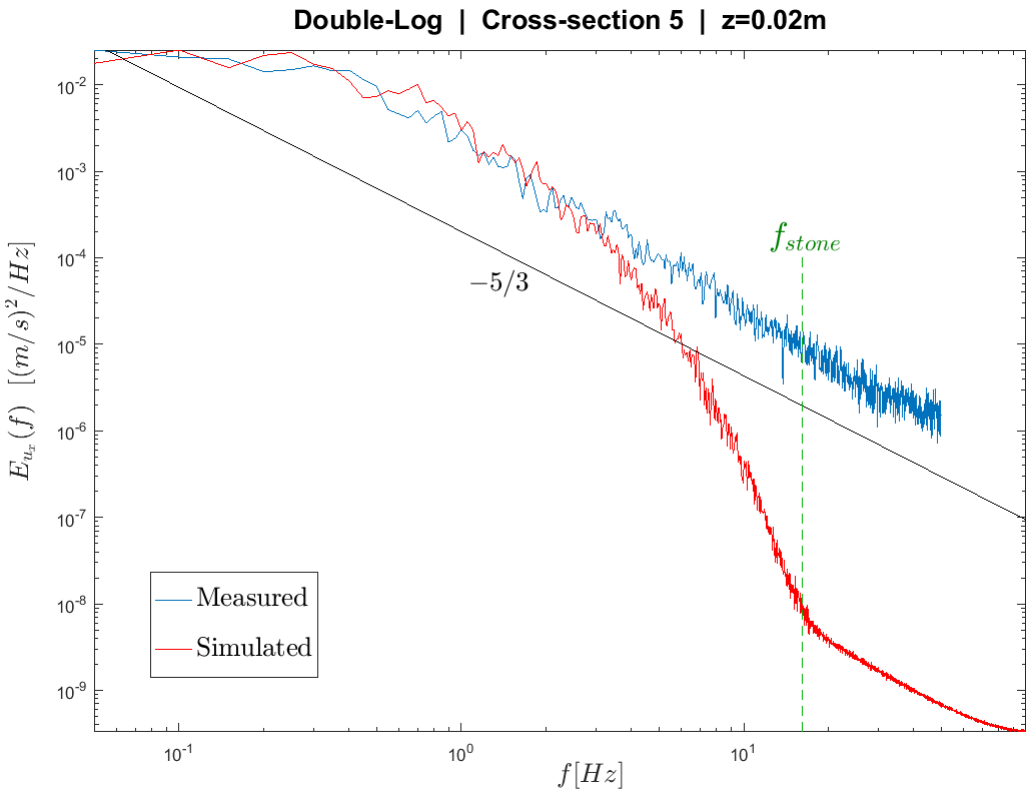

Figure 3.15: Variance density spectrum of u_x on double-logarithmic scale, at cross-section 5, 2 cm above the bed of the long sill simulation with $h = 0.375$ m

From figure 3.15 it can be seen, that the sampling frequency of the measurements was sufficient to perceive the large energy containing turbulent scales. In the higher frequencies the blue line follows the $-\frac{5}{3}$ slope, which indicates that the inertial sub-range is reached.

The red line of the simulated velocity signal, follows the blue line quite accurately, until a frequency of about 2 to 3 Hz, were it starts to drop. The effective grid resolution $f_{g,eff}$ of this IDDES therefore is approximately 2 Hz, which is significantly smaller than the expected grid resolution $f_{g,exp}$ of about 25 Hz. The drop of the simulated spectrum and its tail, explains why in figure 3.14 the resolved TKE is underestimated for the higher frequencies. This part of the simulated spectrum is not physical. The large difference between $f_{g,eff}$ and $f_{g,exp}$ might be explained by the anisotropy of the turbulent fluctuations at this point.

With regard to stone stability, the effective grid resolution $f_{g,eff}$ is considerably smaller than the frequency f_{stone}, corresponding to the turbulent eddies of about $1d_{n50}$. This means that the grid size and the corresponding numerical time step, should be decreased further to obtain the desired effective grid resolution.

3.4.2. Compared to RANS

One of the main reasons to use an eddy resolving simulation technique instead of a RANS model in this thesis, is because an eddy resolving simulation technique is expected to perform better for non-uniform flow conditions. In this section this assumption is tested, by analysing the velocity and TKE profiles of a RANS model.

For this analysis, the model built for the IDDES of the long sill experiment with $h = 0.375$ m, was run in RANS mode. The geometry and boundary condition are exactly similar, except for the upstream turbulence boundary condition. In a RANS model no turbulent fluctuations are present, and therefore the synthetic turbulence boundary condition cannot be used. A comparable turbulence intensity and length scale are applied as an upstream turbulence boundary condition. The grid size is refined until the same level as for the IDDES, which is not really necessary to obtain similar RANS results as shown in figure 3.16 and 3.17.

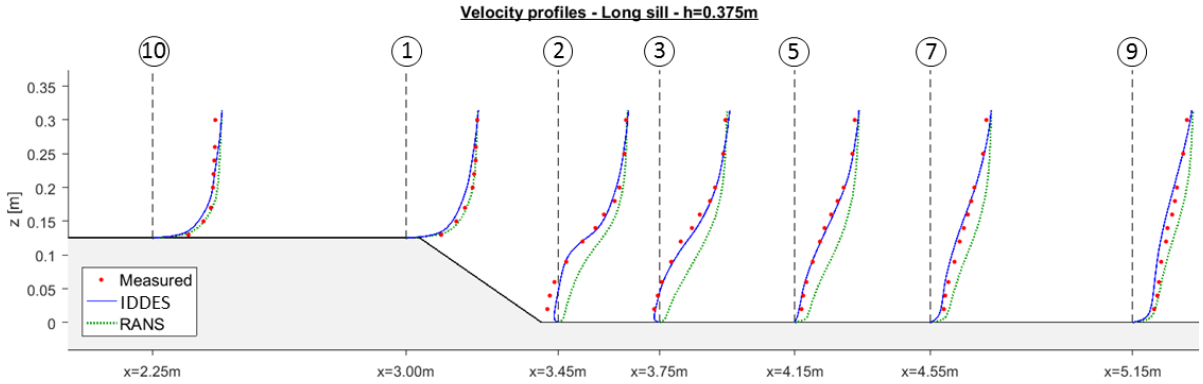

Figure 3.16: Averaged measured and simulated profiles of the velocity in x-direction u_x

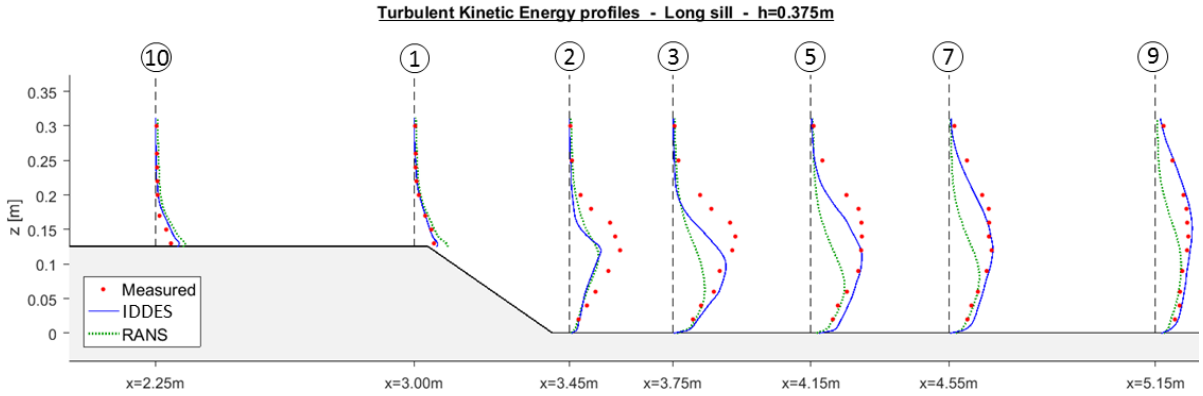

Figure 3.17: Averaged measured and simulated profiles of the total TKE k_{tot}

On top of the sill, the velocities and TKE are predicted well by the RANS model. The profiles of cross-section 10 and 1, of figure 3.16 and 3.17, are in good agreement with the measurements.

In the cross-sections directly behind the sill, the deviation between the measured and simulated RANS profiles are the largest. In cross-section 2 and 3 of figure 3.16, no negative velocities are observed in the RANS profiles. Apparently no separation occurred in the RANS model, and therefore a recirculation zone is absent. The further away from the downstream end of the sill, the more the RANS velocity profiles recover towards the measurements. The same conclusion can be drawn for the TKE profiles. In the RANS model, the total TKE is clearly underestimated.

In the highly turbulent flow region behind the sill, the IDDES results are clearly in better agreement with the measurements, than those of the RANS model. It is possible to obtain better RANS results, but then the geometry or the boundary conditions of the model have to be adjusted (”tuned”). This is done in the CFX models of Jongeling et al. (2003), as described in section 2.3.7. All the boundary conditions used in the presented IDDES and RANS results of figure 3.16 and 3.17, including the turbulent boundary condition, are a direct translation of the measurements and observations. I can be stated, that the results of figure 3.16 and 3.17, are those of models that are not tuned. In contradiction to the IDDES, further grid refinement will not improve the results of the RANS model.

3.5. Conclusions chapter 3

About the IDDESs of the long sill experiments, it can be concluded that the simulated averaged velocity profiles are in good agreement with the measurements. The mean deviation between the simulated and measured velocities is in the same order of magnitude as the measuring error. The largest deviations are observed in the area of interest for this thesis, namely near the bottom. However, this is considered to be inevitable, as this is a very dynamic region with large velocity gradients. It should be kept in mind, that in the near-bottom region, also the largest measuring error will be present.

The simulated averaged TKE profiles of the IDDESs deviate more from the measurements, but are considered to be in good agreement either. As expected, the grid size has a very large influence on the results of the IDDESs. This can especially be observed well in the k_{LES}-profiles of the resolved TKE (appendix E). Further refinement of the grid is expected to improve the IDDES results, but this is considered not feasible for this thesis because of computational limitations.

The overall simulated reproductions of the time dependent velocities ($u(t) = \bar{u} + u'(t)$) are satisfying. Therefore, the assessment of the stone stability in a bed granular protection, will be linked to time dependent output from the long sill IDDESs in the next chapter.

Nevertheless, it should be noted that the intended resolution with respect to the stone diameter is not reached. Preferably, the turbulent scales are resolved to the size of $1d_{n50}$. For the long sill experiment with $h = 0.375$ m, this coincides with a frequency of approximately 25 Hz. The effective resolution of the IDDES of this experiment appeared to be about 2 Hz. Thereby the dominant energy containing eddies are resolved, and therefore the total amount of simulated TKE approaches the measured TKE quite well. However, the effective resolution is not high enough to resolve all energy containing turbulent scales. The extreme values used for the assessment of stone stability, will not (exactly) correspond to the peak values caused by eddies of $1d_{n50}$.

Finally, it can be concluded that for the long sill experiment with $h = 0.375$ m, better results are obtained for the IDDES than for a RANS model with the same boundary conditions. Resolving the energy containing turbulent scales, clearly improves the simulated results in the highly turbulent flow region behind the sill. Compared to the CFX-models of Jongeling et al. (2003), better results seem to be obtained, while no tuning is applied to the IDDESs. The simulated results of an IDDES therefore might be considered more trustworthy than those of a (tuned) RANS model.

Side note: Waves in movie simulation

The validation of the simulation is based on the comparison of averaged profiles. Later on, also a short movie was made of the simulated domain in which an unexpected phenomenon can be observed. Waves appear to be present in the model. If one looks carefully, they can already be observed in figure 3.9. The waves seem to originate from the upstream boundary and partly reflect on the sill. In Jongeling et al. (2003) no similar observations are described, nevertheless this does not necessarily mean they were not present. The possible presence of waves cannot be traced with the measurement nor from the report.

Assuming the waves should not be present in the numerical model, it is expected that they are caused by the upstream boundary conditions. A rigid lid approach is used in the pre-simulation. Therefore the velocity profile that is applied as the upstream boundary condition, only contains information about the flow velocities of the water. The model of the experiment is higher than the pre-simulation, because above the water also an air layer is included. As a consequence, at the upstream boundary of the main model, the flow velocities at the water surface are extrapolated to the area occupied by air. The air layer therefore has a velocity about equal to the velocity of water particles at the water surface, while in reality the velocity of the air will nearly be zero. The relatively high velocities of the air region might cause some initial waves in the simulation. These waves are partly reflected at the sill and after some time arrive back at the upstream boundary. At the upstream boundary a fluctuation in the water surface will cause less or extra inflow of mass. This is why the simulated discharge is fluctuating and probably also why waves are present in the simulation. The fluctuations caused by the synthetic turbulence boundary condition might enlarge this phenomenon.

A separate study can be performed to reveal if the waves influence the results (significantly). For the aim of this thesis, the validation presented earlier is considered reliable enough to proceed.

4

The stability formula

In this chapter, a new stability formula will be evaluated that relies on the output of a validated three-dimensional eddy resolving simulation. Local simulated parameters will be used that represent the physical load terms described in section 2.1.

In the first section of this chapter, a general stability formula is derived that is ought to be applicable with the local output of a IDDES, while representing the physics that are expected to be governing for the stone stability. In the second section, more research is done to the parameters used in the general stability formula, based on output of the long sill simulation with $h = 0.375$ m. With this analysis, the general stability formula can be made more specific, which results in the stability formula proposed and tested in the third section of this chapter. After this, some conclusions are drawn. As the physics included in the Steenstra formula are nearly similar to the physics of the proposed stability formula, also the performance of the Steenstra formula is evaluated. This is done to declare the differences between the results of these two stability formulas. Some final conclusions are drawn at the end of the chapter.

4.1. The general stability formula

The forces listed below are assumed to be predominant for the stability of a stone in a granular bed protection (elaborated in section 2.1.2).

- Flow velocity
- Velocity fluctuations (large scale turbulence)
- Flow acceleration (e.g. due to geometry and waves)
- Acceleration fluctuations (turbulent wall pressures)

This is captured in the general stone stability formula 4.1, copied from Hofland (2005).

$$\Psi_{tot} = \frac{(C_b(\bar{\tilde{u}} + \tilde{u}')^2 + (C_m(\bar{\tilde{a}} + \tilde{a}')d)_{\max}}{\Delta g d} \tag{4.1}$$

In this thesis a stability formula is proposed based on local parameters at the bottom of the modelled domain. Main reasons to use bottom variables is to develop a stability formula that:

1. Has a wide range of applicability. If local bottom parameters are used that represent the physics at the granular bed, the need to calibrate the stability formula for different flow situations will become superfluous.
2. Is independent of the used software and grid size at the bottom, as long as the requirements to obtain accurate IDDES-results are met. Important settings for a IDDES are discussed in section 2.2 and 3.2.
3. The near-bottom flow velocities and accelerations cannot be validated well for the long sill experiments.

(Item 2. and 3. are elaborated in chapter 9 under the topic ”near-bottom flow characteristics”)

One should be aware that at the bottom boundary of a IDDES, the Navier-Stokes equation is solved according to the RANS-formulations. From the results that will be presented in the sections hereafter, it is clear that fluctuations are transmitted from the LES-region to the RANS-region. Therefore a time-dependent signal can be obtained in the RANS-region at the bottom boundary of the model. Nevertheless, the effects of this transmission from the LES-region to the RANS-region are unknown.

At the bottom boundary of the model, the streamwise velocity is forced to zero by the no-slip boundary condition. A consequence of using local bottom parameters therefore is that the flow velocity u cannot be used directly as a load parameter. Alternatively the wall shear stress τ_x or shear velocity u_* in streamwise direction can be used to represent the flow velocity at the bottom. This term then is mainly responsible for the drag force on a stone, but also contributes to the lift force.

The flow acceleration at the bottom can be used directly as an input variable. Referring back to the physics described in section 2.1, also the pressure gradient in streamwise direction $\frac{\partial p}{\partial x}$ might be used as a load parameter. This term expresses the influence of inertia on the stability of a stone in a bed protection. It is largely responsible for the lift force, but also contributes to the drag force on a stone.

Furthermore, research has shown that damages to a granular bed protection generally are caused by a combination of extreme loads, as expressed by equation 4.1 and elaborated in section 2.1 of the literature study. Therefore special attention should be paid to the simultaneous occurrence of peak values for the chosen load parameters. With the use of an eddy resolving modelling technique, predictions can be made of the extreme values of these time dependent variables. In the next section, several distributions are analysed to see how the "maximum" value can be defined.

Based on the above, a general stability formula is proposed that uses other variables to represent the same physical phenomena as captured by equation 4.1. In this stability formula, a preference is given to replace the velocity terms $\tilde{u}+\tilde{u}'$ by the wall shear stress τ_x instead of the shear velocity u_* for the following reasons:

- With the use of τ_x, an attempt is made to revert towards a simplistic stability relation, in which the well-known and generally accepted Shield-formula can be recognised.
- τ_x can be extracted from the model directly. Using u_* as a load parameter could increase the probability of making mistakes, as u_* is applied as a bottom boundary condition in the model. To obtain the correct value of u_*, one should determine it manually according to its definition: $u_* \equiv \sqrt{\frac{\tau}{\rho}}$. The use of τ_x is therefore more straightforward.

From a physical point of view, it now makes sense to replace the acceleration terms $\tilde{a}+\tilde{a}'$ of equation 4.1 by the pressure gradient $\frac{\partial p}{\partial x}$. All terms of the stability relation then have the same units, resulting in a dimensionless stability parameter Ψ_{gen}.

Below the general stability formula based on bottom parameters is presented. This equation will be the starting point for the development of a new stone stability formula.

$$\Psi_{gen} = \frac{\left(\tau_x + C_{m:b}\frac{\partial p}{\partial x}d\right)_{\max}}{(\rho_s - \rho_w)gd} \tag{4.2}$$

In which:

- τ_x represents the forces caused by the flow velocity and large energy containing eddies. It thereby largely represents the drag force and to a smaller extend contributes to the lift force.
- $\frac{\partial p}{\partial x}$ represents the effect of inertia on stone stability. The forces are amongst others caused by spatial accelerations and pressure fluctuations due to waves and turbulent wall pressures. It thereby largely represents the lift force and to a smaller extend contributes to the drag force.
- $C_{m:b} = \frac{C_m}{C_b}$, so this is the coefficient for the added mass divided by the drag and lift coefficient. This is similar as for example done in Steenstra (2014), who found a value of 23 for this combined coefficient.

To determine how the maximum can be defined, in section 4.2.5 the joint distribution of τ_x and $\frac{\partial p}{\partial x}d$ is discussed. Before arriving at this part, a more in-depth analysis is performed on the behaviour of the simulated values of τ_x and $\frac{\partial p}{\partial x}$ separately, to evaluate their robustness and reliability.

4.2. Analysis distribution τ_x and $\frac{\partial p}{\partial x}$

The analysis in this section is based on the output of the long sill simulation with $h = 0.375$ m only. First some values of τ_x and $\frac{\partial p}{\partial x}$ before the sill are extracted from the model, to serve as a kind of reference values. Next the spatial distribution and the distribution over time of τ_x and $\frac{\partial p}{\partial x}$ are analysed separately. After drawing some conclusions, at the end of this section the distribution of the full load-term of equation 4.2 is discussed.

4.2.1. Reference values before the sill

As explained in section 2.3.3, in this experiment the area before the sill is meant to obtain a more or less uniform flow that is adapted to the bottom roughness before the measuring area starts. Although strictly speaking this area is not long enough to obtain a steady uniform flow, the values of τ_x and $\frac{\partial p}{\partial x}$ before the sill can serve as reference values for a relatively uniform flow conditions compared to the turbulent flow after the sill. In table 4.1 the values of τ_x and $\frac{\partial p}{\partial x}$ are given at the bottom, 0.5 m and 1,0 m before the upstream toe of the sill. Points are taken in the centreline of the flume and at $\frac{1}{4}^{th}$ and $\frac{3}{4}^{th}$ of the width.

Y [m]	X [m]	$\bar{\tau_x}$ [Pa]	σ_{τ_x} [Pa]	$\frac{\bar{\partial p}}{\partial x}$ [Pa/m]	$\sigma_{\frac{\partial p}{\partial x}}$ [Pa/m]
0.125	-1.00	0.84	0.18	-7.53	63.80
0.25	-1.00	0.76	0.18	-7.14	63.80
0.375	-1.00	0.84	0.18	-7.52	63.85
0.125	-0.50	0.87	0.23	-6.59	86.49
0.25	-0.50	0.77	0.23	-6.57	86.41
0.375	-0.50	0.87	0.23	-6.60	86.40

Table 4.1: Reference values of τ_x and $\frac{\partial p}{\partial x}$ before the sill

4.2.2. Spatial distribution

A general impression of the spatial distribution of the mean wall shear stress τ_x and the mean pressure gradient $\frac{\partial p}{\partial x}$ can be obtained from figure 4.1 and 4.2. The visualised minima and maxima are adjusted manually to obtain plots with significant colour differences. The peak values are left blank, as they can disturb the colour scheme. Thereby the general spatial distribution of τ_x and $\frac{\partial p}{\partial x}$ is expressed more clearly in these figures.

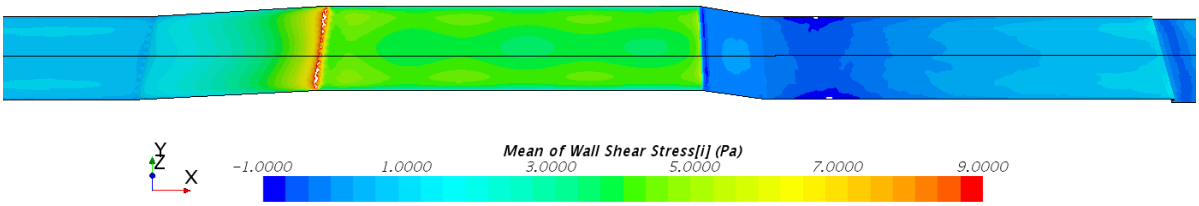

Figure 4.1: 3D colour plot of the distribution of the mean wall shear stress τ_x [Pa]

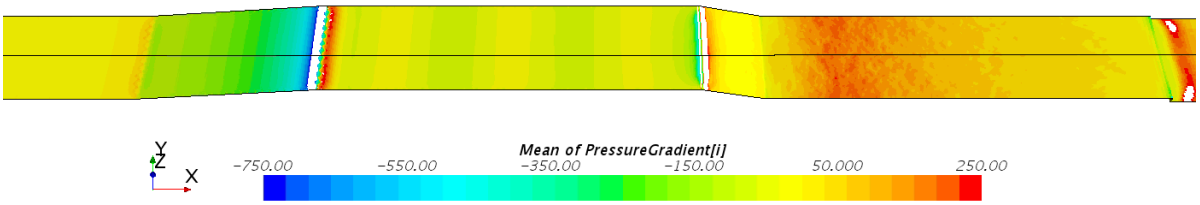

Figure 4.2: 3D colour plot of the distribution of the mean pressure gradient $\frac{\partial p}{\partial x}$ [Pa/m]

In order to evaluate the spatial distribution of τ_x and $\frac{\partial p}{\partial x}$, extra bottom point are added in the model. At these bottom points, the mean values and variances are extracted from the software and placed in table K.1. This tables contains a lot of information and therefore an elaborated analysis is added in appendix K. In the remainder of this subsection, only the conclusions of this analysis are presented.

Over the width of the flume

In general it can be concluded that the geometry of the experiment invokes a two-dimensional approach, but the results show this is not trivial any more for the detailed calculations performed in this thesis. A more in-depth view on the physics around stone stability in which turbulence is taken into account, also means taking into account three-dimensionality. Moreover, the effects of the side walls should not be neglected. As already observed in Jongeling et al. (2003), they do influence the results.

Nevertheless, τ_x and $\frac{\partial p}{\partial x}$ are not randomly distributed. As well the mean values as the standard deviations are in the same order of magnitude for each analysed x-coordinate. Clearly the distribution over the length of the flume is more significant and therefore a two-dimensional approach might still be justified. Furthermore, in the experiment only the stone movements in x-direction are traced. In the remainder of this study therefore the centreline values of τ_x and $\frac{\partial p}{\partial x}$ will be assumed representative for that x-coordinate over the entire width of the flume. The robustness of the stability formula should reveal if this assumption is valid.

Over the length of the flume

The four flow regions, defined in section 3.1.1, can also be identified in the distribution of τ_x and $\frac{\partial p}{\partial x}$ over the length of the flume. The effects of the changing flow velocities and turbulence intensity are clearly visible in the results. The distribution of the variables over the length of the flume is in agreement with the expectations. Some remarks are listed below.

- The spatial distribution of the mean wall shear stress $\bar{\tau_x}$ corresponds to the distribution Xingkui and Fontijn (1993) found for the drag force. The mean values of the pressure gradient $\frac{\bar{\partial p}}{\partial x}$ are positive for the entire downstream area. This is in agreement with the observations Xingkui and Fontijn (1993) described for the lift force.
- In the long sill simulation the reattachment area, as defined in section 3.1.1, is located near cross-section 5 at $x = 4.15$ m. This does not exactly coincide with the reattachment point observed during the experiments, which was stated to be located around cross-section 4 at $x = 3.95$ m. This does not necessarily has to be problematic as in reality the reattachment point is fluctuating over a certain area. Despite that the results at cross-section 4 are not in agreement with the definition of the reattachment region posed in this thesis, it is decided that for the further analysis's cross-section 4 is included in the reattachment area.

Spatial distribution over regions
Table 4.2 can be seen as the end product of the spatial analysis. Important are the characteristics of the different flow regions, as summarised below.

- **Top of the sill**
  High mean value of τ_x. Negative mean value of $\frac{\partial p}{\partial x}$. Relatively low standard deviations.
- **Recirculation area**
  Negative mean value of τ_x. Mean value of $\frac{\partial p}{\partial x}$ and the standard deviations increasing towards the reattachment area.
- **Reattachment area**
  Mean of τ_x nearly 0 and the standard deviation of $\frac{\partial p}{\partial x}$ at its maximum. Relatively high value for the standard deviation of τ_x. Decreasing mean of $\frac{\partial p}{\partial x}$ in downstream direction.
- **Recovery area**
  Increasing mean of τ_x and a slightly decreasing standard deviation in downstream direction. Fast decreasing mean and standard deviation of $\frac{\partial p}{\partial x}$ in downstream direction.

Cross-Section	Z [m]	X [m]	$\bar{\tau_x}$ [Pa]	σ_{τ_x} [Pa]	$\frac{\bar{\partial p}}{\partial x}$ [Pa/m]	$\sigma_{\frac{\partial p}{\partial x}}$ [Pa/m]	Region
10	0.165	2.25	3.68	0.11	-61.42	19.14	Top of sill
1	0.165	3.00	4.11	0.20	-161.98	55.54	Top of sill
2	0.04	3.45	-0.25	0.42	43.63	205.44	Recirculation
3	0.04	3.75	-0.56	0.87	185.15	464.50	Recirculation
4	0.04	3.95	-0.21	0.90	142.59	584.86	Reattachment
5	0.04	4.15	0.05	0.84	107.56	536.76	Reattachment
6	0.04	4.35	0.29	0.79	80.68	480.24	Recovery
7	0.04	4.55	0.34	0.69	62.87	420.34	Recovery
8	0.04	4.95	0.59	0.75	46.83	353.92	Recovery
9	0.04	5.15	0.65	0.64	32.13	292.48	Recovery

Table 4.2: Bottom values of τ_x and $\frac{\partial p}{\partial x}$ in the centreline of the flume

4.2.3. Distribution over time

In this subsection the distributions over time of τ_x and $\frac{\partial p}{\partial x}$ are analysed, based on the time signals extracted at several locations of the CFD model. This is particularly interesting for answering the question how the extreme values of τ_x and $\frac{\partial p}{\partial x}$ should be defined. Besides that, the distributions of τ_x and $\frac{\partial p}{\partial x}$ are compared to the distributions found in literature for the drag and lift force respectively. In this way, an attempt is made to substantiate the chosen approach to assess the stability of a stone, despite the fact that the values of τ_x and $\frac{\partial p}{\partial x}$ cannot be validated.

Time signals of τ_x and $\frac{\partial p}{\partial x}$
First some remarks about the time signals derived from Star CCM+. It is important that these time signals are long enough to obtain sufficient data for a statistical analysis. Long enough here means long compared to the turbulent time scales. A choice is made to use time signals of that are of equal length of the point measurements in Jongeling et al. (2003). These signals are obtained over 180 s. Applying the Taylor hypothesis on the large energy containing eddies results in a maximum time scale of about 0.35 s. In this case (in which implicitly isotropic turbulence is assumed) during the measuring time of 180 s about $\frac{180}{0.35} \approx 514$ eddies would pass the measuring point. Taking into account the anisotropy of the large eddies as seen in section 3.1.2, it appears that even less eddies will pass the measuring point. Therefore it should be noted that longer time signals might be desirable for a proper statistical analysis.

Another thing to keep in mind is the sampling frequency for the pressure gradient data. As stated in Hofland (2005), only the eddies with a size of about one times the stone diameter or larger are of importance for the stone stability. In case one is able to apply a very small grid size together with a very small time scale, the obtained time signal for the pressure gradient should be filtered for the time scale corresponding to a turbulent length scale equal to the stone diameter. The Taylor hypothesis can be used to determine this time scale. For this thesis the time scale corresponding to an eddy size equal to the stone diameter is approximately 0.007 s. The used time step in this thesis is 0.005 s. As these two values are nearly equal, the time signals obtained from the simulation are not filtered.

To get insight in the time-dependent behaviour of τ_x and $\frac{\partial p}{\partial x}$, at each cross-section the probability of occurrence of the simulated values are plotted in a histogram. A Gaussian distribution with the mean and standard deviation obtained from the dataset, is plotted over the histogram to see how the evaluated parameter is distributed over time. Similar to the approach of Hofland and Battjes (2006), on the vertical axis of the plots first a linear scale is used to observe how the variable is distributed around the mean. The shapes of these probability density functions (PDF's) are compared to literature as a kind of validation for the simulated values of τ_x and $\frac{\partial p}{\partial x}$. Subsequently, the probabilities are plotted on a logarithmic scale to evaluate the tails of the distributions. These tails are the area of interest for the stone stability. They can be used to obtain the extreme values of the wall shear stress τ_x and the pressure gradient $\frac{\partial p}{\partial x}$.

PDF's wall shear stress τ_x

The PDF's of the wall shear stress are plotted in appendix G. As an example, the results for cross-section 8 are given below in figure 4.3 and 4.4.

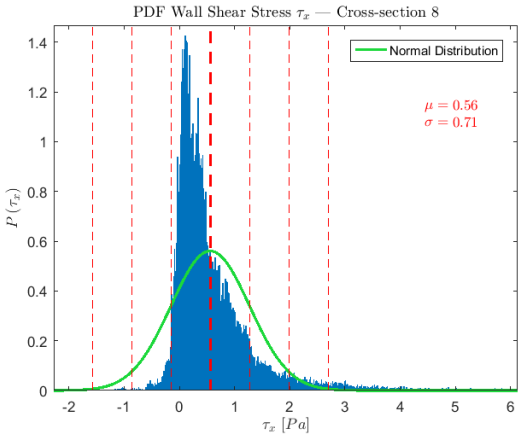

Figure 4.3: PDF of τ_x [Pa] at cross-section 8

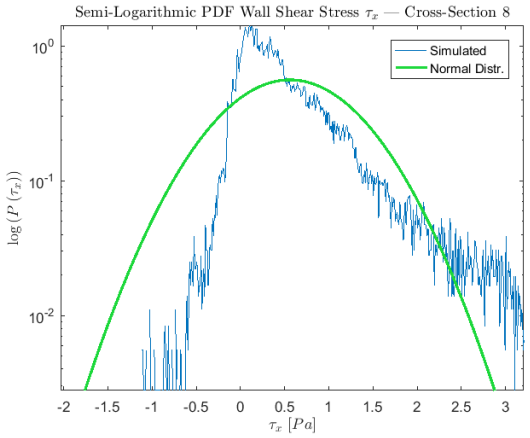

Figure 4.4: Semi-logarithmic PDF of τ_x [Pa] at cross-section 8

Just like the PDF of figure 4.3, at several cross-sections in the area downstream of the sill the distribution of τ_x is clearly skewed. The directions of the stretched tails are equal to the dominant near-bottom flow directions. All PDF's of τ_x in the downstream area show a high kurtosis. As one can see in figure 4.3, the Gaussian distribution does not fit to the wall shear stress data. The cross-sections on top of the sill form an exception on this (see figure G.1 and G.3). Here it seems to be reasonable to describe the data by a Gaussian distribution. On top of the sill, the PDF's of τ_x are not skewed and do not show a high kurtosis.

All these findings are in agreement with an earlier study of Hofland and Battjes (2006), in which the distribution of the shear stress is considered to be similar to the distribution of the drag force. For a further comparison, figure 2 of Hofland and Battjes (2006) is shown below. In this figure the shapes of the PDF of the drag force are given for several turbulence intensities. $\delta = 0$ corresponds to a very high turbulence intensity and $\delta = 6$ to a low turbulence intensity.

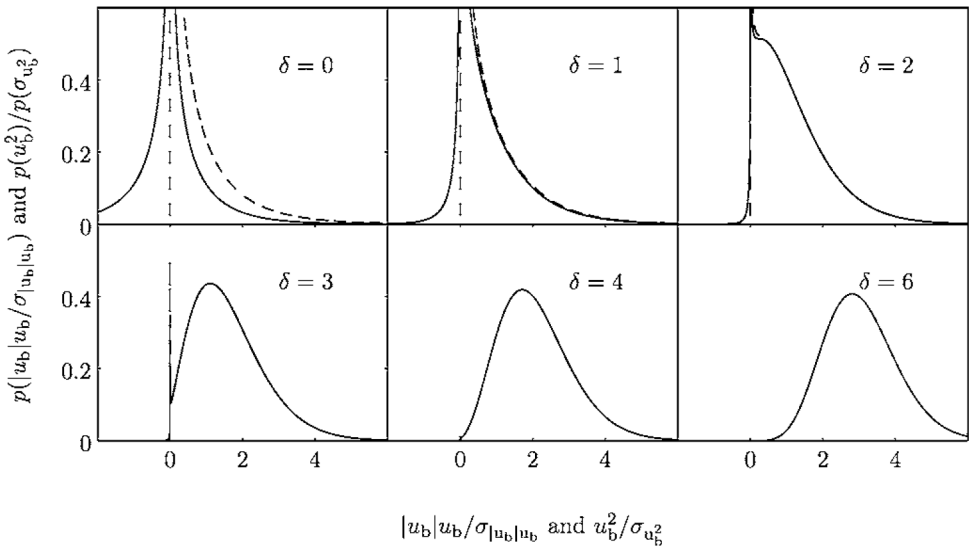

Figure 4.5: PDF's of the drag force for several turbulence intensities (Hofland and Battjes, 2006)

Comparing figure 4.3 and 4.5 visually, the PDF of cross-section 8 seems to in best agreement to the graph for $\delta = 1$ of figure 4.5. Determining δ for cross-section 8 in a way nearly similar to Hofland and Battjes (2006) as $\delta = \frac{\mu_{\tau_x}}{\sigma_{\tau_x}} \left(= \frac{1}{r}\right)$, a value of $\delta \approx 0.8$ is obtained. This is close to the expected value of 1 that Hofland and Battjes describe for this PDF-shape. Thereby the shapes of the PDF's in the downstream area can be explained by the high turbulence intensity, combined with the flow direction and velocity at the bed. Furthermore, figure 4.5 shows that for $\delta > 3$, higher values of δ result in PDF's that tend towards a Gaussian distribution. The Gaussian shape of the PDF's on top of the sill (G.1 and G.3) can therefore be explained by the relatively low turbulence intensity. Earlier a Gaussian distribution of the drag force was already observed in the experimental data of Einstein and El-Samni (1949) and Cheng and Clyde (1972) for uniform flow cases. It can be concluded that the obtained shapes of the PDF's of τ_x are in agreement with one what would expect from literature.

From figure 4.4, it can be seen that the extreme values of the wall shear stress are not predicted well by the Gaussian shape. In Hofland and Battjes (2006) a mathematical description for the PDF of the drag force is derived, based on the assumptions that the drag force is proportional to $F = \alpha u_b|u_b|$ and that the near-bed velocity is Gaussian distributed. During the validation of this PDF, only the positive tail of the distribution appeared to be represented well in case high turbulent intensities are present. This is exactly the area of interest for this thesis and therefore the PDF derived in Hofland and Battjes (2006) is potentially useful for the aim of this thesis. Unfortunately the near-bottom flow velocities should be used as input values for the fitted distribution. In the approach chosen for this thesis, these velocities are replaced by the wall shear stress. The PDF therefore should be adjusted, before it can be applied to obtain the extreme values for stability relation 4.2. This mathematical derivation is left outside the scope of this thesis.

PDF's pressure gradient $\frac{\partial p}{\partial x}$

The resulting PDF's of the pressure gradient $\frac{\partial p}{\partial x}$ can be found in appendix H. As an example, again the results for cross-section 8 are given in figure 4.6 and 4.7.

Just like figure 4.6, all PDF's of $\frac{\partial p}{\partial x}$ show a more or less symmetrical distribution around the mean, indicating a Gaussian distribution of this parameter. A high kurtosis can be observed for all PDF's in the downstream area. This means that here the tail of the distribution of $\frac{\partial p}{\partial x}$ is formed by infrequently occurring peak values. These peaks can be explained by the high turbulence intensity in this area. The PDF's of the cross-sections on top of the sill show no increased kurtosis, as there the turbulence intensity is low. In section 4.1 it is stated that the pressure gradient represents (the largest share of) the lift force. In literature similar descriptions can be found about the distribution of the lift force, as seen for the $\frac{\partial p}{\partial x}$-PDF's. For example Einstein and El-Samni (1949) observed that the lift force has a Gaussian distribution for a flow over a hydraulically rough bed.

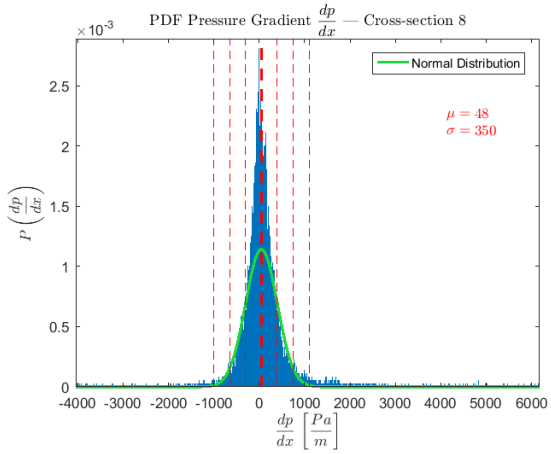

Figure 4.6: PDF of $\frac{\partial p}{\partial x}$ [Pa/m] at cross-section 8

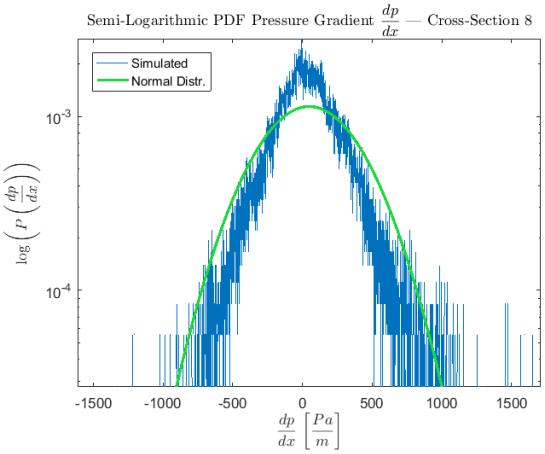

Figure 4.7: Semi-logarithmic PDF of $\frac{\partial p}{\partial x}$ [Pa/m] at cross-section 8

For the cross-sections on top of the sill, figure H.2 and H.4 show that also the tail of the distribution is in reasonable agreement with the Gaussian distribution. Unfortunately the semi-logarithmic PDF's of the downstream area show that the extreme values of $\frac{\partial p}{\partial x}$ deviate from the Gaussian shape in case of high turbulence intensity. Clearly extreme values can be observed that are far greater than the maximum of the Gaussian distribution. This is in agreement with the results found by Xingkui and Fontijn (1993), who also described the peak values of the lift force on the bed behind a backward-facing step. Because of this high kurtosis, the lift force cannot be fully described by a Gaussian distribution. The Gaussian distribution might not predict the extreme values of $\frac{\partial p}{\partial x}$ well enough for stability relation 4.2.

4.2.4. Conclusions about the distribution of τ_x and $\frac{\partial p}{\partial x}$

The conclusions about the spatial distribution summarised in table 4.2. Important to note is that τ_x and $\frac{\partial p}{\partial x}$ switch from positive to negative values in different regions. Absolute values should be used to make stability formula 4.2 generally applicable. The use of absolute values for τ_x and $\frac{\partial p}{\partial x}$ can be justified by the assumptions stated below.

- The direction of the near-bottom flow, and therefore the sign of the wall shear stress τ_x has no influence on the stone stability.
- The pressure gradient $\frac{\partial p}{\partial x}$ represents the effect of inertia, which causes the largest part of the lift force. The horizontal pressure difference is thereby assumed to be representative for the vertical pressure difference over a stone. The direction of the horizontal pressure difference then is insignificant.

In the further analysis, the load-term of 4.2 will therefore be replaced by $\left(|\tau_x| + C_{m:b}|\frac{\partial p}{\partial x}|d\right)$.

From the analysis of the distribution over time, it can be concluded that the PDF's of τ_x and $\frac{\partial p}{\partial x}$ are in good agreement with the distributions for drag and lift respectively, found in literature. This seems to indicate that the governing physics for stone stability are represented well by the chosen variables.

The peak values of τ_x and $\frac{\partial p}{\partial x}$ cannot be predicted well by a Gaussian distribution. In the next subsection, the distribution of $\left(|\tau_x| + C_{m:b}|\frac{\partial p}{\partial x}|d\right)$ will be analysed, to see how the extreme values of the total load can be determined.

4.2.5. Distribution of $\left(|\tau_x| + C_{m:b}|\frac{\partial p}{\partial x}|d\right)$

In appendix L the PDF's are given of the total load-term for a $C_{m:b}$-value of 1. It should not be a surprise that the Gaussian distribution does not fit the data. To make the difference quantitative, a cumulative density function (CDF) is presented next to the PDF. As an example, in figure 4.8 and 4.9 the results are shown for cross-section 8. For a Gaussian distribution, the 0.3%-exceedence probability can be predicted by $\mu + 3\sigma$. In figure 4.9, the load that is exceeded by 0.3% of the simulated results is denoted as $Load99.7\%$. Below this number, the 0.3%-exceedence probability is given in case a Gaussian distribution is assumed. This number is indicated as $Normal99.7\%$. In the third line, the probability is given that a value from the simulated dataset is lower or equal than the extreme value predicted by the Gaussian distribution.

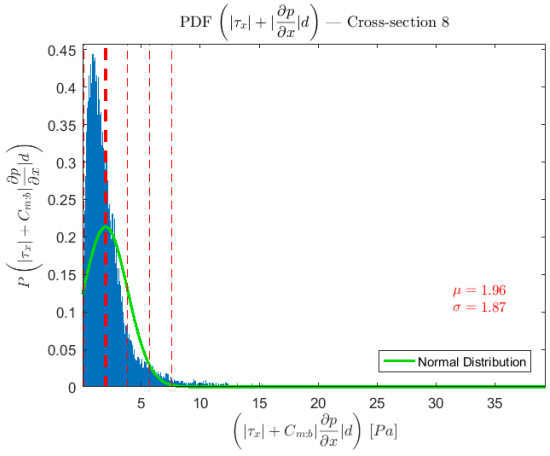

Figure 4.8: PDF $\left(|\tau_x| + |\frac{\partial p}{\partial x}|d\right)$ cross-section 8

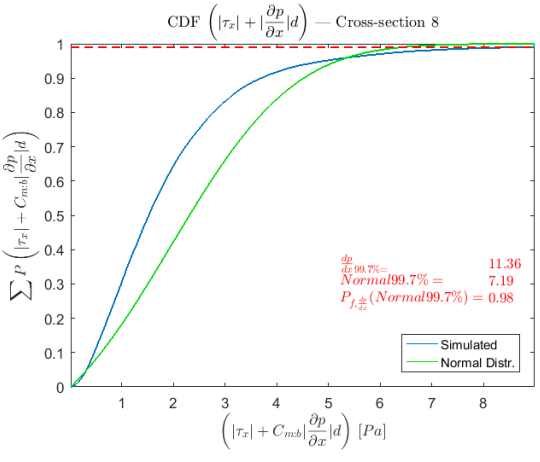

Figure 4.9: CDF $\left(|\tau_x| + |\frac{\partial p}{\partial x}|d\right)$ cross-section 8

In figure 4.9, the value for $Load99.7\%$ is significantly larger than the value $Normal99.7\%$ obtained for the Gaussian distribution. Thereby it can be concluded that the extreme loads of the simulated dataset will be significantly larger than what is predicted by $\mu + 3\sigma$. It is decided that the 0.3%-exceedence probability of the dataset will be used, to test the potential of stability formula 4.2.

Interesting to note is that the PDF's on top of the sill (figure L.1 and L.3) look a lot like those of τ_x (figure G.1 and G.3). In the downstream area, the PDF's of the total load look similar to the PDF's of $\frac{\partial p}{\partial x}$. This could indicate that the wall shear stress is dominant on top of the sill, while the pressure gradient is more dominant in the downstream area. An extra analysis is done to investigate this.

Dominant load-term

In appendix M the time signals for $|\tau_x|$, $|\frac{\partial p}{\partial x}|d$ and $\left(|\tau_x| + |\frac{\partial p}{\partial x}|d\right)$ are given for each cross-section (so $C_{m:b} = 1$). The same is done in appendix O for the $C_{m:b}$-value of 23 that Steenstra found in his thesis.

The figures of appendix M confirm that for $C_{m:b} = 1$, $|\tau_x|$ is dominant on top of the sill and $|\frac{\partial p}{\partial x}|d$ is dominant in the area behind the sill. For a $C_{m:b}$-value of 23, it appears that $23|\frac{\partial p}{\partial x}|d$ becomes the dominant load-term over the entire measuring area. These interesting results will be kept in mind during the evaluation of stability formula 4.2.

4.3. The new stone stability formula

In this section, the general stability relation posed at the beginning of this chapter, is specified further into a new stone stability formula. Subsequently the performance of the formula is tested for the simulated experiment after which some first conclusions are drawn.

4.3.1. Derivation of the new stability formula

Based on the analysis of section 4.2, the general stability formula of equation 4.2 will be slightly adjusted. Absolute values of τ_x and $\frac{\partial p}{\partial x}$ will be used to make the formula generally applicable for all regions of the simulated domain.

Furthermore, the PDF's of appendix L and N reveal that the extreme loads cannot be predicted accurately by $\mu + 3\sigma$. Therefore the values corresponding to the 0.3%-exceedence probabilities of the simulated time signals will be used to test the stability relation. A disadvantage of this approach is that only extreme values are available at the points were time signals are produced. For this simulation this is restricted to the ten cross-sections where the velocities are measured in Jongeling et al. (2003).

With these adjustments, the stone stability formula proposed in this thesis is equation 4.3.

$$\Psi_{new} = \frac{\left(|\tau_x| + C_{m:b}|\frac{\partial p}{\partial x}|d\right)_{0.3\%}}{\left(\rho_s - \rho_w\right) g d} \tag{4.3}$$

Still the proposed stability relation represents the same physics as equation 4.1 and 4.2. Besides this, equation 4.3 also represents nearly the same physics as captured by the stability formula found by Steenstra (2014). Compared to the physics in the Steenstra-formula, only the effect of the pressure gradient fluctuations $\frac{\partial p'}{\partial x}$ will be added to the load-term.

As explained in section 2.1 of the literature study, Steenstra obtained a good fit for a wide range of laboratory experiments. Therefore also a good performance of the proposed stone stability formula 4.3 is expected. Steenstra obtained the best fit for a $C_{m:b}$-value of 23. In this section, the proposed stability formula 4.3 is tested for $C_{m:b} = 1$ and $C_{m:b} = 23$, to evaluate if this method has potential.

Nevertheless, it should be emphasised that from a physical point of view, the testing also could have been done for other large $C_{m:b}$-values of for example 20 or 50. In the tested stability relation 4.3 other load parameters are used than in Steenstra (2014). Therefore, the ratio between the drag and inertia load term will not be the same, and the $C_{m:b}$-value of 23 cannot be copied from the Steenstra formula.

4.3.2. Testing the new stability formula

Similar to figure 2.1 of Steenstra et al. (2016), in this subsection the performance of stability formula 4.3 is evaluated by plotting the Ψ_{new}-values against the entrainment rate Φ_E for both long sill simulations.

The entrainment rate of the experiment is discussed earlier in section 2.3.6. For the long sill simulation with $h = 0.375$ m, in appendix L the PDF's and CDF's of the summoned signals of $|\tau_x|$ and $|\frac{\partial p}{\partial x}|$ are given for $C_{m:b} = 1$. In appendix N the extreme values for $C_{m:b} = 23$ can be found. The numbers for the long sill simulation with $h = 0.50$ m are obtained in a similar way.

$C_{m:b} = 1$

Plotting the Ψ_{new}-values against the entrainment rate, results in figure 4.10 for a $C_{m:b}$-value of 1. For each experiment only seven points are plotted in this graph, as in both experiments Jongeling et al. (2003) found zero damage for three of the ten analysed cross-sections. Furthermore trendlines are fitted through the data points of each experiment separately. Power functions are chosen to express the relation between Φ_E and Ψ_{new}. In the lower left corner the correlations R^2 between the data points and the trendlines are indicated.

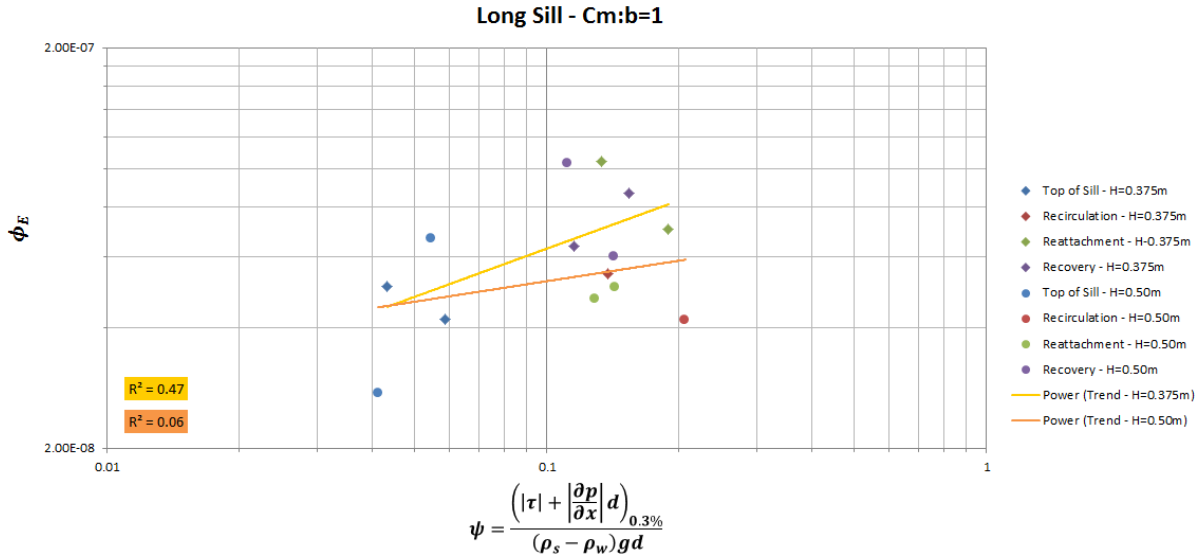

Figure 4.10: Ψ_{new} against Φ_E for $C_{m:b} = 1$ plotted on log-log scale

At first sight, it can be concluded that the proposed stability formula does not predict the measured damages very well. The slopes of both trendlines are positive, which is good because than a higher entrainment rate is predicted for higher Ψ_{new}-values. Nevertheless quite some scatter can be observed and different Ψ_{new}-values are found for cross-sections to which an approximately equal entrainment rate Φ_E is assigned and vice-versa. Both correlations R^2 are low compared to the R^2-value of 0.80 that Steenstra (2014) found for his stability formula, although in section 4.4 it will be discussed if a high value for R^2 is representative for a desirable fit.

Of course the fits presented in figure 4.10 are based on only seven data points each, which is too little to draw firm conclusions. Also the measured damages are considered to be under-sampled as discussed in 2.3.6. Despite this, it is interesting to see how the formula behaves for the different flow regions. Some observations are listed below that will be elaborated further in the remainder of this chapter.

- A distinction is visible between the region on top of the sill and the downstream area. As a reminder, the downstream area consists of the recirculation area, the reattachment area and the recovery area.
- The distinction between the top of the sill and the downstream area is also visible for points with an approximately equal entrainment rate. Note for example the difference between the Ψ_{new}-values of the red marker and the highest blue dot of the simulation with $h = 0.375$ m, while their Φ_E-values are nearly the same.
- In section 4.2.5 it is observed that the wall shear stress is dominant on top of the sill, and the pressure gradient is dominant in the downstream area for a $C_{m:b}$-value of 1.
- The behaviour of stability relation 4.3 is similar for both long sill simulations.

$C_{m:b}$ = 23

In figure 4.11 the relation between the proposed stability relation 4.3 and the entrainment rate is shown for $C_{m:b} = 23$. The value of 23 is used to give an impression of what influence a high $C_{m:b}$-value has on the results. It is not valid to assume that the $C_{m:b}$-value of 23 from Steenstra (2014) can be copied to stability relation 4.3.

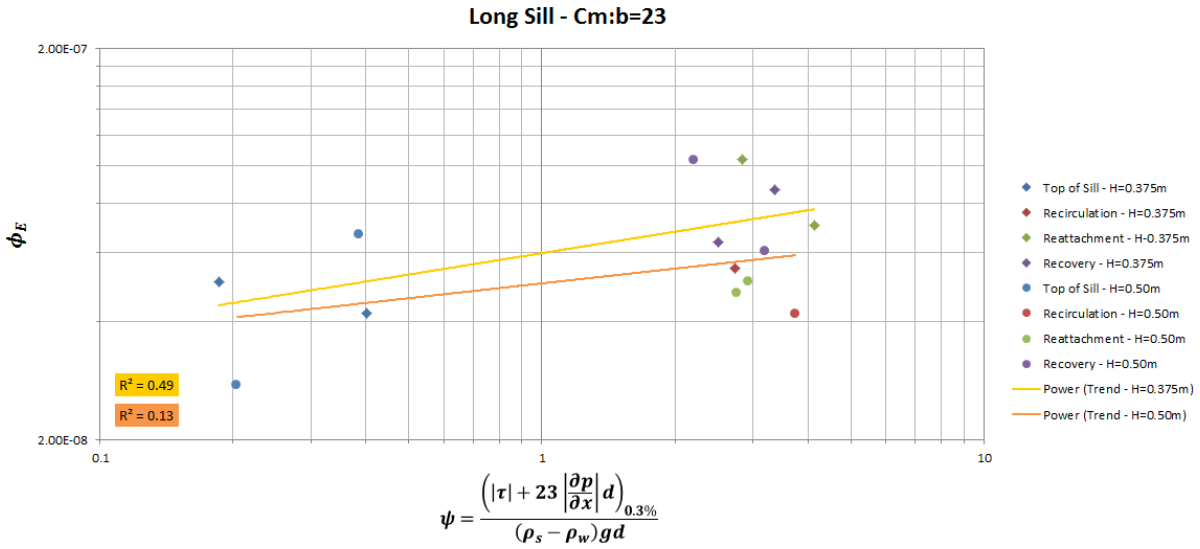

Figure 4.11: Ψ_{new} against Φ_E for $C_{m:b} = 23$ plotted on log-log scale

Compared to figure 4.10, the increased $C_{m:b}$-factor stretches the graph in horizontal direction. The entrainment rates are now spread over a larger range of Ψ_{new}-values. The difference between the region on top of the sill and the downstream area is now expressed even more clearly, while the Φ_E-values remained the same. This indicates that with the proposed stability relation 4.3, the predictions of the damages do not improve in case a $C_{m:b}$-value of 23 is used. The representation of the physics even seems to be a bit worse for the high $C_{m:b}$-value, while the correlation numbers for both simulations are increased a bit.

4.3.3. Conclusions about testing the new stability formula

It can be concluded that the stability parameter Ψ_{new} is not able to predict the observed damages well. The trendlines have a positive slope, which is good. But in figure 4.10 and 4.11 a clear difference can be observed between the results for the region on top of the sill and the downstream area, that should not be there based on the measured entrainment rates. In the previous section 4.2.5 it was concluded that the governing forces in these regions are caused by different physical load terms of the proposed stability formula.

From these observations the idea is originated that the damages on top of the sill and the damages in the downstream area should be split up in two distinct entrainment mechanisms. These two entrainment mechanisms might depend on the same physical load terms as captured by stability relation 4.3. The problem is that the ratios between these load terms on top of sill might be different from those in the downstream area. Therefore the damages for both flow regions might not be predicted well by one stability formula.

In this thesis no firm conclusions can be drawn about this hypothesis, as it is based on a combination of simulated results and literature instead of physical measurements. Nevertheless the idea that the damages in the different region are caused by two distinct entrainment mechanisms, might explain the rather bad performance of equation 4.3, as well as the low correlation number R^2 compared to Steenstra (2014).

The low correlation numbers compared to the R^2-value obtained in Steenstra (2014) are remarkable, as the physics captured by both stability formulas are nearly the same. From a physical point of view, the only difference is that in stability formula 4.3 an extreme value of the inertia-term is taken into account instead of only the mean. Therefore in the next section the performance of stability formula 4.3 will be compared to the stability relation proposed in Steenstra (2014).

4.4. Performance compared to Steenstra

In this thesis, special reference is made to the stone stability formula presented in Steenstra (2014), as Steenstra obtained a power relation between Φ_E and Ψ_{RS} that appeared to be a good fit for a large amount of experiments. In these experiments many different flow phenomena are represented, which might indicate that the Steenstra-formula represents the governing forces on a stone well. The stability formula proposed in this thesis should include nearly the same physical phenomena as the Steenstra-formula. For convenience the similarities and differences between the load terms of these two stability formulas are listed below.

- The physics represented by the depth-averaged flow velocity in the Steenstra-formula, are captured by the local mean wall shear stress in stability relation 4.3.
- The physics represented by the turbulent kinetic energy in the Steenstra-formula, are captured by the wall shear stress fluctuations in stability relation 4.3.
- The physics represented by the depth-averaged acceleration in the Steenstra-formula, are captured by the mean pressure gradient at the bed in stability relation 4.3.
- Next to the physics captured by the Steenstra-formula, the stability relation 4.3 also includes the load caused by the pressure gradient fluctuations.

As equation 4.3 represents nearly the same physics as the Steenstra-formula, it is expected that their performances will also be comparable. Nevertheless in the previous section it is concluded that the proposed stability parameter Ψ_{new} is not predicting the measured damages well. Therefore in this section a closer look is taken to the performance of the Steenstra-formula for the long sill experiments.

In Steenstra (2014) also data of the experiments of Jongeling et al. (2003) is used to derive a stability formula. Of the long sill experiments, Steenstra only used the data of the experiment with $h = 0.50m$. The performance of his stability formula for this experiment can be checked by figure 4.12, copied from Steenstra et al. (2016). For convenience the relevant markers are indicated by a red line for the downstream area and a green line for the cross-sections on top of the sill.

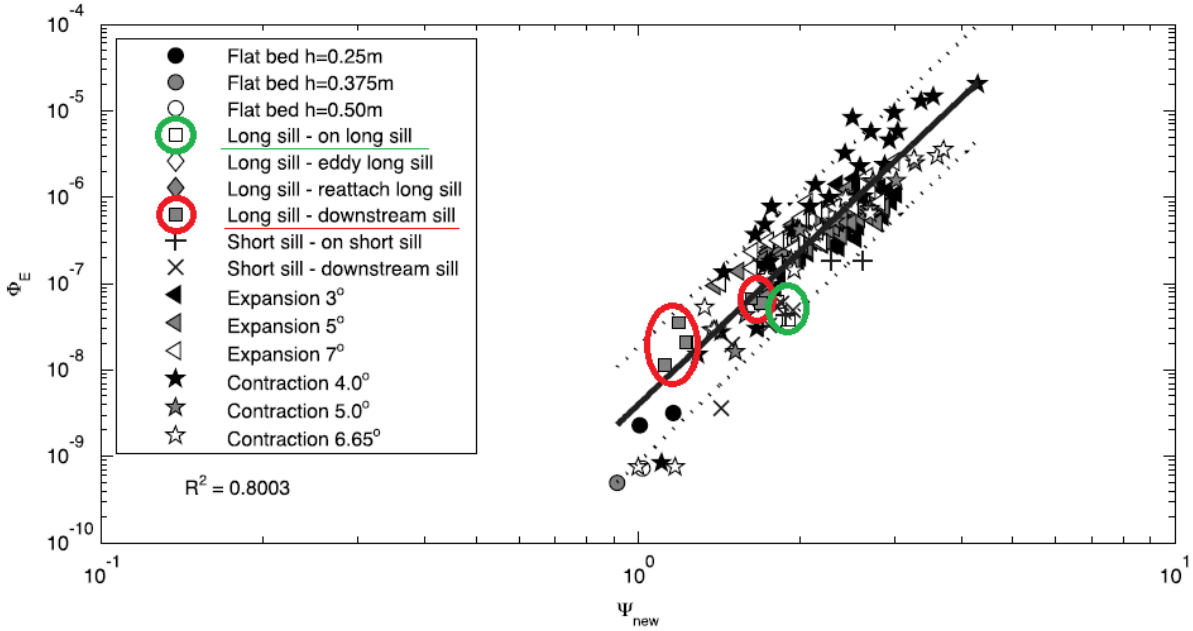

Figure 4.12: Ψ_{RS} against Φ_E plotted on log-log scale (from: Steenstra et al. (2016))

The figure shows that the Ψ_{RS}-values for the experiment long sill with $h = 0.50$ m fall in a small range between 1 and 2. It therefore can be doubted if, based on Ψ_{RS}, a distinction can be made between the different amount of stone movements observed for the cross-sections of this experiment. Furthermore the markers for the cross-sections on top of the sill are at the right of the markers in the downstream area. This is indicating a higher stability for the stones in the downstream area than for the stones on top of the sill, while it should be the other way around.

These observations show that the Steenstra-formula probably is too robust to make a distinction between the different flow regions of the experiment. Using the Steenstra-formula to design a granular bed protection for the long sill experiments, would result in one governing stone diameter for the entire measuring area. In this thesis an attempt is made to develop a stability relation that is capable of predicting the expected damages more accurately. In this way different stone sizes can be applied for flow regions with different bed loads.

With this analysis an explanation is found why the proposed stability relation 4.3 seems to perform bad compared to the Steenstra-formula, while almost the same physics are included. It can be concluded that a high correlation number R^2 is not necessarily representative for a desirable fit through the obtained data points. The stability formula proposed in Steenstra (2014) is too robust to make a distinction between the different entrainment rates measured for the long sill experiments.

4.5. Conclusions chapter 4

In the beginning of this chapter, the choice is made to use the wall shear stress τ_x and the pressure gradient $\frac{\partial p}{\partial x}$ to represent the extreme forces by drag and inertia respectively. The behaviour of these bottom parameters is analysed, to see how the general stability formula based on τ_x and $\frac{\partial p}{\partial x}$ can be specified into an usable stability formula.

The simulated (peak) values of τ_x and $\frac{\partial p}{\partial x}$ are not validated, but it appears that their distributions are in agreement with what one would expect from literature and engineering common sense. Their extreme values do not follow a Gaussian distribution, and therefore cannot be predicted by $\mu + 3\sigma$. Besides that, τ_x and $\frac{\partial p}{\partial x}$ are not simultaneously switching sign throughout the domain. Therefore it is decided to use absolute values of these parameters.

A combined load term $\left(|\tau_x| + C_{m:b}|\frac{\partial p}{\partial x}|d\right)$ is defined, which is used in the stability relation 4.3. It is found that the extreme values of this combined load term also cannot be predicted by $\mu + 3\sigma$. To check the performance of stability formula 4.3, only the extreme values of the simulated time signals can be used. The 0.3%-exceedence probabilities of these datasets are taken as the governing loads.

With these loads, the performance of the proposed stability relation 4.3 is tested. It must be concluded that the measured damages are not predicted well. The stability of the stones on top of the sill might be predicted by the same load terms as the stability of the stones in the downstream area, but is seems that the ratio between these load terms is different for both regions. From this, the idea is originated that the damages on top of the sill are caused by a different entrainment mechanism as the damages in the downstream area. It might be the case that the entrainment rates in these distinct flow regions therefore cannot be predicted by the same stability formula.

Remarkable is also the large difference found between the correlation numbers R^2 found for stability relation 4.3, and the R^2 found in Steenstra (2014). The poor performance of the proposed stability formula was not expected, as it represent nearly the same physical forces as those captured in the Steenstra-formula. The performance of the Steenstra-formula for the long sill experiment with $h = 0.50$ m is analysed, to study why the performance of stability relation 4.3 at first sight seems to be worse.

From this analysis it appeared that the relation between Φ_E and Ψ_{RS} found in Steenstra (2014) is too robust to predict distinct damages for the different flow regions of the long sill experiment. This explains why stability relation 4.3 at first sight appears to result in a bad fit compared to the Steenstra-formula. It can be concluded that a higher correlation number R^2 in this case is not an indicator for the desired stability formula.

5

Stability Formula Downstream Region

In the previous chapter it is shown that applying stability formula 4.3, does not result in a good prediction of the damages over the full domain of the long sill experiments. Nevertheless, it is expected that the chosen load terms are governing for the stone stability in general. The ratio between the load terms on top of the sill might be different from the ratio between these terms in the downstream area. With respect to the Eastern Scheldt case, especially the prediction of the stone stability in the area behind the sill is of interest (see section 2.3.2).

In this chapter the load terms of stability relation 4.3 will be analysed further. The aim is to derive a stability formula that represents the physics in the turbulent downstream region of the long sill experiments. In the first section, the approach will be explained and elaborated. After this, the effect of the different load terms on the prediction of the stone stability will be studied. In the third section, a stability relation will be derived based on the data of the downstream region of the long sill simulations only. This equation is assumed to be appropriate to assess the stone stability of the granular bed protection around the Eastern Scheldt barrier.

One should be aware of the fact that in this chapter, the physics concerning the stone stability is studied based on the output of a simulation. This simulated output is not directly validated. Therefore the posed methodology and hypothesis about the stone stability can considered to be more valuable than the resulting stability formula.

5.1. Governing physics behind the sill

In section 4.2 it is demonstrated that the maxima of τ_x and $\frac{\partial p}{\partial x}$ cannot be predicted accurately by an Gaussian distribution. Nevertheless in this chapter μ+3σ will be used to study the physics involved in the stone stability of different flow regions. In the next subsections, this approach will be explained theoretically, and it is shown that the applied methodology is likely to result in plausible outcomes. After this, the stresses by τ_x and $\frac{\partial p}{\partial x}$ will be related to the damage pattern observed in the long sill experiments. Finally this section is concluded by the explanation of the hypothesis about the two distinct entrainment mechanisms that can cause stone movement.

5.1.1. Theoretical background alternative approach

In hydraulic engineering it is common practise to determine the near-bed velocity as $u = \bar{u}(1+3r)$, in which r is the turbulence intensity. The turbulence intensity is defined as $r = \frac{\sigma_u}{\mu_u}$. Putting the expressions of u and r together, it is clear that the near-bed velocity is predicted by $u = \mu_u + 3\sigma_u$. This coincides with the empirical 0.3%-exceedence probability of a Gaussian distribution, and thereby represents a peak value of the near-bed flow velocity. The $(\mu+3\sigma)$-rule can safely be used for the near-bed flow velocity, as u generally is Gaussian distributed.

It is already shown that the (tails of the) distributions of τ_x and $\frac{\partial p}{\partial x}$ do not fit to a Gaussian distribution (section 4.2). Applying $\mu+3\sigma$ to the data of τ_x and $\frac{\partial p}{\partial x}$ therefore will not result in the extreme value corresponding to the 0.3%-exceedence probability (hereafter called 0.3%-value). Nevertheless, it can be argued if one really needs the 0.3%-value of τ_x and $\frac{\partial p}{\partial x}$ to make predictions about the stability of a stone.

As mentioned in 2.1, the occurrence of an extreme lift force followed by an extreme drag force is governing for the stability of a stone in a bed protection. In stability relation 4.3 this consecutive occurrence is taken into account by determining the 0.3%-value of the joint time signals of τ_x and $\frac{\partial p}{\partial x}$. An alternative option is to determine the extreme values of τ_x and $\frac{\partial p}{\partial x}$ separately. These peak values then might not always appear simultaneously, and therefore might not result in stone movement. This would justify the use of extreme values with a slightly higher exceedence probability than the 0.3%-value. Although not accurately, these peak values with a higher exceedence probability maybe can be reproduced by using the Gaussian $(\mu+3\sigma)$-rule. In the next subsection, it is analysed if using the $(\mu+3\sigma)$-rule results in extreme values of τ_x and $\frac{\partial p}{\partial x}$.

5.1.2. Gaussian distribution $\mu+3\sigma$

In this subsection the values obtained by $\mu+3\sigma$ are compared to the 0.3%-values of the time signals of τ_x and $\frac{\partial p}{\partial x}$. After this comparison, it can be decided if $\mu+3\sigma$ can be used to obtain extreme values for τ_x and $\frac{\partial p}{\partial x}$.

For this analysis, cumulative density functions (CDF's) are made for the time signals of τ_x and $\frac{\partial p}{\partial x}$ from the long sill simulation with $h=0.375m$. In figure 5.1 and 5.2 the CDF's of cross-section 8 are given as an example. The CDF's of the other cross-sections can be found in appendix I and J. Below the meaning of the red numbers in these plots are explained from the top down.

- $\tau_{x,99.7\%}$ and $\frac{\partial p}{\partial x}_{99.7\%}$ are the values corresponding to the 0.3%-exceedence probability of the dataset
- $Normal99.7\%$ is the value obtained by $\mu+3\sigma$
- $P_{f,\tau_x}(Normal99.7\%)$ and $P_{f,\frac{\partial p}{\partial x}}(Normal99.7\%)$ indicate the probability that τ_x or $\frac{\partial p}{\partial x}$ is lower than the value predicted by $\mu+3\sigma$

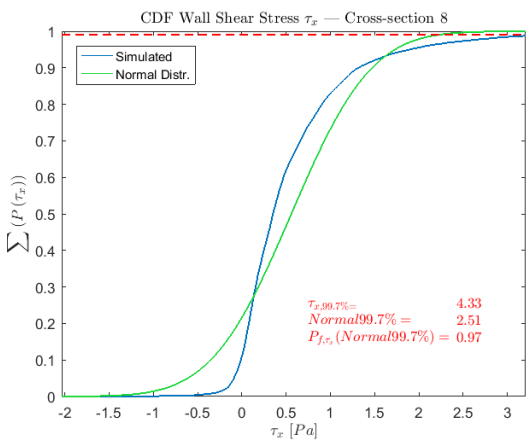

Figure 5.1: CDF of τ_x [Pa] at cross-section 8

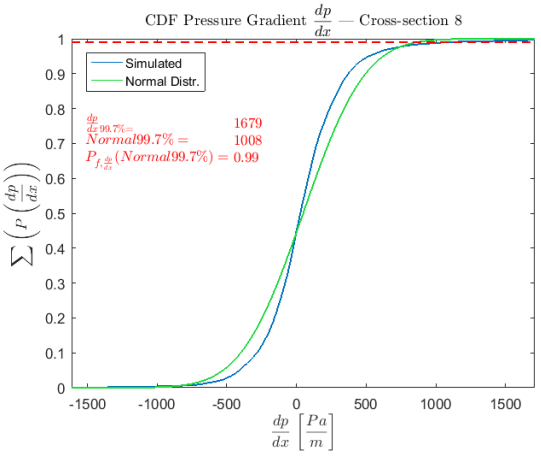

Figure 5.2: CDF of $\frac{\partial p}{\partial x}$ [Pa/m] at cross-section 8

From these CDF's, it can be concluded that the difference between the 0.3%-values and the values obtained by $\mu+3\sigma$ can be significantly. More than once, the value obtained by $\mu+3\sigma$ is only 55 to 60 percent of the 0.3%-value. Nevertheless, the $P_{f,\tau_x}(Normal99.7\%)$-values in all cases are 0.97 or higher. This means that for all cross-sections, the $\mu+3\sigma$-value is corresponding to the 3%-exceedence probability or lower.

Apparently the peak values of τ_x and $\frac{\partial p}{\partial x}$ are very high, as the 0.3%-value is sometimes almost twice the value corresponding to the 3%-exceedence probability. However, because these peak values occur so infrequently, the values predicted by $\mu+3\sigma$ still represent extreme values with a low exceedence probability. This is in agreement with the observation made in section 4.2 based on the PDF's of τ_x and $\frac{\partial p}{\partial x}$.

Although using $\mu+3\sigma$ is not the proper way of obtaining extreme values for τ_x and $\frac{\partial p}{\partial x}$, it does result in values with a low exceedence probability. Therefore $\mu+3\sigma$ can be used to study the influence of the mean values and the standard deviations i.e. the fluctuations of τ_x and $\frac{\partial p}{\partial x}$ separately. The behaviour of these different load-term can be studied with the adjusted form of stability relation 4.3 given by equation 5.1.

$$\Psi_{new} = \frac{\left(|\bar{\tau_x}| + 3\tau_x'\right) + C_{m:b}\left(|\frac{\partial \bar{p}}{\partial x}| + 3\frac{\partial p'}{\partial x}\right) d}{\left(\rho_s - \rho_w\right) g d} \tag{5.1}$$

A big advantage of using $\mu+3\sigma$ for the simulated results in this thesis, is that much more data points can be created. No time signals are needed any more to reproduce an extreme value at a certain location. Furthermore the load caused by the mean and the load caused by fluctuations can be studied separately.

Therefore in the remainder of this section, the maxima of τ_x and $\frac{\partial p}{\partial x}$ are determined with the $\mu+3\sigma$-rule. It should be noted that the dependency between the extreme values of τ_x and $\frac{\partial p}{\partial x}$ is not studied in this thesis. Using $\mu+3\sigma$ to obtain an extreme value of τ_x and $\frac{\partial p}{\partial x}$ will introduce inaccuracies. Still this approach is believed to result in valuable insights in the physics involved in the stability of a stone in a granular bed protection.

5.1.3. Performance for $max = \mu + 3\sigma$

In this subsection figure 4.10 and 4.11 are reproduced with data points obtained by using stability relation 5.1. Values of μ and σ are available for every bottom cell of the modelled domain. Therefore these values are extracted in the centre of each flat (not sloping) strip of the long sill experiments of which the damage is measured. For convenience, the damages of the long sill experiment with $h = 0.375m$ are shown in figure 5.3. The green bars are the strips of which data points are visible in figure 5.4 and 5.5. For the experiment with $h = 0.50m$, data of the same strips are used to obtain the markers in these figures.

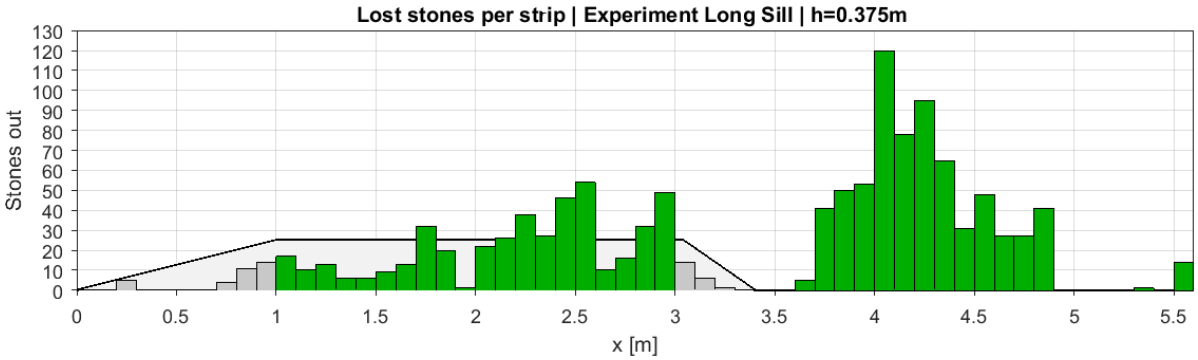

Figure 5.3: Stones lost per strip during the experiment long sill with $h = 0.375m$.
The green columns indicate the strips for which data points are made.

In figure 5.4 and 5.5 the Ψ_{new}-values are plotted against the entrainment rate observed for the strips indicated in 5.3. This is done for both long sill experiments with $C_{m:b}$-values of 1 and 23 respectively. The coloured markers are obtained with stability relation 5.1, and the black markers with stability relation 4.3. This to indicate the difference between these two equations.

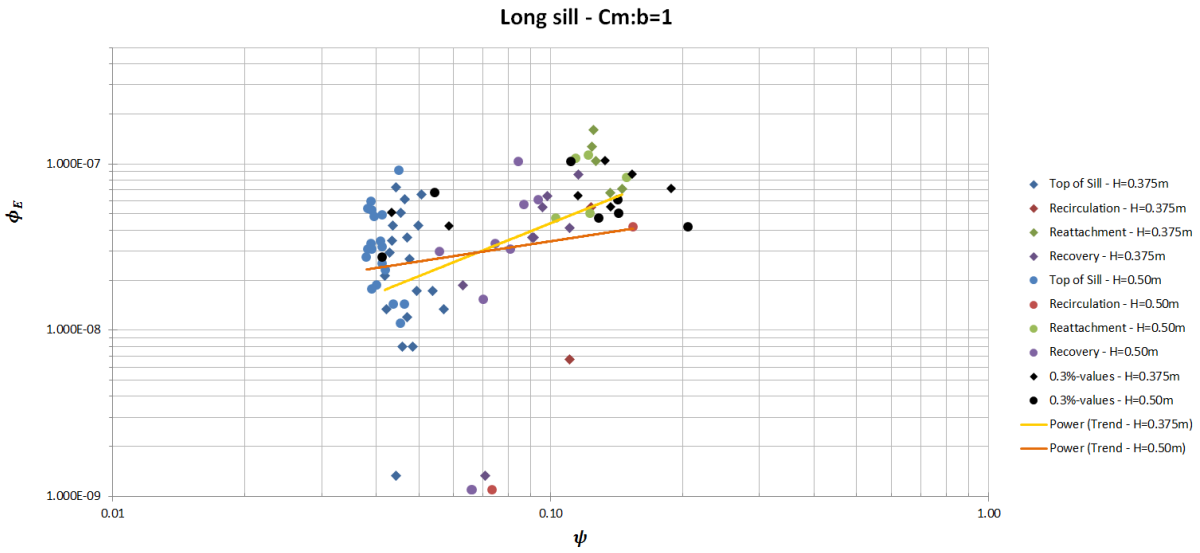

Figure 5.4: Ψ_{new} against Φ_E for stability relation 4.3 (black) and 5.1 (coloured) for both long sill experiments with $C_{m:b} = 1$

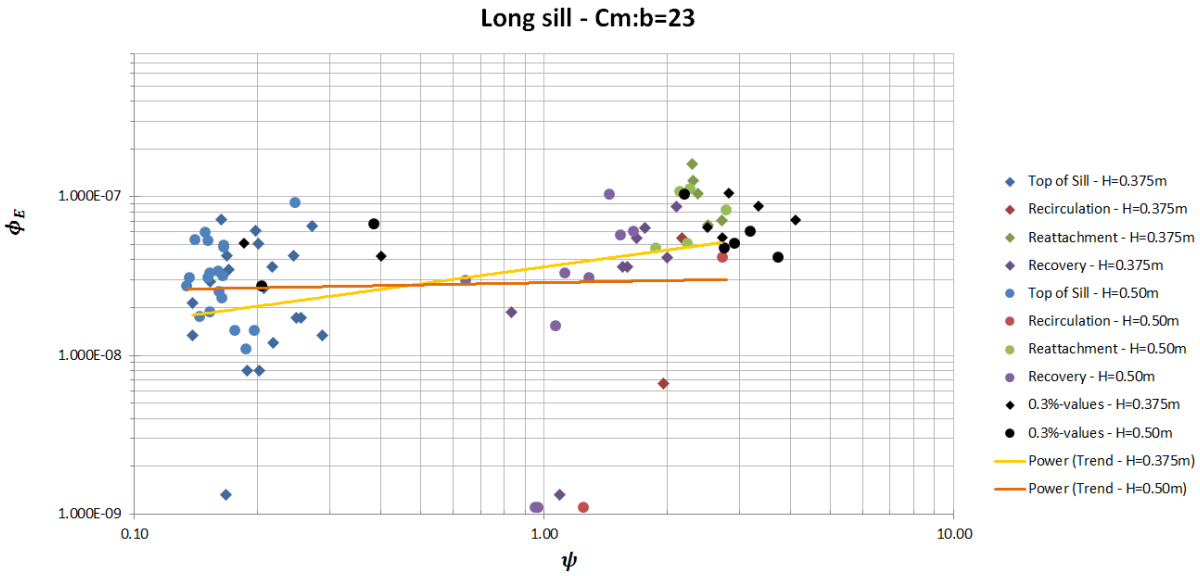

Figure 5.5: Ψ_{new} against Φ_E for stability relation 4.3 (black) and 5.1 (coloured) for both long sill experiments with $C_{m:b} = 23$

The black markers of figure 5.4 and 5.5 are a bit more at the right of the graph than the coloured ones. It shows that the predicted loads of stability relation 4.3 are a bit larger than the loads predicted by stability relation 5.1. This is in agreement with the expectations, as the simulated peak values of τ_x and $\frac{\partial p}{\partial x}$ are larger than what is predicted by the $\mu + 3\sigma$-rule.

The general picture shown by the coloured markers is similar to the behaviour of the black markers. Therefore it can be concluded that using stability relation 5.1 for $C_{m:b} = 1$ and $C_{m:b} = 23$ would result in the same conclusions as drawn earlier for stability relation 4.3 at the end of chapter 4. This confirms that the load terms of the original stability formula 4.3 can be studied more in-depth by the use of stability relation 5.1 posed in this section.

5.1.4. Stresses to damage

As stated earlier, the load on the bed of stability relation 5.1 is determined for every strip on top of the sill and in the downstream area. The resistance term of the stability formula i.e. the under-water weight of the used stones is the same over the whole domain. Therefore the measured damages are directly linked to loads at a particular cross-section. In this subsection, the different load-terms are plotted over the observed damages, to see if this can reveal more about the governing physics for the stone stability in a certain region. In this way also the effect of the combined added mass and drag-lift coefficient $C_{m:b}$ can be studied.

The plots are made for the long sill experiment with $h = 0.375m$. Figure 5.6 shows the result for a $C_{m:b}$-value of 1 and figure 5.7 is the result for $C_{m:b} = 23$. The legends of these figures are clarified below.

- Total WSS = Total Wall Shear Stress = $\left(|\bar{\tau_x}| + 3\tau'_x\right)$
- Mean WSS = Mean Wall Shear Stress = $|\bar{\tau_x}|$
- Total PG = Total Pressure Gradient = $C_{m:b}\left(|\frac{\partial \bar{p}}{\partial x}| + 3\frac{\partial p'}{\partial x}\right)d$
- Mean PG = Mean Pressure Gradient = $C_{m:b}|\frac{\partial \bar{p}}{\partial x}|d$

The difference between the Total-line and the Mean-line visualises the load caused by the fluctuations of the analysed parameter. Now first the result of figure 5.6 with a $C_{m:b}$-value of 1 is analysed.

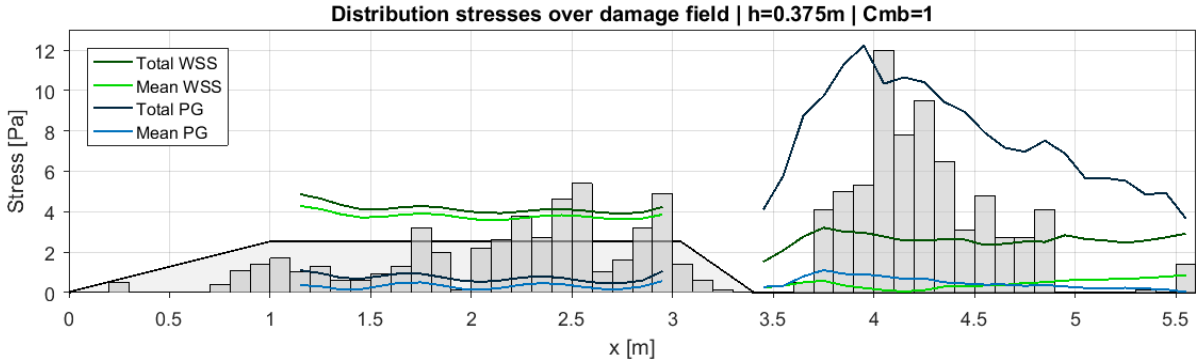

Figure 5.6: Distribution different load-terms plotted over the measured damage. Experiment long sill with $h = 0.375m$ and $C_{m:b} = 1$

Figure 5.6 confirms the conclusion drawn in section 4.2.5. For $C_{m:b} = 1$ the wall shear stress is governing on top of the sill and the pressure gradient in the downstream area. Furthermore it can be seen that on top of the sill the mean-values are the dominant part of the total force, while in the downstream area the fluctuating part of the load is dominant.

Interesting to note is that in the downstream area, the shape of the line for the total pressure gradient is following the shape of the observed damages quite well. Taking the line of the mean pressure gradient into account, this is clearly caused by the effect of the pressure gradient fluctuations. Figure 5.6 therefore seems to confirm the hypothesis that the assessment of the stone stability in this experiment should be split up into two distinct entrainment mechanisms for the region on top of the sill and the downstream area. On top of the sill the mean values are dominant, and in the downstream area the fluctuations are governing.

Next the results for $C_{m:b} = 23$ are shown in figure 5.7 to visualise the effect of this coefficient.

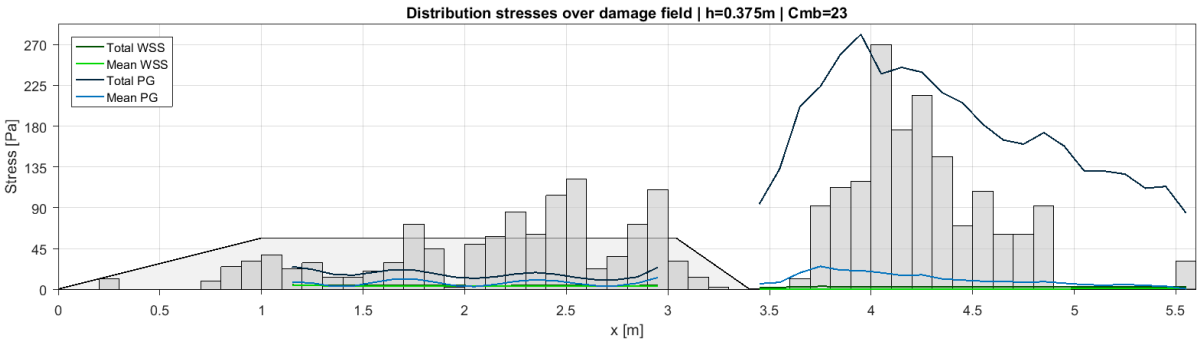

Figure 5.7: Distribution different load-terms plotted over the measured damage. Experiment long sill with $h = 0.375m$ and $C_{m:b} = 23$

For a $C_{m:b}$-value of 23, the pressure gradient becomes the dominant load term over the entire domain, so again the conclusions based on the time signals (section 4.2.5) are confirmed. On top of the sill, the wall shear stress and the pressure gradient are now in the same order of magnitude. In the downstream area the wall shear stress becomes negligible compared to the pressure gradient fluctuations.

Furthermore, also in figure 5.7 the distribution of the measured damages in the downstream area seems to coincide with the load caused by the pressure gradient fluctuations. This is in agreement with the presumption that the pressure gradient fluctuations are important for the stone stability in the downstream area. Including this load-term in the stability formula therefore might improve the prediction of stone stability in the downstream region, while it worsened the prediction of stone stability over the entire domain. Besides that, the ratio between the load-terms on top of the sill deviates so much from the ratio between the load-terms in the downstream area, that a $C_{m:b}$-value of 23 might work well for the one region, while is worsens the performance of the stability formula in the other region.

Wavy lines on top of the sill

On top of the sill, figure 5.6 and 5.7 show a wavy pattern for the total and mean stresses of τ_x and $\frac{\partial p}{\partial x}$. These wavy mean values cannot be declared from the geometry of the model. A plausible explanation for the wavy distribution are the waves described earlier in 3.5. These waves therefore seem to influence the simulated results on top of the sill.

Nevertheless the variation caused by the waves, seem to be quite insignificant. It does not change the general picture about the distribution of the different load terms. In the downstream area, which is the area of interest for the Eastern Scheldt case, the wavy pattern is not observed. Therefore it can be concluded that although the waves might not be physically correct, they do not seem to influence the results of this study significantly.

5.1.5. Hypothesis: two entrainment mechanisms

For the assessment of the stability of the granular bed protection near the Eastern Scheldt barrier, especially the damage in the downstream region of the experiment long sill should be predicted well, as explained in section 2.3.2. Based on the results presented earlier, it seems plausible that this prediction in the downstream area can be improved by taking the load caused by pressure gradient fluctuations into account. Nevertheless, in chapter 4 it is already concluded that including $\frac{\partial p'}{\partial x}$ in the stability formula, does not give good results for the entire modelled domain.

It seems likely that the damages to the granular bed protection on top of the sill are caused by a different entrainment mechanism than those in the downstream area. The ratio between the load term in these two flow regions are different, by which the entrainment rates will be different as well. Probably the prediction of the stone stability can be improved if these two entrainment mechanisms are not captured into one stability formula. In this section these entrainment mechanisms are explained more elaborately.

On top of the sill

The flow on top of sill is characterised by a high flow velocity and a relatively low turbulence intensity. Damages to the granular bed protection therefore are expected to be caused mainly by the high flow velocities. Also a smaller load due to the acceleration of the flow will be present (inertia). Translated to the bottom parameters used in stability relation 4.3 and 5.1, the mean wall shear stress $\bar{\tau_x}$ is expected to be governing in this region. The mean pressure gradient $\frac{\bar{\partial p}}{\partial x}$ includes the main load caused by inertia. The stresses visualised in figure 5.6 are in agreement with these expectations.

Important to realise is that the flow velocity, and therefore the wall shear stress $\bar{\tau_x}$, is high for the entire area on top of the sill. All stones in this region experience a relatively high load compared to their resistance. The distinction between a higher or lower amount of stone movements is made by including the mean pressure gradient $\frac{\bar{\partial p}}{\partial x}$ in the stability formula.

In probabilistic terms, on top of the sill the mean values of the load parameters are high, but the standard deviations are relatively small. The frequency by which a critical load for stone movement is reached, seems to be lower than for the downstream area. This is indicated in the example of figure 5.8.

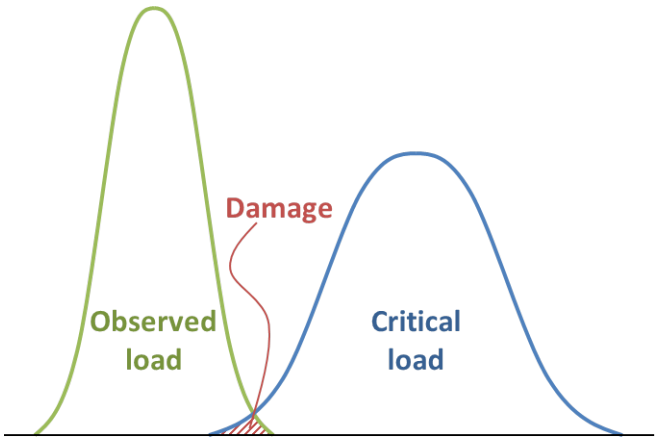

Figure 5.8: Ratio between load terms of the entrainment mechanism on top of the sill visualised in a probabilistic image

Downstream area
The flow in the area behind the sill is best described as a highly turbulent, decelerating flow. Earlier studies have shown that in general most damages to the granular bed protection occur near the reattachment point. This is the region where a lot of turbulence is reaching the bed, but also were the flow velocities are nearly zero. The damages are therefore expected to be caused mainly by the turbulent fluctuation. Translated to the parameters used in stability relation 4.3 and 5.1, τ_x' and especially $\frac{\partial p}{\partial x}'$ are expected to give the highest contribution to the total load on the bed. The image sketched by figure 5.6 is in agreement with these expectations.

A big difference compared to the flow region on top on the sill, is that the turbulent fluctuations are attacking the granular bed protection from above. Stones in this region are relatively stable until a small-scale eddy causes a high pressure gradient over the stone. Thereby the critical loads exerted on the bed are much more local. The high pressure gradient is included in the stability formula by $\frac{\partial p}{\partial x}'$. Consecutively the stone is moved in the near-bottom flow direction by the temporarily velocity caused by a large-scale eddy. This effect is included in the stability formula by τ_x'. Near the reattachment point, most damage is therefore caused by peak values of τ_x' and $\frac{\partial p}{\partial x}'$.

In probabilistic terms, in the downstream area the mean values are relatively small, while the standard deviations of the load terms are large. The frequency by which a critical load for stone movement is reached, seems to be higher than for the flow region on top of the sill. This is indicated in the example of figure 5.9.

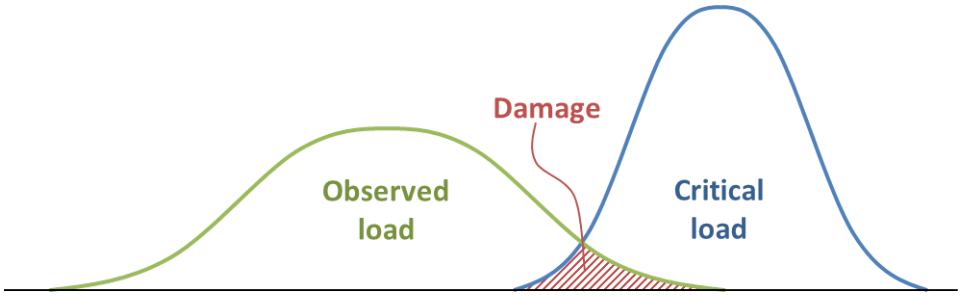

Figure 5.9: Ratio between load terms of the entrainment mechanism of the downstream area visualised in a probabilistic image

The difference between figure 5.8 and figure 5.9 visualise how the different ratio between the load terms of stability relation 5.1, can be the cause that the dimensionless entrainment rates on top of the sill, cannot be predicted by the same stability formula as those in the downstream area. In the next section, the influence of the different load terms on the prediction of the stone stability will be demonstrated by imitating stability formulas presented in earlier studies.

5.2. Effect of the load-terms on the prediction of stone stability

With the use of $\mu+3\sigma$, the mean and fluctuating load-terms can be included in a stability formula separately. This makes it possible to mimic other stability formulas presented in earlier studies. In this section, some stability formulas are elaborated in short to build up towards the formula presented in Steenstra (2014). In this way the effect of the different load-terms on the prediction of stone stability is studied. A more in-depth analysis is done on a Steenstra-type formula and the effect of including the pressure gradient fluctuations. In the last subsection, conclusions are drawn about the way to proceed for the final sections of this thesis.

5.2.1. Shields

The stability formula proposed in Shields (1936) is described earlier in 2.1.3. Because of its simplicity, this formula is still used a lot in practise. The Shields-formula proposed is given by equation 5.2. In this method only the mean wall shear stress is used to evaluate the stone stability.

$$\Psi_{Sh} = \frac{\bar{\tau}_x}{(\rho_s - \rho_w)\, g d} \tag{5.2}$$

Some important characteristics of the original Shield-formula are listed below.

- The Shields-formula is based on a momentum balance approach for an area considerably larger than one stone diameter
- Strictly speaking the original Shields-formula is only valid for uniform flow
- A Ψ_{Sh}-value of 0.03 or lower is considered to be safe for the design of a granular bed protection (Schiereck and Verhagen, 2012)

In figure 5.10 Ψ_{Sh} is plotted against Φ_E for both of the simulated long sill experiments.

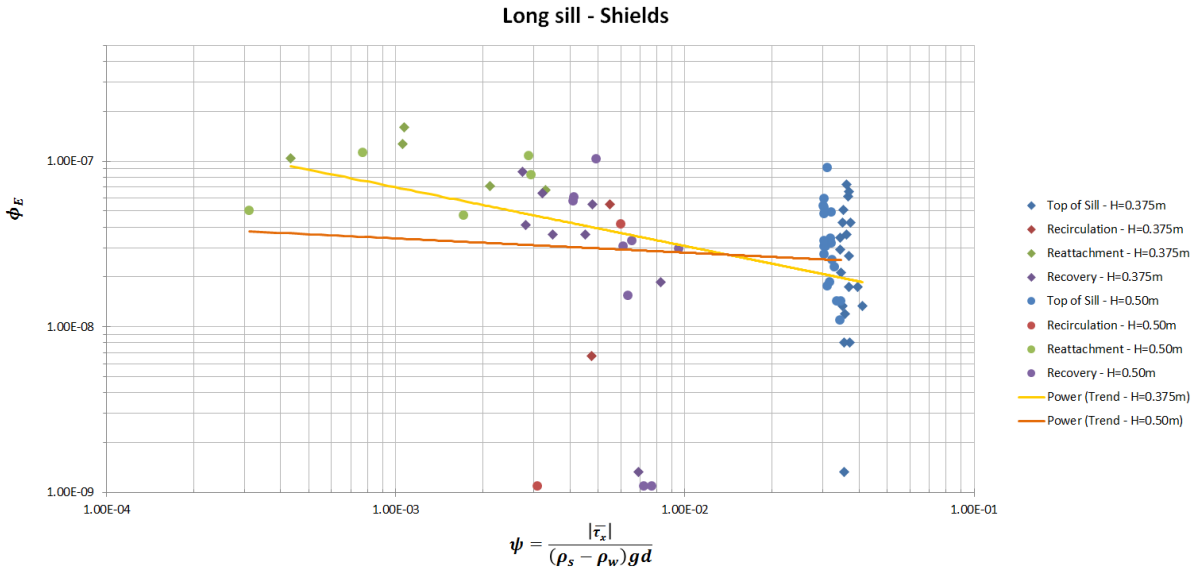

Figure 5.10: Ψ_{Sh} against Φ_E for both long sill experiments

As expected, in figure 5.10 a clear distinction can be observed between the markers for the region on top of the sill and the markers for the downstream area. Almost all data points for the region on top of the sill are in between $\Psi_{Sh} = 0.03 - 0.04$. Apparently on top of the sill the load was just above the criterion of $\Psi_{Sh} \leq 0.03$, and therefore damages could be expected here. The amount of damage (entrainment rate) clearly cannot be predicted by the Shields-formula, as the blue markers almost form a vertical line.

Furthermore, the figure shows that the Shields-formula should not be applied to non-uniform flow cases. For the downstream area, low Ψ_{Sh}-values are predicted, while significant damages occurred in this region. In the downstream region the damages are caused by the turbulent fluctuations instead of the flow velocity. This physical phenomenon is not included in the Shields-formula.

5.2.2. Jongeling-type stability formula

As elaborated in section 2.3, the series of experiments of which the long sill ones are used in this thesis, are executed to derive a new stone stability formula. This stability formula includes a load caused by large-scale turbulence and can be applied with the results of a RANS-model. The proposed stability formula of Jongeling et al. (2003) is given in equation 5.3.

$$\Psi_{Jong} = \frac{\left(u + 6\sqrt{k}\right)^2_{ad}}{\Delta g d} \tag{5.3}$$

In this equation, the subscript ad stands for the averaging depth, for which a value of $5D_{n50} + 0.2h$ is advised. In case one wants to express the turbulent fluctuations as a certain coefficient a times the standard deviation of the velocity σ_u, according to Jongeling et al. (2003) the term $6\sqrt{k}$ corresponds to $4.7\sigma_u$. In reality the value of a deviates for different flow configurations and heights above the bed.

To show the effect of including large-scale turbulent fluctuations in the assessment for stone stability, a Jongeling-type stability formula is demonstrated based on the $\mu + 3\sigma$-approach. The Jongeling-type stability parameter, indicated as $\Psi_{J'}$, is given by equation 5.4.

$$\Psi_{J'} = \frac{\left(|\bar{\tau_x}| + 3\tau'_x\right)}{\left(\rho_s - \rho_w\right) g d} \tag{5.4}$$

Note that the only difference with the Shields-formula is that now an extreme value of the wall shear stress is used, instead of only the mean. The resulting $\Psi_{J'}$-values for the long sill experiments are shown in figure 5.11.

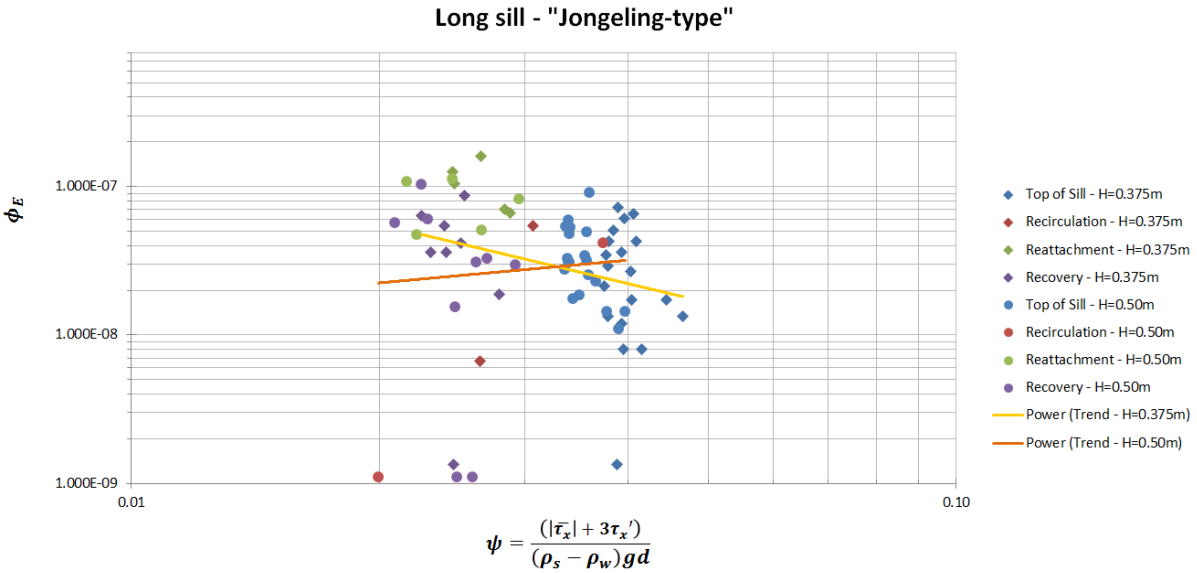

Figure 5.11: $\Psi_{J'}$ plotted against Φ_E for both long sill experiments

With respect to the Shields-formula, the plot shows a clear improvement for the downstream area. Nevertheless the markers for the downstream area are still all at the left of the markers on top of the sill, while for some downstream cross-sections higher damages were observed. The overall performance for the full domain is therefore still not satisfying.

5.2.3. Steenstra-type stability formula

In Steenstra (2014) an inertia term is added to the stability formula proposed in Hofland (2005). More about the thesis of Steenstra is described in section 2.1.3. For convenience the Steenstra-formula is repeated below.

$$\Psi_{RS} = \frac{\left(\max\left[\left\langle \bar{u} + \alpha\sqrt{k}\right\rangle_{L_m} \frac{L_m}{z}\right]^2\right) + C_{m:b}\left(\bar{u}\frac{\partial \bar{u}}{\partial x}\right)_{h_a} d}{K(\beta)\Delta g d} \tag{5.5}$$

Translated to the parameters used in this thesis, the effect of adding the acceleration term can be demonstrated by the Steenstra-type stability formula given in equation 5.6.

$$\Psi_{RS'} = \frac{\left(|\bar{\tau_x}| + 3\tau'_x\right) + C_{m:b}|\frac{\partial \bar{p}}{\partial x}|d}{\left(\rho_s - \rho_w\right) g d} \tag{5.6}$$

Compared to the Jongeling-type formula tested in the previous subsection, only the inertia term $C_{m:b}|\frac{\partial \bar{p}}{\partial x}|d$ is added. In figure 5.12 the result for this Steenstra-type stability formula is shown. Similar to Steenstra (2014), a $C_{m:b}$-value of 23 is used to determine the Steenstra-type stability parameter $\Psi_{RS'}$.

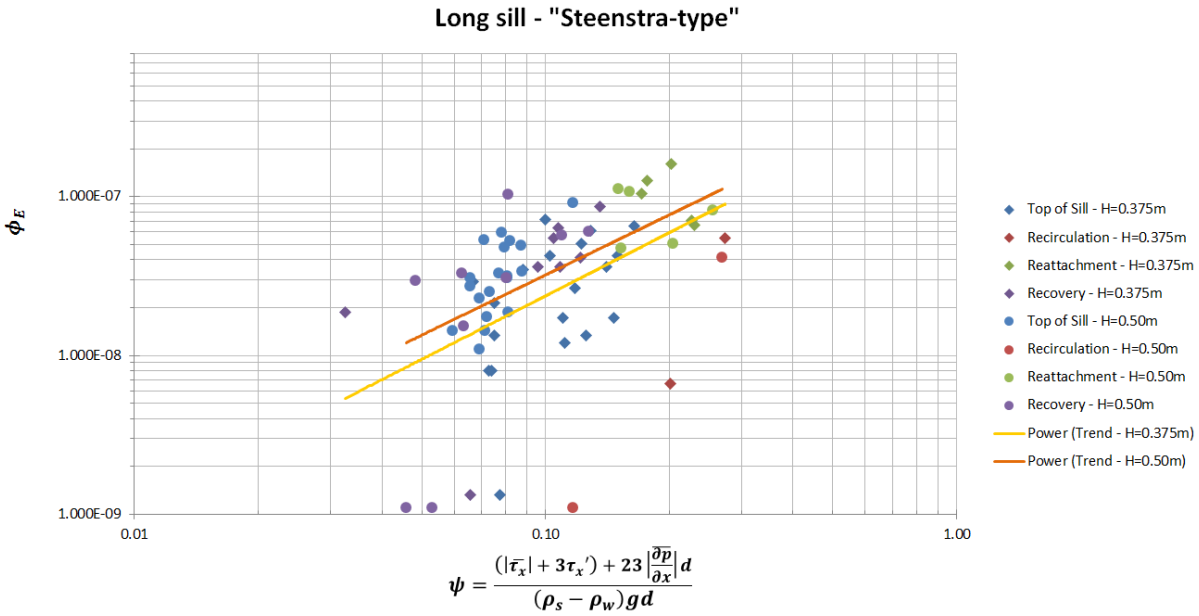

Figure 5.12: $\Psi_{RS'}$ plotted against Φ_E for both long sill experiments

In contradiction to what in section 4.4 is concluded for the Steenstra-formula, the Steenstra-type stability formula 5.6 performs quite well for the long sill experiments. Figure 5.12 shows a clear trend in predicting higher entrainment rates for higher values of $\Psi_{RS'}$. The trendlines are comparable for both simulated experiments. Although still a lot of scatter is present, this definitely is the best relation between a stability parameter Ψ and the entrainment rate Φ_E found so far.

Despite the relatively good result, it is doubted if stability formula 5.6 represents the governing physics involved in stone stability. As demonstrated earlier with figure 5.6 and 5.7, the $C_{m:b}$-value of 23 causes the pressure gradient to be dominant over the entire modelled domain. Similar to these figures, in figure 5.13 the loads of equation 5.6 are plotted over the damage field. Compared to figure 5.7, the difference is that now the pressure gradient fluctuations are not taken into account.

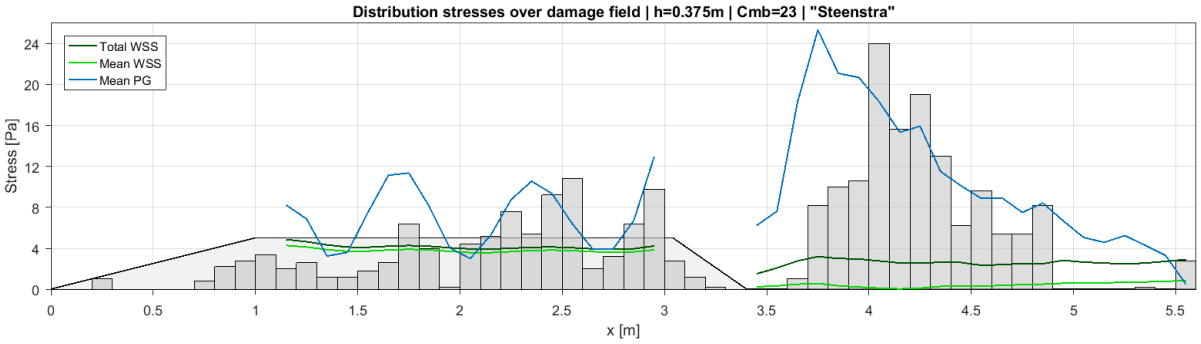

Figure 5.13: The load-terms of the Steenstra-type stability formula 5.6 plotted over the measured damage field. Experiment long sill with $h = 0.375m$ and $C_{m:b} = 23$

Most striking about figure 5.13 probably are the large waves in the line of the mean pressure gradient on top of the sill. These are expected to be a result of the waves observed in the movie of the simulated flow, described in section 3.5.

For now it is important to see that for the Steenstra-type formula, the term $\left(23\frac{\partial \bar{p}}{\partial x}d\right)$ will be the dominant load over the entire modelled domain. Nevertheless, according to the hypothesis described in section 5.1.5, the wall shear stress should be the governing load on top of the sill. Taking the mean pressure gradient into account only should improve the prediction between a low or high entrainment rate in this region.

Furthermore figure 5.13 shows that for the largest part of the downstream area, the mean pressure gradient is the dominant load term. Again this is is not in agreement with the expected governing physics for the downstream area described in section 5.1.5. For the downstream area the fluctuation terms are expected to be governing. Also the distribution of $\frac{\partial p'}{\partial x}$ (shown in figure 5.6 and 5.7) is in better agreement with the damage pattern than the distribution of $\frac{\partial \bar{p}}{\partial x}$.

To strengthen the presumption that stability relation 5.6 not necessarily represents the governing physics in a certain region, a stability formula including only the mean pressure gradient $\frac{\partial \bar{p}}{\partial x}$ is tested. This formula is given by equation 5.7.

$$\Psi_{mpg} = \frac{C_{m:b}|\frac{\partial \bar{p}}{\partial x}|d}{(\rho_s - \rho_w)gd} \tag{5.7}$$

In figure 5.14 the result of stability relation 5.7 is shown. A $C_{m:b}$-value of 23 is used.

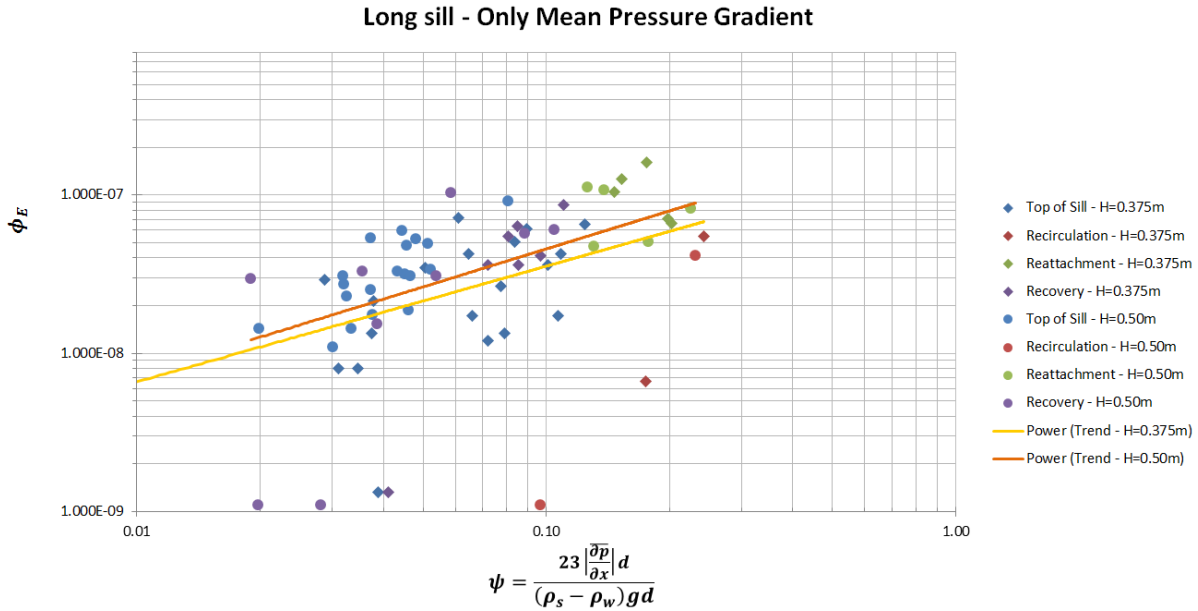

Figure 5.14: Ψ_{mpg} plotted against Φ_E for both long sill experiments

Figure 5.14 shows quite similar results as figure 5.12 shows for the Steenstra-type formula 5.6. Nevertheless, in literature no indication can be found that the mean pressure gradient is this governing for the stability of a stone in a granular bed protection. This weakens the trustworthiness of the Steenstra-type formula. Still it is found interesting that the damages and the mean pressure gradient seem to be directly related. Therefore this is though to be an interesting topic for further research.

5.2.4. Stability relation 5.1

Keeping the tested stability formulas in mind, the next step taken in this thesis is adding the load by the pressure gradient fluctuations. Adding $\frac{\partial p}{\partial x}'$ to the Steenstra-type stability relation 5.6, results in equation 5.1. The performance of this stability relation is already evaluated in section 5.1.3. It appeared that including the pressure gradient fluctuations does not improve the prediction of stone stability for the whole domain. The Steenstra-type stability formula 5.6 gives the best relation between Ψ and Φ_E for the whole domain of the long sill experiments.

Nevertheless, the physical correctness of the governing loads described by the Steenstra-type formula is doubted. The dominance of the mean pressure gradient is not in agreement with what one would expect based on literature, the entrainment mechanisms described in section 5.1.5 and figure 5.6. Therefore it is decided to derive a stability formula that is valid for the physics in the downstream area only. In this stability formula, the loads caused by the fluctuations should be governing, according to the entrainment mechanism described in section 5.1.5. The focus will be on the downstream area, as this is the region in which the flow phenomena are expected to be similar to those in the Eastern Scheldt simulation. The similarities between these cases are elaborated earlier in section 2.4.

5.3. Stability relation for highly turbulent flow behind a sill

As a result of the previous work, in the first subsection stability relation 5.1 will be calibrated to the simulated results of the long sill experiments. Based on the hypothesised entrainment mechanism in section 5.1.5, this stability formula is expected to be valid for a highly turbulent flow behind a sill or backward-facing step. Therefore the resulting stability relation is expected to be applicable to the Eastern Scheldt case described in section 2.4. The stability formula that will be applied to the Eastern Scheldt case is presented in the second subsection.

5.3.1. Stability relation for the downstream area

In this subsection a stability relation is derived for the downstream region of the long sill experiments only. For the derivation, stability formula 5.8 is taken as a starting point. With respect to equation 5.1, two differences can be observed.

1. The combined added mass and drag and lift coefficient $C_{m:b}$ is split up in C_m and C_b again. This to allow a zero value for one of the two coefficients, meaning that also the option of taking into account only τ_x or $\frac{\partial p}{\partial x}$ is analysed.
2. The coefficients before the fluctuation terms are replaced by a and b. Thereby the option of taking into account the mean value or an extreme value of τ_x or $\frac{\partial p}{\partial x}$ is analysed.

$$\Psi_{new} = \frac{C_b\left(|\bar{\tau_x}| + a\tau'_x\right) + C_m\left(|\frac{\bar{\partial p}}{\partial x}| + b\frac{\partial p'}{\partial x}\right)d}{\left(\rho_s - \rho_w\right)gd} \tag{5.8}$$

Formula 5.8 is calibrated by taking the following calibration-ranges into account:

- C_m and C_b are varied between values from 0 to 50. Not every combination is analysed. Decision are made based on observed improvements for higher or lower values of one of the two calibration parameters.
- a and b are chosen to be 0 or 3. A value of 0 means that only the mean value of that specific parameter will be taken into account. A value of 3 represents that an extreme value of that parameter is taken into account.

The calibration is done for both long sill experiments for which separate trendlines are used. During the calibration, attention is paid to the following aspects:

- Positive relation between Ψ and Φ_E, meaning that higher Ψ-value should correspond to a higher entrainment rate Φ_E
- The correlation numbers R^2 for both trendlines should be as high as possible

The result of this calibration exercise is shown in figure 5.15.

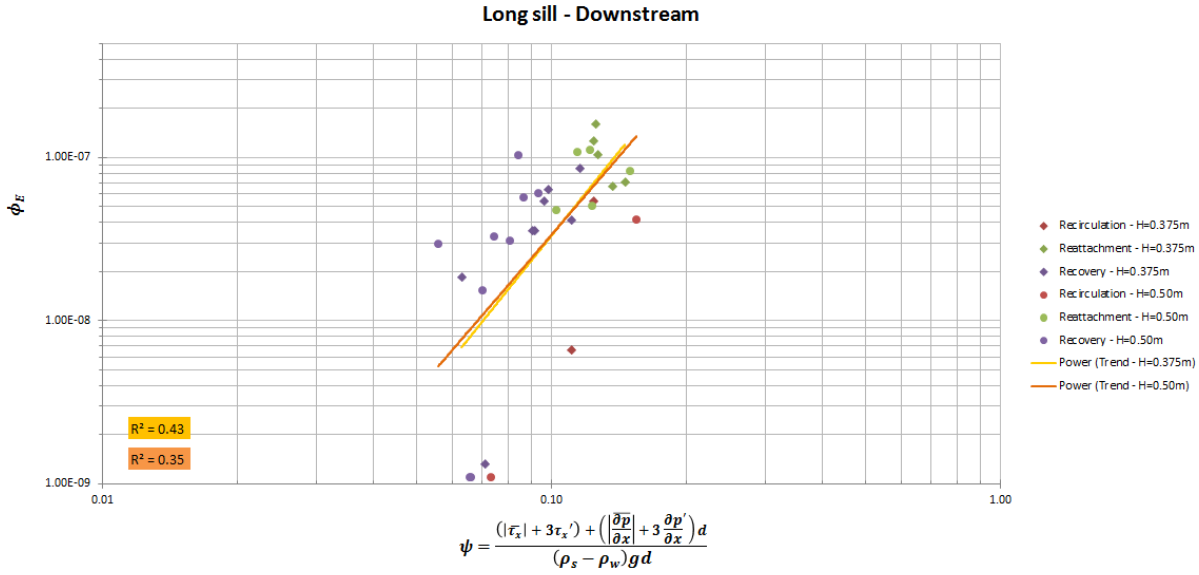

Figure 5.15: Calibrated formula included $\frac{\partial p'}{\partial x}$ for long sill experiments, downstream area

It appears that the best results for the downstream area are obtained when the both the fluctuation terms of τ_x and $\frac{\partial p}{\partial x}$ are taken into account. The highest correlation is found for $C_b = 1$. The added mass coefficient C_m can be varied over a range from about 1 to 50 without changing the correlation number too much, because the extreme pressure gradient is already dominant for a C_m-value of 1. This was also observed in figure 5.6 and is in agreement with the entrainment mechanism described in 5.1.5. For convenience a value of 1 is chosen for C_m. The resulting stone stability formula for the downstream region of the long sill experiments is given by equation 5.9. The subscript of the stability parameter Ψ_{htf} stands for the Highly Turbulent Flow region for which it is calibrated.

$$\Psi_{htf} = \frac{\left(|\bar{\tau_x}| + 3\tau_x'\right) + \left(|\frac{\partial \bar{p}}{\partial x}| + 3\frac{\partial p'}{\partial x}\right)d}{\left(\rho_s - \rho_w\right)gd} \tag{5.9}$$

As one might notice, this equation is equal to stability formula 5.1 with a $C_{m:b}$-value of 1. The power relation between Ψ_{htf} and Φ_E corresponding to the trendlines of figure 5.15 is given by equation 5.10.

$$\Phi_E = 6.34 * 10^{-5}\Psi_{htf}^{3.27} \tag{5.10}$$

The damages corresponding to the dimensionless entrainment rates Φ_E of figure 5.15, are given in table 2.1. However, the plot is assumed to be also valid for the assessment of stone stability in cases with larger dimensions, as explained in section 2.1.5. An example is shown in appendix A.

5.3.2. Stability relation Eastern Scheldt case

To assess the stability of the granular bed protection at the Eastern Scheldt barrier, several time signals of τ_x and $\frac{\partial p}{\partial x}$ are extracted from the Eastern Scheldt model. Thereby the 0.3%-value can be produced again, instead of the $(\mu + 3\sigma)$-values used throughout this chapter. The stability relation that will be used for the Eastern Scheldt case thereby will be similar to stability formula 4.3 with a $C_{m:b}$-value of 1. For convenience the final stability formula is given in equation 5.11

$$\Psi_{htf} = \frac{\left(|\tau_x| + |\frac{\partial p}{\partial x}|d\right)_{0.3\%}}{\left(\rho_s - \rho_w\right)gd} \tag{5.11}$$

The relation between Φ_E and Ψ_{htf} is assumed similar to equation 5.10, as at the beginning of this chapter it is proven that applying $\mu+3\sigma$ will give similar results as obtained for the 0.3%-values of the combined signals of τ_x and $\frac{\partial p}{\partial x}$.

5.4. Conclusions chapter 5

In this chapter, the extreme values of τ_x and $\frac{\partial p}{\partial x}$ are obtained by using the $\mu+3\sigma$-rule that belongs to a Gaussian distribution. It is proven that this approach gives similar results as obtained in the previous chapter for the 0.3%-exeedence probability of $\left(|\tau_x| + C_{m:b}|\frac{\partial p}{\partial x}|d\right)$. Because of this methodology, much more data points could be created of which the mean values and fluctuating parts of τ_x and $\frac{\partial p}{\partial x}$ are known from the simulations. Besides that, the effect of the different load-terms on the prediction of stone stability can now be studied separately.

A hypothesis is posed that the stone movements on top of the sill are caused by another entrainment mechanism than the damages in the downstream area. The analysis about the influence of different load-terms on the prediction of stone stability seem to be in agreement with this hypothesis. In all plots a deviant behaviour can be observed between the results of the two distinct flow regions.

The best results for the whole domain of the long sill experiments are obtained for a Steenstra-type stability formula, given by equation 5.6. Adding the load by the pressure gradient fluctuations does not improve the predictions for the whole domain, as already concluded in the previous chapter. Nevertheless for the Steenstra-type stability formula, the mean pressure gradient is the dominant load-term over the whole domain. This cannot be substantiated with the results of earlier studies. Furthermore it is not in agreement with the observed damage pattern and the hypothesis about the entrainment mechanisms that cause stone movements in the different flow regions.

Based on these observations, the choice is made to derive a stability relation for the downstream area of the long sill simulations only. Equation 5.9 appears to give the best predictions of the entrainment rates in this region. The fluctuating terms of the derived stability formula are governing, which is in agreement with the hypothesised entrainment mechanism for the downstream area. This entrainment mechanism is also expected to be governing for the stability of the granular bed protection behind the Eastern Scheldt barrier.

For the Eastern Scheldt case at several points time signals of τ_x and $\frac{\partial p}{\partial x}$ are available. Instead of applying the $\mu+3\sigma$-rule, the 0.3%-values can be used again to produce the extreme values. The stability formula that will be applied on the data from the Eastern Scheldt simulations is equation 5.12.

$$\Psi_{htf} = \frac{\left(|\tau_x| + |\frac{\partial p}{\partial x}|d\right)_{0.3\%}}{\left(\rho_s - \rho_w\right) g d} \tag{5.12}$$

The corresponding power relation between the entrainment rate and the stability parameter is given by equation 5.13.

$$\Phi_E = 6.34 * 10^{-5} \Psi_{htf}^{3.27} \tag{5.13}$$

6

The Eastern Scheldt case

In this chapter the stability of the granular bed protection at the Eastern Scheldt barrier will be assessed, to determine the influence of the tidal energy turbines on this part of the sea defence. The assessment will be based on the output of two Improved Delayed Detached Eddy Simulations (IDDESs), made of the flow through the eighth gate at the Roompot channel (Roompot 8). The stone stability will be assessed, based on a comparison between the loads on the bed in both simulations. The load term of stability relation 5.12 will be used for this.

One should be aware that the comparisons in this section are based on simulated results only, as no velocity measurements are available at the analysed locations. It is assumed that the simulations are validated well enough to apply the chosen methodology. Still, the assessment in this chapter only serves as a test case, to determine if the applied methodology has enough potential to be investigated further.

In the first section of this chapter, the applied methodology of the stone stability assessment is elaborated. Next the stability of the granular bed protection is determined for the Roompot 8 simulation without tidal energy turbines. A similar approach is used for the Roompot 8 simulation with turbines, and the results of the two models are compared. In the end some conclusions will be drawn about the applied methodology and the main uncertainties it includes.

6.1. Methodology

In this section the approach to analyse the stability of the granular bed protection will be explained. After that, the energy density spectra of the simulations with and without energy turbines will be evaluated, to determine to what extend the important turbulent scales are resolved in these models. This can serve as an indication for the quality of a DES. Moreover, resolved turbulent scales can be linked to the local stone diameter, as done earlier in section 3.4.1. From this evaluation, it can be concluded how the use of a three-dimensional eddy resolving technique is scaled to the large dimensions of the Roompot 8 simulations.

6.1.1. Approach Eastern Scheldt case

In this chapter, two of the simulations made of the flow at Roompot 8 are compared to analyse the influence of the tidal energy turbines on the stability of the granular bed protection. In both models the flow during flood is simulated, by which the attack on the granular bed protection is most severe at the east side (landward side) of the Eastern Scheldt barrier. In one of the simulations the tidal energy turbines are included, and in the other simulation they are absent. The difference between the results of these simulations therefore can be ascribed to the presence of the tidal energy turbines. More information about the Roompot 8 models is given in section 2.4.

In both Roompot 8 models, eight points are made perpendicular to the centre of the gate. Four of those points are at the bottom of the model at approximately 50 m, 100 m, 150 m and 200 m distance from the barrier. The other four points are placed at the same distances from the barrier, 10 m below the water surface. The bottom points are visualised in figure 6.1 and 6.2.

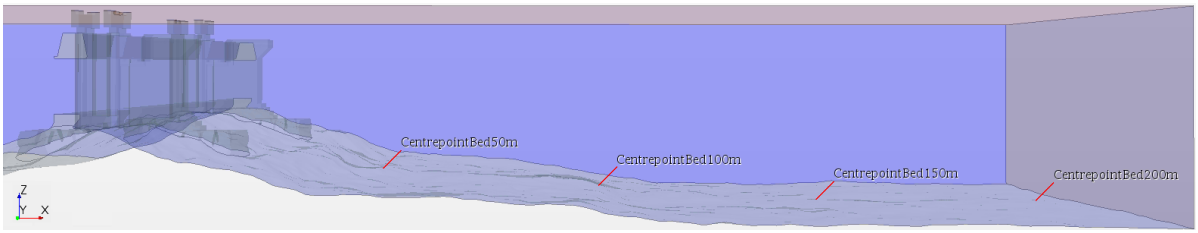

Figure 6.1: Bottom points taken in the Eastern Scheldt model (side view)

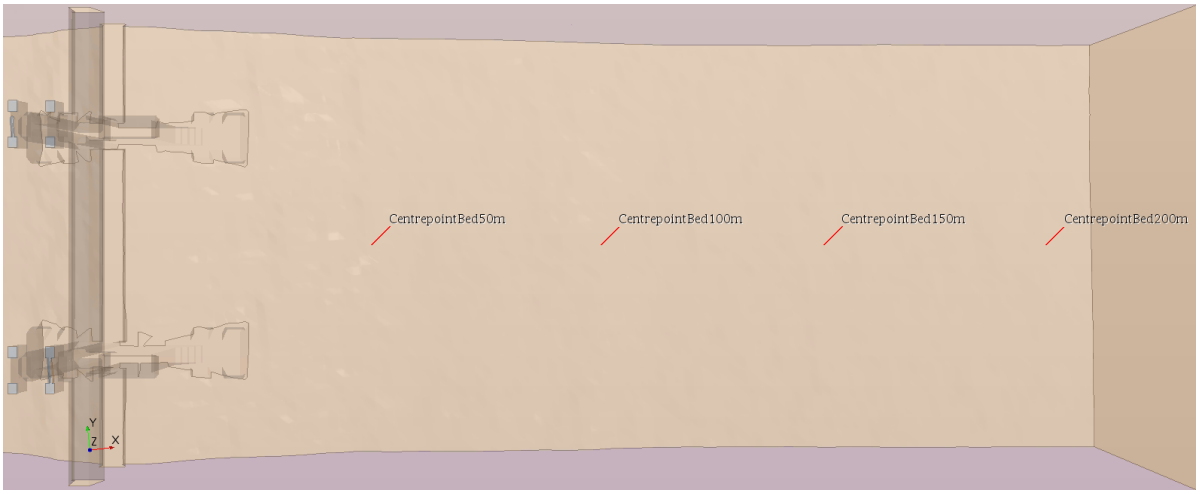

Figure 6.2: Bottom points taken in the Eastern Scheldt model (top view)

At these bottom points, time signals of τ_x and $\frac{\partial p}{\partial x}$ are recorded. They will be used for the assessment of the stability of the granular bed protection around those locations. Nevertheless, as explained in section 2.4, the way in which the bottom roughness is included in the Roompot 8 models differs from the method applied for the long sill simulations. It should be emphasised that the influence on the results, of these different methods to include the bottom roughness, is not known.

At the points that are located 10 m below the water surface, time signals of the flow velocity u_x are recorded. Similar to section 3.4.1, spectra are made of these velocity signals to analyse to what extend the important turbulent scales are resolved in the Roompot 8 simulations. The spectra at a distance of 100 m from the barrier, are used for the analysis in the next subsection.

6.1.2. Resolved turbulent scales Roompot 8 simulations

As concluded earlier, the quality of an IDDES is highly dependent on the applied grid size, i.e. the amount of turbulent scales that are resolved. In this subsection, two spectra of the velocity signal at a distance 100 m from the Eastern Scheldt barrier (ESB) are shown. It is analysed if the inertial sub-range is reached, and how the resolved fluctuations relate to the stone diameter at that location. The spectra are made from the velocity signal u_x of the simulations with, and without turbines.

Due to time constraints in this research, the velocity signals used for this analysis are not of equal length. Furthermore, the grid size and the numerical time step in the simulation with turbines, are smaller than those of the simulation without turbines. These differences can have a significant influence on the resulting bed loads in the next section. In table 6.1 first some extra information is given about both Roompot 8 simulations and desired resolution at a distance 100 m from the ESB. The assumptions made to obtain this information, are similar to those of section 3.4.1. For convenience they are repeated below.

- At least two grid cells are needed to resolve one eddy
- The Taylor hypothesis can be used to estimate the time scale of a turbulent fluctuation
- The desired resolution is equal to the frequency f_{stone} at which all turbulent scales, larger than or equal to the nominal stone diameter d_{n50}, are resolved

	Without turbines	**With turbines**
Grid size [m]	0.60	0.32
Numerical time step t_n [s]	1.79	0.52
Averaged velocity u_x [m/s]	1.63	1.25
Time scale grid T_{grid} [s]	0.74	0.51
Expected grid resolution $f_{g,exp}$ [Hz]	0.28	0.96
Stone diameter d_{n50} [m]	1.19	1.19
Desired resolution f_{stone} [Hz]	1.37	1.05

Table 6.1: Table with extra information about the Roompot 8 simulations with and without turbines

Table 6.1 shows that for both Roompot 8 simulations, the numerical time step t_n is larger than the time scale of a water particle flow through a grid cell T_{grid}. Therefore, in both cases t_n is governing for the expected grid resolution. It can already be concluded, that in both simulation the desired resolution of f_{stone} will not be reached, as in both cases $f_{g,exp} < f_{stone}$.

In figure 6.3, the variance density spectra of the time signals are plotted on a double-logarithmic scale. From this plot the effective grid resolution $f_{g,eff}$ will be deduced.

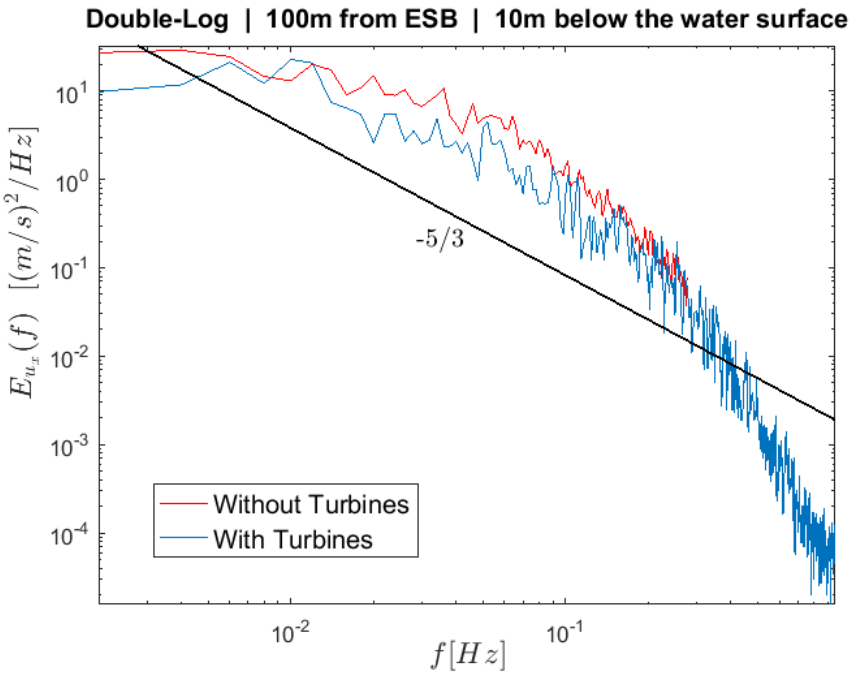

Figure 6.3: Variance density spectrum on double-logarithmic scale, 100 m from the Eastern Scheldt Barrier

As can be expected from the information in table 6.1, more turbulent scales are resolved in the simulation with turbines, than in the simulation without turbines. The spectra of figure 6.3 stop exactly at the expected grid resolutions $f_{g,exp}$, as calculated in table 6.1. Nevertheless, the effective grid resolution $f_{g,eff}$ is expected to be lower.

Due to the complex flow patterns behind the Eastern Scheldt barrier, it is hard to predict how the variance density spectrum of the streamwise velocity should look like. It is assumed that a clear inertial sub-range with a $-\frac{5}{3}$ slope should be present, because of the high Reynold number that will be in the order of $2.5 * 10^7$. The effective grid resolution $f_{g,eff}$ is assumed to be at the point were a spectrum starts to deviate from the $-\frac{5}{3}$ slope.

In this way, the effective resolution of the simulation without turbines $f_{g,eff,without}$ is determined to be about 0.09 Hz. The effective resolution of the simulation with turbines $f_{g,eff,with}$ is estimated to be about twice as high, $f_{g,eff,with} \approx 0.17$ Hz. As expected, the effective grid resolution $f_{g,eff}$ of both simulations is lower than the desired grid resolution f_{stone}.

Next, in figure 6.4, the pre-multiplied energy density spectra of the streamwise velocities are given. This plot gives an overview about amount of kinetic energy certain turbulent scales contain. Furthermore, the area underneath the spectra, is representative for the total amount of resolved turbulent kinetic energy (TKE) at that location.

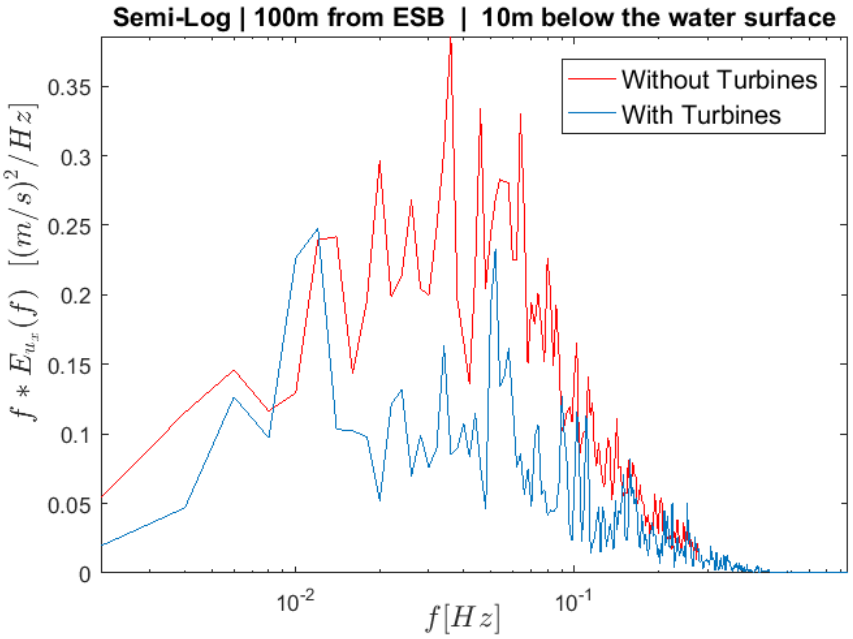

Figure 6.4: Pre-multiplied energy density spectrum on semi-logarithmic scale, 100 m from the Eastern Scheldt Barrier

Clearly, the area underneath the spectrum of the simulation with turbines, is smaller than the area underneath the red line of the simulation without turbines. Therefore, it can be concluded from figure 6.4, that at the chosen location, less TKE is present in the simulation with turbines, compared to the simulation without turbines.

The difference in the amount of resolved TKE in both simulations, might partly be ascribed to the shorter velocity signal that is used for the simulation with turbines. A second explanation might be, that the tidal energy turbines cause the TKE to be distributed differently throughout the modelled domain. The TKE at the analysed point is less when the tidal energy turbines are included in the model, but at another point the total amount of TKE might be increased. A third theory about the tidal energy turbines "cutting" the large eddies, from the separation over the sill, into smaller scales, is not supported by this graph. The TKE in the lower frequencies indeed is smaller, but the energy in the higher frequencies is not increased. However, it is possible that the effective resolution is not high enough to observe is phenomenon in the spectrum of figure 6.4.

From the analysis in this section, it can be concluded that the different lengths of the velocity signals, and the different grid sizes and time steps used for the two Roompot 8 simulations, impede a honest comparison of the simulation with and without turbines. Similar to the simulated long sill experiment with $h = 0.375$ m, the desired effective grid resolution is not reached. At the analysed location, the amount of resolved TKE is smaller for the simulation with turbines, than for the simulation without turbines. The most plausible causes for this are mentioned above.

6.2. Roompot 8 without turbines

In this section the distribution of the wall shear stress τ_x and the pressure gradient $\frac{\partial p}{\partial x}$ will be analysed briefly, followed by an evaluation of the total load term of stability formula 5.12. Consequently, the Ψ_{htf}-values for the Roompot 8 simulation without turbines are calculated. Finally, this is made more specific by an example in which the predicted entrainment rate is compared against an assumed critical entrainment rate. In this way it is assessed if the situation without tidal energy turbines meets the safety requirements with regard to the granular bed protection.

6.2.1. τ_x and $\frac{\partial p}{\partial x}$ for Roompot 8 - Without Turbines

The four bottom points, indicated in figure 6.1 and 6.2, are used to analyse the behaviour of the wall shear stress τ_x and the pressure gradient $\frac{\partial p}{\partial x}$ for the Roompot 8 simulations. In this subsection, first the simulation without the tidal energy turbines is evaluated. Similar to the plots shown in appendix H and J, PDFs and CDFs are made of τ_x and $\frac{\partial p}{\partial x}$ at a distance of 50 m, 100 m, 150 m and 200 m from the Eastern Scheldt barrier (ESB). In table 6.2 and 6.3 the resulting numbers are given.

Distance from ESB [m]	$\bar{\tau_x}$ [Pa]	τ_x' [Pa]	$\tau_{x,0.3\%}$ [Pa]
50	-3.77	4.40	-25.63
100	-0.93	2.42	-11.78
150	0.77	1.91	11.93
200	1.00	1.14	7.11

Table 6.2: Bottom values of τ_x from simulation: Roompot 8 - Without Turbines

Distance from ESB [m]	$\frac{\bar{\partial p}}{\partial x}$ [Pa/m]	$\frac{\partial p}{\partial x}'$ [Pa/m]	$\frac{\partial p}{\partial x}_{0.3\%}$ [Pa/m]
50	58	250	1145
100	40	158	608
150	-25	103	-625
200	-2	32	-145

Table 6.3: Bottom values of $\frac{\partial p}{\partial x}$ from simulation: Roompot 8 - Without Turbines

From table 6.2 it can be seen that τ_x switches sign between a distance of 100 m and 150 m from the barrier. The reattachment point therefore should be located somewhere in that area. The highest values for τ_x and $\frac{\partial p}{\partial x}$ are found at 50 m from the Eastern Scheldt barrier instead of near or just behind the reattachment point. A possible explanation for this, is that the water depth h at 50 m from the barrier is smaller than the water depth above the other bottom points.

In contradiction to the long sill simulations, table 6.3 shows that $\frac{\partial p}{\partial x}$ is switching sign after the reattachment point. Apparently the main flow is accelerating again in this area, although it most be noted that the values for $\frac{\partial p}{\partial x}$ are relatively low compared to those of the long sill experiments.

This does not mean that the significance of $\frac{\partial p}{\partial x}$ is low for the Roompot 8 simulations, because large stones with diameters between 0.5 m and 2.0 m are present in these models. In fact, keeping in mind the load as defined in stability relation 5.12, it can already be concluded that the pressure gradient $\frac{\partial p}{\partial x}$ will be the dominant load-term over the entire modelled domain. More specifically, the pressure gradient fluctuations $\frac{\partial p'}{\partial x}$ will be governing. This can be interpreted as an indication that stability relation 5.12 should be applicable to the results of this simulation.

6.2.2. Ψ_{htf} for Roompot 8 - Without Turbines

In the last column of table 6.4, the values for stability parameter Ψ_{htf} of the simulation without turbines are given. The other columns contain the information needed to obtain these Ψ_{htf}-values, which now will be elaborated briefly. The effect of the slope of the sill at the Eastern Scheldt barrier is assumed to be negligible, and therefore left out of this analysis.

In the second column, the stone classes, present at the chosen bottom points, are listed. They are retrieved from a AutoCAD drawing, in which all stone deposits near the Eastern Scheldt barrier are indicated (Rijkswaterstaat, 2017). For the bottom points at a distance of 150 m and 200 m from the barrier, two stone classes are taken into account, as they are located at a transition between two former stone deposit regions.

The spherical stone sizes of the third column are determine by:

$$d_{n50} = \sqrt[3]{\frac{M_{50}}{\rho_s}} \tag{6.1}$$

In which:

- M_{50} is the median stone weight of a certain stone class
- ρ_s is the density of a stone. A value of 2650 kg/m^3 is assumed for this

In the fourth column the 0.3%-values of the load of stability relation 5.12 are given. These values are obtained in a similar way as done in section 4.3.2.

Distance from ESB [m]	Stone class [kg]	Stone size d_{50} [m]	$Load_{0.3\%}$ [Pa]	Ψ_{htf}
50	1000 - 3000	0.91	1354	0.09
100	3000 - 6000	1.19	1129	0.06
150	1000 - 3000	0.91	699	0.05
150	300 - 1000	0.63	487	0.05
200	300 - 1000	0.63	116	0.01
200	60 - 300	0.41	73	0.01

Table 6.4: Load and Ψ_{htf}-values for the simulation Roompot 8 without turbines

Similar to the load, Ψ_{htf} is the largest at the bottom point 50 m from the barrier. This means that at this point, the local resistance against the local loads is the lowest. This makes sense, as the loads at 50 m from the barrier are the largest, while the stone diameter is not. By far the largest part of the total load, can be allocated to the pressure gradient fluctuations $\frac{\partial p'}{\partial x}$.

The results, at a distance of 150 m and 200 m from the barrier, prove that the Ψ_{htf}-values are not depending (a lot) on the stone diameter.

6.2.3. Predicted damage for Roompot 8 - Without Turbines

To give the resulting Ψ_{htf}-values some physical meaning, they are converted into predicted dimensionless entrainment rates $\Psi_{E,p}$ by relation 5.13. In table 6.5, the $\Psi_{E,p}$-values are converted into a number of stone movement per hour over an area of 5.000 m^2. Thereby, the bottom points are assumed to be representative for an area of 50 meters perpendicular to the Eastern Scheldt barrier and 100 m parallel to the barrier. This assumption is just to get some feeling for the magnitude of the predicted damage, the obtained $\Psi_{E,p}$-value represent.

Distance from ESB [m]	Stone class [kg]	Stone size sphere d [m]	Ψ_{htf}	$\Phi_{E,p}$	Predicted damage n [# stones/hour/5.000 m^2]
50	1000 - 3000	0.91	0.09	2.58E-08	2.4
100	3000 - 6000	1.19	0.06	5.88E-09	0.3
150	1000 - 3000	0.91	0.05	2.97E-09	0.3
150	300 - 1000	0.63	0.05	3.10E-09	0.7
200	300 - 1000	0.63	0.01	2.83E-11	0.0
200	60 - 300	0.41	0.01	2.50E-11	0.0

Table 6.5: Results for the test case of the Roompot 8 simulation without turbines

Table 6.5 shows, that most predicted entrainment rates $\Phi_{E,p}$ are below 10^{-8}, which is stated as the upper limit for insignificant damages in section 2.1.5. Only the dimensionless entrainment rate $\Phi_{E,p}$ for the bottom point at 50 m from the barrier is above 10^{-8}. The translation of $\Phi_{E,p}$ into n, shows that at this point, each 2 hours approximately 5 stones will move over an analysed area of 5.000 m^2.

The flow in this simulation is corresponding to a water level difference of 0.50 m over the barrier. This is far below the design conditions of the granular bed protection. The expected damages should therefore be negligible at all analysed points. Following this reasoning, the predicted damages are considered to be too large. This probably is an indication, that the equation 5.12 and 5.13 are not yet calibrated enough to be applied in practice. It is hypothesised that the chosen $C_{m:b}$-value might be too large, by which too much weight is attributed to the pressure gradient (fluctuations).

6.3. Roompot 8 with turbines

In this section the Roompot 8 simulation with turbines is analysed in an exactly similar way as the simulation without turbines. First the distribution of τ_x and $\frac{\partial p}{\partial x}$ will be discussed briefly, followed by the Ψ_{htf}-values. Finally the predicted dimensionless entrainment rates will be computed, and translated into a number of stones movements n per hour per 5.000 m ^{2}.

6.3.1. τ_x and $\frac{\partial p}{\partial x}$ for Roompot 8 - With Turbines

In table 6.6 and 6.7 the values of τ_x and $\frac{\partial p}{\partial x}$ for the simulation with the tidal energy turbines are given.

Distance from ESB [m]	$\bar{\tau_x}$ [Pa]	τ_x' [Pa]	$\tau_{x,0.3\%}$ [Pa]
50	-1.16	2.2	-9.78
100	-0.96	1.39	-5.12
150	0.62	1.55	6.83
200	1.12	1.11	5.97

Table 6.6: Bottom values of τ_x from simulation: Roompot 8 - With Turbines

Distance from ESB [m]	$\frac{\partial \bar{p}}{\partial x}$ [Pa/m]	$\frac{\partial p'}{\partial x}$ [Pa/m]	$\frac{\partial p}{\partial x}_{0.3\%}$ [Pa/m]
50	41	125	800
100	34	78	395
150	1	75	269
200	3	39	174

Table 6.7: Bottom values of $\frac{\partial p}{\partial x}$ from simulation: Roompot 8 - With Turbines

Similar to the simulation without the energy turbines, table 6.6 shows that τ_x switches sign between a distance 100 m and 150 m from the Eastern Scheldt barrier, indicating that somewhere in between the reattachment point is located. Strikingly, the pressure gradient $\frac{\partial p}{\partial x}$ is not switching sign at this point. The mean values only become very small, which is hard to declare physically at those points. Still, also in this simulation $\frac{\partial p}{\partial x}$ will be the dominant load over the entire domain, because of the fluctuating part $\frac{\partial p'}{\partial x}$.

Again the largest loads can be found at 50 m from the barrier. Apart from the mean pressure gradient, the behaviour of τ_x and $\frac{\partial p}{\partial x}$ are quite similar for both Roompot 8 simulations.

6.3.2. Ψ_{htf} for Roompot 8 - With Turbines

In table 6.8, the loads and Ψ_{htf}-values from stability relation 5.12 are given, when applied to the simulation with the tidal energy turbines.

Distance from ESB [m]	Stone class [kg]	Stone size sphere d [m]	$Load_{0.3\%}$ [Pa]	Ψ_{htf}
50	1000 - 3000	0.91	1022	0.07
100	3000 - 6000	1.19	471	0.02
150	1000 - 3000	0.91	407	0.03
150	300 - 1000	0.63	283	0.03
200	300 - 1000	0.63	170	0.02
200	60 - 300	0.41	106	0.02

Table 6.8: Load and Ψ_{htf}-values for the simulation Roompot 8 with turbines

Again the highest load can be found closest to the barrier, probably because here the water depth is the smallest. Furthermore, table 6.8 shows that, also in this simulation, the Ψ_{htf}-values at 150 m and 200 m are not influenced by the stone diameter.

Comparing the Ψ_{htf}-values of table 6.8, to those of table 6.4, slightly lower values are predicted for the simulation with turbines, than for the simulation without turbines. This is in contradiction to the expectation, that the turbines cause extra turbulence, and thereby an extra load on the granular bed protection. The lower values of $\frac{\partial p'}{\partial x}$ in the simulation with turbines, are causing the largest discrepancy between the total loads of both simulations. Nevertheless, the overall difference between the results with and without tidal energy turbines is considered to be small.

A physical explanation for the discrepancy between the simulated results could be, that the tidal energy turbines "cut" the large eddies, caused by the separating flow over the sill of the Eastern Scheldt barrier, into smaller turbulent scales. Therefore, a large part of the total turbulent kinetic energy is already dissipated, before it reaches the bed. The load on the granular bed protection then decreases because of the presence of the turbines.

Furthermore, it might be the case that, the turbulent kinetic energy is distributed differently over the modelled domain, because of the presence of the tidal energy turbines. The bed loads at the analysed bottom points are reduced, but it is possible that at other locations, the bed loads are increased.

Nevertheless, it should be emphasised that the differences between the results of the simulation with and without turbines can as well be caused by the applied methodology. Next to the uncertainties discussed earlier throughout this thesis, inaccuracies can be introduced by the Roompot 8 simulations. Some possible flaws, that might directly influence the results between the simulation with and without turbines, are listed below.

- The time signals retrieved from the simulation with turbines, are significantly shorter than those of the simulation without turbines. The time signal of the simulation with turbines might be too short for a proper analysis
- The exact influence of the different effective resolutions is unknown

- The production of turbulence by the tidal energy turbines might not be included (well) in the simulation. This is hard to achieve, and was not required for the original aim of this simulation. In figure 6.4, no peaks are observed that can be attributed to the turbulence created by the energy turbines

6.3.3. Predicted damage for Roompot 8 - With Turbines

To finalise the analysis of the simulation with the tidal energy turbines, in table 6.9 the predicted dimensionless entrainment rates $\Phi_{E,p}$ are given. Similar as for the simulation without turbines, these values are converted into a number of stone movement per hour over an area of 5.000 m ^{2}.

Distance from ESB [m]	Stone class [kg]	Stone size sphere d [m]	Ψ_{htf}	$\Phi_{E,p}$	Predicted damage n [# stones/hour/5.000 m^2]
50	1000 - 3000	0.91	0.07	1.03E-08	0.9
100	3000 - 6000	1.19	0.02	3.36E-10	0.0
150	1000 - 3000	0.91	0.03	5.06E-10	0.0
150	300 - 1000	0.63	0.03	5.27E-10	0.1
200	300 - 1000	0.63	0.02	9.96E-11	0.0
200	60 - 300	0.41	0.02	8.69E-11	0.1

Table 6.9: Results for the test case of the Roompot 8 simulation with turbines

Table 6.9 shows that, compared to the simulation without turbines, the predicted damages are decreased. Logically, this is in agreement with the decreased bed loads, so table 6.9 gives no new insights. The analysis about the lower bed loads in the previous subsection is therefore not extended here.

Still the predicted damage at a distance of 50 m from the barrier is rather high, for the regular flow condition of the simulation. Based on this evaluation, it can be concluded that the tidal energy turbines do not seem to have a negative influence on the stability of the stones in the bed protection at the Eastern Scheldt barrier.

6.4. Conclusions chapter 6

In the previous chapter a method is derived to assess the stone stability in a highly turbulent flow behind a sill or back-ward facing step, based on the output of an IDDES. In this chapter this method is applied to the Roompot 8 simulations of the flow around the Eastern Scheldt barrier.

The methodology, as well as the numerical models, contain a lot of uncertainties. A few aspects that can directly influence the differences found between the simulation with and without turbines are listed in section 6.3.2. This exercise therefore only serves as a test case, and no value should be given to the reduced bed loads in case the tidal energy turbines are present in the model. As mentioned earlier, possibly the loads on the bed are increased elsewhere due to the presence of the tidal energy turbines.

The only conclusion that can be drawn about the tidal energy turbines, is that the overall influence on the stability of the granular bed protection near the Eastern Scheldt barrier, seems to be small. The remaining conclusions drawn for this chapter will only be about the potential of the applied methodology.

The spectra of figure 6.3 show that the desired effective resolution is not yet reached for both Roompot 8 simulations. The ratio between the desired resolution and the effective resolution for the simulation with turbines is: $\frac{f_{stone}}{f_{g,eff}} = 0.162$. For the long sill simulation with $h = 0.375$ m, this ratio is 0.125. Considering the fact that the computational requirements of these two simulations are also comparable, it seems that the applied methodology can be scaled to the large dimensions of the Roompot 8 simulations.

With the computational power used in this thesis, the time-dependent velocity signals of the long sill experiment are reproduced well. Taking into account that the available computational power will keep on increasing in the nearby future, using IDDES for the determination of stone stability seems to have a lot of potential, also for bed protections around large hydraulic structures.

About the applied stability relation, it can be concluded that the predicted damages seem to be too high. The stability formula should be calibrated further before it can be applied in practice. It is advised to focus future research on this topic amongst others on the items below.

- The validation of the simulated results for τ_x and $\frac{\partial p}{\partial x}$. Not only the mean values, but also the maxima should be verified by measurements
- The value of the combined added mass, drag and lift coefficient $C_{m:b}$. The predicted damages by stability relation 5.12 are considered to be too high. Therefore it is expected that predicted loads also are too high, which is most likely to be caused by a too large value of the $C_{m:b}$-value
- The influence of the different methods to model the bottom roughness (geometry or artificial roughness)
- The influence of the RANS-region on the simulated results

Furthermore, the methodology to optimise a granular bed protection by using detailed models like those of the Eastern Scheldt barrier and the long sill experiments, in itself can be an expensive job. Changing the bottom roughness to different values for different regions in a IDDES, and still obtaining accurate results, is laborious and not easy. Besides that, one should be aware that the model has to converge again to a new solution, which can take about a month for these detailed simulations.

7

Discussion

In this chapter a critical view is given to the limitations and uncertainties that are included in this study. Introducing inaccuracies starts with the measurements done during the experiments, and is increased by the CDF-modelling and the applied method to predict the start of stone movement. In the upcoming sections, the topics that are considered most relevant for the results of this thesis, are discussed.

7.1. Experiments

The aspects mentioned in this section are thought to be important to place the accuracy of the measurements in perspective. For the near-bed velocities also the link is made to the observed deviation between the measurements and the simulated values.

Measured damage
A large part of this study is based on the simulations of the long sill experiments described in Jongeling et al. (2003). During the execution of these experiments, the discharge is increased gradually until "start of stone movement" occurred. This state was defined as 5 to 10 stone movements during 5 minutes over the full measuring area. Apart from that this definition of the start of stone movement is rather arbitrary, it results in relatively little stone movements during the long measuring time of about 8 to 10 hours. For example, the long sill experiment with h = 0.50 m lasted for 10 hours and 35 minutes. In this timespan, only 102 moved stones were counted for the strip in which most damage occurred. Moreover, for several strips no damage was observed at all. The measured damages therefore are considered to be under-sampled for the derivation of a proper statistical damage field.

Furthermore, for the long sill experiment with h = 0.375 m, the total measured damage defined as "Stones out" deviates about 100 stones from the total damage defined as "Net stones out (out - in)". Relative to the total damage of about 1100 to 1200 stones, this is a significant difference.

Finally, in this thesis a certain coefficient is taken into account to compensate for the stone movements within a strip. Nevertheless this coefficient, derived in Hofland (2005), cannot be validated.

Near-bottom velocities
For the validation of the simulations, only the measured velocities in the streamwise x-direction are used. These measurements are considered to be accurate. The measuring error is expected to be the largest near the bottom, as there the velocity gradients are the largest. A vertical discrepancy between the noted measuring height and the real measuring height can have a significant influence on the measured velocities. In the region near the bottom also the largest deviations between the simulated and measured velocities are found.

7.2. Modelling

The items treated in this section are about the accuracy of the simulated results.

Validation τ_x and $\frac{\partial p}{\partial x}$
The simulated values for τ_x and $\frac{\partial p}{\partial x}$ are not validated. Although their distributions seem to be in agreement with what is described in literature, it is not sure if the produced values can be trusted. Especially the prediction of the extreme values should be checked thoroughly, before a stability formula, like the one proposed in this thesis, can be used in practise. Not in the last place because this prediction is also dependent on the applied grid sizes.

RANS region
Clearly the resolved fluctuations of the LES region are transferred into the RANS region near the bed, as time dependent signals of τ_x and $\frac{\partial p}{\partial x}$ are used to determine the stone stability. Nevertheless in the RANS region itself, turbulence is fully modelled, so originally no fluctuations are present here. It is unknown what influence the RANS region has on the fluctuating signal. Also the influence of the transfer from the LES region to the RANS region is unknown.

Law of the wall
In the long sill simulations, it is strived to obtained wall $z+$-values between 30 and 150 for the entire domain. With these values, a wall function is used to model the effect of the boundary layer. A wall function generally makes use of the law of the wall, which strictly speaking is only valid for uniform flow. The effect of the used wall function on the simulated results of τ_x and $\frac{\partial p}{\partial x}$ is unknown.

7.2.1. Long sill simulation

Artificial bottom roughness
In the long sill simulations, the bottom is modelled flat. A general roughness, defined by the roughness height k_s, is applied on the bottom to include the effect that the stones have on the flow. This value is used in the wall function to arrive at a velocity profile that corresponds to the flow over a rough bed. In reality the near-bottom flow will be much more complicated. The influence of this technique to model the bottom roughness, on the values of τ_x and $\frac{\partial p}{\partial x}$, is unknown.

Wall roughness
As mentioned in section 3.2.3, a wall roughness of 0.005 m was applied for the glass walls in the CFX-models of Jongeling et al. (2003). In the DESs of this thesis, smooth side walls are assumed, as the real wall roughness is unknown. Although the roughness of 0.005 m seems small, it does influence the three-dimensional flow field and therefore the values of τ_x and $\frac{\partial p}{\partial x}$ in the centre of the flume. It is good to realize that for detailed simulations, a lot of information is needed to obtain results that can be used for detailed calculations.

Water levels
The water levels of the long sill simulations are not validated. The accuracy and trustworthiness of the model might be increased even further when also the water levels are compared to the measurements at several locations throughout the domain.

Waves in the model
In this thesis, several remarks are made about the waves that are observed in the video of the simulated experiment. These waves seem to be visible in the resulting mean values of τ_x and $\frac{\partial p}{\partial x}$ on top of the sill. The exact effect on the simulated results is not studied, as it is unknown if some waves were present during the execution of the experiments.

7.2.2. Roompot 8 simulation

Validation
The Roompot 8 simulations are mainly validated on the discharge and flow velocities through this gate of the Eastern Scheldt barrier. The flow velocities at a larger distance from the barrier are compared to measurements, but the agreement was not always satisfying. This discrepancy is not of main concern for the original aim of the Roompot 8 simulations. Nevertheless, for the stability calculations, a higher degree of accuracy is required as the results are directly dependent on the near-bed flow velocities and turbulent fluctuations.

Roughness in geometry
In the Roompot 8 simulations, a radar image of the granular bed is implemented as the bottom of the model. The bed roughness is thereby included in the geometry of the model. The surfaces of this rough geometry are modelled smooth, and the cavities between stones are not taken into account. One can imagine the modelled bed of the Roompot 8 simulations as a kind of bumpy, glass sheet. It is not validated if this modelling method results in an accurate representation of the flow over a granular bottom.

Tidal energy turbines
No concessions are made by the modelling of the tidal energy turbines. They are included in the Roompot 8 model by rotating blades, surrounded by a rotating mesh. What effects the locally rotating mesh has on flow downstream of this area, is not studied. Furthermore, the turbines are expected to produce a certain amount of kinetic energy in the smaller turbulent scales. However, no peak is visible in the higher frequencies of figure 6.4.

7.3. Stone stability

In this section some uncertainties considering stone stability are discussed.

Validation stability formula
The stone stability formula applied on the Eastern Scheldt case is derived from the data of the downstream region of the long sill simulations only. The formula should be calibrated to other experiments in which flow separation occurred behind a sill or back-ward facing step. Other flow configurations, in which the same entrainment mechanism as described in section 5.1.5 is expected to be present, can be taken into account as well, to test this hypothesis.

Sensitivity to model set-up
The set-up and settings of the long sill simulations are exactly similar. It is not studied if the simulated results change significantly if for example one of the boundary conditions is derived in a different way. Besides that, especially the extreme values of τ_x and $\frac{\partial p}{\partial x}$ are very dependent on the applied grid sizes. It is not studied how the stability relation behaves if the mesh is changed.

Absolute value $\frac{\partial p}{\partial x}$
In the final stability formula 5.12, absolute values are used for τ_x and $\frac{\partial p}{\partial x}$. Using the absolute value of τ_x makes sense, as the stability of a stone is not dependent on the direction of a flow. The assumption made for including the absolute pressure gradient is less arbitrary. It is assumed that the horizontal pressure gradient is representative for the vertical pressure gradient over a stone and thereby the lift force. Nevertheless, the horizontal pressure gradient is present and will in reality cause a horizontal force on a stone. The horizontal direction and magnitude of this force might be very relevant for the stability of a stone.

$C_{m:b}$-value
In the proposed stability relation 5.12, a $C_{m:b}$-value of 1 is used. However, for the Eastern Scheldt case of chapter 6 the predicted damages are considered to be too high for the simulated flow situation. As the fluctuation pressure gradient $\frac{\partial p}{\partial x}'$ is the dominant load term for both analysed cases, this can be an indication that the $C_{m:b}$-value of 1 might be too high. The dominance of fluctuating load terms is expected, but for a $C_{m:b}$-value of 1 the load by the pressure gradient fluctuations is an order of magnitude larger than the shear stress fluctuations. This dominance of $\frac{\partial p}{\partial x}'$ is not necessarily expected from a physical point of view.

Uniqueness
Every stone is unique and so every stone movement will be unique too. Important aspects, such as the shape of a stone, stone grades or the stone placement, are not taken into account in the proposed stability relation. An exact fit between a stability parameter and the entrainment rate will probably never be found. The correlation numbers found in this thesis, or in Steenstra (2014), might be close to the upper limit of what can be reached without taking more physical aspects into account.

Entrainment rate
Last but not least, the use of the entrainment rate can be treacherous. Before using a relation between any Ψ and Φ_E, it should be defined which amount of damages one wants to be able to distinguish. For example, due to the definition of the entrainment rate, the entrainment rates of the long sill experiments were all in the same order of magnitude. Yet, in this thesis an attempt is made to distinguish an observed damage of 50 stone movements on top of the sill, from a damage of about 100 stones movements near the reattachment point. Compared to the relation between Ψ and Φ_E found in Steenstra (2014), the relation required for the long sill experiments needs to be much more sensitive. Other cases might be thinkable for which the relation found in Steenstra (2014) is not too robust. During the calibration of a stability formula, one can play with the relation between Ψ and Φ_E, depending on the aim of its application. This indicates that using the entrainment rate might never result in a stability method that is generally applicable.

8

Conclusions

In this research, an attempt is made to answer the following research question.
How to determine the stone stability in the top layer of a granular bed protection located in a non-uniform flow, with the use of local parameters extracted from a three-dimensional eddy resolving simulation, in order to determine the influence of tidal energy turbines on the stability of the granular bed protection of the Eastern Scheldt barrier?

The answer to this extensive research question is built up by the conclusions of three sub-questions. A fourth sub-question is answered to evaluate the use of a 3D eddy resolving simulation technique for the intended purpose.

Which 3D eddy resolving modelling technique is most appropriate to determine the stone stability in a granular bed protection around a hydraulic structure?

In this thesis, a three-dimensional eddy resolving modelling technique is used to simulate the long sill experiments of Jongeling et al. (2003). With regard to modelling accuracy, one would like to build a Direct Numerical Simulation or a Large Eddy Simulation (LES). Nevertheless, based on section 2.2, it can be concluded that for the present and the nearby future, these modelling techniques require too much computational power to be applicable in practice for most hydraulic engineering problems.

The most appropriate 3D eddy resolving simulation technique for the purpose of this thesis is found to be the Improved Delayed Detached Eddy Simulation (IDDES). This is an improved version of the original Detached Eddy Simulation, and is comparable to a Wall-Modelled LES. More information about this modelling technique can be found in section 2.2.

It should be noted that to apply this modelling technique, the upper limit of the available computational power for this thesis was required. Using 10 nodes with 4 cores simultaneously to run one simulation, at least one month was needed to produce a time signal that is sufficiently long to derive some statistical values.

For the long sill simulations this still appeared inadequate to reach the desired effective grid resolution. Despite that, satisfying agreements are obtain between the measured and simulated time-dependent velocity signals. Thereby, the potential of using IDDES is demonstrated. Applying an upstream boundary condition in which initial disturbances are added to the implemented velocity profile, appeared to be essential to obtain good IDDES results.

How to include the predominant physical forces into a stability formula that uses the output of a 3D eddy resolving technique?

The choice is made to derive a stability formula based on simulated bottom parameters. This prevents the method to be directly dependent on the grid size just used above the bed. The wall shear stress τ_x and the horizontal pressure gradient $\frac{\partial p}{\partial x}$ are used to represent the main forces by drag and inertia respectively.

The simulated values of τ_x and $\frac{\partial p}{\partial x}$ are not validated, but their distributions are found to be in agreement with those described in literature for the drag and lift force respectively. Moreover, it is concluded that the extreme forces on a stone do not follow a Gaussian distribution.

A new stability formula is proposed, based on the assumptions listed below.

- The predominant forces for stone stability are:
  1. The mean wall shear stress $\bar{\tau}_x$ - Force due to the near-bed flow velocity
  2. The wall shear stress fluctuations τ'_x - Force due to large-scale energy containing eddies
  3. The mean pressure gradient $\frac{\bar{\partial p}}{\partial x}$ - Force due to spatial accelerations (e.g. geometry) and waves
  4. The pressure gradient fluctuations $\frac{\partial p}{\partial x}'$ - Force caused by turbulent wall pressures
- Stone movement is caused by the occurrence of an extreme lift force, which increases the exposed area of a stone, followed by an extreme drag force that moves the stone in the near-bottom flow direction.
- Absolute extreme values of τ_x and $\frac{\partial p}{\partial x}$ can be used, as stone stability is not dependent on the direction of the near-bed flow velocity, and both negative as positive pressure gradients can result in an extreme lift force.

The new stability formula is given by equation 4.3. It appears that over the full domain, the measured stone movements are not predicted well by this stability formula.

For the full domain, the best relation between the entrainment rate Φ_E and the tested stability parameters, is obtained with the Steenstra-type formula, given by equation 5.6. In this formula, the load by the turbulent wall pressures is excluded. Apart from that, the Steenstra-type formula is similar to the proposed stability relation 4.3 with a $C_{m:b}$-value of 23.

It is made plausible, that the reasonable performance of the Steenstra-type formula can mainly be attributed to the heavy weight ascribed to the inertia term $\frac{\bar{\partial p}}{\partial x}$. In the used data, a direct link seems to be present between this inertia term and the entrainment rate. However, this link cannot be substantiated yet from literature, and it is doubted to be representative for the physical forces on a granular bed protection. It must be noted that in the original Steenstra formula, the ratio between drag and inertia will be different than in the Steenstra-type formula, as different load parameters are used in both stability relations.

In section 5.1.5, a hypothesis is posed about the entrainment mechanisms that are expected to be governing for the damages in the different flow regions of the long sill experiments. On top of the sill, the ratio between the used load parameters differs from the ratio between the load terms in the area behind the sill. Therefore, these entrainment mechanisms might not be captured well into one stability formula.

With regard to the Eastern Scheldt case, a stability formula is derived based on the highly turbulent flow region, downstream of the separation point. The observed damage field (figure 5.6) of the long sill experiments, as well as the derived stability formula, seem to be in agreement with the hypothesised entrainment mechanism for this area.

The stability relation derived for the highly turbulent flow region downstream of the sill is given below.

$$\Psi_{htf} = \frac{\left(|\tau_x| + |\frac{\partial p}{\partial x}|d\right)_{0.3\%}}{\left(\rho_s - \rho_w\right) g d} \tag{8.1}$$

This stability formula is applied to the Eastern Scheldt case, together with the power relation found between the dimensionless entrainment rate Φ_E and the stability parameter Ψ_{htf} given by equation 8.2.

$$\Phi_E = 6.34 * 10^{-5} \Psi_{htf}^{3.27} \tag{8.2}$$

What is the influence of the tidal energy turbines on the stability of the granular bed protection at the Eastern Scheldt barrier?

In order to determine the influence of the tidal energy turbines on the stability of the granular bed protection, an IDDES of the flow through the barrier without turbines is compared to an IDDES with turbines. In the simulation with turbines, a finer grid size is applied, whereby more turbulent scales are resolved in this simulation than in the simulation without turbines. The computational requirements of the simulation with turbines are comparable to those of the long sill simulations. Moreover, also the ratio between the desired and achieved effective resolution is about equal to that of the long sill simulations. The applied methodology therefore seems scalable to the large dimensions of the Eastern Scheldt simulations.

For the assessment of the stability of the granular bed protection, at several points a comparison is made between the bed loads in the two simulations. After applying stability formula 8.1, it is concluded that the influence of the tidal energy turbines on the stability of the granular bed protection seems to be small. In the simulation with turbines, the loads on the bed are slightly lower than in the simulation without turbines. This might have a physical explanation, but could as well be caused by inaccuracies in the model or the applied methodology.

In contrast to the expectations, in the simulation with turbines, no extra turbulent kinetic energy is generated by the tidal energy turbines. The turbines seem to initiate a different distribution of the turbulent kinetic energy over the modelled domain, whereby at least locally, the loads on the bed are slightly reduced. The main reduction is caused by the decrease of $\frac{\partial p}{\partial x}'$, which is the dominant load term in both simulations. The overall magnitudes of the predicted bed loads are expected to be too high, as also the predicted damages are considered to be too large. The proposed stability relation 8.1 should be calibrated further, before it can be applied in practise.

Answer to the main research question

Below a generalised approach is given to assess the stability of the top layer of a granular bed protection in a highly turbulent flow region, based on the output of a 3D eddy resolving simulation technique. To answer the main research question of this thesis, only step 3, 4 and 5 of this approach have to be executed for the simulations with and without turbines. The influence of the tidal energy turbines can then be determined, based on a comparison between the extreme loads of both simulations.

The steps to be taken, in order to assess the stability of the top layer of a granular bed protection in a highly turbulent flow region, based on the output of a 3D eddy resolving simulation technique, are given below.

1. Determine critical entrainment rates $\Phi_{E,c}$ for some pre-defined regions of a granular bed protection
2. Build and validate an IDDES of the flow above the granular bed protection that needs to be evaluated
3. Define the load term $\left(|\tau_x| + |\frac{\partial p}{\partial x}|d\right)$ as a parameter in the numerical software
4. Produce time signals of this parameter in each pre-defined region
5. Extract these time signals from the model and determine the 0.3%-exceedence probability of each time signal separately
6. Use stability relation 8.1 to determine stability parameter Ψ_{htf} for each pre-defined region
7. Use stability relation 8.2 to determine the predicted entrainment rates $\Phi_{E,p}$
8. Check for each region if $\Phi_{E,p} < \Phi_{E,c}$
9. If this criterion is not met, the stone diameter in the model should be adjusted for these regions and step 4 to 8 should be repeated

Does the use of a 3D eddy resolving technique add value to the assessment of stone stability in a granular bed protection, compared to methods that rely the output of a RANS model?

The use of a 3D eddy resolving technique is especially valuable if stability formula 8.1 is used. In this equation, a fluctuating load term for the turbulent wall pressures is taken into account, that cannot be extracted from a RANS model. Nevertheless, it is not proven that this formula performs better than other stability formulas that can be used with the output of RANS models. It only is made plausible that the governing forces on the bed in a highly turbulent flow region are represented better by stability formula 8.1, than by the other tested stability relations.

Many more options can be studied to assess the stability of a granular bed protection, based on the output of an IDDES. The main advantages of an IDDES are that it creates time-dependent signals, and that for non-uniform flow cases, IDDES seems to require less tuning than a RANS model. At least for the long sill experiments, the averaged velocity and turbulent kinetic energy profiles are reproduced more accurately by the IDDES. The main disadvantage is that an IDDES requires more computational time and power than a RANS model.

One should be aware that an IDDES offers more detailed information. To justify the use of this information, also the validation should be done to a higher degree of detail. Further research is needed to determine if the effort required to use (the detailed information of) an IDDES, pays off in a more economic design of a granular bed protection.

The choice between using a RANS model or IDDES should depend on a trade-off between computational power, time, and required accuracy. With this research, it is shown that using IDDES might be a valuable alternative for stability methods based on the output of RANS models.

9 Recommendations

In this thesis, it is the first time that a detailed eddy resolving modelling technique is used for the aim of determining the stone stability in a granular bed protection. The applied methodology in this thesis definitely seems to have potential, but it must be concluded that more research is needed before it can be applied in practice. It appears that many new challenges come along with the use of a much more detailed modelling technique. In this chapter, recommendations are given about the way to proceed with further research on this topic.

9.1. Experiments

Steenstra (2014)
In Steenstra (2014), the data of many experiments is analysed to obtain a calibrated stability formula. It would be interesting to study the results, when these experiments are all simulated according to the methodology described in chapter 3. In this way more information can be obtained about the physics and load terms described in this thesis.

Besides that, the relation between Φ_E and Ψ_{htf} can be specified further as, for other experiments than those of Jongeling et al. (2003), other damage criteria were used. As described in the discussion, it should be taken into account which ranges of possible damages one wants to be able to distinguish when studying this relation. The steepness of the relation between Φ_E and Ψ determines the robustness. As an example, one should determine it is required to distinguish damages of 0, 10 and 20 stone movements in a certain timespan over a certain area, or the difference between damages of 0, 100 and 200 stone movements.

Amir et al. (2014)
In the introduction of the article Amir et al. (2014), a lot of interesting studies are mentioned and sometimes their results are briefly summarised. The article itself, as well as the described studies, are expected to be useful to obtain more understanding about the behaviour of the wall shear stresses and pressure gradients on a granular bed. Some of these studies are experimental and therefore might be used for the validation of τ_x or $\frac{\partial p}{\partial x}$ when simulated according to the methodology described in this thesis. Furthermore, they can be a source of inspiration for new experiments that combine the measurement of flow characteristics and damages to a granular bed protection.

Jongeling et al. (2003)
Besides the modelling of the experiments described in Jongeling et al. (2003), it would be interesting to repeat this experimental series for different definitions of the "start of stone movement". The definition of the start of stone movement can be interpreted as a criterion for the entrainment rate. More understanding about the behaviour of the entrainment rate and its relation to a certain Ψ-value can be gained, if similar experiments are repeated for different definitions of the start of stone movement.

Attention should be paid to the timespan of the measurements. For the low entrainment rates, it should be long enough to obtain a damage field that represents the statistical averaged damages. With respects to the executed experiments by Jongeling et al. (2003), a longer timespan would have been chosen for the long sill experiments. It should be facilitated that it is possible to have a significant amount of stone movements in a certain strip. In a ideal case, one can trace the exact movement of each stone individually.

Another improvement to the experiments of Jongeling et al. (2003), is the measurement of the water levels. To ease the modelling, it is advised to at least measure the water levels at the start and the end of the flume. Extra measurements of the water levels can serve as an extra validation measure. For example for the long sill simulations extra accuracy can be obtained if just before the sill, on top of the sill and just after the sill, the water levels are also recorded and validated.

9.2. Modelling

RANS

Compared to RANS models, the results of a DES might be more trustworthy, as more accurate results can be obtained with less tuning. For example, if the model made for the IDDES of the long sill experiments is solved in RANS mode, no separation occurs at the downstream edge of the sill. However, the RANS model can be tuned such that separation does occur. For example, by cutting a piece from the downstream slope of the sill, whereby the shear gradients at the downstream edge are enlarged. Despite this small adjustment to the sill's geometry, the flow characteristics behind the sill might be in agreement with the measurements. In this way, smart tuning of a RANS model, based on engineering understanding of the flow physics, can result in quite accurate RANS results.

The big advantage of using a RANS model instead of a DES, is that for a RANS model much less computational time and power is required. A RANS model will be converged towards a new solution must faster than a DES, whereby the effect of adjustments can be analysed faster. The advantage of using a DES is that turbulence is resolved to a certain extent, and therefore fluctuations like $\frac{\partial p}{\partial x}'$ can be taken into account. Nevertheless, in this thesis it is concluded that including $\frac{\partial p}{\partial x}'$ in the stability formula does not improve the predictions of the entrainment rate for the entire domain. Moreover, it is not yet proven that better results are obtained when τ_x' (or u_x') is used instead of the k-values that can be extracted from a RANS model.

It should be analysed further for which cases the use of DES is worth the effort, compared to the use of much simpler RANS models. For academic research the use of DES is certainly valuable, because with a well-validated DES, more insight can be obtained in the physics regarding stone stability. It is thought that, especially for practical purposes, the potential of using RANS models should not be depreciated. The choice of the appropriate modelling method depends on the aim of the simulation.

Turbulence model

In this thesis, a IDDES is performed that uses the SST k-ω turbulence model in the RANS-region. During the start of the modelling exercises, it was found that the chosen turbulence model does influence the simulated results. Although this modelling choice should not be the first priority with respect to the formulation of a method to assess the stone stability, a well-performing turbulence model can ease the modelling itself and can improve the simulated results.

An example of a relatively new turbulence model is the Elliptic Blending k-ε (EB k-ε) model. This turbulence model is an improved version of the original k-ε model, and therefore also based on the Boussinesq hypothesis. In Star CCM+ (2017) it is claimed that the EB k-ε model currently is the best available turbulence model for non-uniform flow situations like those in this thesis.

Another option is to look into the use of the Reynolds Stress Turbulence Model (RSTM). With this modelling technique, no isotropic eddy viscosity is assumed. Nevertheless RSTM is rather unpopular because of its complexity. A RSTM solves the Navier-Stokes equation by assuming additional transport equations for all six independent Reynolds stresses. One more equation is needed to model the turbulent dissipation. Based on literature, the performances and computational requirements seem to be comparable to a DES. In some cases, a RSTM even performs better than a DES, as concluded in Probst et al. (2010).

Boundary layer
In an IDDES, the boundary layer is modelled by the use of a wall function. In this near-bottom area, the turbulent quantities are modelled as well, as here the model is solved by the RANS equations. It is unknown what the effects of these approximations are on the results of τ_x, $\frac{\partial p}{\partial x}$ and the near-bottom flow characteristics.

In addition to a validation by measurements, a comparison to a LES is expected to provide valuable insights on this. In a LES, the boundary layer is resolved, as well a significant part of the turbulent characteristics. Because of computational constraints, the domain for this LES should be of a limited size. Still it has to reproduce the flow physics at a point of interest, and therefore it might be challenging to find the correct boundary conditions.

9.3. Stone stability

Entrainment rate
As mentioned in the discussion, multiple relations can be found between the entrainment rate Φ_E and a certain stability parameter Ψ. The idea behind the entrainment rate is the design philosophy that more economical designs can be made, if during certain governing flow conditions a certain amount of damage to a granular bed protection is allowed. In case the chosen design conditions occur, the bed protection can be inspected and repaired if needed.

However, no guidelines about the use of the entrainment rate are available yet. This makes the use of the entrainment rate rather arbitrary, and difficult to interpret for practical purposes. Before continuing with studies to obtain a "better" or "worse" relation between Φ_E and Ψ, it is advised to study the use of the entrainment rate itself.

One of the problems is that a higher value of the entrainment rate Φ_E can be caused by:
1. The use of a larger stone diameter d
2. Measuring over a shorter amount of time T
3. Measuring over a smaller area A

These variables can be adjusted independently, and therefore endless combinations are possible. It would be useful to define constraints whereby the amount of possibilities is reduced.

For the definition of time, one can think of relating the entrainment rate to a governing storm of for example six hours, as done for the Eastern Scheldt case in chapter 6. In case of river flow, one can think of a governing discharge during a flood wave of for example 5 days. Furthermore, it might be possible to define a certain ratio between the stone diameter and the evaluated area. With respect to the allowable damage, one can ask opinions of for example Rijkswaterstaat, or experimentally determine a limit between controllable and uncontrollable damages. Besides that, one can repeat experiments like those of Jongeling et al. (2003) with different definitions of the "start of stone movement", whereby a more trustworthy relation can be derived between Φ_E and Ψ.

Mean pressure gradient

From the data used in this study, it can be concluded that the mean pressure gradient $\frac{\bar{\partial p}}{\partial x}$ seems to be related to the entrainment rate Φ_E. Earlier, Steenstra (2014) obtained a well-correlated fit between Φ_E and Ψ_{RS} for several distinct experimental series. It is expected that this fit can largely be attributed to the dominance of the inertia term $u\frac{\bar{\partial u}}{\partial x}$ in the Steenstra formula. It therefore seems plausible that the entrainment rate can be predicted well by the mean inertia term determined as $\frac{\bar{\partial p}}{\partial x}$ or $u\frac{\bar{\partial u}}{\partial x}$.

The relation between this load term and the entrainment rate can not yet be supported physically from earlier studies, and is also not in direct agreement with the hypothesised entrainment mechanisms. Nevertheless it might be very useful for the prediction of the stone stability in a granular bed protection, and therefore further research on this is recommended.

Near-bottom flow characteristics
The stability formula proposed in this thesis is based on bottom parameters, to avoid the direct dependency on the near-bottom grid size. In the stability formulas presented in earlier studies, frequently use is made of depth-averaged flow parameters like the flow velocity and acceleration. Both approaches result in methods comparable to the stability formula proposed by Shields (1936).

In this thesis also the choice could have been made to determine the stone stability based on the near-bottom flow velocity and acceleration, like the approach chosen by Isbash (1932). The input parameters then should be determined on a certain height z above the bed. Based on Xingkui and Fontijn (1993) a logical choice would have been to choose a height z of $0.15d$. For the long sill experiment this would result in $z = 0.93$ mm. The wall cell of the simulation with $h = 0.375$ m has a height of 3 mm. This means that one should interpolate between $u = 0$, and the velocity at $z = 3mm$, to obtain the velocity at a height of $0.15d$.

For the long sill simulations, it cannot be validated if this interpolated velocity would be in agreement with reality. However, it is known that the differences between the simulated and measured velocities are the largest near the bottom. These are important reasons why this approach is not chosen in this thesis.

If one wants to study the performance of a stability formula that is based on the local near-bottom characteristics, it is advised to use an experiment in which much attention is paid to an accurate measurement of the velocities very close to the bed. Then, it can be validated if these values are simulated well in an IDDES. Nevertheless, it is expected that in many cases it is required to resolve the boundary layer to obtain accurate results this close to the bed. Then a full LES should be built instead of an IDDES. When validated well, and sufficient computational power is available, this methodology might have a lot of potential. In particular because the velocities and accelerations are easier to measure, and therefore this eases the validation of the simulation.

Prediction extreme values
If the possibilities of stability relation 5.12 are elaborated further in other studies, in first instance attention should be paid to the validation of τ_x and $\frac{\partial p}{\partial x}$. Not only the mean values, but especially the prediction of the extreme values should be studies well, as the extreme values are more difficult to approximate accurately by a numerical model.

Furthermore, if possible, it would be useful to fit mathematical relations through the distributions of the wall shear stress and the pressure gradient. The extreme values of τ_x and $\frac{\partial p}{\partial x}$ can then be estimated by an empirical relation. The estimate of the extreme pressure gradient might be based on a Gaussian distribution with an high kurtosis. For the wall shear stress one might use the relation derived in Hofland and Battjes (2006).

Three-dimensionality
In this thesis, the simulated velocities in the y- and z-direction are not validated. However, this can be interesting when a more in-depth study is done to the three-dimensionality of the simulated flow. With regard to stone stability, especially near the reattachment point three-dimensional eddies are expected to cause significant forces in the y-direction. For the long sill experiments, it is observed that the pressure gradient fluctuations in y-direction $\frac{\partial p'}{\partial y}$ are in the same order of magnitude as $\frac{\partial p'}{\partial x}$. It is suggested to study if stability formula 5.12 can be improved, by taking bottom vectors into account instead of only the streamwise direction.

Bibliography

Addad, Y., Gaitonde, U., Laurence, D., and Rolfo, S. (2008). Optimal unstructured meshing for large eddy simulations. In *Quality and reliability of large-eddy simulations*, pages 93–103. Springer.

Amir, M., Nikora, V. I., and Stewart, M. T. (2014). Pressure forces on sediment particles in turbulent open-channel flow: a laboratory study. *Journal of Fluid Mechanics*, 757:458–497.

Anderson, J. D. (2005). Ludwig prandtls boundary layer. *Physics Today*, 58(12):42–48.

Biesboer, F. (2011). De Oosterschelde bracht het keerpunt. *De Ingenieur*.

Blocken, B., Stathopoulos, T., and Carmeliet, J. (2007). CFD simulation of the atmospheric boundary layer: wall function problems. *Atmospheric Environment*, 41:238–252.

Blom, A. (2017). Powerpoint River Engineer - Lecture 4: Turbulence and bed friction, TU Delft.

Cebeci, T. and Bradshaw, P. (1977). Momentum transfer in boundary layers. *Washington, DC, Hemisphere Publishing Corp.; New York, McGraw-Hill Book Co., 1977. 407 p.*

Cheng, E. and Clyde, C. (1972). Instantaneous hydrodynamic lift and drag forces on large roughness elements in turbulent open channel flow. *Sedimentation (Einstein), Fort Collins, Colorado*, pages 3–1.

Classification of Flows, Laminar and Turbulent Flows (2005). Aerospace, mechanical and mechatronic engineering, university of sydney.

De Gunst, M. (1999). Steenstabiliteit in een turbulente stroming achter een afstap. Master's thesis, TU Delft.

Dessens, M. (2004). The influence of flow acceleration on stone stability. Master's thesis, TU Delft.

Einstein, H. A. and El-Samni, A. E.-S. (1949). Hydrodynamic Forces on a Rough Wall. *Reviews of Modern Physics*, 21:520–524.

Gritskevich, M. S., Garbaruk, A. V., Schütze, J., and Menter, F. R. (2012). Development of ddes and iddes formulations for the k-ω shear stress transport model. *Flow Turbulence Combust*, 88:431–449.

Hoan, N. (2008). *Stone Stability Under Non-uniform Flow*. PhD thesis, TU Delft.

Hoffmans, G. (2006). Stability of Stones Under Non-Uniform. Master's thesis, Rijkswaterstaat.

Hofland, B. (2000). Literature Survey - Stability of stones in the top layer of a granular filter. Technical report, Delft Hydraulics.

Hofland, B. (2005). *Rock & Roll - Turbulence-induced damage to granular bed protections*. PhD thesis, TU Delft.

Hofland, B. and Battjes, J. A. (2006). Probability Density Function of Instantaneous Drag Forces and Shear Stresses on a Bed. *Journal of Hydraulic Engineering*, 132:1169–1175.

Huijsmans, M. (2006). The influence of flow acceleration on the stability of stones. Master's thesis, TU Delft.

Isbash, S. (1932). Construction of dams by dumping stones into flowing water. Technical report, USACE.

Jiménez, J. (2004). Turbulent flows over rough walls. *Annual Review of Fluid Mechanics*, 36:173–196.

Jongeling, T., Blom, A., Jagers, H., Stolker, C., and Verheij, H. (2003). Ontwerpmethodiek granulaire verdediginen.pdf. Technical report, Delft Hydraulics.

Menter, F. (1994). Two-equation eddy-viscosity transport turbulence model for engineering applications. *AIAA Journal*, 32:1598–1605.

Menter, F., Kuntz, M., and Langtry, R. (2003). Ten years of industrial experience with the sst turbulence model. *Turbulence, Heat and Mass Transfer 4*.

Ministerie van Verkeer en Waterstaat (1991). Ontwerpnota stormvloedkering oosterschelde, boek 2: De waterbouwkundige werken. Technical report.

Mockett, C. and Thiele, F. (2007). Overview of detached-eddy simulation for external and internal turbulent flow applications. *Fifth International Conference on Fluid Mechanics*.

Mosselman, E. and Akkerman, G. J. (1998). Low-mobility transport of coarse-grained material. Technical report.

Nezu, I. and Nakagawa, H. (1989). Turbulent Structure of Backward-Facing Step Flow and Coherent Vortex Shedding from Reattachment in Open-Channel Flows. In *Turbulent shear flows 6*, pages 313–337. Springer.

Nikora, V., Goring, D., McEwan, I., and Griffiths, G. (2001). Spatially Averaged Open-Channel Flow over Rough Bed. *Journal of Hydraulic Engineering*, 127:123–133.

Peters, R. (2014). Stone stability in breakwater toes based on local hydraulic conditions. Master's thesis, TU Delft.

Probst, A., Radespiel, R., Wolf, C., Knopp, T., and Schwamborn, D. (2010). A comparison of detached-eddy simulation and reynolds-stress modeling applied to the flow over a backward-facing step and an airfoil at stall.

Raaijmakers, T., Van Velzen, G., Hoffmans, G., Bijlsma, A., Verbruggen, W., and Stark, J. (2012). Stormvloedkering Oosterschelde: ontwikkeling ontgrondingskuilen en stabiliteit bodembescherming - Deelrapportage "Ontgrondingen". Technical report, Deltares.

Rijkswaterstaat (2017). Overzicht bodembescherming oosterscheldekering. AutoCAD drawing.

Rodi, W., Constantinescu, G., and Stoesser, T. (2013). *Large-Eddy Simulation in Hydraulics*. International Association for Hydro-Environment Engineering and Research (IAHR).

Saadati, E. (2009). *Introductory FLUENT Training - Chapter 6: Turbulence modeling*. Sharif University of Technology.

Schiereck, G. and Verhagen, H. (2012). *Introduction to bed, bank and shore protection*. VSSD, Delft, 2nd edition.

Shields, A. (1936). *Anwendung der Aehnlichkeitsmechanik und der Turbulenzforschung auf die Geschiebebewegung*. PhD thesis, Berlin.

Shur, M. L., Spalart, P. R., Strelets, M. K., and Travin, A. K. (2008). A hybrid rans-les approach with delayed-des and wall-modelled les capabilities. *International Journal of Heat and Fluid Flow*, 29:1638–1649.

Southard, J. (2006). Lecture notes: Introduction to Fluid Motions, Sediment Transport, and Current-Generated Sedimentary Structures - Chapter 4, Massachusetts Institute of Technology.

Spalart, P. R. (2009). Detached-eddy simulation. *Annual Review Fluid Mechanics*, 41:181–202.

Star CCM+ (2017). *Spotlight on: Turbulence*. Siemens.

Star CCM+ (2018). *User Guide*. Siemens.

Steenstra, R. (2014). Incorporation of the effects of accelerating flow in the design of granular bed protections. Master's thesis, TU Delft.

Steenstra, R., Hofland, B., Smale, A., Paarlberg, A., Huthoff, F., and Uijttewaal, W. (2016). Stone stability under stationary nonuniform flows. *Journal of Hydraulic Engineering*, 142(12).

Stoesser, T. (2010). Physically realistic roughness closure scheme to simulate turbulent channel flow over rough beds within the framework of les. *Journal of Hydraulic Engineering*, 136:812–819.

Stoutjesdijk, T., De Kleine, M., De Ronde, J., and Raaijmakers, T. (2012). Stormvloedkering Oosterschelde: ontwikkeling ontgrondingskuilen en stabiliteit bodembescherming, Hoofdrapport. Technical report, Deltares.

Thompson, D. J., Iglesias, E. L., Liu, X., Zhu, J., and Hu, Z. (2015). Recent developments in the prediction and control of aerodynamic noise from high-speed trains. *International Journal of Rail Transportation*, 3(3):119–150.

Tromp, M. (2004). Influences of fluid accelerations on the threshold of motion. Master's thesis, TU Delft.

Uijttewaal, W. (2002). Lecture notes: Turbulence in Hydraulics, TU Delft.

Van Heijst, G. and Van de Vosse, F. (2002). Lecture notes: Stroming en diffusie, tu eindhoven.

Verhagen, H. (2016-2017). Flow loads - lecture 2 of bed, bank and shoreline protection, tu delft.

Xingkui, W. and Fontijn, H. (1993). Experimental study of the hydrodynamic forces on a bed element in an open channel with a backward-facing step. *Journal of Fluids and Structures*, 7:299–318.

Zhang, D. (2017). Comparison of various turbulence models for unsteady flow around a finite circular cylinder at re =20000. *Journal of Physics: Conference Series*, 910.

A

Example: use of Φ_E

Below assumptions are made, in an attempt to obtain some feeling for what a certain Φ_E-value means in practise.

- $\Delta = \frac{\rho_s - \rho_w}{\rho_w} = \frac{2650-1000}{1000} = 1.65$
- $A = 1\ \text{m}^2$
- $T = 1$ hour $= 3600$ s

With these assumptions, n represents number of moved stones /m^2 /hour. In table A.1, the resulting number of moved stones /m^2 /hour n for some common Φ_E and stone diameters of $d = 1.00$ m and $d = 0.01$ m, are presented.

Φ_E	n-value for $d = 1.00$ m	n-value for $d = 0.01$ m
10^{-6}	$1.448 * 10^{-02}$	1448
10^{-7}	$1.448 * 10^{-03}$	144.8
10^{-8}	$1.448 * 10^{-04}$	14.48
10^{-9}	$1.448 * 10^{-05}$	1.448

Table A.1: Number of stone movements /m^2 /hour for several common Φ_E-values for stone diameters $d = 1.00$ m and $d = 0.01$ m

From table A.1, it can be seen that Φ_E and n are linearly related, i.e. if Φ_E goes up by a factor 10, n goes up by a factor 10 as well. Also both n-values for each Φ_E-value are related by a factor $d^{-2.5}$.

Still, from the n-values corresponding to $d = 1.00$ m, not much can be said about the meaning of Φ_E. The n-values corresponding to $d = 0.01$ m might speak more to the imagination. Assuming that $\frac{1^2}{0.01^2} = 10000$ stones with $d = 0.01$ m are present in 1 m^2, table A.2 shows how much each n-value means percentage-wise.

Φ_E	n-value for $d = 0.01$ m	% of 10000 stones /m^2
10^{-6}	1448	14.48
10^{-7}	144.8	1.45
10^{-8}	14.48	0.14
10^{-9}	1.448	0.01

Table A.2: Φ_E linked to the damage per 10.000 stones per hour for $d = 0.01$ m

As a comparison, now the n-values for $d = 1.00$ m are determined for an area of 10.000 m^2. Similar to table A.2, the damage can than be expressed in a % of 10.000 stones. In table A.3 the results are shown.

Φ_E	n-value for d = 1.00 m /10.000 m^2	% of 10000 stones /10.000 m^2
10^{-6}	144.8	1.45
10^{-7}	14.48	0.14
10^{-8}	1.448	0.01
10^{-9}	0.1448	0.001

Table A.3: Φ_E linked to the damage per 10.000 stones per hour for d = 1.00 m

Now lets assume that, for both cases, a damage of approximately 15 stone movements per hour per 10.000 stones is stated as the critical upper limit. This example shows that, the critical Φ_E-value for d = 1.00 m is 10^{-7}, while the critical Φ_E-value for d = 0.01 m is 10^{-8}.

Of course, this comparison is not fully honest, as also the flow forces to move 15 stones with d = 0.01 m will deviate a lot from the forces to move 15 stones with d = 1.00 m. The example is only meant to indicate that the use of Φ_E can be treacherous. For practical purposes, a certain Φ_E-value becomes more meaningful if it is linked to a case specific area and time scale.

B

Roughness in Star CCM+

Star CCM+

The software used in this thesis is Star CCM+. It is a commercial finite volume software package, that is applied in many different industries. In this thesis it is used to simulate water flowing over a rough bottom. As mentioned in section 2.2.5, there are two ways to model a rough bottom. In this appendix, an explanation is given about how the wall functions are defined in Star CCM+.

Roughness in Star CCM+

The roughness in Star CCM+ is taken into account by a equivalent sand-grain roughness height approach. In Star this parameter is denoted by r, while in literature more often k_s is used to indicate the equivalent sand-grain roughness height. With the given roughness height, the software determines the value of the "roughness parameter" R^+, by the formula: $R^+ = \frac{ru^*}{\nu}$. The roughness parameter R^+ is similar to what in literature is called the "boundary Reynolds number" or "roughness Reynolds number" or "shear Reynolds number" R^*. This parameter indicates if a roughness element will be larger than the viscous sublayer or not, and thus if a boundary is hydraulically smooth or rough.

Depending on the value of R^+, the roughness function f for the smooth, rough or transitional regimes is used. The limits of the different regimes are derived for the use of the equivalent sand-grain roughness height specifically by Ioselevich and Pilipenko, based on the roughness data of Nikuradse (Cebeci and Bradshaw, 1977). The formulas for f and the default values of the coefficient used can be found in Cebeci and Bradshaw (1977).

Subsequently the log-law coefficient E is divided by the calculated value of f to obtain a corrected value of E, denoted as E'. The default value of E is 9.0, but the origin of this value could not be traced. The corrected wall coefficient coefficient E' is put into the log-law formula, and causes a downward shift of the idealised logarithmic velocity profile. This downward shifting of the logarithmic velocity profile is a common method to account for roughness in numerical simulations. It causes the velocities to be distributed more equally over the water depth, and higher flow velocities are present near the bottom. This is in accordance with the physical behaviour of a turbulent flow above a rough bottom as explained in (Southard, 2006).

As a last remark about the calculation procedure of Star CCM+, it should be noted that the software uses the dimensionless parameters $u+$ and $z+$ to determine the shape of the velocity profile. $u+$ is the local velocity in x-direction u_x made dimensionless by the shear velocity u_*. $z+$ is the dimensionless wall distance, as already mentioned in section 2.2.5.

Roughness Limiter of Star CCM+

An important assumption, required for the calculation procedure described above to result in solutions that are physically possible, is that the distance from the wall to the centroid of the first cell z should be considerably larger than the roughness length z_0.

The roughness length z_0 is the point where the idealized velocity profile goes to zero, in case the profile would be extended down to this height (Southard, 2006). An empirical estimate of the closely-packed sand-grain roughness length in hydraulically rough flow is $\frac{k_s}{30}$, and thus independent of the Reynolds number. If a value of $2d_n50$ is assumed for the equivalent sand-grain roughness height, the centroid of the first cell z should be higher than: $z >> z_0 = \frac{k_s}{30} = \frac{2d_n50}{30}$.

To adhere this requirement, Star CCM+ included a roughness limiter. This tool artificially suppresses the roughness height when the entered roughness height is larger than the centroid of the first cell z at the solid boundary. Star CCM+ then automatically uses the height of the wall-cell as the roughness height of the bottom, instead of what the user defined as the roughness height.

This function (the "Roughness limiter") can be deactivated, but then the user should take care that the requirement of $z >> z_0$ is still met. Based on some trial-and-error research for this project, in practise this appeared to mean that physically possible results can be obtained if $2z \geq k_s$. In other words, when using the $k-\varepsilon$ turbulence model, the size of the first cell above the bottom boundary should be about equal or larger than the roughness height that the user defines.

Keeping the theory about stone stability explained in section 2.1 in mind, this implicitly means that the grid sizes used for the simulation will be larger than the desired maximum size of one time the stone diameter directly above the bottom boundary.

C

SST k-ω turbulence model

In this thesis the SST k-ω turbulence model is used to calculate the eddy viscosity μ_t. μ_t is linked to the Reynolds stresses by the Boussinesq hypothesis. The difference between the RANS formulation and the LES formulation of the model will be indicated.

RANS formulation

The SST k-ω model uses two transport equations to determine the eddy viscosity. The given equations are retrieved from the Star CCM+ manual and therefore include some extra modification factors, as for example f_{β^*} and f_β, to improve the performances of the original SST k- ω model. Of all constant model factors the numerical values are noted. The remaining model constant are listed at the end of this paragraph.

1. The transport equation for the turbulent kinetic energy k

$$\frac{\partial}{\partial t}(\rho k) + \nabla \cdot (\rho k \bar{\boldsymbol{v}}) = \nabla \cdot [(\mu + \sigma_k \mu_t)\nabla k] + G_k + G_{nl} + G_b - 0.09\rho f_{\beta^*}(\omega k - \omega_0 k_0) + S_k$$

   In which:
   - $\frac{\partial}{\partial t}(\rho k)$ is the transient term.
   - $\nabla \cdot (\rho k \bar{\boldsymbol{v}})$ is the convection term.
   - $\nabla \cdot [(\mu + \sigma_k \mu_t)\nabla k]$ is the diffusion term.
   - $G_k + G_{nl} + G_b$ are all production terms.
   - $\rho\beta^* f_{\beta^*}(\omega k - \omega_0 k_0)$ is the dissipation term.
   - S_k is a user defined source term.

2. The transport equation for the specific dissipation rate ω

$$\frac{\partial}{\partial t}(\rho\omega) + \nabla \cdot (\rho\omega \bar{\boldsymbol{v}}) = \nabla \cdot [(\mu + \sigma_\omega \mu_t)\nabla\omega] + G_\omega + D_\omega - \rho\beta f_\beta(\omega^2 - \omega_0^2) + S_\omega$$

   In which:
   - $\frac{\partial}{\partial t}(\rho\omega)$ is the transient term.
   - $\nabla \cdot (\rho\omega \bar{\boldsymbol{v}})$ is the convection term.
   - $\nabla \cdot [(\mu + \sigma_\omega \mu_t)\nabla\omega]$ is the diffusion term.
   - G_ω is the production term.
   - D_ω is a cross-diffusion term which arises when the k-ε equations are rewritten to the k-ω model.
   - $\rho\beta f_\beta(\omega^2 - \omega_0^2)$ is the dissipation term.
   - S_ω is a user defined source term.

For the production ("G") terms of these two equations is referred to the Star CCM+ user guide. The cross-diffusion term D_ω is given by the equation below.

$$D_\omega = 1.712\rho(1-F_1)\frac{1}{\omega}\nabla\cdot\nabla\omega$$

In this equation the first of two blending functions F_1 appears. It has a value of one near a solid boundary to activate the k-ω mode and a value of zero away from the boundary where the rewritten k-ε mode is used. The first blending function F_1 is given by:

$$F_1 = \tanh\left(\left[\min\left(\max\left(\frac{\sqrt{k}}{0.09\omega z},\frac{500\nu}{z^2\omega}\right),\frac{2k}{z^2 CD_{k\omega}}\right)\right]^4\right)$$

With the cross-diffusion coefficient $CD_{k\omega} = \max\left(\frac{1}{\omega}\nabla k\cdot\nabla\omega, 10^{-20}\right)$

Ones the values for the turbulent kinetic energy k and the specific dissipation rate ω are calculated, the eddy viscosity ν_t can be determined by the formula:

$$\nu_t = \rho k T$$

In which the turbulent time scale T is defined as:

$$T = \min\left(\frac{1}{\max\left(\omega,\frac{SF_2}{0.31}\right)},\frac{0.6}{\sqrt{3}S}\right)$$

In this equation S is the modulus of the mean strain rate tensor. For a boundary layer this parameter is equal to the mean velocity gradient normal to the solid surface. Furthermore the equation to calculate the eddy viscosity includes a limit function. With this limitation the value for the shear stress is restricted in case of adverse-pressure gradient boundary layers, where the production of k can be significantly larger that the dissipation. In this limit function, the second blending function F_2 takes care that the restriction is only active for wall-bounded flows. This blending function is formulated as:

$$F_2 = \tanh\left(\left(\max\left(\frac{2\sqrt{k}}{0.09\omega z},\frac{500\nu}{z^2\omega}\right)\right)^2\right)$$

The model constants of which no numerical value is filled in yet are all dependent of the first blending function F_1. They will be listed below. The equations for the production ("G") terms, the modulus of the mean strain rate tensor S and the modification factors f_{β^*} and f_β can be found in the Star CCM+ user guide. The remaining parameters $\rho, k, \bar{\mathbf{v}}, \mu, \omega$ and z are already defined earlier in this thesis, and therefore can be found in the nomenclature.

Model constants:

- $\beta = -0.0078F_1 + 0.0828$
- $\sigma_k = -0.15F_1 + 1$
- $\sigma_\omega = -0.356F_1 + 0.856$

IDDES formulation

The modelling activities in this thesis are done according to the Improved Delayed Detached Eddy Simulation (IDDES) formulation proposed by Shur et al. (2008). The mean adjustment compared to the original RANS equations is that in the IDDES formulation, the specific dissipation rate ω is replaced by $\tilde{\omega}$, which is defined as:

$$\tilde{\omega} = \frac{\sqrt{k}}{0.09 l_{HYBRID} f_{\beta^*}}$$

The equations for l_{HYBRID} and f_{β^*} can be found in the Star CCM+ user guide, together with some extra model coefficients.

In the IDDES model also the formulation for the mesh length scale Δ is adjusted compared to a normal DES. The mesh length scale or subgrid length scale is length scale used for the determination of the eddy viscosity μ_t when the model is in LES mode. Furthermore this length scale is important for the determination if the model switches to the LES mode or stays in the default Unsteady RANS mode, as explained in section 2.2.2. The mesh length scale used for the IDDES is determined by:

$$\Delta_{IDDES} = \min(\max(0.15d, 0.15\Delta, \Delta_{min}), \Delta)$$

where:

- Δ is equal to the longest edge of the grid cell under consideration
- Δ_{min} is the smallest centre-to-centre distance with one of the neighbouring cells

Because of this adjusted subgrid length-scale, a proper switch to the LES mode can be made already within the boundary layer.

D

Velocity profiles

For the performances of a DES, the grid size plays a special role as elaborated in section 2.2.6. The importance of an appropriate mesh can nicely be visualised in the results of the simulation for the velocity and the turbulent kinetic energy. This is why in this evaluation of the modelling results special attention will be paid to effect of mesh refinement. The process of refining the grid itself is described in section 3.2.2.

In these figures, the height with respect to the mean bed level z_{mbl} is made dimensionless by the initial water depth h of 0.375 m. In all figure, a small mistake is made in the ratio $\frac{z}{h}$. The profiles should be shifted downwards, but the shapes will be exactly similar. Due to time constraints, no new figures are made as the results are not influenced by this small inaccuracy. The flow velocity in x-direction u_x is made dimensionless by the mean flow velocity u_{mean}, determined as:

$$u_{mean} = \frac{Q}{A} \approx 0.505[m/s]$$

The purple lines of the 0.005m-mesh are the final result used in this thesis. They are equal to the blue velocity profiles of figure 3.10. The green stars are in accordance with the red dots of figure 3.10.

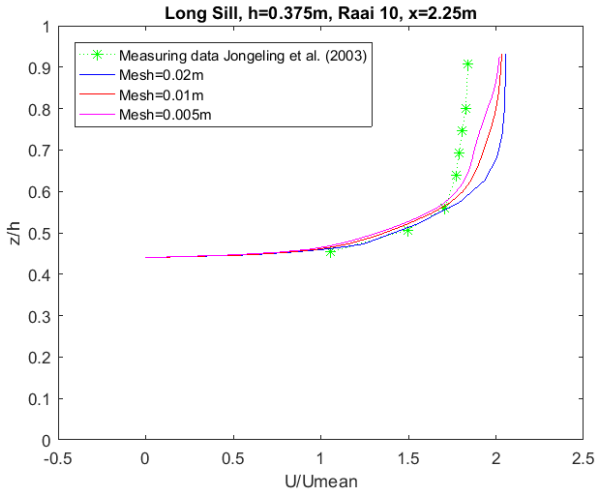

Figure D.1: u_x profile cross-section 10

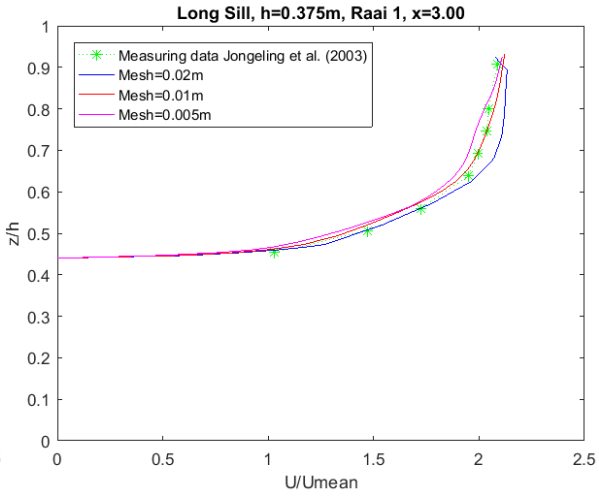

Figure D.2: u_x profile cross-section 1

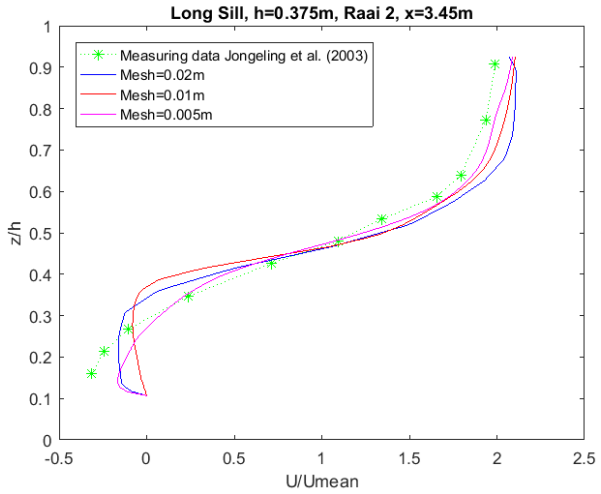

Figure D.3: u_x profile cross-section 2

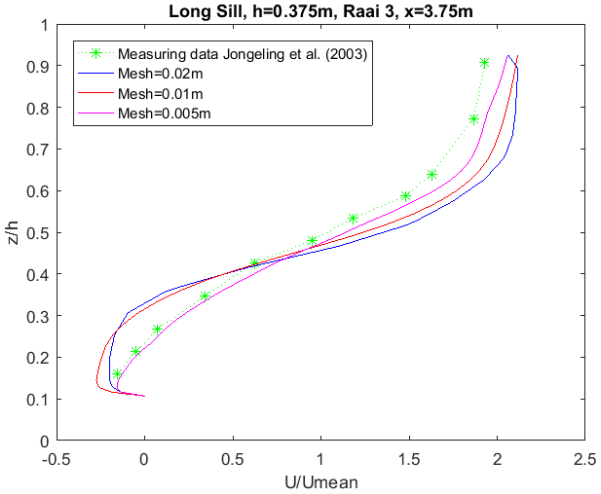

Figure D.4: u_x profile cross-section 3

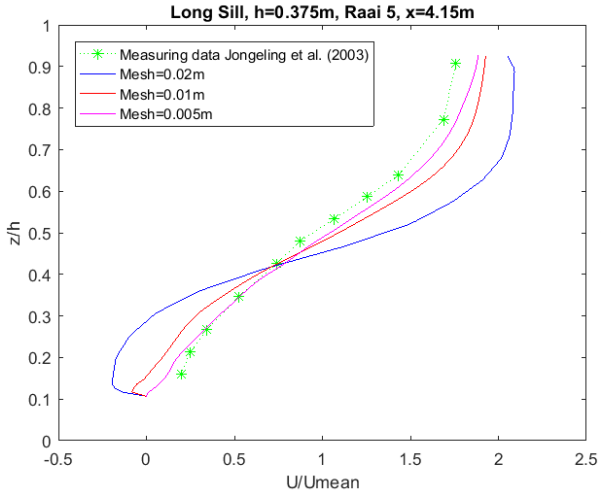

Figure D.5: u_x profile cross-section 5

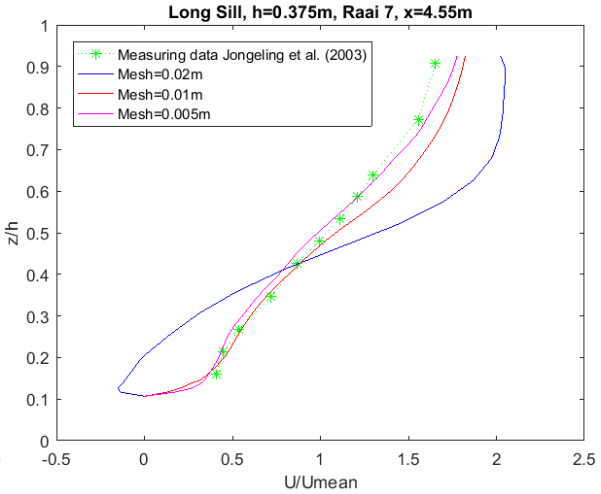

Figure D.6: u_x profile cross-section 7

Mesh=0.02 m (Blue lines)
Starting with the coarsest mesh of 0.02 m, large differences are present between the simulated and measured velocities. Especially at the end of the measuring area, the velocity profile of the measurements is a lot steeper than the simulated one. Apparently after the sill in reality the energy is redistributed faster over the water depth than in the simulation. Turbulent eddies are largely responsible for this redistribution of energy and therefore the flatter velocity profile of the simulation can be interpreted as an under-prediction of the turbulent kinetic energy. This makes sense as the model is solving the main flow in LES-mode, but the grid is not yet fine enough to resolve all energy containing eddies. In this simulation, turbulent scales to a size of about 0.04 m are resolved. For the smaller scales a subgrid-scale model is assumed, which probably under-predicts the turbulence intensity. This shortcoming is observed earlier, as described in Rodi et al. (2013).

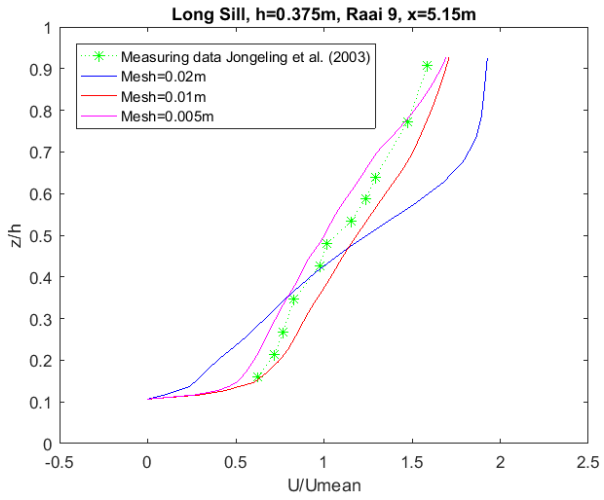

Figure D.7: u_x profile cross-section 9

Mesh=0.01 m (Red lines)
A significant improvement can be observed for the mesh refinement to 0.01 m. Especially at the end of the measuring area (figure D.5 to D.7), the steepness of the simulated velocity profiles are now in much better agreement with the measurements than those obtained with the 0.02m-mesh. In LES-mode the resolved turbulent scales are proportional to two times the grid size. The difference between the 0.01m-mesh and the 0.02m-mesh is therefore that now also the turbulent scales of about 0.02 m to 0.04 m are resolved. The large difference in steepness of the blue and red velocity profiles indicate that eddies of these sizes have a large contribution to the redistribution of energy in this area.

In the cross-sections of figure D.3 and D.4 closer to the downstream end of the sill, the refinement from the 0.02 m to the 0.01m-mesh has less impact on the results. Here the measured velocity profiles are still a lot steeper than the simulated ones. Probably the energy containing eddies are smaller in this area and therefore not resolved yet by the 0.01m-grid. This is plausible as the turbulent scales grow from the point of separation on, with a magnitude approximately equal to the growth of the mixing layer.

Mesh=0.005 m (Purple lines)
Again the velocity profiles for the 0.005m-mesh are in better agreement with the measurements than those of the coarser meshes. Especially in the area close to the sill, the mesh refinement significantly improves the results. The steepness of the purple lines are now nearly equal to those of the measurements and the near-bottom velocities close to the sill are reproduced much better for the 0.005m-mesh compared to the other meshes. This means that again important energy containing turbulent scales are resolved by the 0.005m-grid which were not yet resolved for the coarser meshes.

Furthermore the simulated purple lines are sometimes at the left and sometimes at the right of the measured green profiles. Especially at the upper part of figure D.1 and D.2 the differences between the simulated and measured velocities are remarkable. For these cross-sections one would expect simulated results that have a similar ratio to the measurements, as except for acceleration no deviant flow features are present on top of the sill. Nevertheless the simulated velocities are larger than the measured results at cross-section 10, while the simulated velocities at cross-section 1 are lower than the measured ones. A possible declaration for this is that the simulated water levels are not in agreement with those of the experiment. Due to the flow acceleration above the sill, the water level will lower. Possibly the water level at cross-section 10 is simulated a bit too low, which results in too high flow velocities and the water level at cross-section 1 is simulated in quite good agreement with reality.

E

Turbulent kinetic energy profiles

For convenience the modelled TKE k_{RANS} is visualised separately from the resolved TKE k_{LES}. Again the results are given for several grid sizes to map the development of the TKE profiles in case mesh refinements are applied. The height with respect to the bottom of the flume z is made dimensionless by the initial water depth h of the experiment, being 0.375 m. In all figure, a small mistake is made in the ratio $\frac{z}{h}$. The profiles should be shifted downwards, but the shapes will be exactly similar. Due to time constraints, no new figures are made as the results are not influenced by this small inaccuracy.

The TKE k is made dimensionless by the squared shear velocity $(u_*)^2$. For this purpose a value of 0.05 m/s is assumed for u_*, based on some numbers observed in the model.

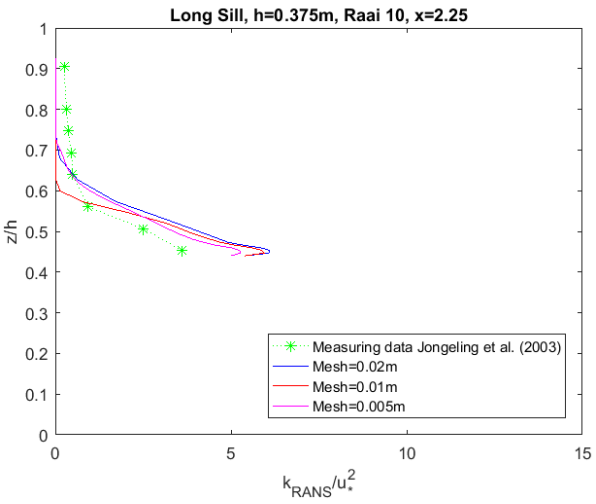

Figure E.1: k_{RANS} profile cross-section 10

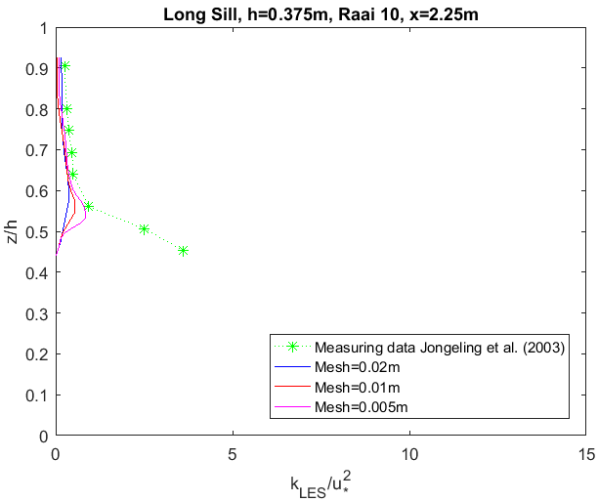

Figure E.2: k_{LES} profile cross-section 10

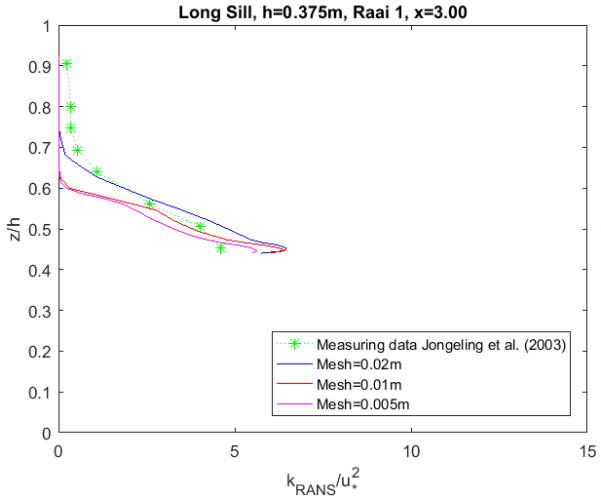

Figure E.3: k_{RANS} profile cross-section 1

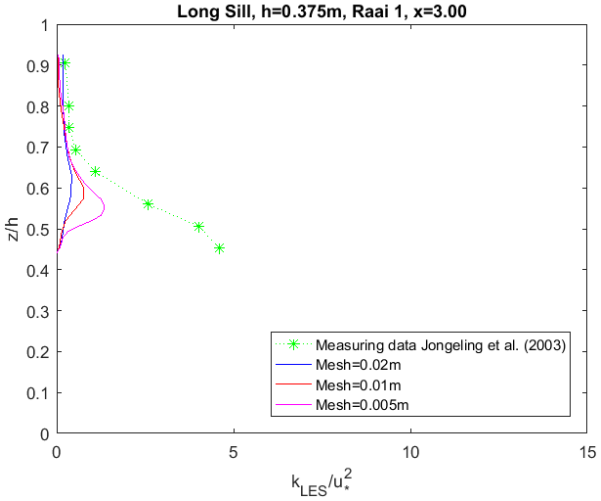

Figure E.4: k_{LES} profile cross-section 1

On top of the sill

Due to the large difference between the TKE profiles on top of the sill and the rest of the cross-sections, first figure E.1 and E.4 will be discussed here separately. On top of the sill, a relatively large part is of the TKE profile is modelled compared to the other cross-sections after the sill. The near-bottom area has a significant amount of k_{RANS}, and k_{LES} is present higher in the water column. This is in agreement with the distribution of the RANS- and LES-regions depicted in figure 3.6.

Furthermore a small area can be detected in which k_{RANS} and k_{LES} are in the same order of magnitude. This is the blending area, created to avoid mismatches between the two regions. When adding the k_{RANS} and k_{LES} profiles up, it shows that k_{tot} on top of the sill is in good agreement with the measured TKE profiles. Especially from the k_{LES}-plots, one can see that the simulated TKE profiles on top of the sill improve when the grid size is decreased.

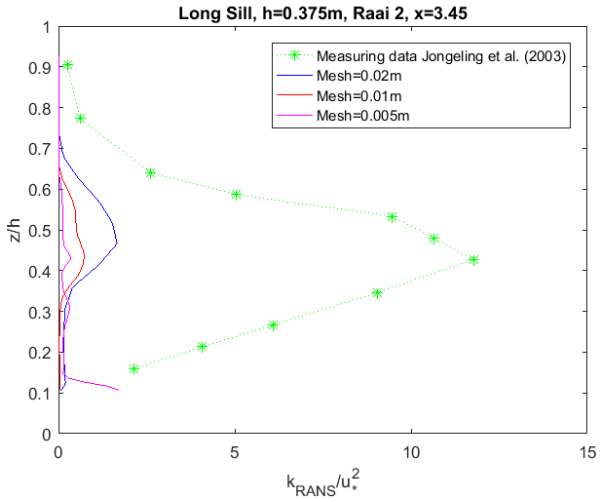

Figure E.5: k_{RANS} profile cross-section 2

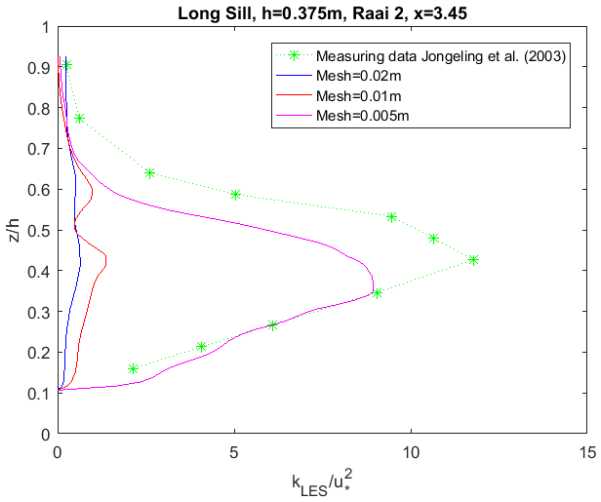

Figure E.6: k_{LES} profile cross-section 2

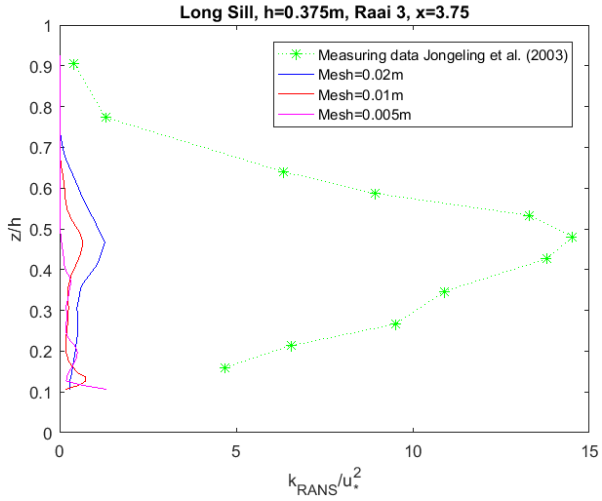

Figure E.7: k_{RANS} profile cross-section 3

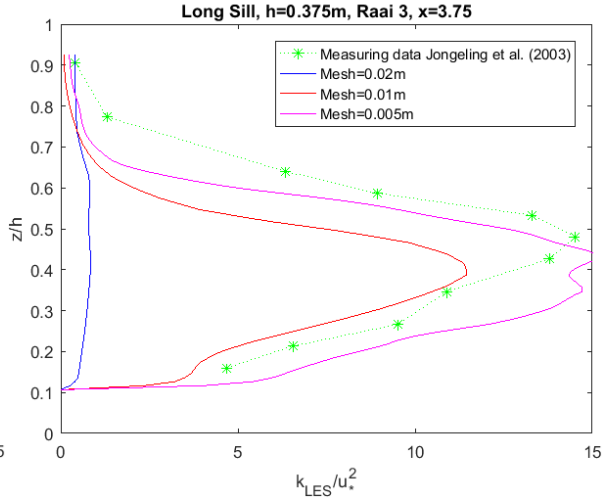

Figure E.8: k_{LES} profile cross-section 3

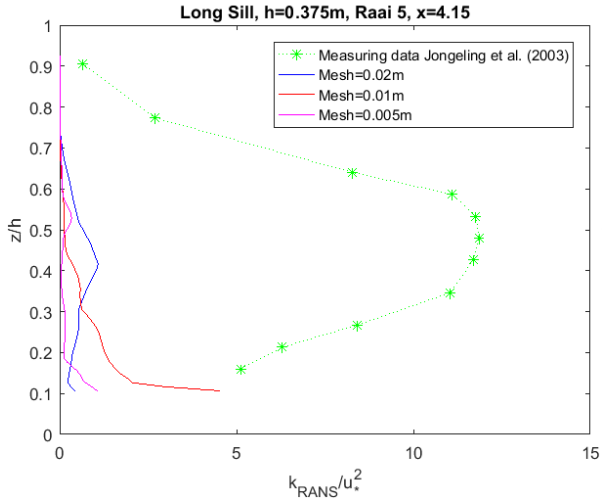

Figure E.9: k_{RANS} profile cross-section 5

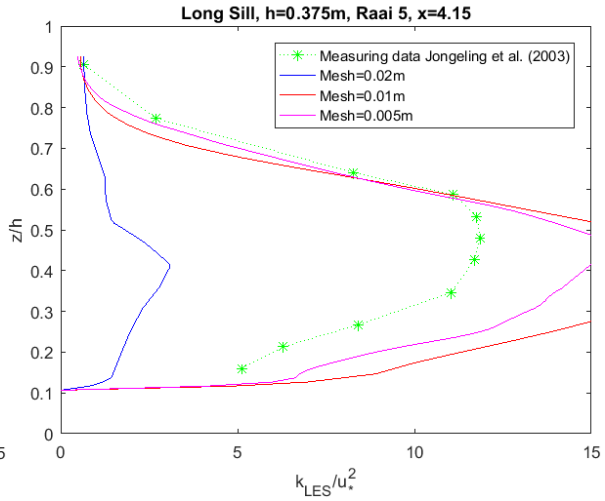

Figure E.10: k_{LES} profile cross-section 5

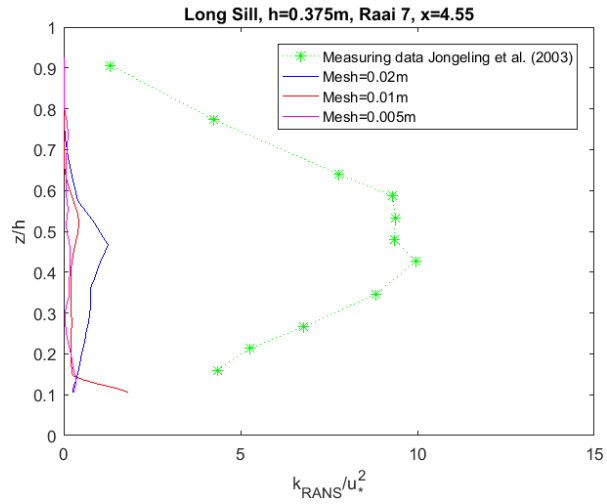

Figure E.11: k_{RANS} profile cross-section 7

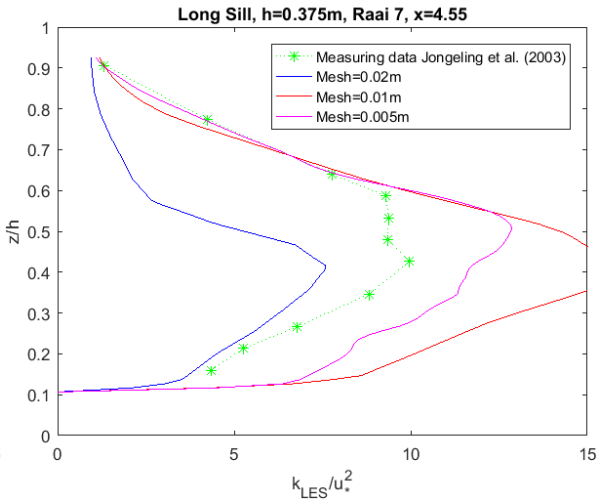

Figure E.12: k_{LES} profile cross-section 7

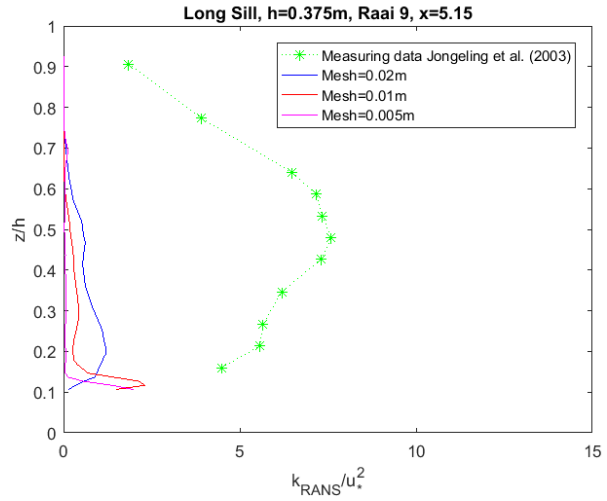

Figure E.13: k_{RANS} profile cross-section 9

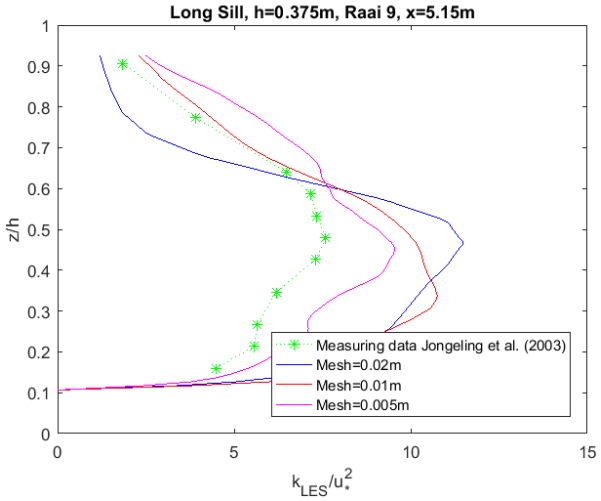

Figure E.14: k_{LES} profile cross-section 9

k_{RANS} after the sill
After sill only very close to the bottom sometimes an increased value for k_{RANS} can be detected. For these TKE profiles this indicates that only this part of the flow is solved in RANS-mode, which is in agreement with the thin RANS-region described in section 3.2.2.

For the coarsest mesh of 0.02 m (blue lines), also halfway the cross-sections some higher values of k_{RANS} are visible, especially in figure E.5 and E.7 closest to the downstream end of the sill. Apparently the 0.02m-grid size is, relative to the turbulent scales, so coarse that the model is partly modelling the turbulence in RANS-mode. An explanation for this could be that just after the point of separation the turbulent scales are still very small, whereby the model is near the limit of the switch between RANS- and LES-mode.

k_{LES} after the sill
By far the largest part of the flow depth is solved by the LES-formulations of the SST k-ω model. The resolved turbulent scales of the LES-region are directly dependent on the grid size. The effects of mesh refinement should therefore be visible in the k_{LES} profiles, as long as the inertial subrange of the energy density spectrum is not yet reached.

To start with the blue lines of the coarsest mesh size of 0.02 m, it appears that the energy containing eddies just behind the sill are smaller than the resolved turbulent scales. In the cross-sections of figure E.6 and E.8 almost no k_{LES} is reproduced. Further downstream the eddies are increasing in size, as the mixing layer is expanding. Therefore the energy containing eddies further downstream do have a magnitude of 0.04 m or larger, which are resolved for the 0.02m-mesh. This is why the amount of resolved k_{LES} increases together with the increasing distance from the point of flow separation. At the last cross-section (E.14) (already) an over-prediction of the simulated TKE is observed, which probably indicates that a significant amount of the energy containing turbulent scales are resolved by the 0.02m-grid.

For the red lines of the 0.01m-mesh, the same phenomena can be observed but now for the cross-sections closer to the downstream end of the sill. The larger the distance from the point of separation, the more important the turbulent scales become that are resolved for the chosen grid size. Again the model over-predicts the TKE at some of the cross-section, but now at cross-section E.10 and E.12. At the last cross-section of the measuring area (E.14), the mesh refinement results in a different distribution of k_{LES} over the water depth, which seems to be a small improvement.

The final mesh refinement to a 0.005 m grid size results in an improvement for all the TKE-profiles. In the cross-section nearest to the sill (E.6), for the first time some important turbulent scales are resolved. One cross-section further downstream (E.8), the mesh refinement causes an over-prediction of k_{LES}. In the other three downstream cross-sections (E.10, E.12 and E.14), a clear decay in the over-prediction of the TKE can be observed. The increase in the amount of resolved turbulent scales, result in a better representation of the TKE profiles for these cross-sections.

F

Quantitative comparison $u_{x,meas}$ and $u_{x,sim}$

z_{meas} $[m]$	$u_{x,meas}$ $[m/s]$	$u_{x,sim}$ $[m/s]$	Δ_{u_x} $[m/s]$
0.17	0.532	0.387	-0.145
0.19	0.755	0.693	-0.062
0.21	0.863	0.839	-0.024
0.24	0.895	0.927	0.032
0.26	0.904	0.946	0.042
0.28	0.914	0.964	0.050
0.30	0.923	0.986	0.063
0.34	0.930	1.018	0.088

Table F.1: Quantitative comparison u_x cross-section 10

z_{meas} $[m]$	$u_{x,meas}$ $[m/s]$	$u_{x,sim}$ $[m/s]$	Δ_{u_x} $[m/s]$
0.17	0.520	0.383	-0.137
0.19	0.744	0.681	-0.063
0.21	0.872	0.834	-0.038
0.24	0.986	0.953	-0.033
0.26	1.008	0.985	-0.023
0.28	1.030	1.002	-0.028
0.30	1.033	1.023	-0.010
0.34	1.054	1.061	0.007

Table F.2: Quantitative comparison u_x cross-section 1

z_{meas} $[m]$	$u_{x,meas}$ $[m/s]$	$u_{x,sim}$ $[m/s]$	Δ_{u_x} $[m/s]$
0.06	-0.159	-0.080	0.079
0.08	-0.123	-0.049	0.074
0.10	-0.054	-0.005	0.049
0.13	0.120	0.107	-0.013
0.16	0.361	0.317	-0.044
0.18	0.552	0.541	-0.011
0.20	0.678	0.744	0.066
0.22	0.836	0.871	0.035
0.24	0.906	0.941	0.035
0.29	0.979	1.004	0.025
0.34	1.005	1.051	0.046

Table F.3: Quantitative comparison u_x cross-section 2

z_{meas} $[m]$	$u_{x,meas}$ $[m/s]$	$u_{x,sim}$ $[m/s]$	Δ_{u_x} $[m/s]$
0.06	-0.077	-0.064	0.013
0.08	-0.026	-0.012	0.014
0.10	0.036	0.058	0.022
0.13	0.173	0.196	0.023
0.16	0.314	0.376	0.062
0.18	0.479	0.523	0.044
0.20	0.596	0.666	0.070
0.22	0.747	0.800	0.053
0.24	0.822	0.898	0.076
0.29	0.943	0.978	0.035
0.34	0.975	1.034	0.059

Table F.4: Quantitative comparison u_x cross-section 3

z_{meas} [m]	$u_{x,meas}$ [m/s]	$u_{x,sim}$ [m/s]	Δ_{u_x} [m/s]
0.06	0.100	0.061	-0.039
0.08	0.126	0.103	-0.023
0.10	0.172	0.166	-0.006
0.13	0.266	0.268	0.002
0.16	0.374	0.398	0.024
0.18	0.441	0.488	0.047
0.20	0.539	0.588	0.049
0.22	0.634	0.685	0.051
0.24	0.724	0.766	0.042
0.29	0.853	0.891	0.038
0.34	0.888	0.948	0.060

Table F.5: Quantitative comparison u_x cross-section 5

z_{meas} [m]	$u_{x,meas}$ [m/s]	$u_{x,sim}$ [m/s]	Δ_{u_x} [m/s]
0.06	0.206	0.185	-0.021
0.08	0.226	0.220	-0.006
0.10	0.272	0.250	-0.022
0.13	0.363	0.325	-0.038
0.16	0.439	0.413	-0.026
0.18	0.501	0.471	-0.030
0.20	0.560	0.542	-0.018
0.22	0.611	0.613	0.002
0.24	0.657	0.677	0.020
0.29	0.786	0.810	0.024
0.34	0.835	0.891	0.056

Table F.6: Quantitative comparison u_x cross-section 7

z_{meas} [m]	$u_{x,meas}$ [m/s]	$u_{x,sim}$ [m/s]	Δ_{u_x} [m/s]
0.06	0.316	0.270	-0.046
0.08	0.363	0.314	-0.049
0.10	0.387	0.346	-0.041
0.13	0.420	0.397	-0.023
0.16	0.493	0.450	-0.043
0.18	0.513	0.492	-0.021
0.20	0.583	0.527	-0.056
0.22	0.624	0.567	-0.057
0.24	0.653	0.611	-0.042
0.29	0.746	0.738	-0.008
0.34	0.802	0.844	0.042

Table F.7: Quantitative comparison u_x cross-section 9

G

Probability Density Functions: Wall Shear Stress

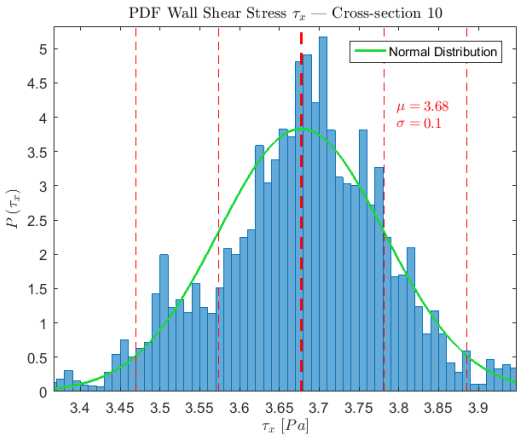

Figure G.1: PDF wall shear stress τ_x cross-section 10

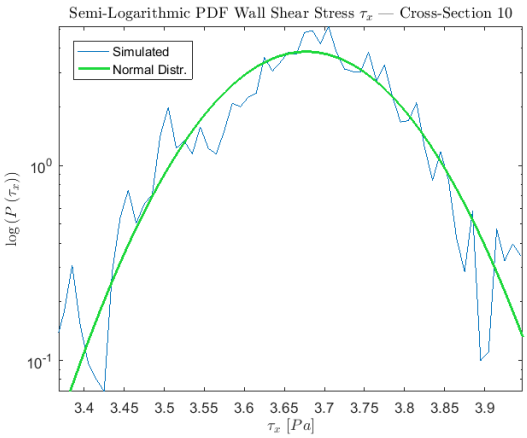

Figure G.2: Semi-logarithmic PDF τ_x cross-section 10

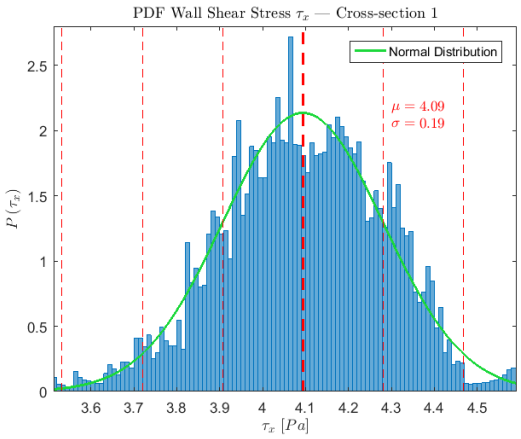

Figure G.3: PDF wall shear stress τ_x cross-section 1

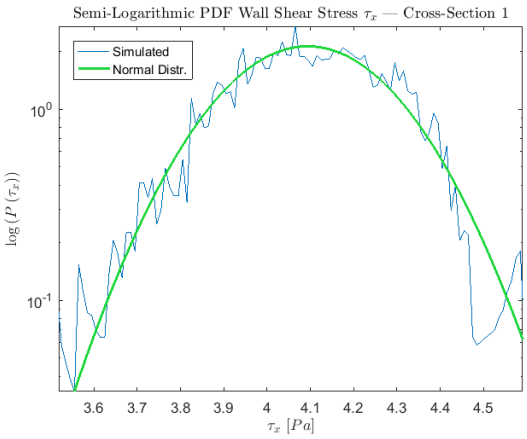

Figure G.4: Semi-logarithmic PDF τ_x cross-section 1

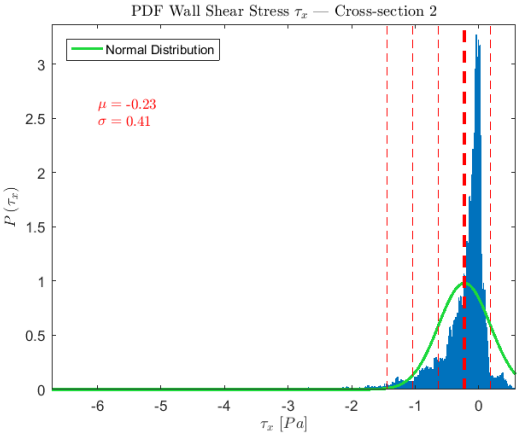

Figure G.5: PDF wall shear stress τ_x cross-section 2

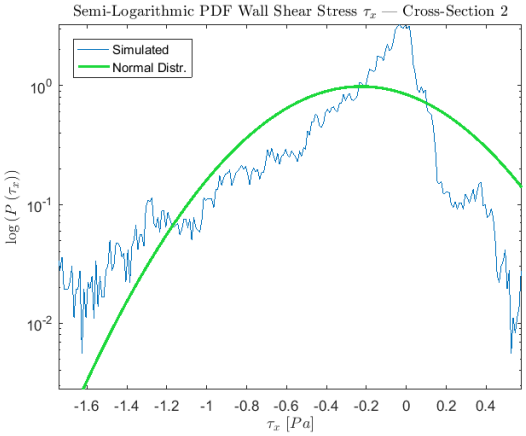

Figure G.6: Semi-logarithmic PDF τ_x cross-section 2

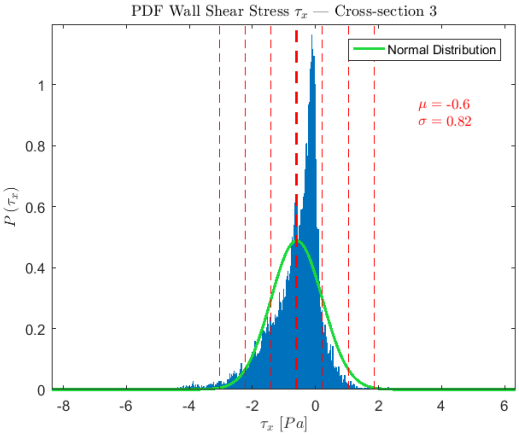

Figure G.7: PDF wall shear stress τ_x cross-section 3

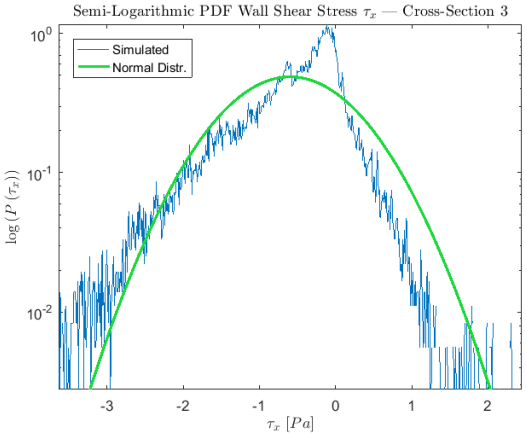

Figure G.8: Semi-logarithmic PDF τ_x cross-section 3

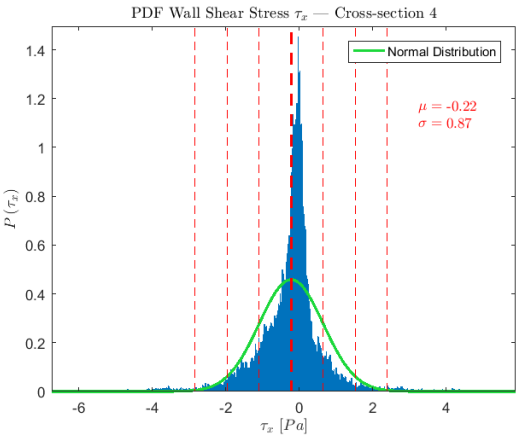

Figure G.9: PDF wall shear stress τ_x cross-section 4

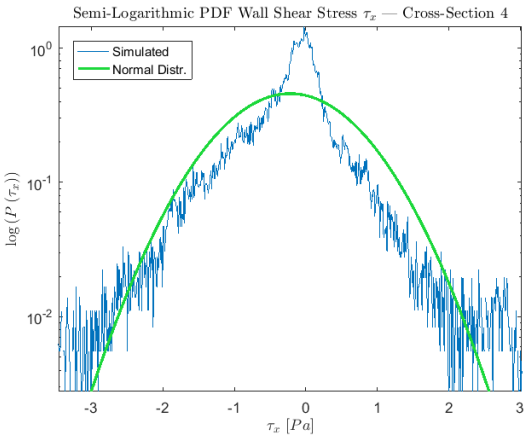

Figure G.10: Semi-logarithmic PDF τ_x cross-section 4

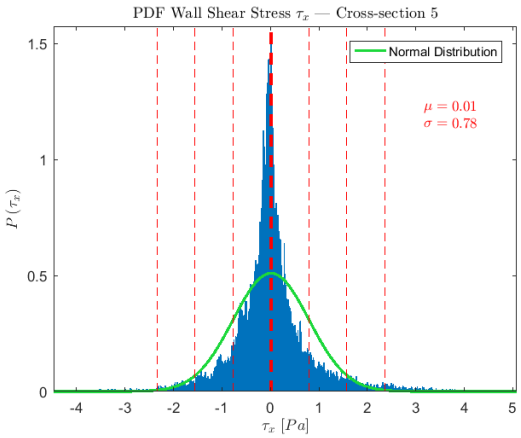

Figure G.11: PDF wall shear stress τ_x cross-section 5

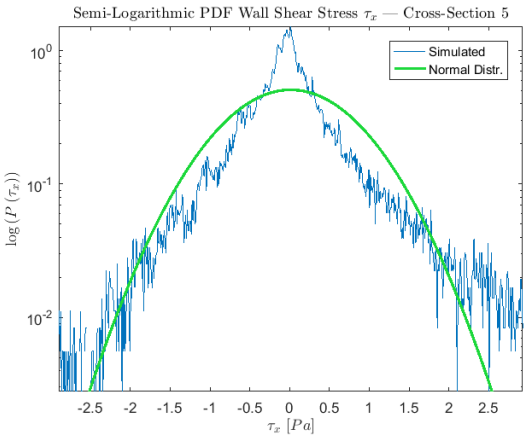

Figure G.12: Semi-logarithmic PDF τ_x cross-section 5

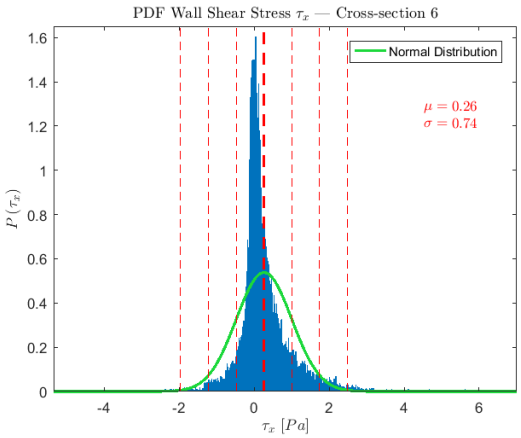

Figure G.13: PDF wall shear stress τ_x cross-section 6

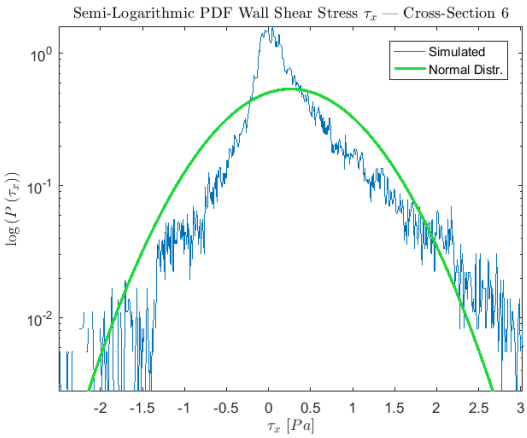

Figure G.14: Semi-logarithmic PDF τ_x cross-section 6

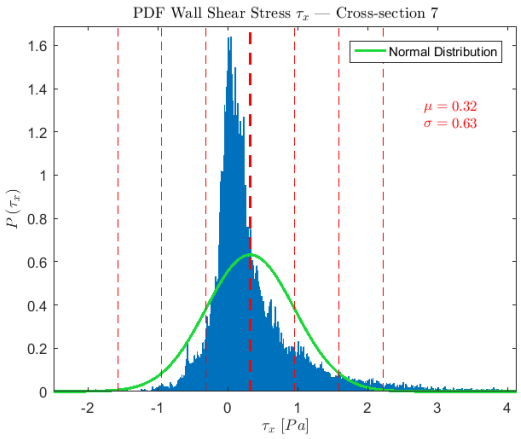

Figure G.15: PDF wall shear stress τ_x cross-section 7

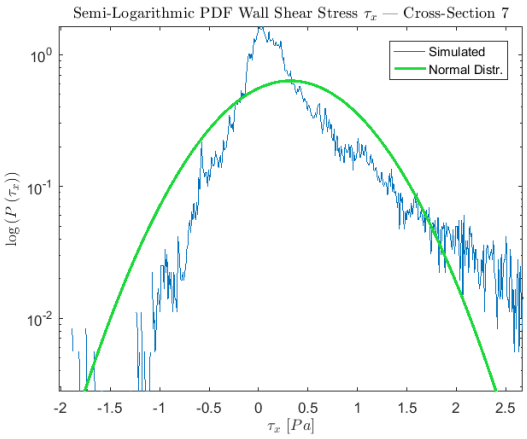

Figure G.16: Semi-logarithmic PDF τ_x cross-section 7

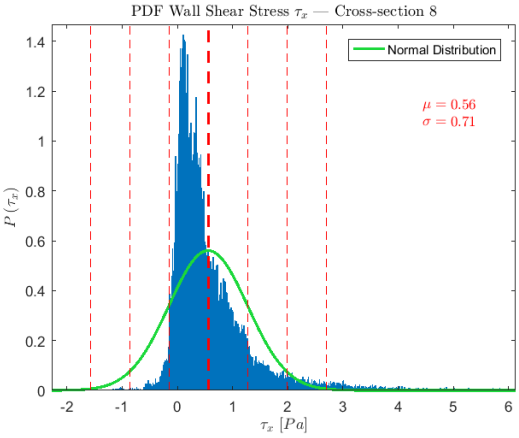

Figure G.17: PDF wall shear stress τ_x cross-section 8

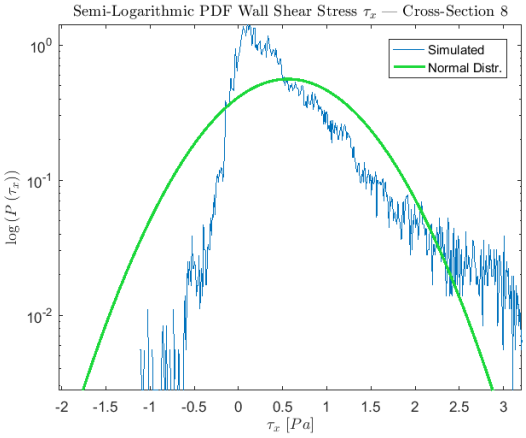

Figure G.18: Semi-logarithmic PDF τ_x cross-section 8

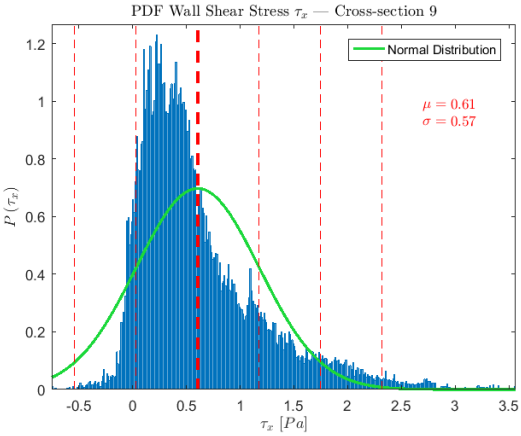

Figure G.19: PDF wall shear stress τ_x cross-section 9

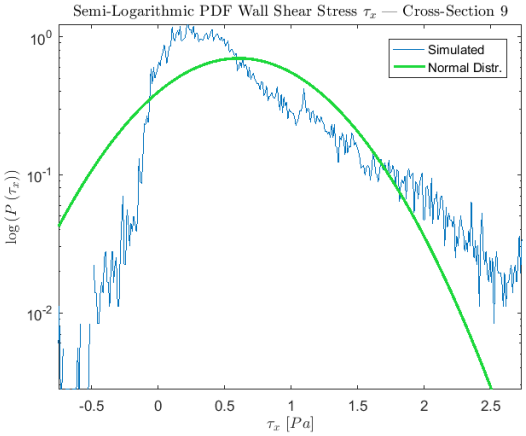

Figure G.20: Semi-logarithmic PDF τ_x cross-section 9

Probability Density Functions: Pressure Gradient

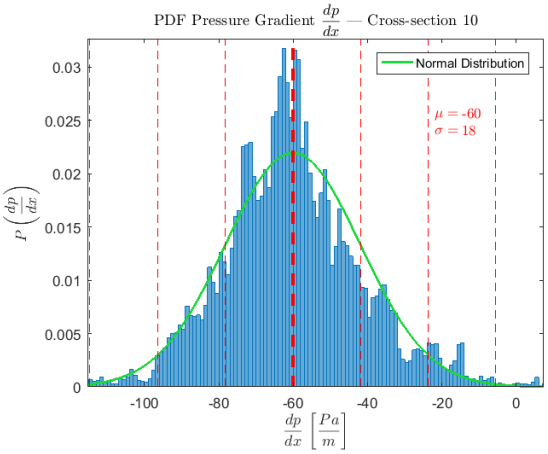

Figure H.1: PDF pressure gradient $\frac{\partial p}{\partial x}$ cross-section 10

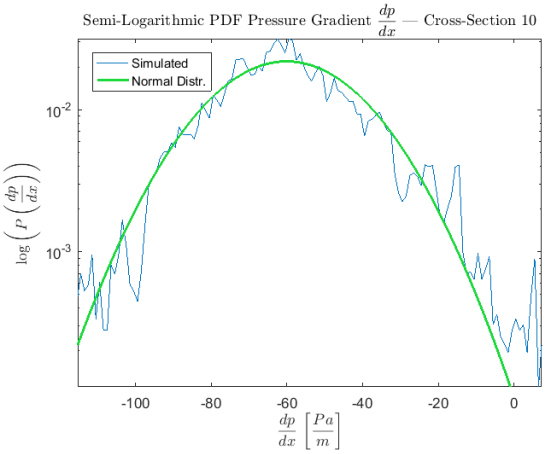

Figure H.2: Semi-logarithmic PDF $\frac{\partial p}{\partial x}$ cross-section 10

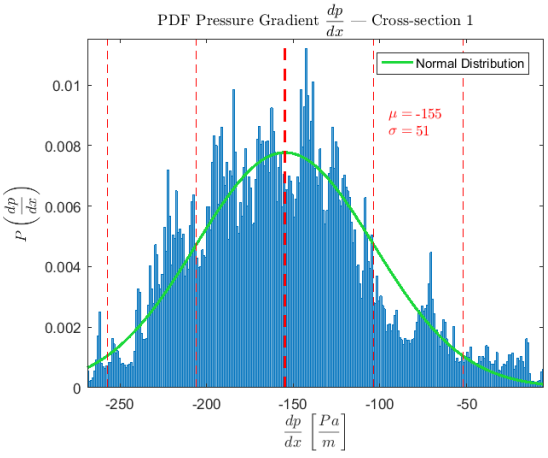

Figure H.3: PDF pressure gradient $\frac{\partial p}{\partial x}$ cross-section 1

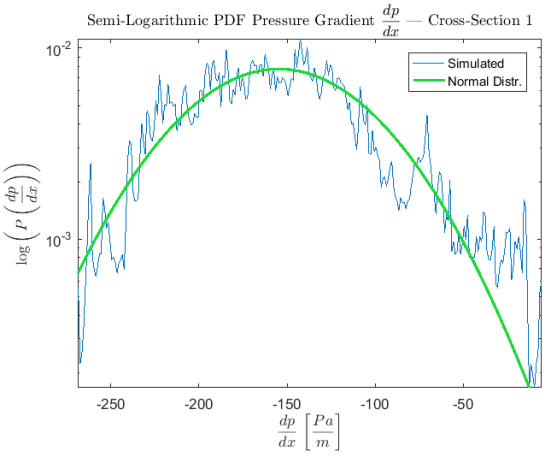

Figure H.4: Semi-logarithmic PDF $\frac{\partial p}{\partial x}$ cross-section 1

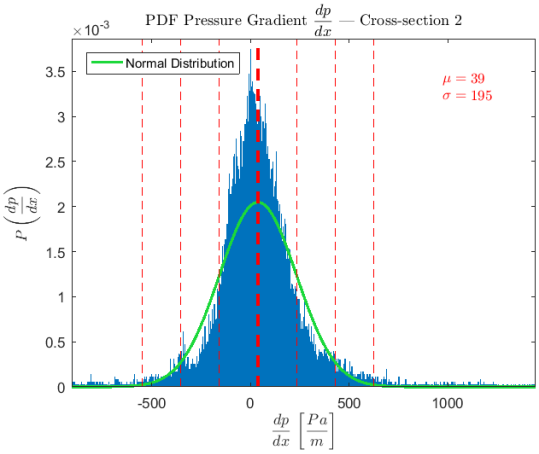

Figure H.5: PDF pressure gradient $\frac{\partial p}{\partial x}$ cross-section 2

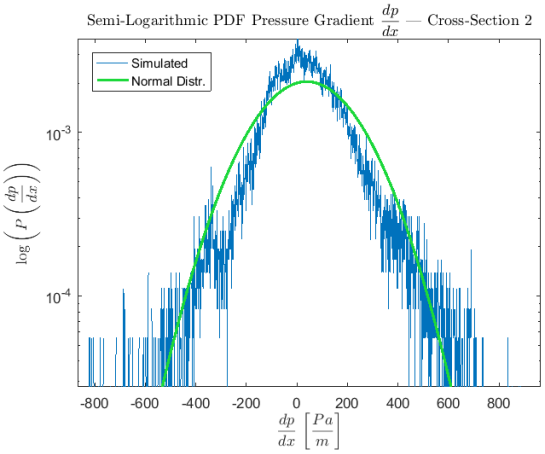

Figure H.6: Semi-logarithmic PDF $\frac{\partial p}{\partial x}$ cross-section 2

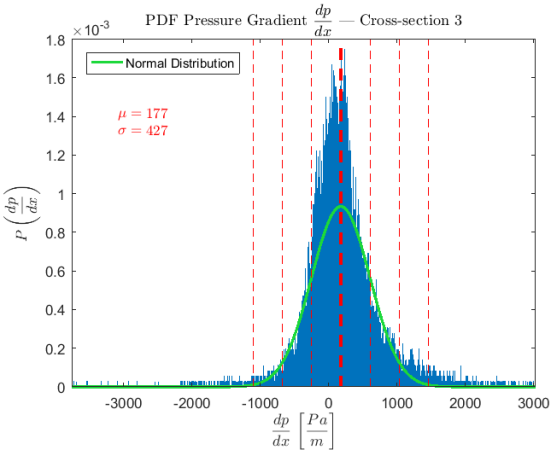

Figure H.7: PDF pressure gradient $\frac{\partial p}{\partial x}$ cross-section 3

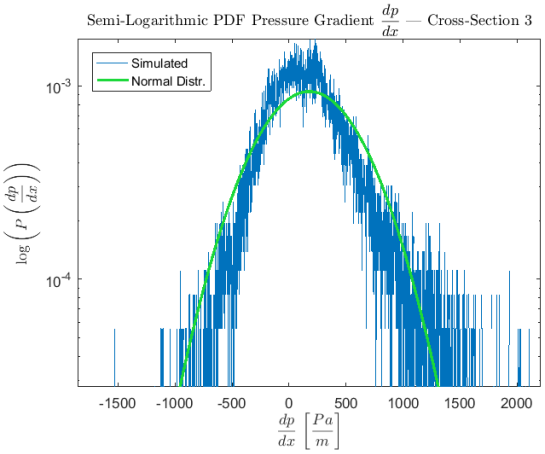

Figure H.8: Semi-logarithmic PDF $\frac{\partial p}{\partial x}$ cross-section 3

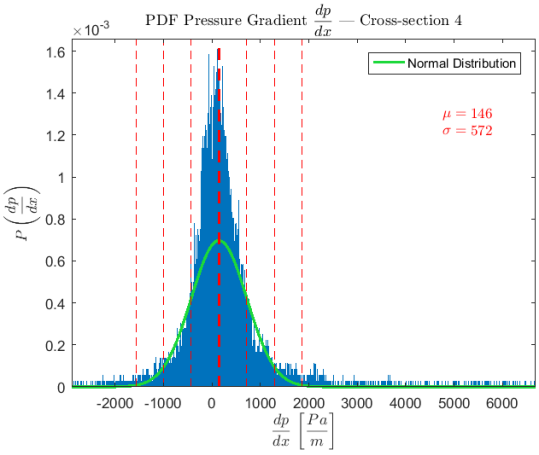

Figure H.9: PDF pressure gradient $\frac{\partial p}{\partial x}$ cross-section 4

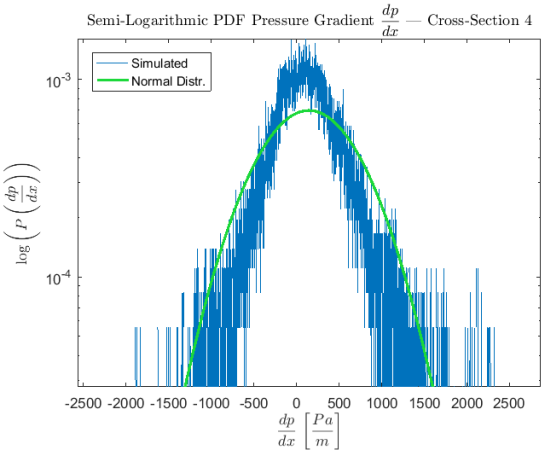

Figure H.10: Semi-logarithmic PDF $\frac{\partial p}{\partial x}$ cross-section 4

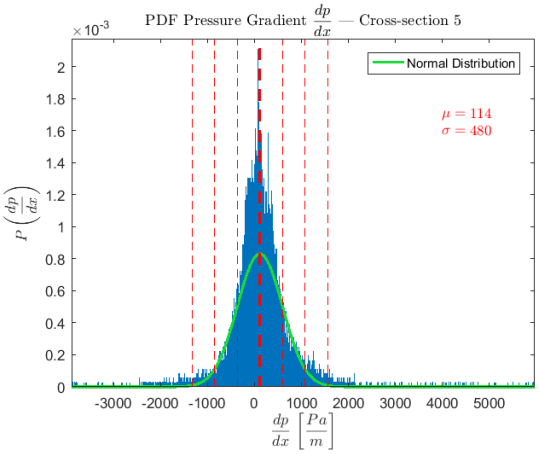

Figure H.11: PDF pressure gradient $\frac{\partial p}{\partial x}$ cross-section 5

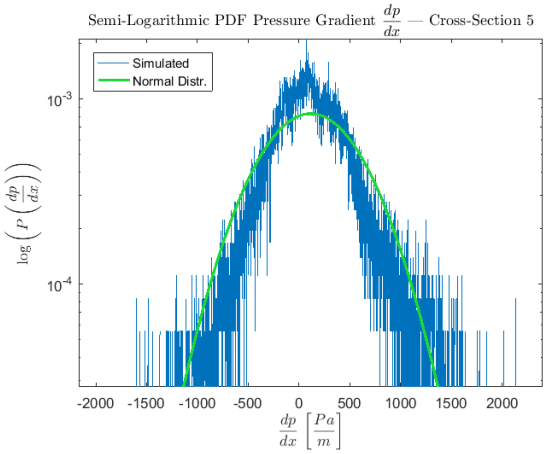

Figure H.12: Semi-logarithmic PDF $\frac{\partial p}{\partial x}$ cross-section 5

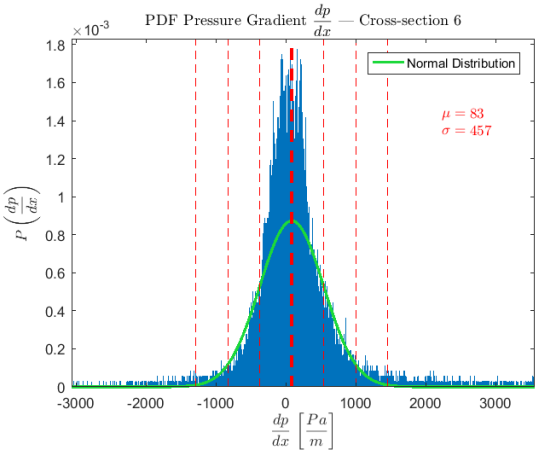

Figure H.13: PDF pressure gradient $\frac{\partial p}{\partial x}$ cross-section 6

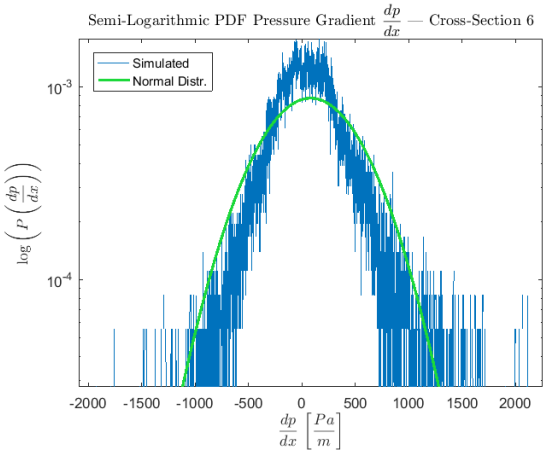

Figure H.14: Semi-logarithmic PDF $\frac{\partial p}{\partial x}$ cross-section 6

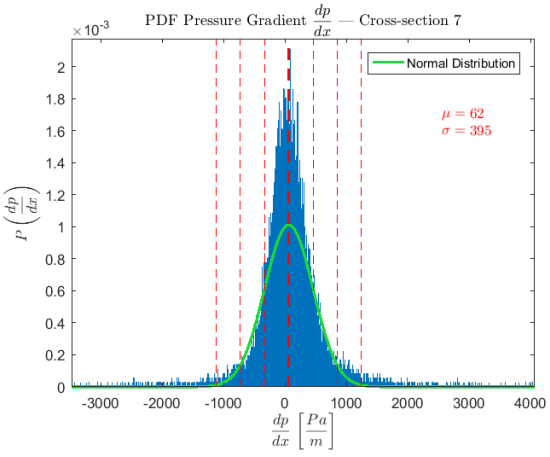

Figure H.15: PDF pressure gradient $\frac{\partial p}{\partial x}$ cross-section 7

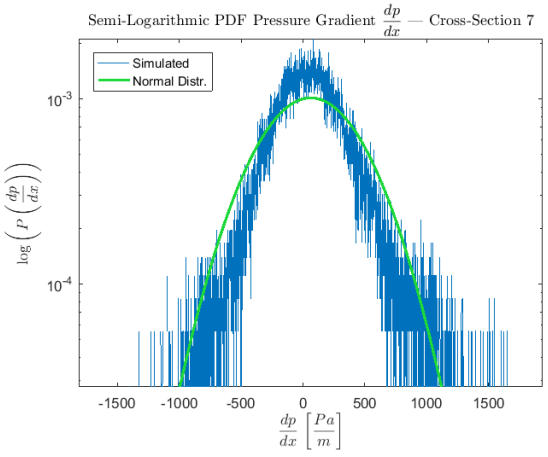

Figure H.16: Semi-logarithmic PDF $\frac{\partial p}{\partial x}$ cross-section 7

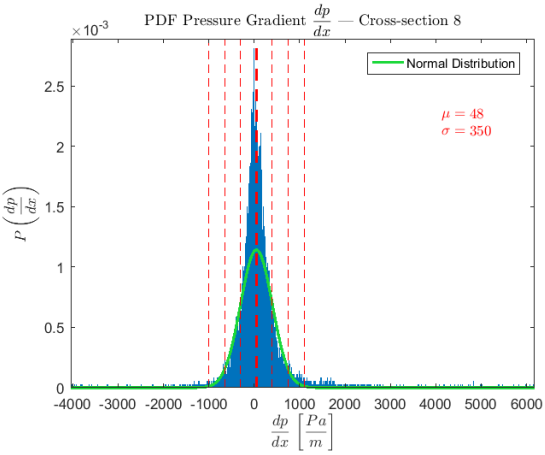

Figure H.17: PDF pressure gradient $\frac{\partial p}{\partial x}$ cross-section 8

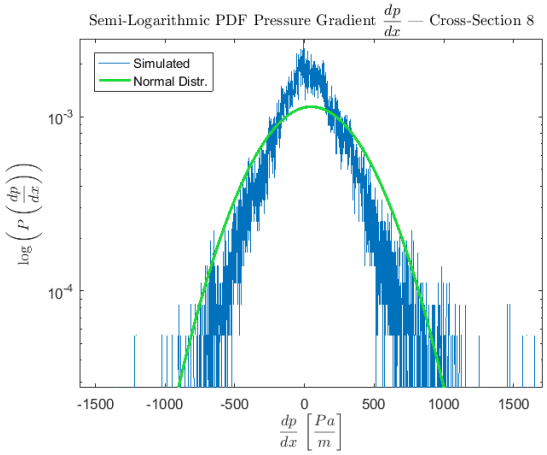

Figure H.18: Semi-logarithmic PDF $\frac{\partial p}{\partial x}$ cross-section 8

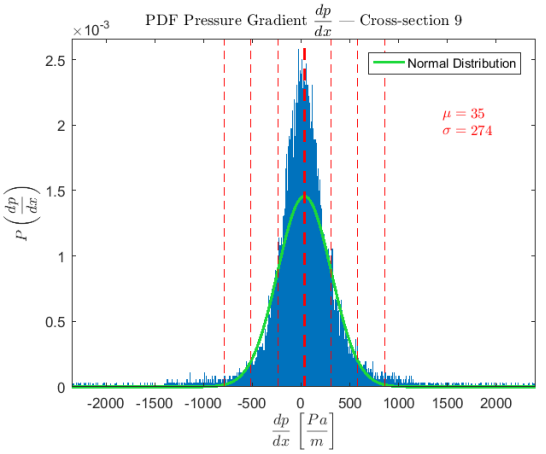

Figure H.19: PDF pressure gradient $\frac{\partial p}{\partial x}$ cross-section 9

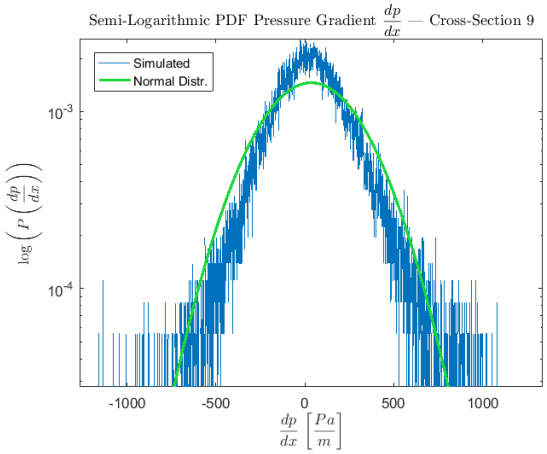

Figure H.20: Semi-logarithmic PDF $\frac{\partial p}{\partial x}$ cross-section 9

Cumulative Density Functions: Wall Shear Stress

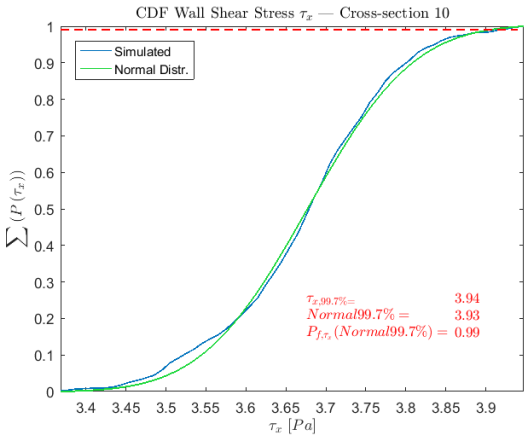

Figure I.1: CDF wall shear stress τ_x cross-section 10

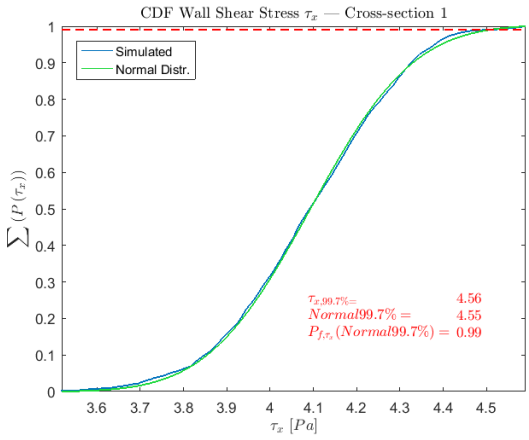

Figure I.2: CDF wall shear stress τ_x cross-section 1

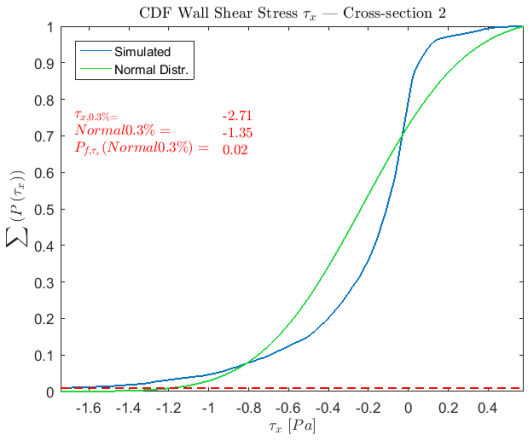

Figure I.3: CDF wall shear stress τ_x cross-section 2

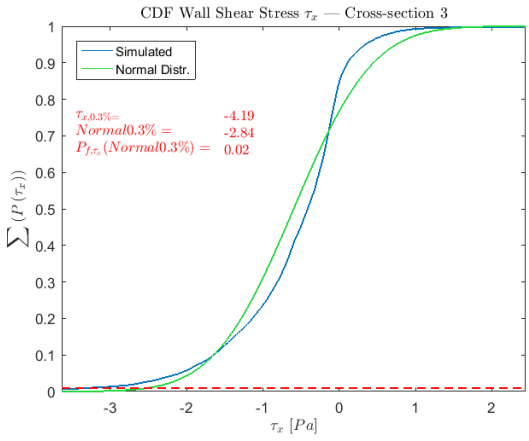

Figure I.4: CDF wall shear stress τ_x cross-section 3

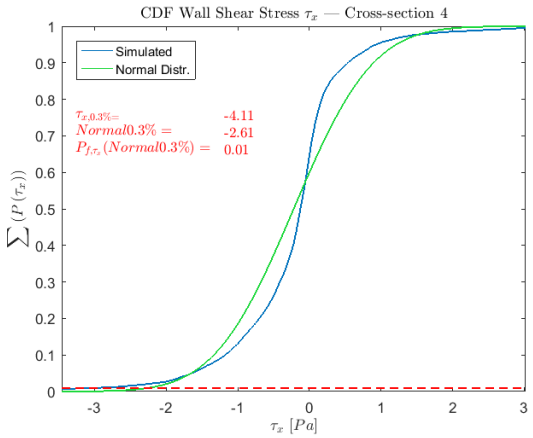

Figure I.5: CDF wall shear stress τ_x cross-section 4

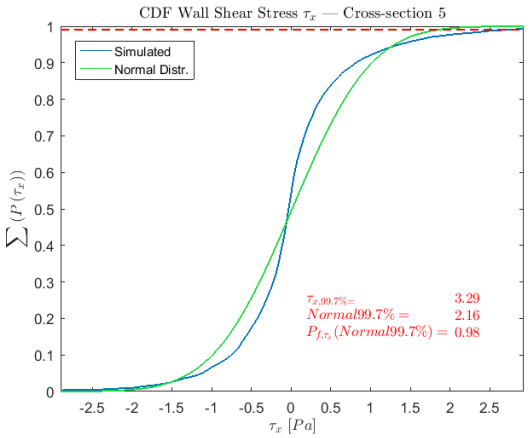

Figure I.6: CDF wall shear stress τ_x cross-section 5

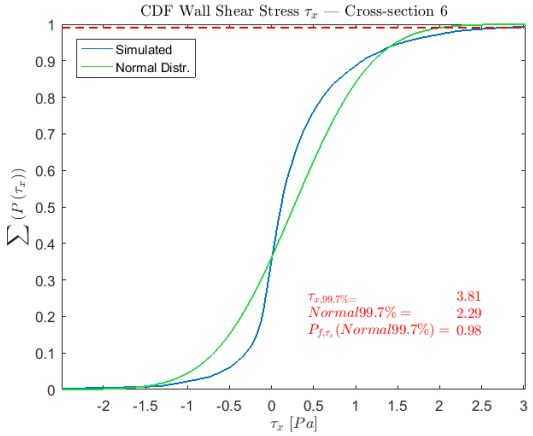

Figure I.7: CDF wall shear stress τ_x cross-section 6

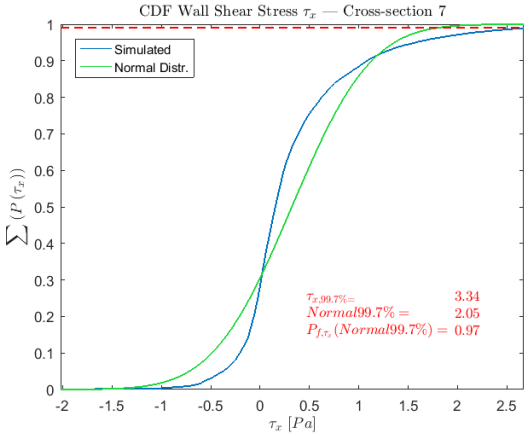

Figure I.8: CDF wall shear stress τ_x cross-section 7

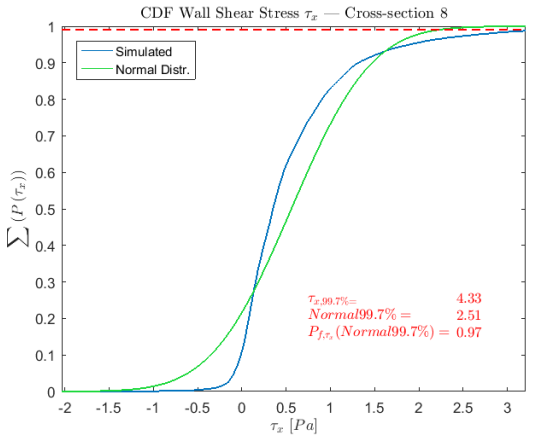

Figure I.9: CDF wall shear stress τ_x cross-section 8

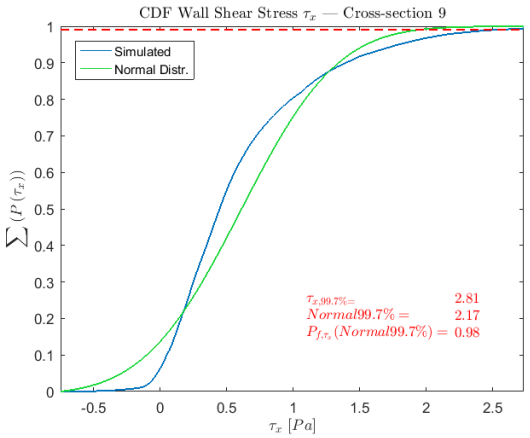

Figure I.10: CDF wall shear stress τ_x cross-section 9

J

Cumulative Density Functions: Pressure Gradient

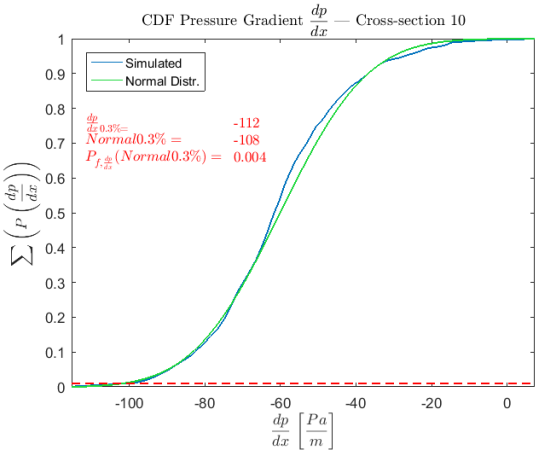

Figure J.1: CDF pressure gradient $\frac{\partial p}{\partial x}$ cross-section 10

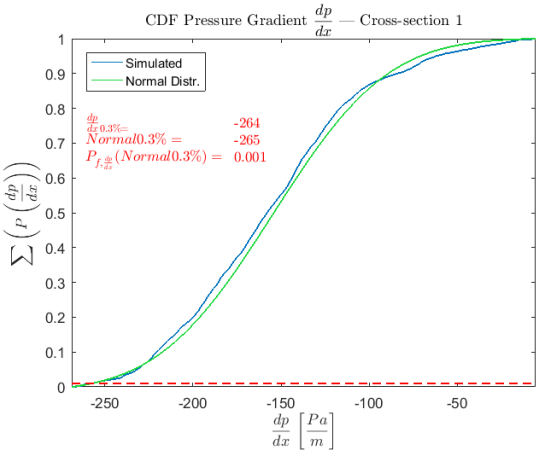

Figure J.2: CDF pressure gradient $\frac{\partial p}{\partial x}$ cross-section 1

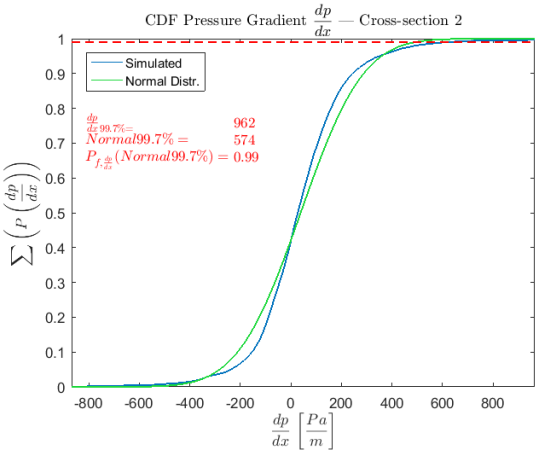

Figure J.3: CDF pressure gradient $\frac{\partial p}{\partial x}$ cross-section 2

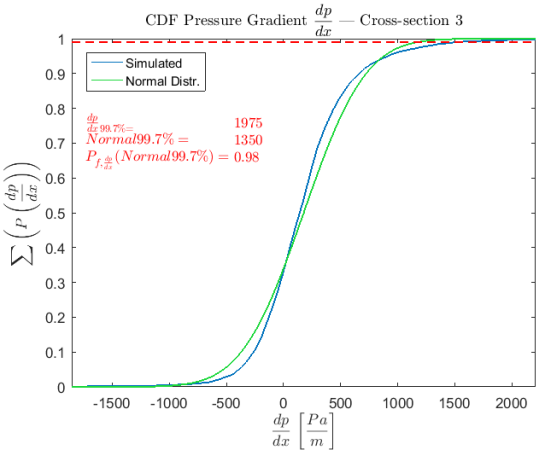

Figure J.4: CDF pressure gradient $\frac{\partial p}{\partial x}$ cross-section 3

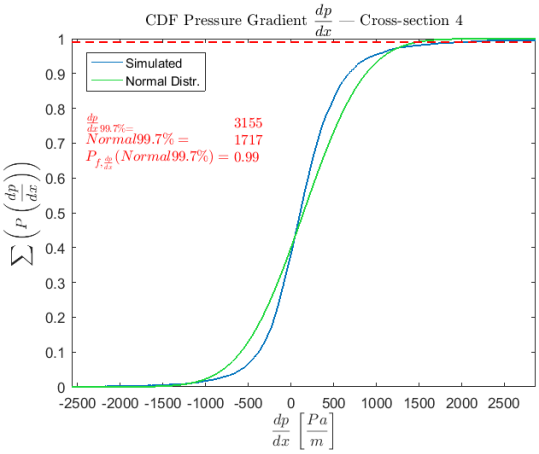

Figure J.5: CDF pressure gradient $\frac{\partial p}{\partial x}$ cross-section 4

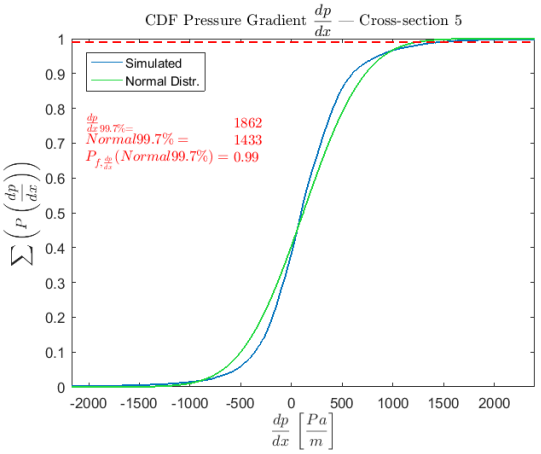

Figure J.6: CDF pressure gradient $\frac{\partial p}{\partial x}$ cross-section 5

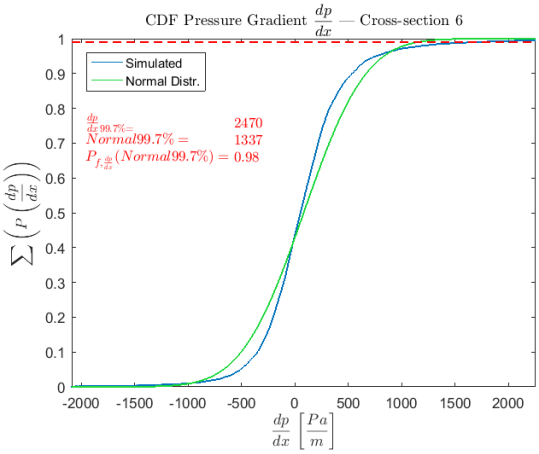

Figure J.7: CDF pressure gradient $\frac{\partial p}{\partial x}$ cross-section 6

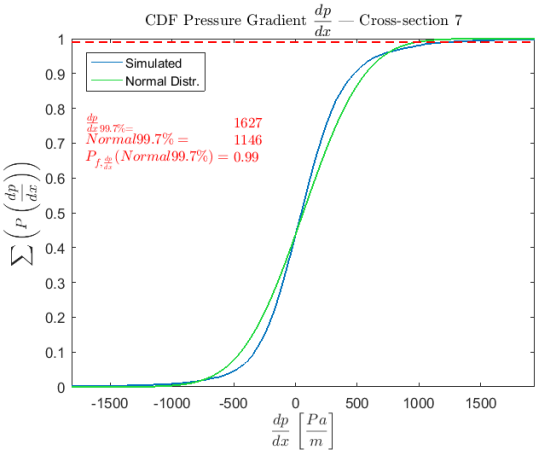

Figure J.8: CDF pressure gradient $\frac{\partial p}{\partial x}$ cross-section 7

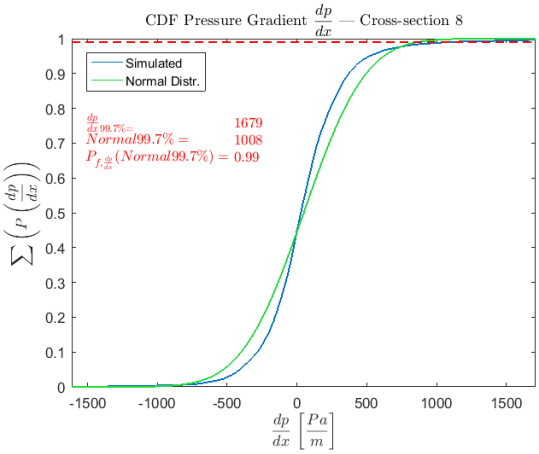

Figure J.9: CDF pressure gradient $\frac{\partial p}{\partial x}$ cross-section 8

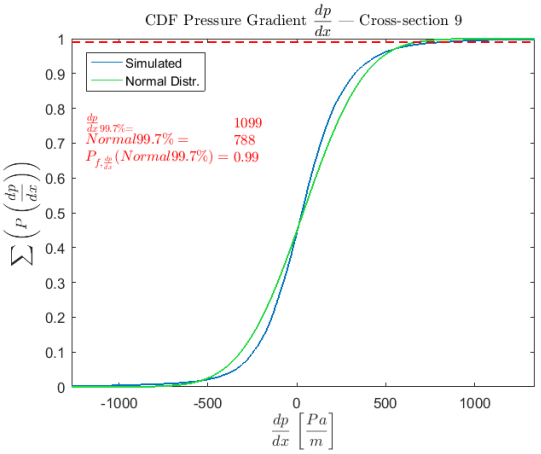

Figure J.10: CDF pressure gradient $\frac{\partial p}{\partial x}$ cross-section 9

K

Spatial distribution of τ_x and $\frac{\partial p}{\partial x}$

Cross-Section	Z [m]	Y [m]	X [m]	$\bar{\tau_x}$ [Pa]	σ_{τ_x} [Pa]	$\frac{\partial \bar{p}}{\partial x}$ [Pa/m]	$\sigma_{\frac{\partial p}{\partial x}}$ [Pa/m]
10	0.165	0.125	2.25	4.08	0.13	-59.56	20.29
	0.165	0.250	2.25	3.68	0.11	-61.42	19.14
	0.165	0.375	2.25	4.05	0.13	-60.08	20.17
1	0.165	0.125	3.00	4.51	0.20	-170.99	51.83
	0.165	0.250	3.00	4.11	0.20	-161.98	55.54
	0.165	0.375	3.00	4.48	0.20	-157.81	52.47
2	0.04	0.125	3.45	-0.22	0.39	31.14	198.04
	0.04	0.250	3.45	-0.25	0.42	43.63	205.44
	0.04	0.375	3.45	-0.22	0.35	14.04	186.19
3	0.04	0.125	3.75	-0.65	0.98	161.88	524.88
	0.04	0.250	3.75	-0.56	0.87	185.15	464.50
	0.04	0.375	3.75	-0.57	0.90	166.33	499.29
4	0.04	0.125	3.95	-0.25	0.91	166.36	547.37
	0.04	0.250	3.95	-0.21	0.90	142.59	584.86
	0.04	0.375	3.95	-0.33	0.93	159.59	486.43
5	0.04	0.125	4.15	0.05	0.85	117.57	529.62
	0.04	0.250	4.15	0.05	0.84	107.56	536.76
	0.04	0.375	4.15	0.03	0.85	127.40	520.23
6	0.04	0.125	4.35	0.30	0.79	85.69	468.14
	0.04	0.250	4.35	0.29	0.79	80.68	480.24
	0.04	0.375	4.35	0.27	0.77	95.42	476.03
7	0.04	0.125	4.55	0.44	0.79	68.05	420.09
	0.04	0.250	4.55	0.34	0.69	62.87	420.34
	0.04	0.375	4.55	0.44	0.76	73.94	421.26
8	0.04	0.125	4.95	0.78	0.78	41.85	358.49
	0.04	0.250	4.95	0.59	0.75	46.83	353.92
	0.04	0.375	4.95	0.64	0.70	53.41	350.42
9	0.04	0.125	5.15	0.83	0.73	36.53	305.29
	0.04	0.250	5.15	0.65	0.64	32.13	292.48
	0.04	0.375	5.15	0.76	0.68	36.05	298.93

Table K.1: My caption

Distribution over the width of the flume

In table K.1 a trend can be observed for the distribution of the mean wall shear stresses over the width of the flume. At cross-sections were the flow should be relatively uniform (10, 1, 8 and 9), the mean wall shear stress in the centre of the flume is lower than at the sides, while the values at the sides are approximately equal to each other. At the reference points before the sill (table 4.1) a similar distribution can be observed. Although the difference might appear to be insignificant, it is in contradiction with the general idea that the flow velocities are the highest in the centre of the flume and similarly the wall shear stress should be in case of uniform flow. Most probably the higher values at the side points are caused by the high shear stresses at the side walls of the flume, where also no-slip boundary conditions are present.

For the pressure gradient in table K.1 the deviations between the mean values in the centreline and the values at the sides, seem to be random but not significant compared to its order of magnitude or the standard deviation. The latter is quiet trivial for the downstream area (cross-section 2 to 9), as there the standard deviation is larger than the mean itself. Nevertheless also on top of the sill (cross-section 10 and 1), were the standard deviation of the pressure gradient is relatively low, the differences between the centreline values and the sides seem to be insignificant. It can be concluded that for the pressure gradient, the values from the centreline of the flume can assumed to be representative for the full width of flow at that x-coordinate.

In general the differences in streamwise direction are significantly larger than those perpendicular to the flow. Also during the experiment only the stone movements in x-direction are measured. Therefore, for the derivation of the stability formula, the centreline values of τ_x and $\frac{\partial p}{\partial x}$ will be used. It should be validated if the stability formula is robust enough to allow for this two dimensional approach.

Distribution over the length of the flume

Top of the sill
On top of the sill, the simulated results show a mean negative pressure gradient that is increasing in magnitude in downstream direction. Furthermore a relatively high wall shear stress can be observed that is similarly increasing in downstream direction. This is in agreement the expectations for an accelerating flow over a sill. The standard deviations of the pressure gradient and the wall shear stress are relatively low compared to the values downstream of the sill. This can be explained by the fact that the turbulence intensity on top of the sill is much lower than after the sill.

Recirculation area
The simulated mean pressure gradient in the recirculation area is positive and reaching high values in cross-section 3 and 4. Apparently somewhere in between the area directly after the sill (cross-section 2) and the reattachment area, the flow is decelerating the most. In other words, the transfer rate of kinetic energy of the main flow into the large scale eddies is predicted to be the highest in this area, which seems to be in agreement with Nezu and Nakagawa (1989) (figure 17).

The large standard deviation of the pressure gradient can be explained by the high turbulence intensity. Logically the values are increasing towards the reattachment point, as this is where the mixing layer is touching the bottom.

Looking from the reattachment area in upstream direction (along with the negative flow velocities), the absolute mean value of the wall shear stress is increasing from cross-section 4 to 3, and decreasing again from cross-section 3 to 2. This can be linked to flow velocities in negative direction that, from the reattachment point on, first become a bit larger after which the negative flow velocities are decreasing again towards the toe of the sill. This is in agreement with the expected flow pattern behind the sill. The standard deviation of the wall shear stress is increasing towards the reattachment area, which again can be explained by the increased turbulence intensity towards this location.

Reattachment area
For the current definition, the reattachment area is located around cross-section 5 at $x = 4.15m$, as this is where the mean wall shear stress is smaller than $0.1N/m^2$. In the report of Jongeling et al. (2003), the reattachment point is described to be located around $x = 3.95m$, which is the x-coordinate of cross-section 4. Most damage was observed in the sections directly behind this point.

Based on the physics involved around the location were the mixing layer hits the bottom and the measurements of Jongeling et al. (2003), a choice is made to include the area around cross-section 4 in the reattachment area of the simulated results.

Recovery area
In the recovery area the flow is still very turbulent but the flow velocities at the bottom are positive again and building up towards the uniform flow state as before the sill. Correspondingly the mean shear stress is positive and increasing in downstream direction. The standard deviation of the wall shear stress is dropping down very moderately.

After the reattachment point, the turbulence intensity will decrease, and so the standard deviation of the pressure gradient is decreasing quiet fast in downstream direction. The mean values of the pressure gradient are decreasing in the recovery area but still positive, indicating that the flow is still decelerating.

PDF's and CDF's of $\left(|\tau_x| + |\frac{\partial p}{\partial x}|d\right)$

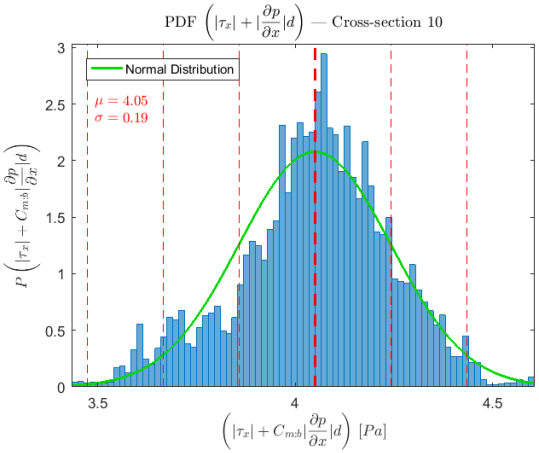

Figure L.1: PDF $\left(|\tau_x| + |\frac{\partial p}{\partial x}|d\right)$ cross-section 10

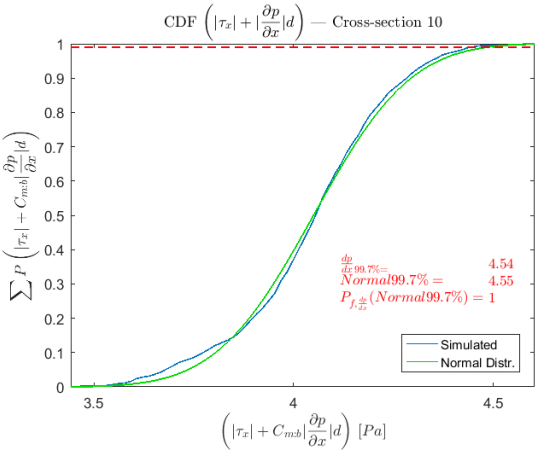

Figure L.2: CDF $\left(|\tau_x| + |\frac{\partial p}{\partial x}|d\right)$ cross-section 10

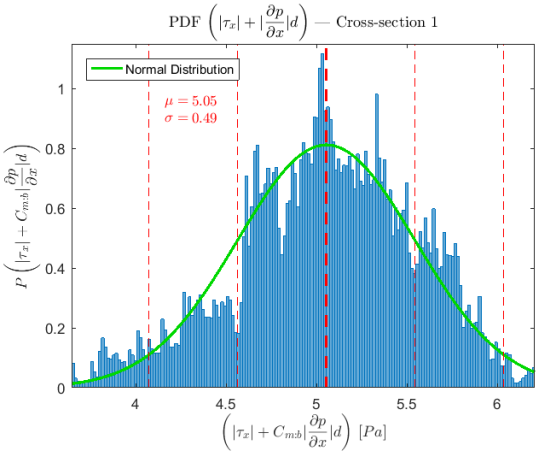

Figure L.3: PDF $\left(|\tau_x| + |\frac{\partial p}{\partial x}|d\right)$ cross-section 1

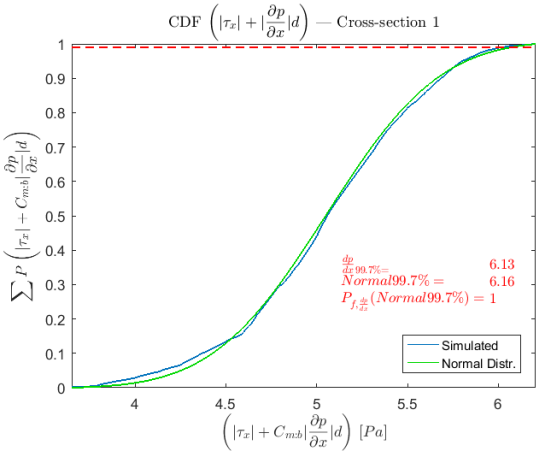

Figure L.4: CDF $\left(|\tau_x| + |\frac{\partial p}{\partial x}|d\right)$ cross-section 1

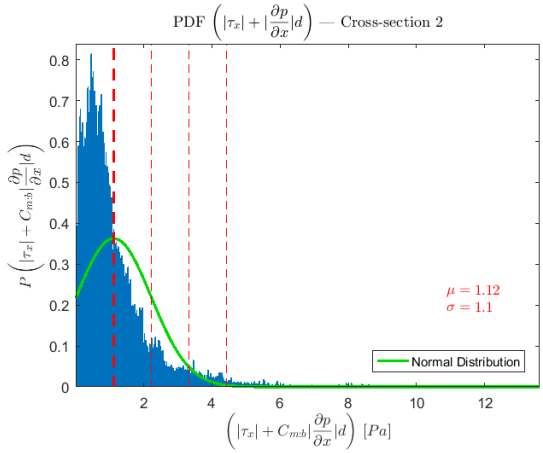

Figure L.5: PDF $\left(|\tau_x| + |\frac{\partial p}{\partial x}|d\right)$ cross-section 2

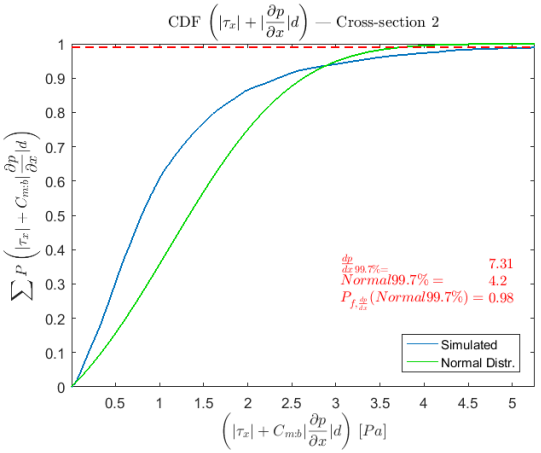

Figure L.6: CDF $\left(|\tau_x| + |\frac{\partial p}{\partial x}|d\right)$ cross-section 2

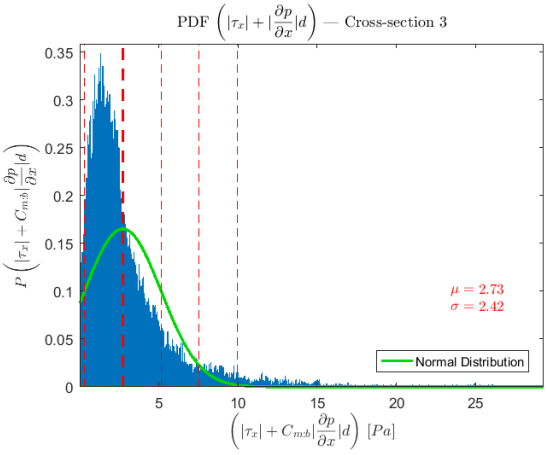

Figure L.7: PDF $\left(|\tau_x| + |\frac{\partial p}{\partial x}|d\right)$ cross-section 3

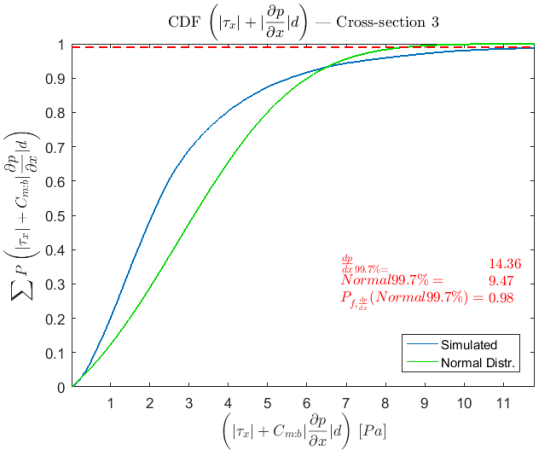

Figure L.8: CDF $\left(|\tau_x| + |\frac{\partial p}{\partial x}|d\right)$ cross-section 3

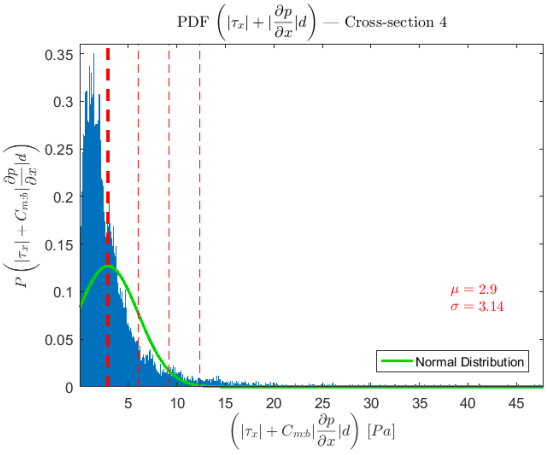

Figure L.9: PDF $\left(|\tau_x| + |\frac{\partial p}{\partial x}|d\right)$ cross-section 4

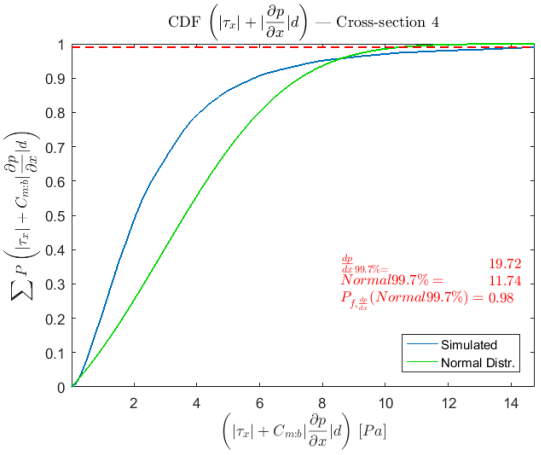

Figure L.10: CDF $\left(|\tau_x| + |\frac{\partial p}{\partial x}|d\right)$ cross-section 4

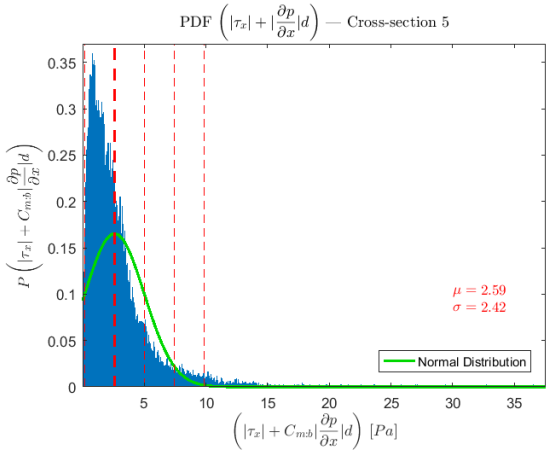

Figure L.11: PDF $\left(|\tau_x| + |\frac{\partial p}{\partial x}|d\right)$ cross-section 5

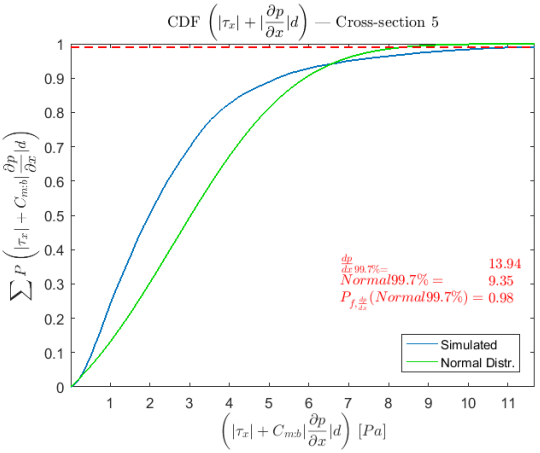

Figure L.12: CDF $\left(|\tau_x| + |\frac{\partial p}{\partial x}|d\right)$ cross-section 5

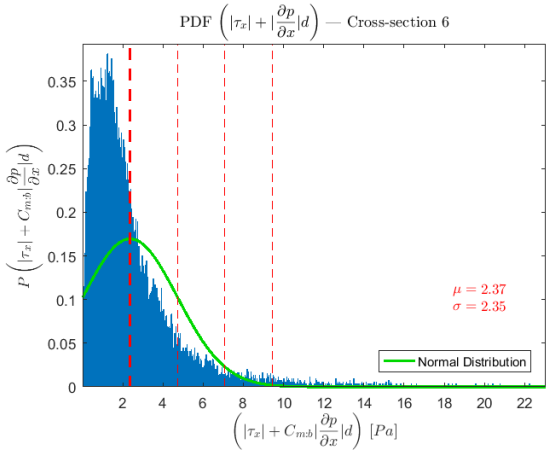

Figure L.13: PDF $\left(|\tau_x| + |\frac{\partial p}{\partial x}|d\right)$ cross-section 6

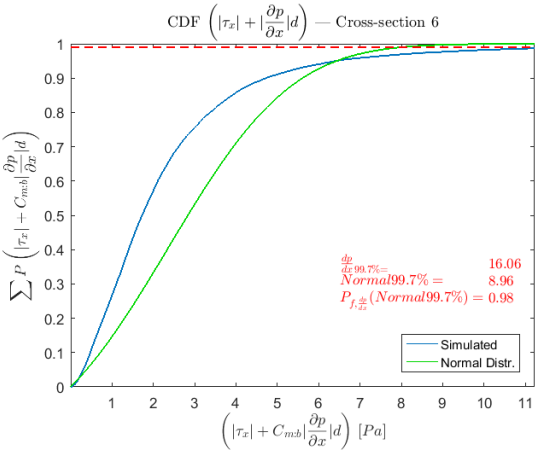

Figure L.14: CDF $\left(|\tau_x| + |\frac{\partial p}{\partial x}|d\right)$ cross-section 6

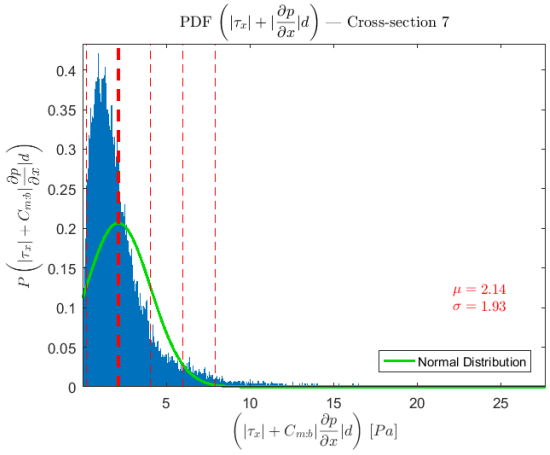

Figure L.15: PDF $\left(|\tau_x| + |\frac{\partial p}{\partial x}|d\right)$ cross-section 7

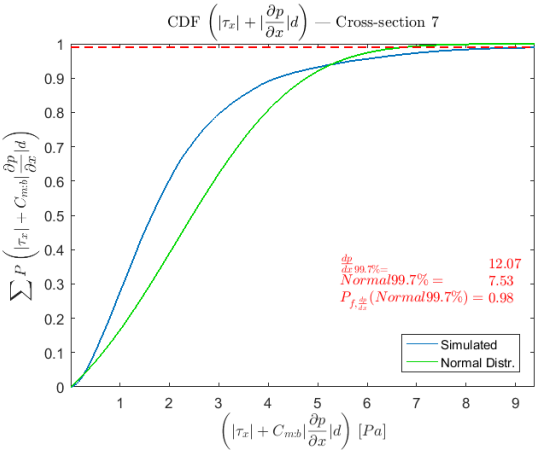

Figure L.16: CDF $\left(|\tau_x| + |\frac{\partial p}{\partial x}|d\right)$ cross-section 7

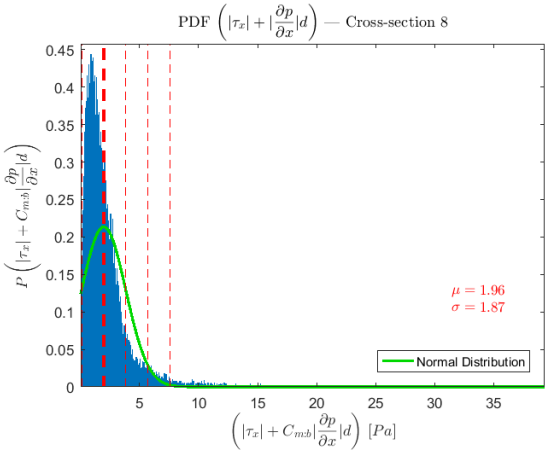

Figure L.17: PDF $\left(|\tau_x| + |\frac{\partial p}{\partial x}|d\right)$ cross-section 8

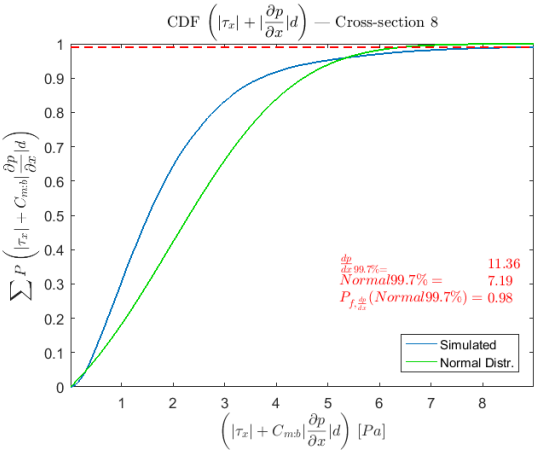

Figure L.18: CDF $\left(|\tau_x| + |\frac{\partial p}{\partial x}|d\right)$ cross-section 8

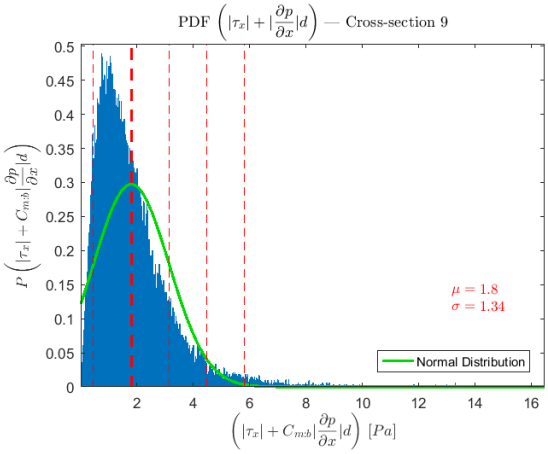

Figure L.19: PDF $\left(|\tau_x| + |\frac{\partial p}{\partial x}|d\right)$ cross-section 9

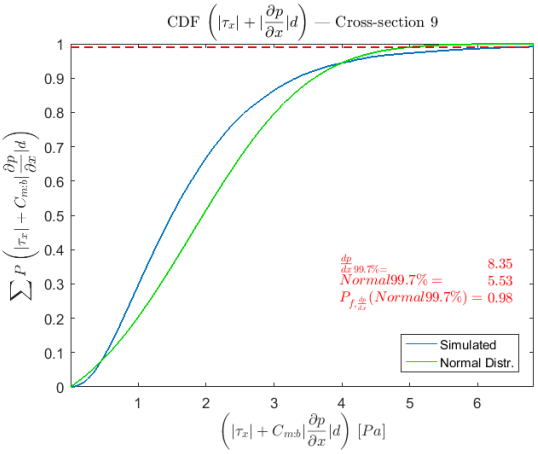

Figure L.20: CDF $\left(|\tau_x| + |\frac{\partial p}{\partial x}|d\right)$ cross-section 9

M

Time signals of $\left(|\tau_x| + |\frac{\partial p}{\partial x}|d\right)$

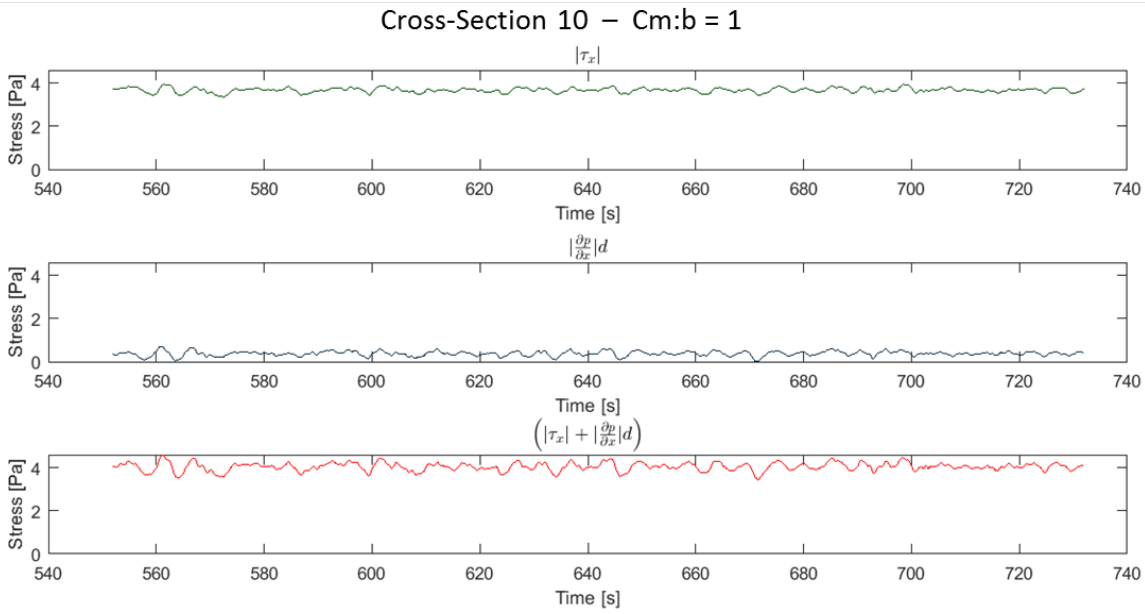

Figure M.1: Time signal $\left(|\tau_x| + |\frac{\partial p}{\partial x}|d\right)$ cross-section 10

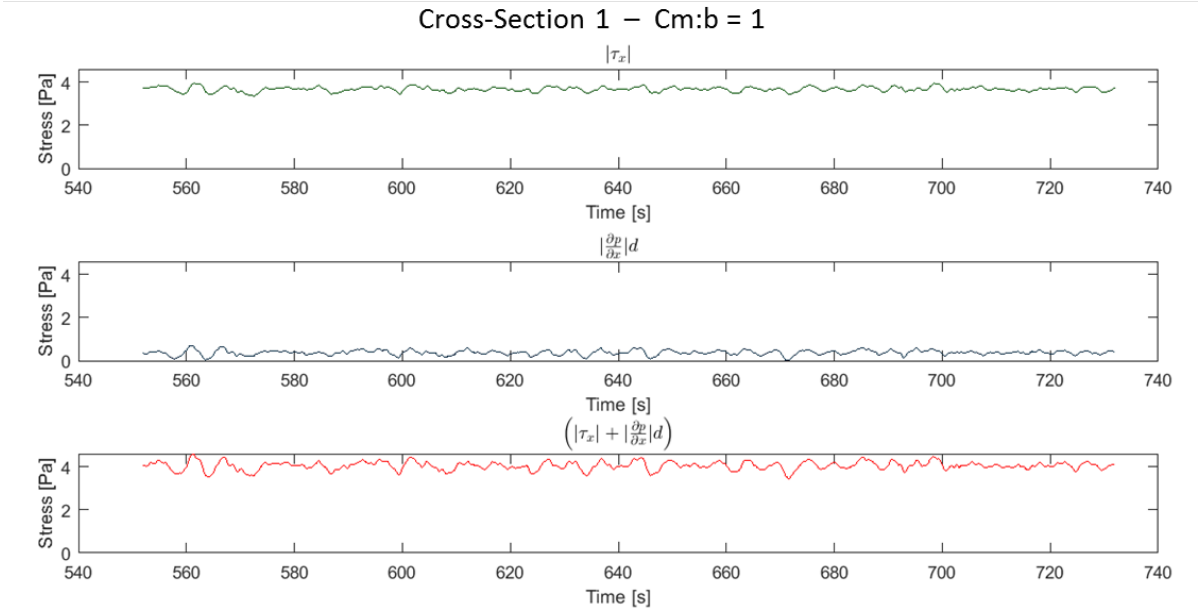

Figure M.2: Time signal $\left(|\tau_x| + |\frac{\partial p}{\partial x}|d\right)$ cross-section 1

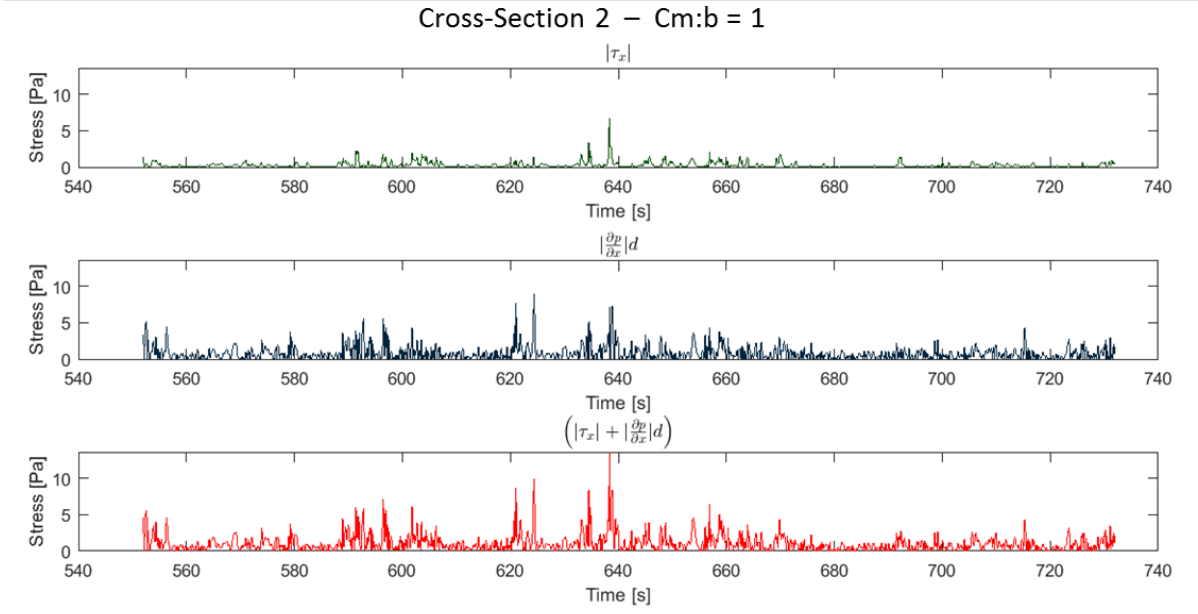

Figure M.3: Time signal $\left(|\tau_x| + |\frac{\partial p}{\partial x}|d\right)$ cross-section 2

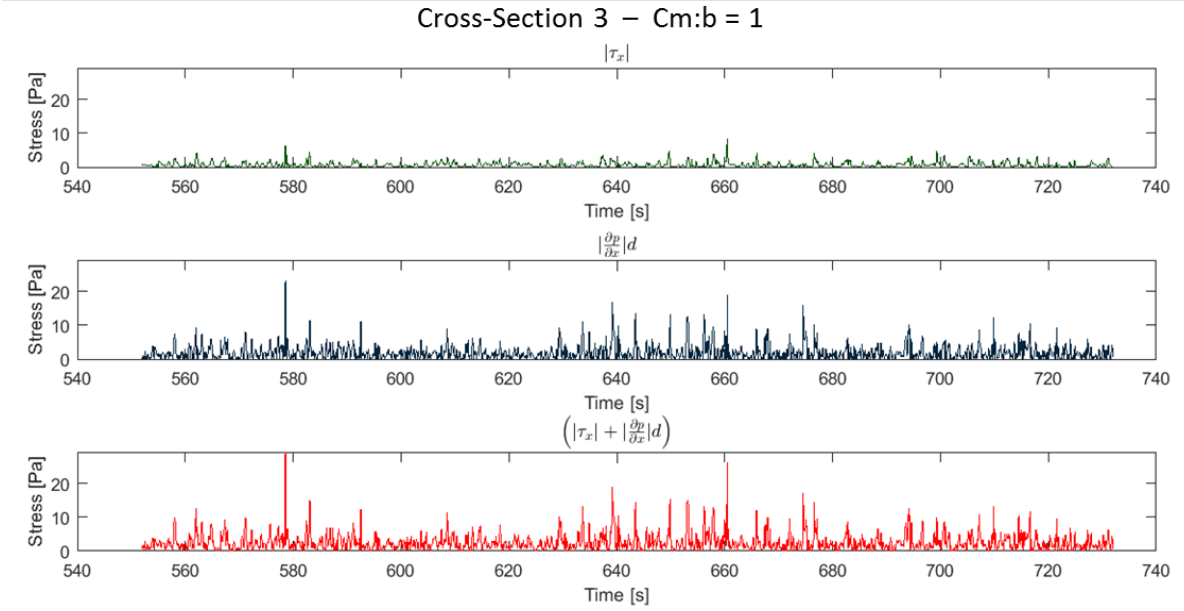

Figure M.4: Time signal $\left(|\tau_x| + |\frac{\partial p}{\partial x}|d\right)$ cross-section 3

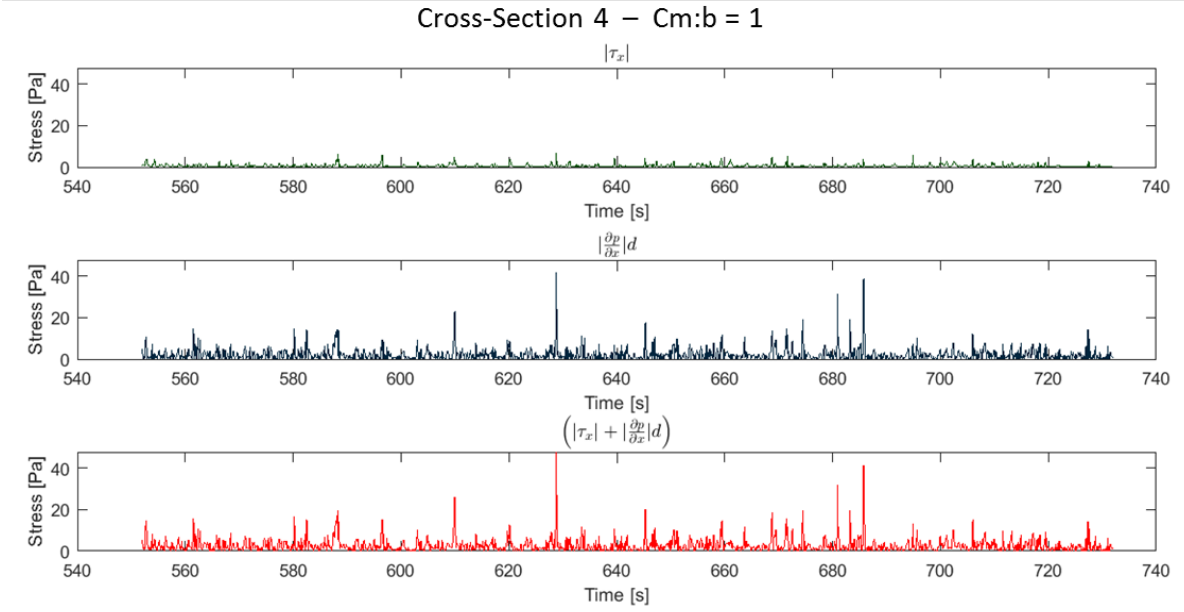

Figure M.5: Time signal $\left(|\tau_x| + |\frac{\partial p}{\partial x}|d\right)$ cross-section 4

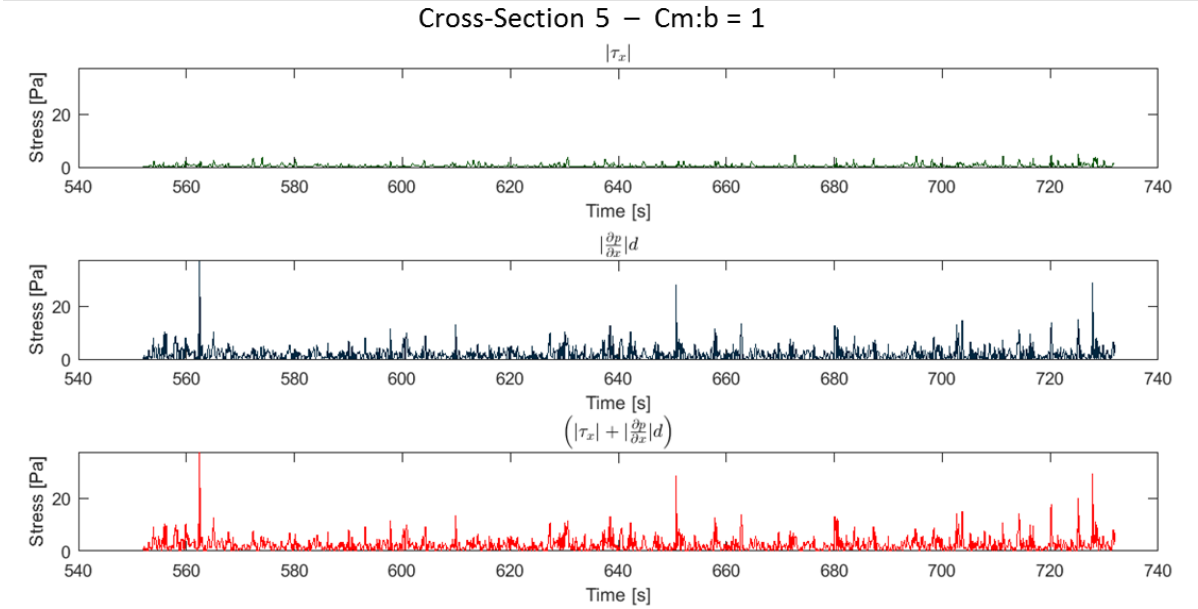

Figure M.6: Time signal $\left(|\tau_x| + |\frac{\partial p}{\partial x}|d\right)$ cross-section 5

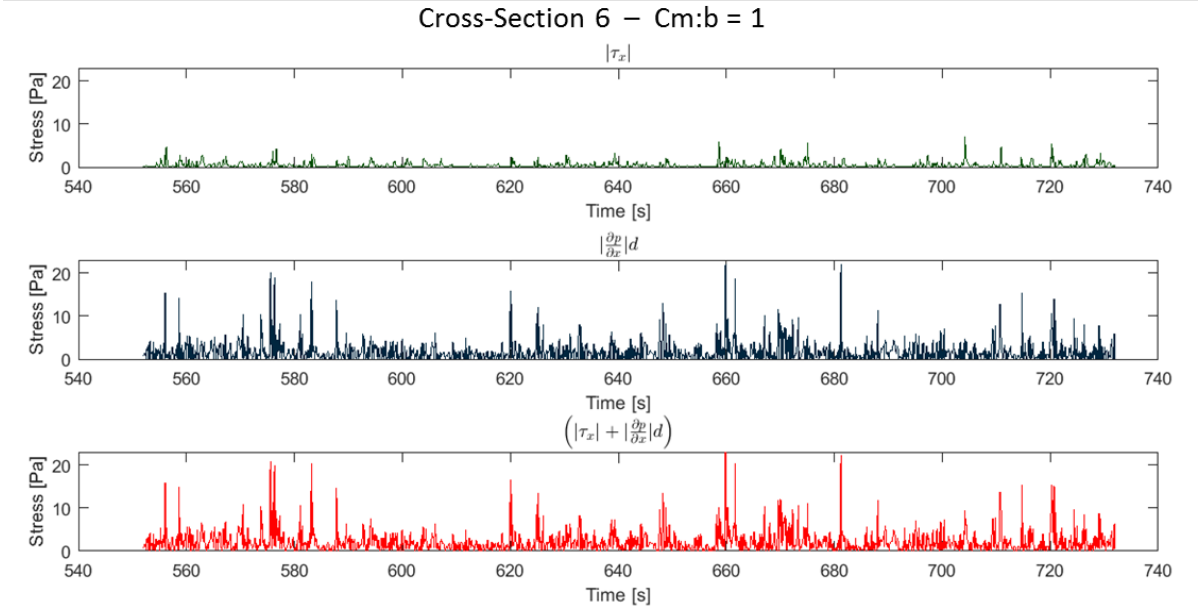

Figure M.7: Time signal $\left(|\tau_x| + |\frac{\partial p}{\partial x}|d\right)$ cross-section 6

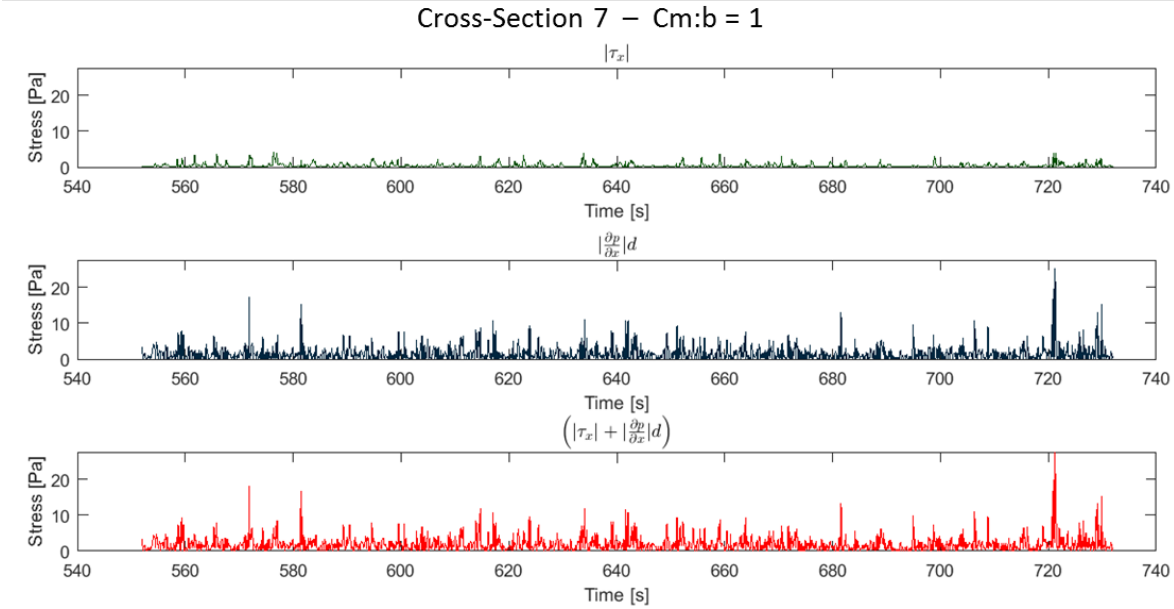

Figure M.8: Time signal $\left(|\tau_x| + |\frac{\partial p}{\partial x}|d\right)$ cross-section 7

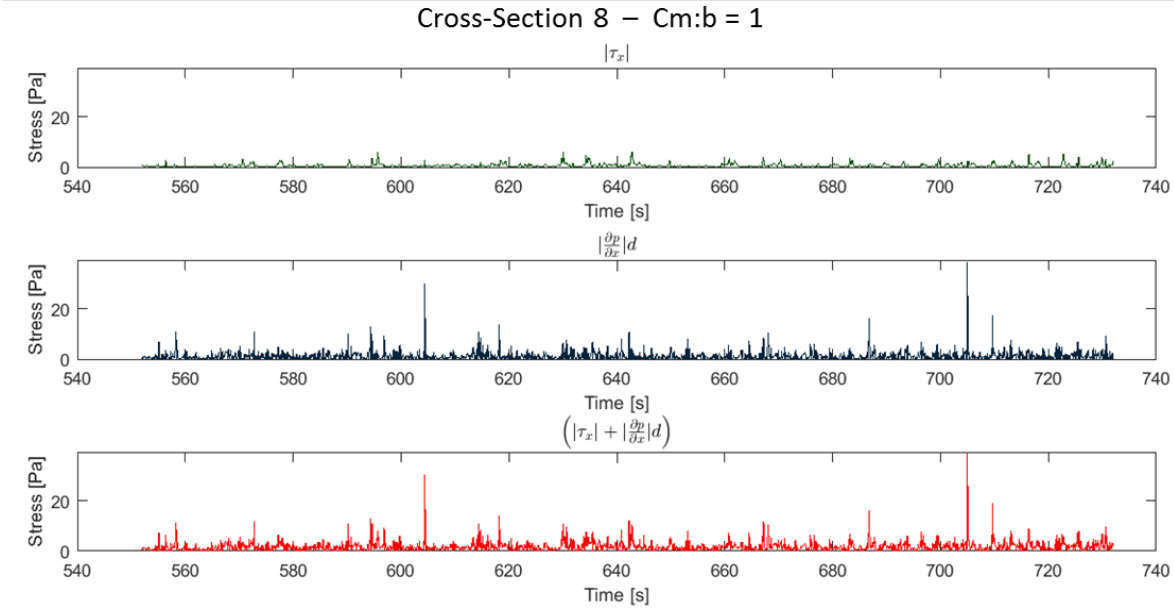

Figure M.9: Time signal $\left(|\tau_x| + |\frac{\partial p}{\partial x}|d\right)$ cross-section 8

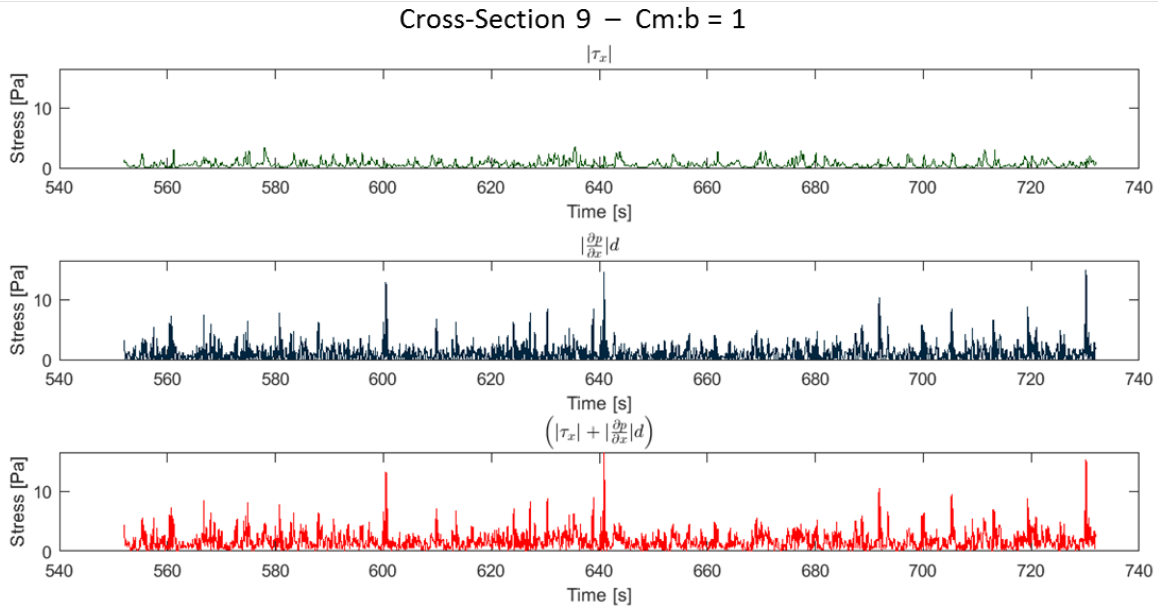

Figure M.10: Time signal $\left(|\tau_x| + |\frac{\partial p}{\partial x}|d\right)$ cross-section 9

N

PDF's and CDF's of $\left(|\tau_x| + 23|\frac{\partial p}{\partial x}|d\right)$

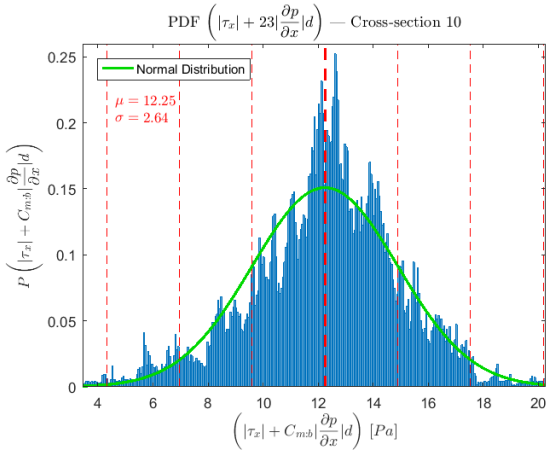

Figure N.1: PDF $\left(|\tau_x| + 23|\frac{\partial p}{\partial x}|d\right)$ cross-section 10

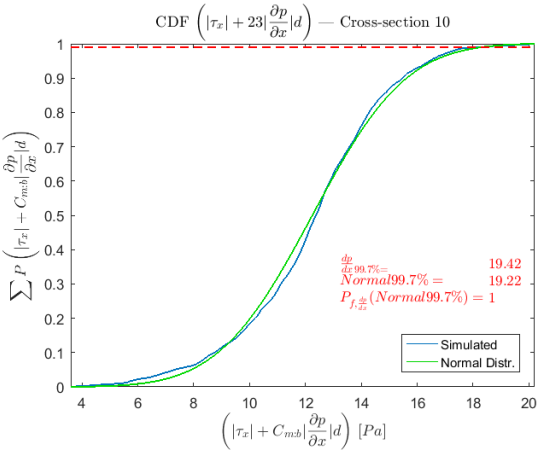

Figure N.2: CDF $\left(|\tau_x| + 23|\frac{\partial p}{\partial x}|d\right)$ cross-section 10

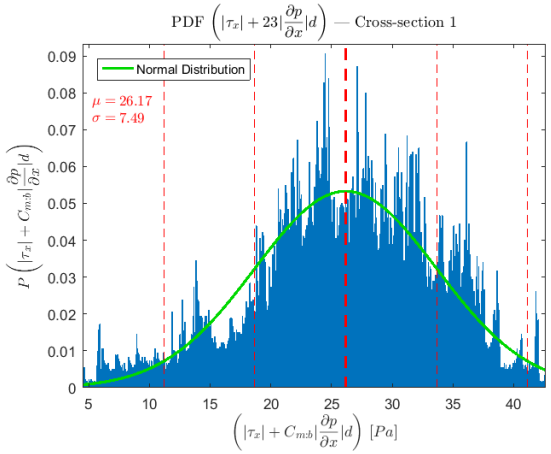

Figure N.3: PDF $\left(|\tau_x| + 23|\frac{\partial p}{\partial x}|d\right)$ cross-section 1

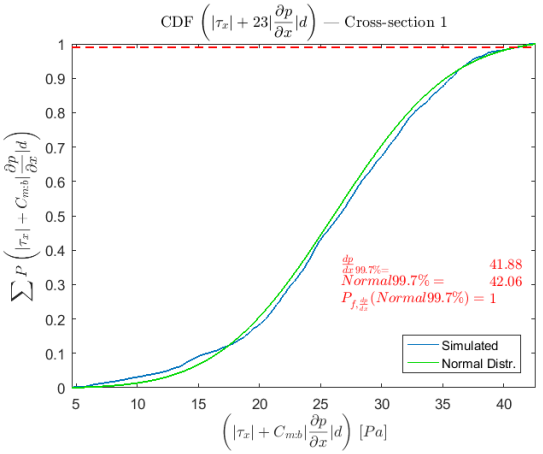

Figure N.4: CDF $\left(|\tau_x| + 23|\frac{\partial p}{\partial x}|d\right)$ cross-section 1

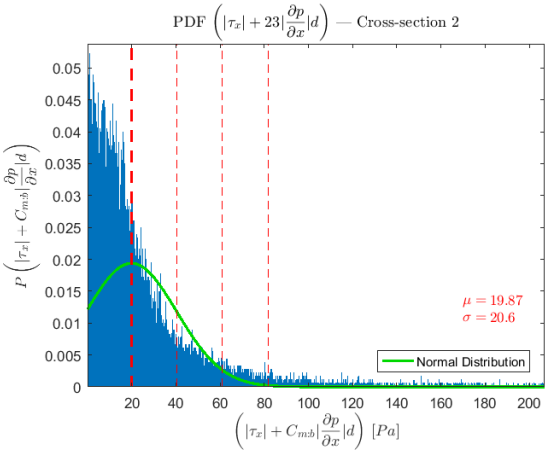

Figure N.5: PDF $\left(|\tau_x|+23|\frac{\partial p}{\partial x}|d\right)$ cross-section 2

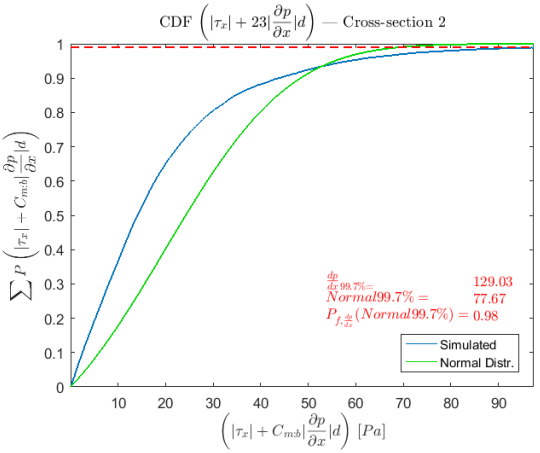

Figure N.6: CDF $\left(|\tau_x|+23|\frac{\partial p}{\partial x}|d\right)$ cross-section 2

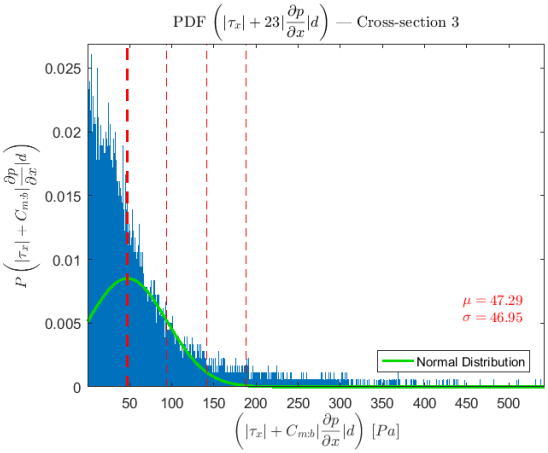

Figure N.7: PDF $\left(|\tau_x|+23|\frac{\partial p}{\partial x}|d\right)$ cross-section 3

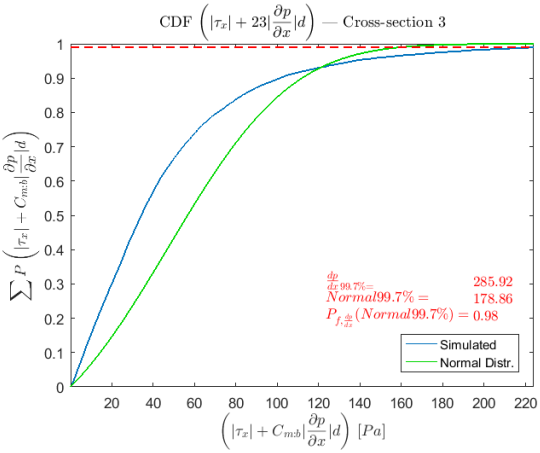

Figure N.8: CDF $\left(|\tau_x|+23|\frac{\partial p}{\partial x}|d\right)$ cross-section 3

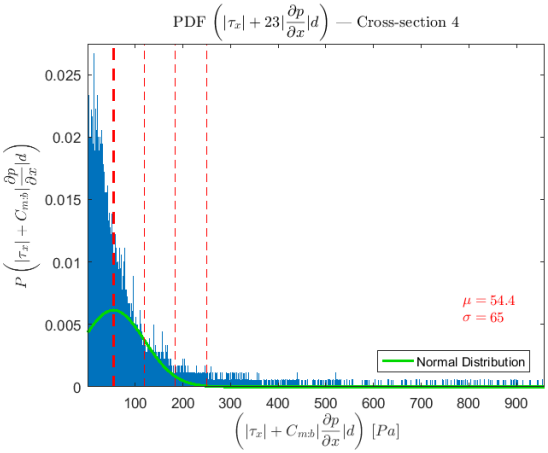

Figure N.9: PDF $\left(|\tau_x|+23|\frac{\partial p}{\partial x}|d\right)$ cross-section 4

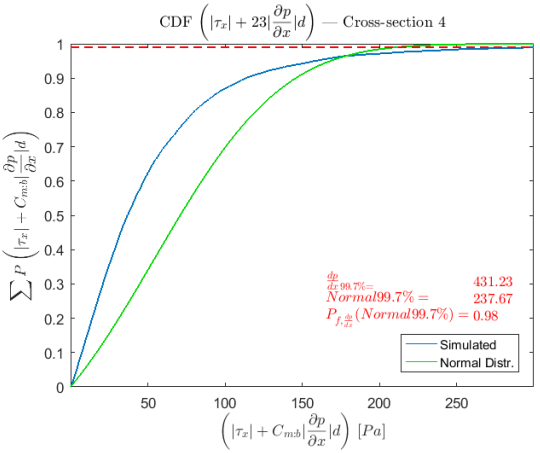

Figure N.10: CDF $\left(|\tau_x|+23|\frac{\partial p}{\partial x}|d\right)$ cross-section 4

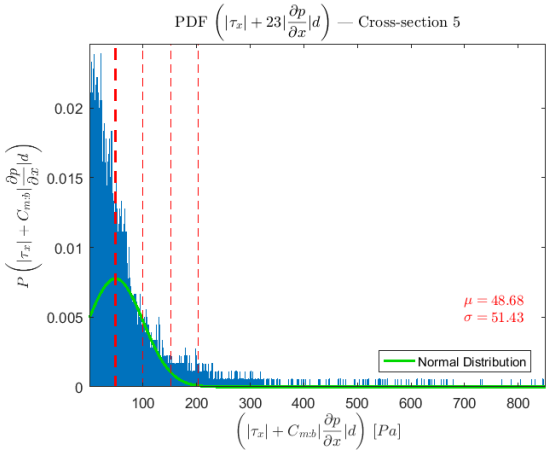

Figure N.11: PDF $\left(|\tau_x|+23|\frac{\partial p}{\partial x}|d\right)$ cross-section 5

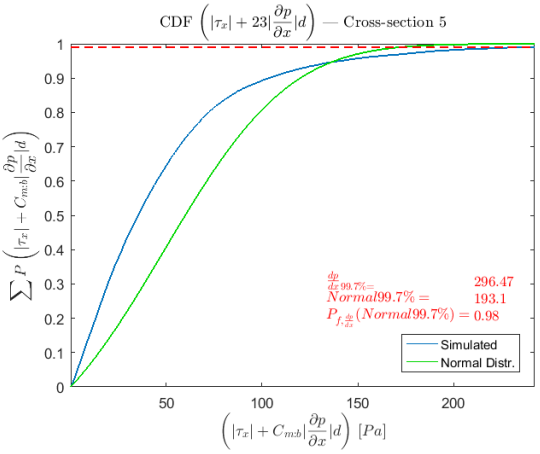

Figure N.12: CDF $\left(|\tau_x|+23|\frac{\partial p}{\partial x}|d\right)$ cross-section 5

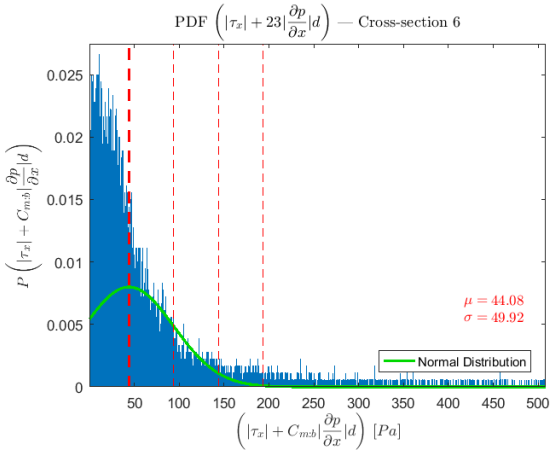

Figure N.13: PDF $\left(|\tau_x|+23|\frac{\partial p}{\partial x}|d\right)$ cross-section 6

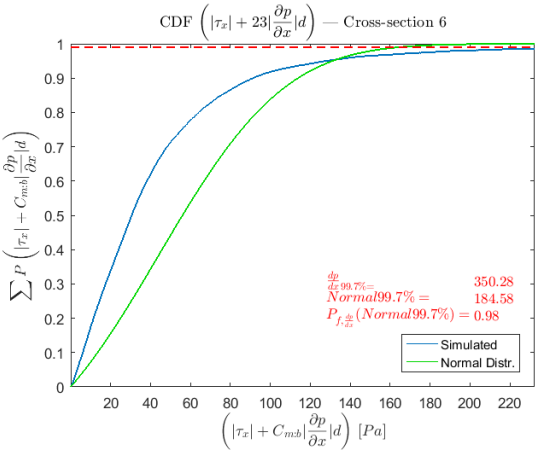

Figure N.14: CDF $\left(|\tau_x|+23|\frac{\partial p}{\partial x}|d\right)$ cross-section 6

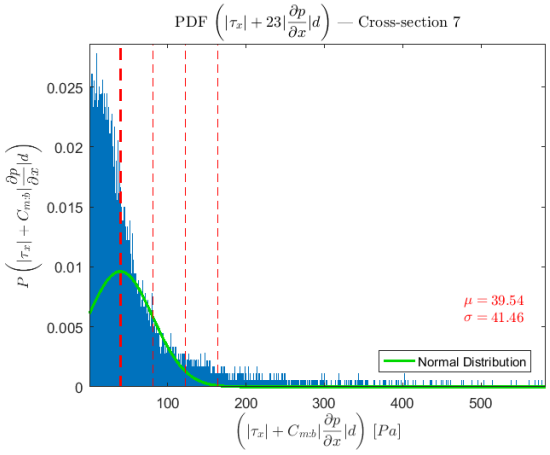

Figure N.15: PDF $\left(|\tau_x|+23|\frac{\partial p}{\partial x}|d\right)$ cross-section 7

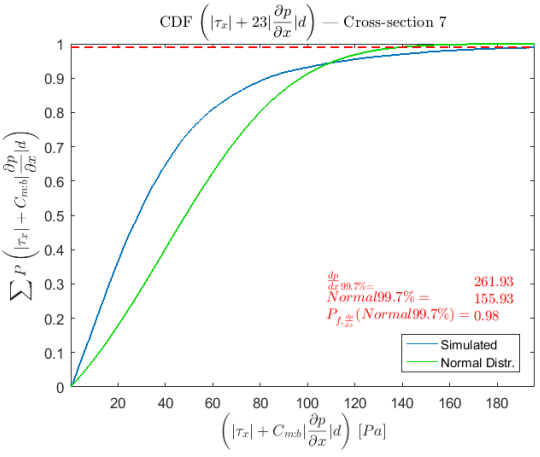

Figure N.16: CDF $\left(|\tau_x|+23|\frac{\partial p}{\partial x}|d\right)$ cross-section 7

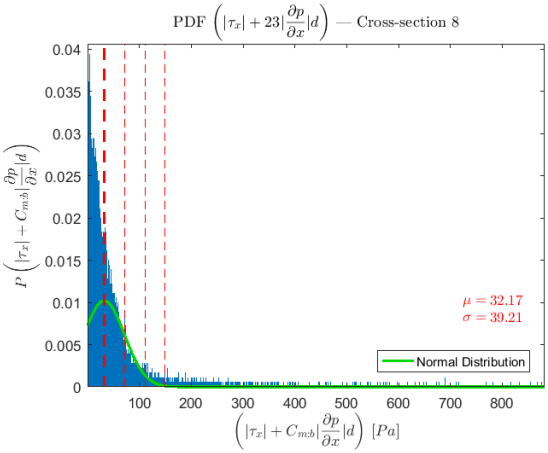

Figure N.17: PDF $\left(|\tau_x| + 23|\frac{\partial p}{\partial x}|d\right)$ cross-section 8

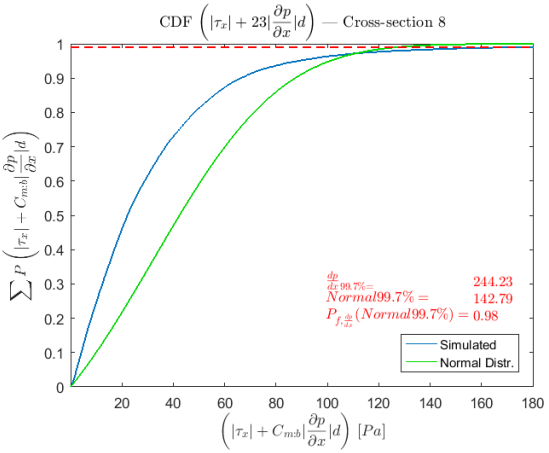

Figure N.18: CDF $\left(|\tau_x| + 23|\frac{\partial p}{\partial x}|d\right)$ cross-section 8

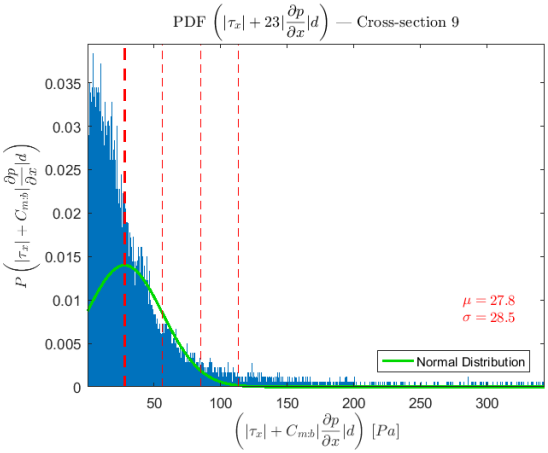

Figure N.19: PDF $\left(|\tau_x| + 23|\frac{\partial p}{\partial x}|d\right)$ cross-section 9

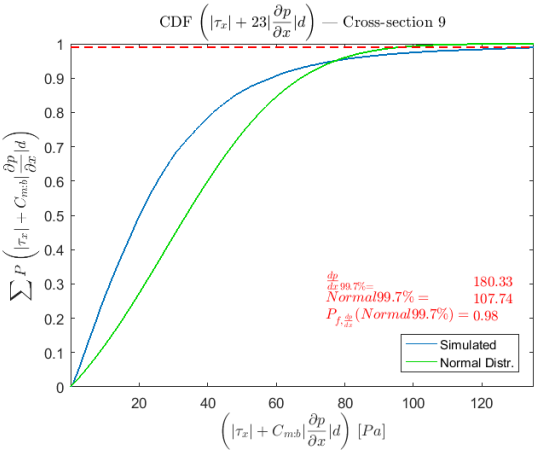

Figure N.20: CDF $\left(|\tau_x| + 23|\frac{\partial p}{\partial x}|d\right)$ cross-section 9

O

Time signals of $\left(|\tau_x| + 23|\frac{\partial p}{\partial x}|d\right)$

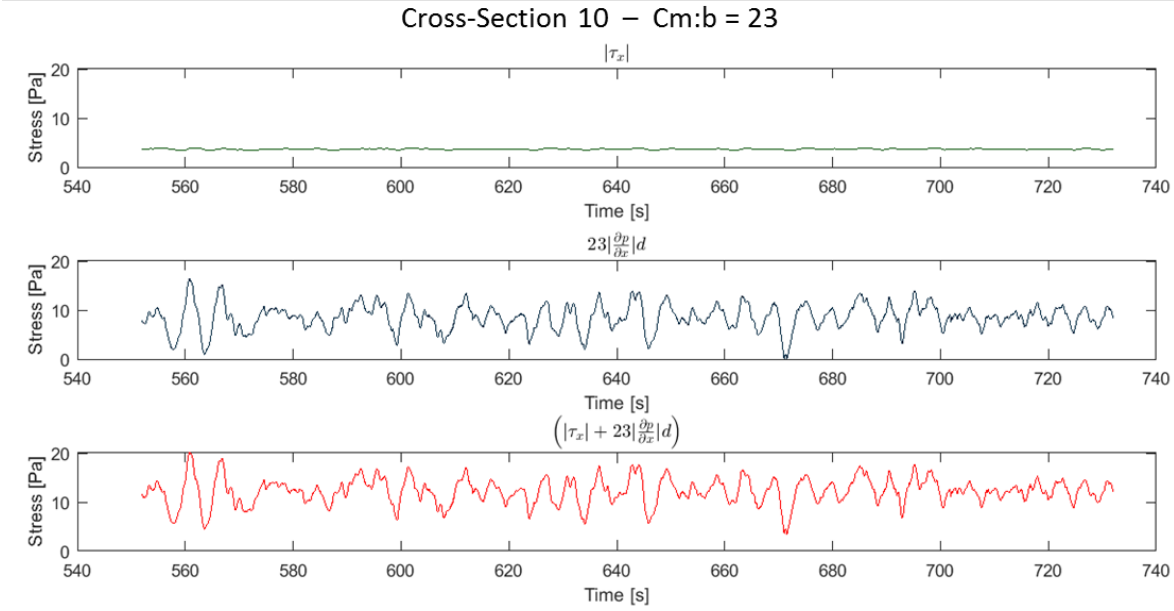

Figure O.1: Time signal $\left(|\tau_x| + 23|\frac{\partial p}{\partial x}|d\right)$ cross-section 10

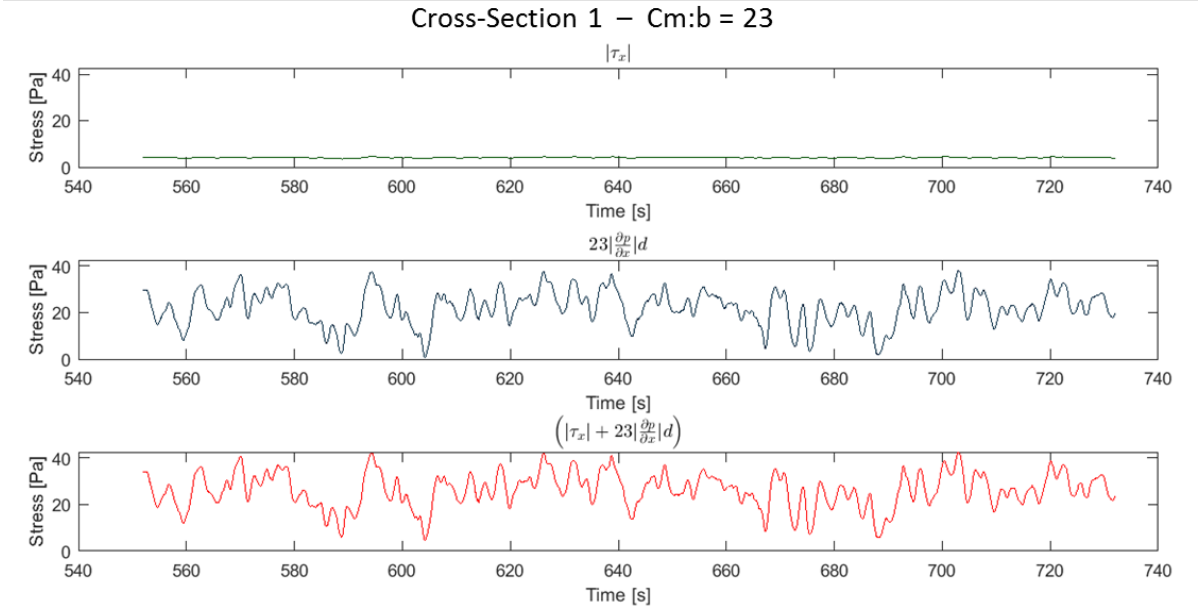

Figure O.2: Time signal $\left(|\tau_x| + 23|\frac{\partial p}{\partial x}|d\right)$ cross-section 1

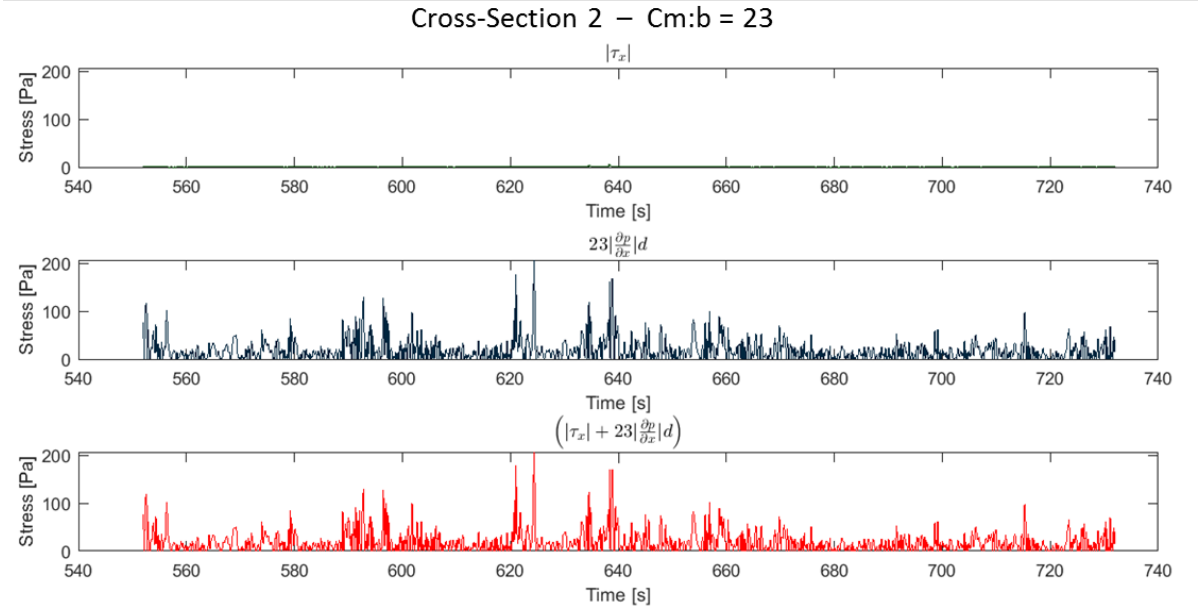

Figure O.3: Time signal $\left(|\tau_x| + 23|\frac{\partial p}{\partial x}|d\right)$ cross-section 2

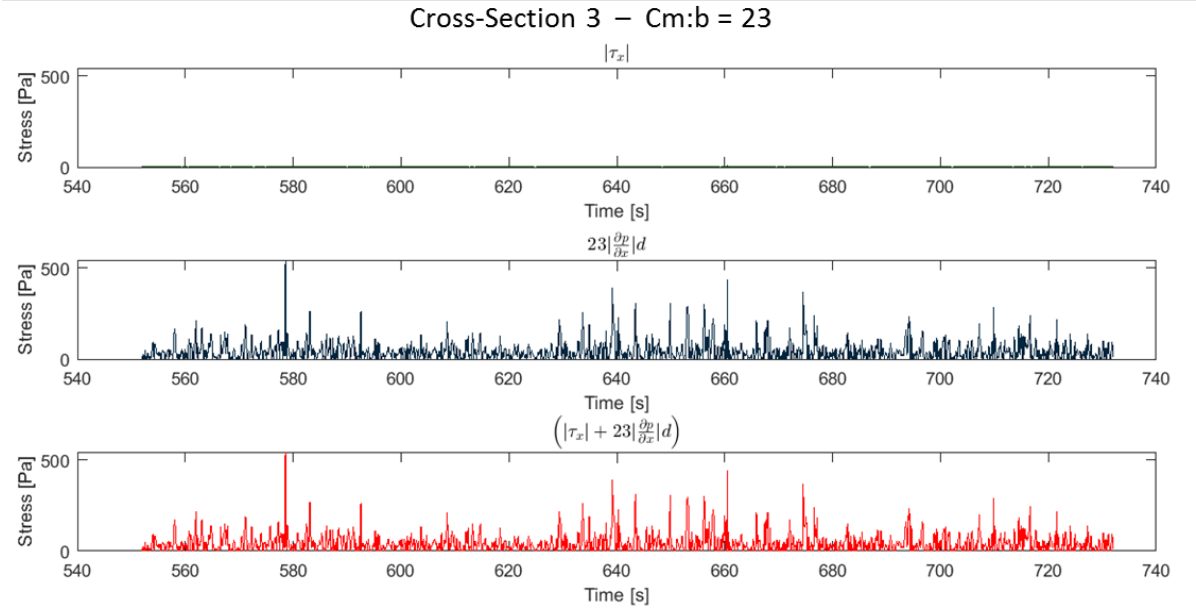

Figure O.4: Time signal $\left(|\tau_x| + 23|\frac{\partial p}{\partial x}|d\right)$ cross-section 3

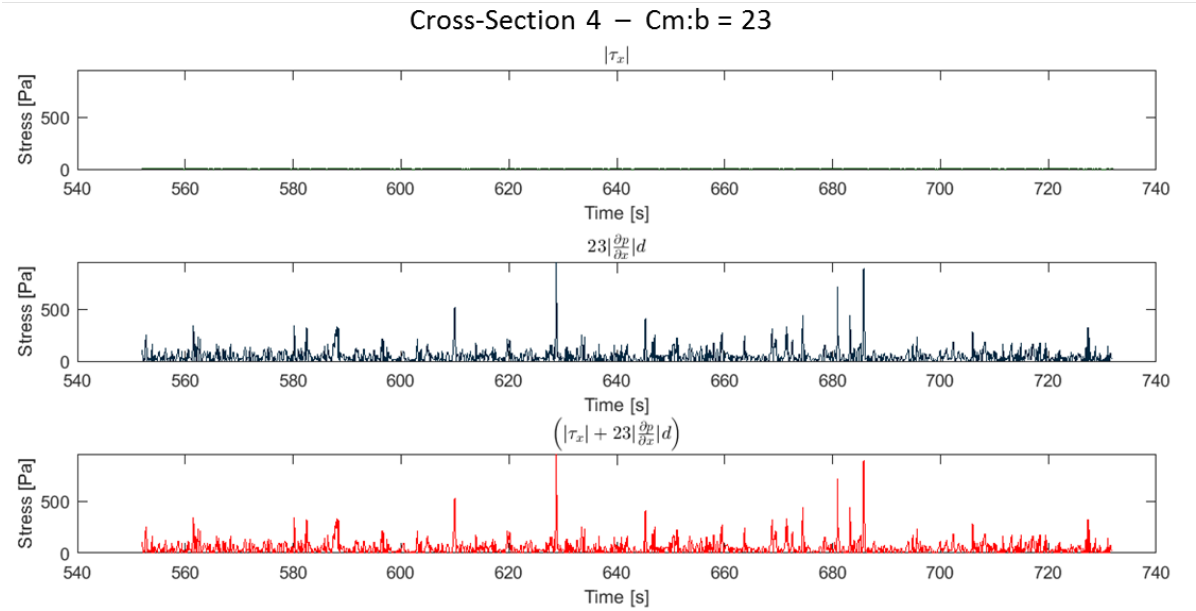

Figure O.5: Time signal $\left(|\tau_x| + 23|\frac{\partial p}{\partial x}|d\right)$ cross-section 4

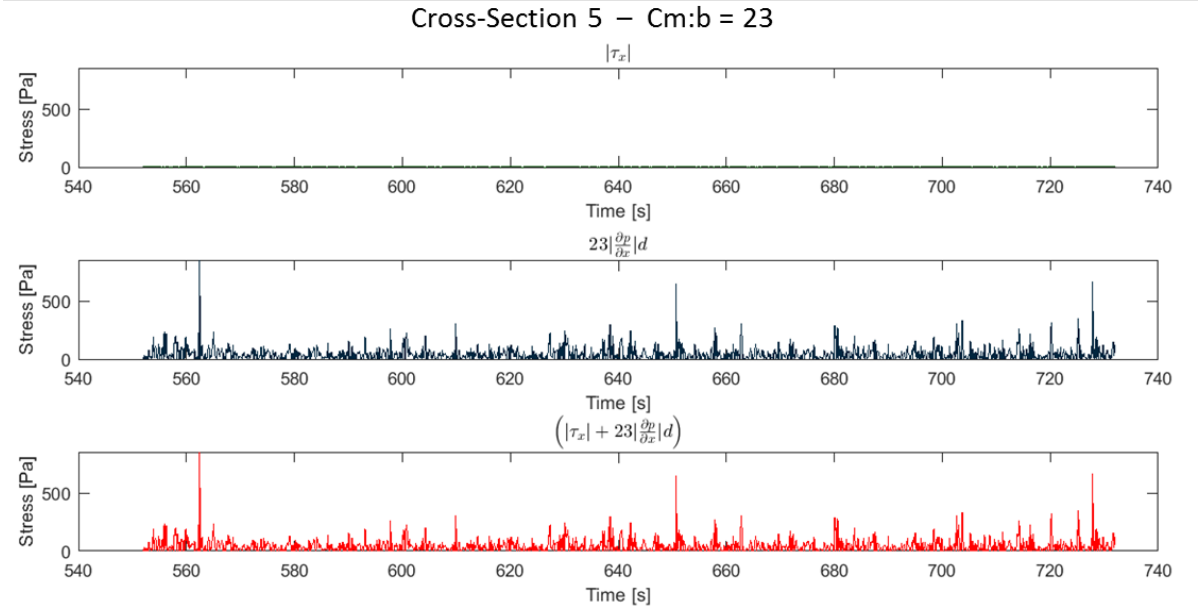

Figure O.6: Time signal $\left(|\tau_x| + 23|\frac{\partial p}{\partial x}|d\right)$ cross-section 5

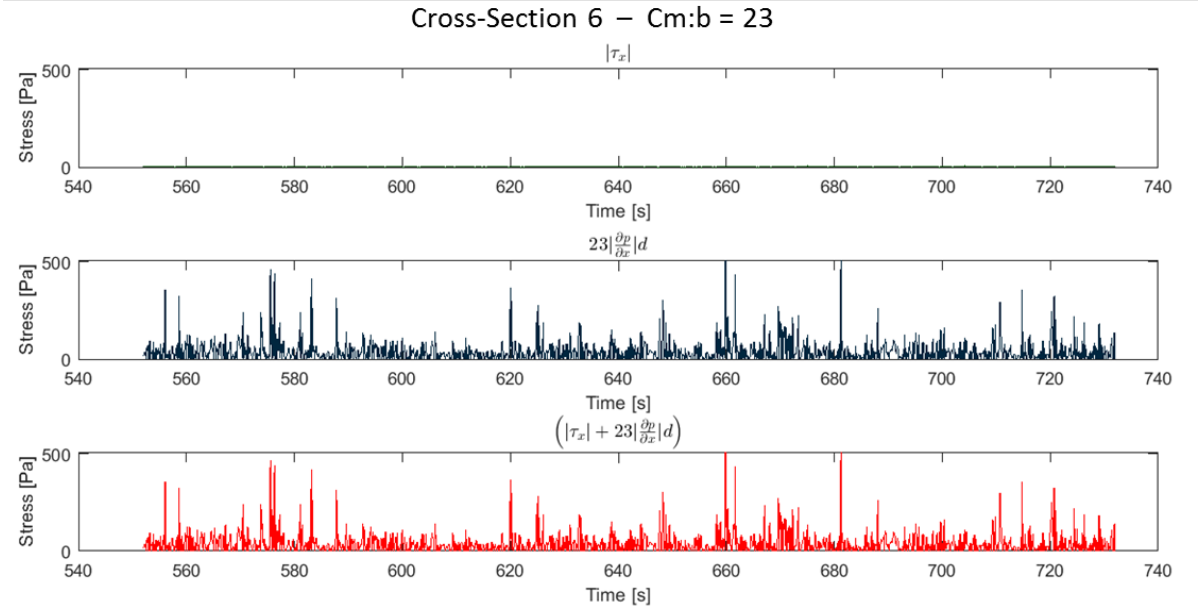

Figure O.7: Time signal $\left(|\tau_x| + 23|\frac{\partial p}{\partial x}|d\right)$ cross-section 6

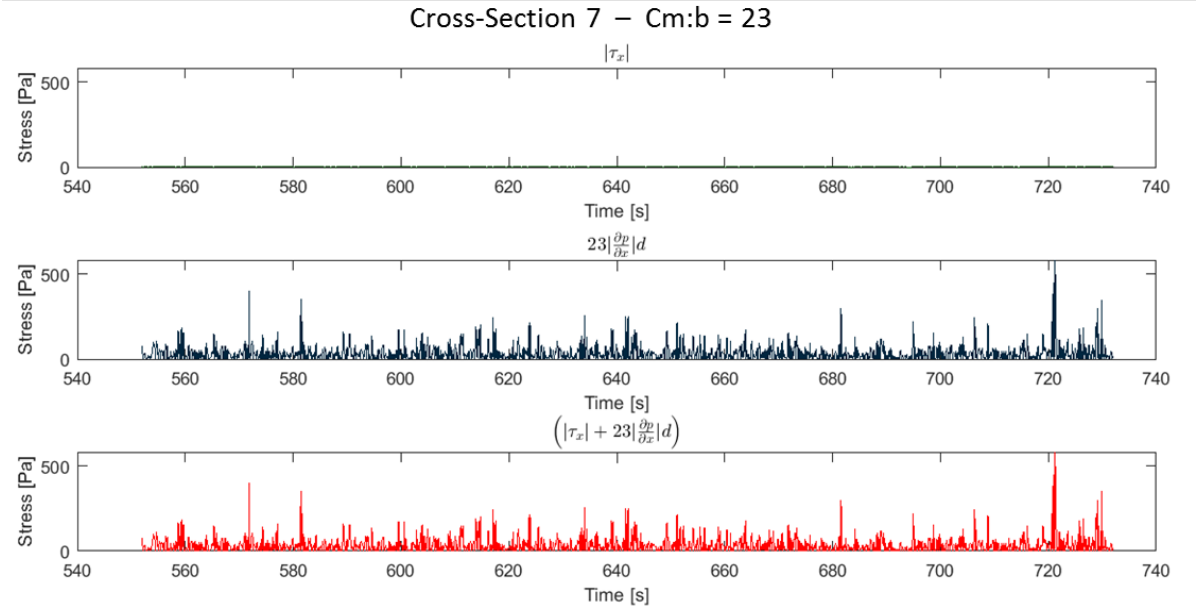

Figure O.8: Time signal $\left(|\tau_x| + 23|\frac{\partial p}{\partial x}|d\right)$ cross-section 7

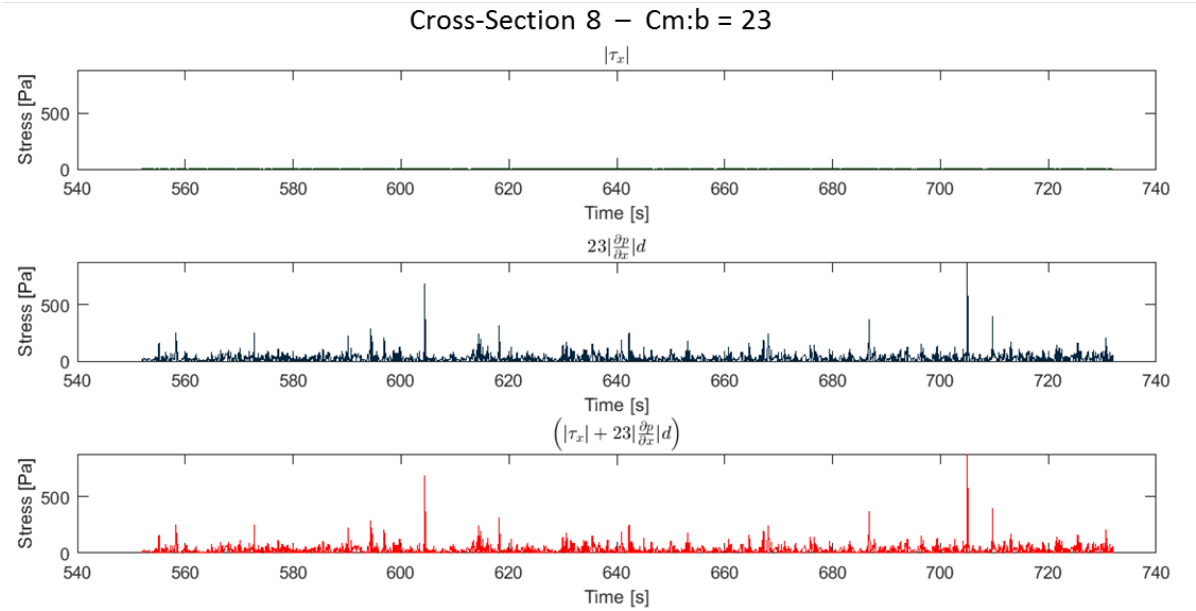

Figure O.9: Time signal $\left(|\tau_x| + 23|\frac{\partial p}{\partial x}|d\right)$ cross-section 8

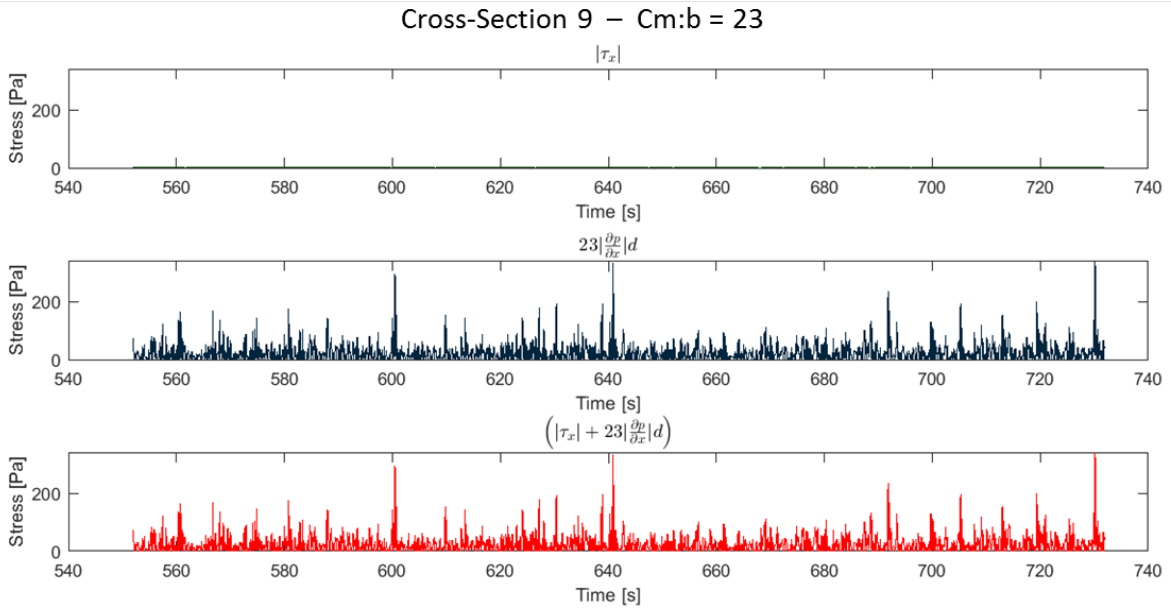

Figure O.10: Time signal $\left(|\tau_x| + 23|\frac{\partial p}{\partial x}|d\right)$ cross-section 9

P

Additional information literature study

P.1. Boundary layer

This section will provide the information needed to understand the interaction between the bottom and the main flow. The transition from a solid boundary to the dynamic free stream can be divided into several regions which together form the boundary layer. A distinction will be made between a smooth and a rough boundary and the use of wall functions is explained.

In section 2.1.4 the definitions of viscous shear stresses and turbulent shear or Reynolds stresses are not yet given. They can be found in the glossary or paragraph P.2.1.

P.1.1. Smooth boundary

The main concepts of the boundary layer theory of Ludwig Prandtl (1928) are that (Anderson, 2005):

1. The flow velocity at a bodies surface can assumed to be equal to the velocity of the body itself
2. The frictional effects are limited to the extents of a certain boundary layer

In other words, at a solid surface in a fluid a no-slip condition can be assumed and only in the boundary layer effects of the fluids viscosity play a significant role. Outside this boundary layer inertial effects are dominant and therefore the flow there can assumed to be inviscid (frictionless) (Anderson, 2005). The boundary layer itself can again be split-up into several regions with as primary dissimilarity the ratio between the effects of inertia and viscosity.

Furthermore a distinction can be made between hydraulically smooth and hydraulically rough surfaces. For convenience, first the structure of a boundary layer above a hydraulically smooth bed will be presented in this section.

Starting from the solid surface, the boundary layer can be divided in an inner boundary layer and an outer boundary layer. In the outer boundary layer, the viscous stresses are already negligible compared to the Reynolds stresses. The flow in the outer boundary layer therefore can be described by the same formulas as the inviscid free flow outside the boundary layer, only the boundary conditions are different (Southard, 2006). In particular the kinematic boundary conditions, which states that the normal velocity of the fluid at the wall should go to zero for a stagnant bottom, and the no-slip condition is valid as explained earlier. The inner boundary layer can again be split-up in three parts, the viscous sublayer, the buffer layer and the inertial sublayer. The **viscous sublayer** is the layer present at the solid surface. In this very thin layer the viscous shear stresses are dominant and the turbulent shear stresses can be neglected. Because only the viscous shear is of importance in this layer, the velocity profile is linear. Hence the viscous sublayer is also known as the linear sublayer. Above the viscous sublayer, the buffer layer is present. In the **buffer layer**, both turbulent and viscous shear stresses are of importance and therefore cannot be neglected. The flow in the buffer layer is already strongly turbulent and a lot of kinetic energy from the mean flow is turned into turbulent kinetic energy inside this layer. The large amount of different instabilities inside the buffer layer are the cause of the generation of very energetic small-scale turbulent eddies (Southard, 2006). In literature the buffer layer therefore sometimes is called the turbulence-generation layer. The outer part of the inner boundary layer is often referred to as the **inertial sublayer**, fully turbulent region or **log-law region**. The last two names for this layer already tell what need to be said about this layer. The flow is fully turbulent and a large group of scientists believe that the velocity profile can be described by a logarithmic function here, although there are ongoing discussions if it should be a power law instead of a log law. In hydraulic engineering frequently use is made of the predictable course of this part of the velocity profile, which will be elaborated in section P.1.3.

P.1.2. Rough boundary

As mentioned in the previous paragraph, the boundary layer above a rough surface can differ from the boundary layer above a smooth surface. A distinction can be made between:

1. **Hydraulically smooth surfaces**: the surface is physically smooth or the roughness height is smaller than the height of the viscous sublayer, as depicted on the left side of figure P.1 The roughness elements are fully located in the viscous sublayer and no instabilities are caused by the flow around the roughness elements. The main flow therefore does not feel the presence of the rough surface and it will behave similar as in case of a physically smooth boundary.
2. **Hydraulically rough surfaces**: the roughness elements are larger than what normally would be the height of the viscous sublayer. The rough surface protrudes into the turbulent flow and thereby will influence the flow field to a certain extent. Turbulent eddies will be present between the roughness elements and no general viscous sublayer is present like for hydraulically smooth surfaces, as visualised at the right side of figure P.1 .

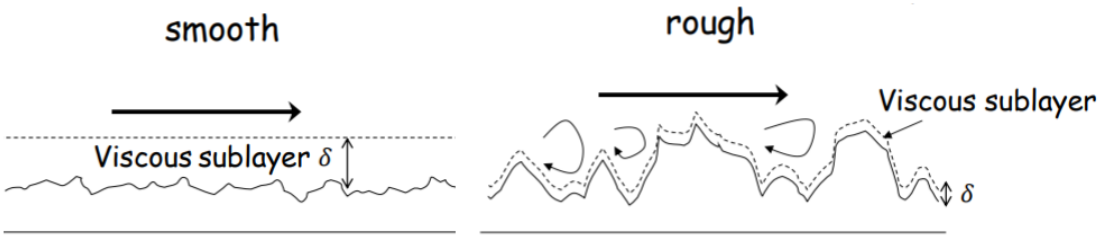

Figure P.1: The difference between a smooth and a rough boundary (adjusted from Blom, 2017)

For many other cases in hydraulic engineering the bottom boundary of the flow will be hydraulically rough and therefore it is important to understand that this has a significant influence on the velocity and turbulence profiles above the bed.

P.1.3. Law of the wall

In fluid dynamics frequently use is made of the law of the wall, which states that a certain region of a velocity profile is ought to follow a distribution that is on average proportional to the logarithm of the distance to the solid boundary (Jiménez, 2004). For fully developed flows this region is more or less known, as indicated in the previous two sections. Because of the predictability of the distribution of the velocity profile, for fully developed flow the velocity profile can be reproduced without the need of totally resolving the physics inside the inner boundary layer. A wall function can be assumed that accounts for the physics of the layers between the solid boundary and the log-law region, without introducing significant errors in the representation of the rest of the flow (Jiménez, 2004).

Strictly speaking, the law of the wall is not valid for highly variable flows like those discussed in this thesis, as locally the logarithmic part of the velocity profile might be smaller, at another height or even be absent. Nevertheless, in practise also for these cases the law of the wall is used because it still will provide valuable insight in the general flow characteristics over the rough bottom. In fact the law of the wall has quite a large area of applicability, even in case of the presence of substantial pressure gradients (Southard, 2006).

The logarithmic part of the velocity profile is often visualised as the linear part in a semi-logarithmic Clauser plot. In this graph the dimensionless wall distance z^+ is plotted against the dimensionless velocity u^+, as shown for a flow over a hydraulically smooth bed in figure P.2.

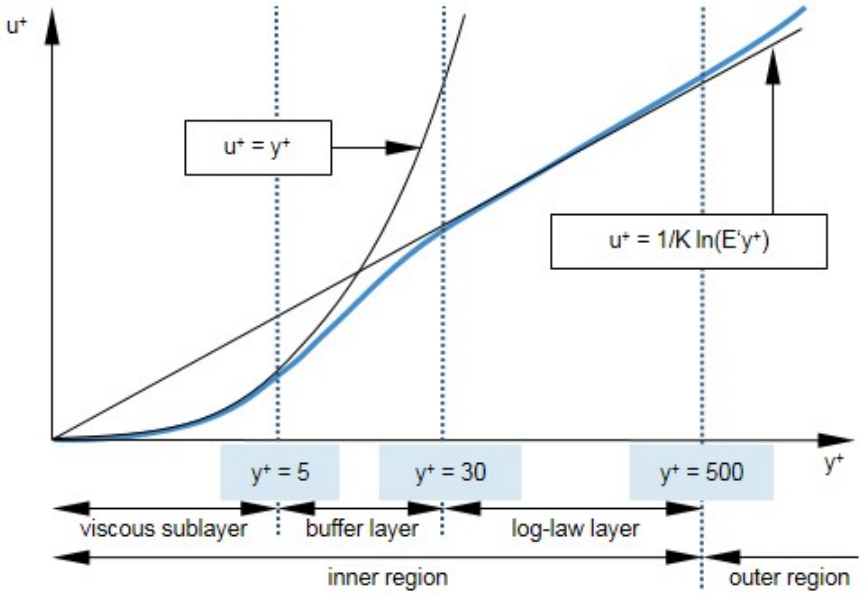

Figure P.2: Law of the Wall on a Clauser Plot (adjusted from (Star CCM+, 2018))

The dimensionless velocity u^+ is defined as the ratio between the local velocity parallel to the wall u and the friction velocity u_*.

$$u^+ \equiv \frac{u}{u_*}$$

The dimensionless wall distance z^+ is defined as:

$$z^+ \equiv \frac{u_* z}{\nu}$$

In accordance with equation 2.2 of the previous subsection about the boundary layer above a rough surface.

When assuming a wall function, the only difference between a hydraulically smooth or rough surface is that the corresponding flow characteristics of the skipped layers need to be modelled differently. For example, in case of a constant flow velocity u, the shear velocity u_* will be larger as the roughness of the surface increases. In numerical modelling tools it is therefore common practise to take the surface roughness into account by the lowering the velocity profile, as shown in figure P.3.

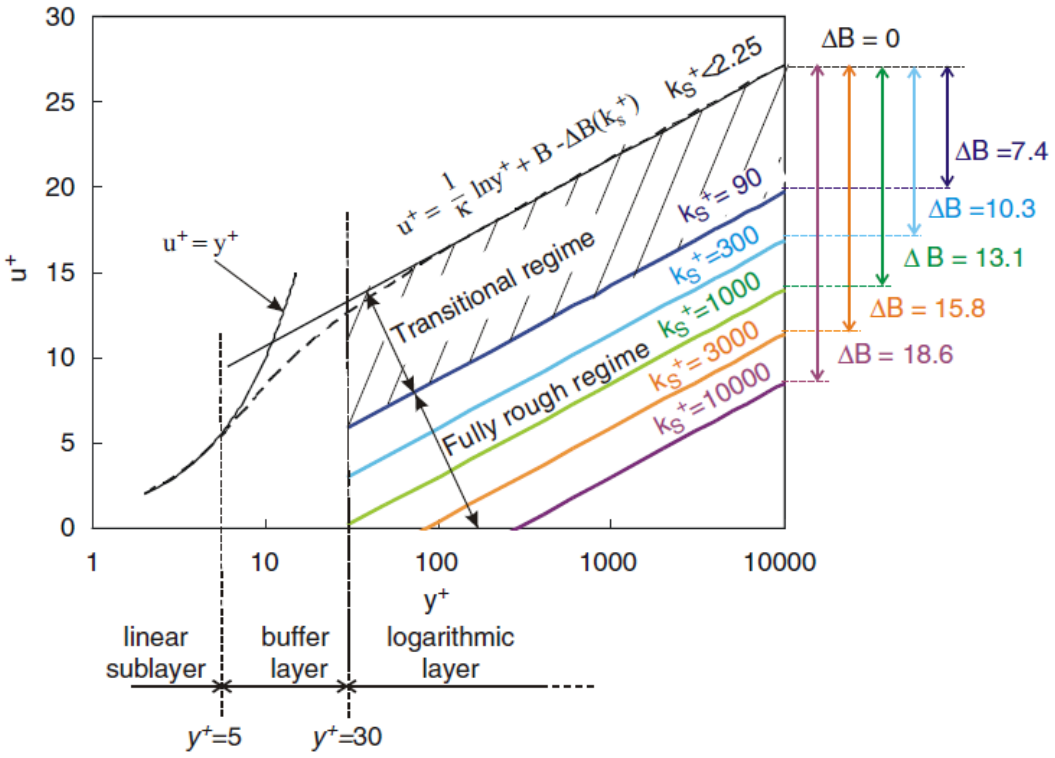

Figure P.3: Lowering the velocity profile to take the effect of surface roughness into account, visualised on a Clauser Plot (adjusted from Blocken et al. (2007))

P.2. Flow characteristics

In this section some flow characteristics are discussed that are relevant for the sections about stone stability and numerical modelling. Especially turbulence will play an important role for both of these subjects.

P.2.1. Turbulence

In fluid dynamics, two distinct flow regimes can be discerned i.e. laminar flow and turbulent flow. This difference between the two can be expressed by the Reynolds number. The Reynolds number Re is a dimensionless ratio between inertia and viscosity. The general definition of the Reynolds number is given by the equation:

$$Re \equiv \frac{uL}{\nu}$$

in which:

- u is the flow velocity $[m/s]$
- L is a characteristic length $[m]$
- $\nu \equiv \frac{\mu_w}{\rho}$ is the kinematic viscosity $[m^2/s]$

Laminar flow matches with low Reynolds numbers, which means that the effects of viscosity are about the same order of magnitude as the inertia effects. In hydraulic engineering this will almost never occur, therefore laminar flow will only be elaborated when useful for the explanation of turbulent flow properties.

In this study only high-Reynolds-number flows are considered. In case of Reynolds numbers of 1000 and higher, in the main flow the effects of viscosity are negligible compared to the effects of the flow velocity (Uijttewaal, 2002). Instabilities will then enter the main flow, often referred to as eddies, and a flow containing these eddies is called turbulent. Turbulence is a three-dimensional phenomenon that can be observed by the velocity fluctuations in the velocity signal of a steady uniform flow, as visualised in figure P.4.

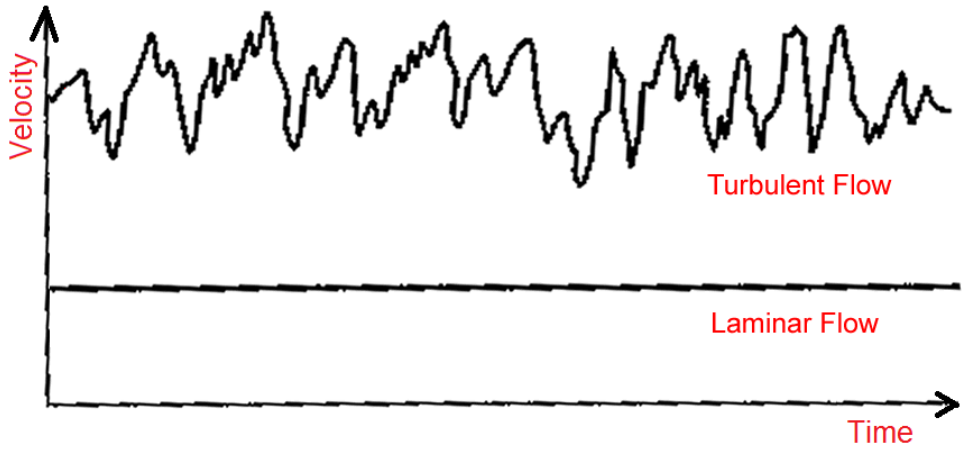

Figure P.4: Difference between a laminar and turbulent velocity signal (adjusted from Classification of Flows, Laminar and Turbulent Flows (2005))

In a turbulent flow, kinetic energy from the main flow is transferred into large eddies. These large eddies transfer their energy to smaller eddies. This process continues until the smallest possible turbulent scale is reached, the Kolmogorov length scale. At the Kolmogorov length scale, viscosity becomes dominant and thereby the kinetic energy is turned into heat (Uijttewaal, 2002). This process of energy breakdown is called the **energy cascade**. When the turbulent structures become smaller, they also become more isotropic and forget their origin. For the turbulent scales between the largest and the smallest eddies, often referred to as the **inertial subrange**, the turbulence breakdown to smaller eddies follows a fixed pattern (Uijttewaal, 2002). This is an useful property for turbulence modelling and therefore will reappear in section P.3.

In laminar flow, momentum is only exchanged on a molecular scale called molecular diffusion. It is caused by **viscous shear stresses** between fluid particles. This interaction between molecules has a tendency of equally distributing materials or properties over the entire water column but it only happens on micro scale. In turbulent flow, the large eddies are very effective in transporting momentum on a much larger scale in directions normal to the main flow, with a dominant tendency towards the bottom boundary. The transfer of momentum is caused by **turbulent shear stresses**, also known as the Reynolds stresses **Reynolds stresses** touched upon in the section P.1 about the boundary layer and treated further in paragraph P.2.2 about the Navier-Stokes equation. These stresses cause a more equally distributed velocity profile over the water depth compared to the parabolic profile that can be found for laminar flow, as visualised in figure P.5.

Over the entire water column the turbulent shear stresses are much larger than the viscous shear stresses, except near a solid boundary, as explained in section P.1.2. It is important to understand what happens in the near-wall area to grasp the physics involved in stone stability and to correctly mimic a real open-channel flow with help of a numerical simulation tool.

Furthermore a frequently used property of turbulence is described by the **Taylor's hypothesis**, also called the "frozen turbulence approximation. The hypothesis assumes a linear relation between the length scale of a turbulent eddy L_t and the time scale t_t depending on the flow velocity u (Uijttewaal, 2002).

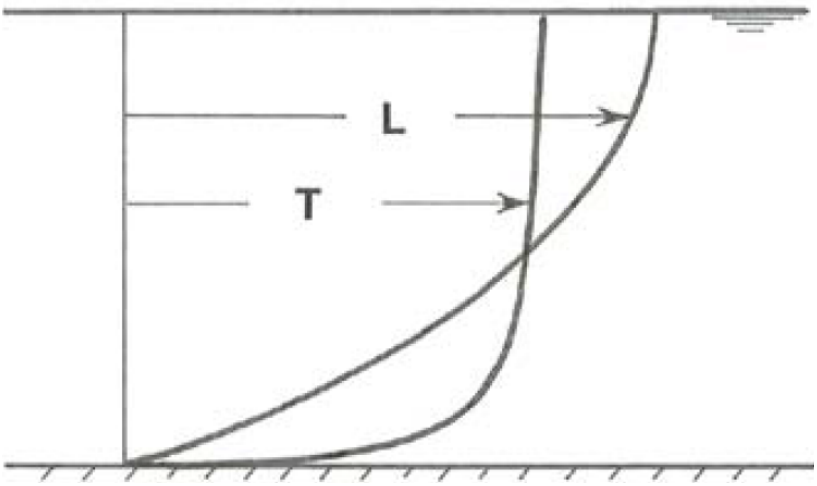

Figure P.5: Sketch difference between velocity profile of laminar (L) and turbulent (T) flow (Southard, 2006)

P.2.2. Navier-Stokes equation

A viscous flow, like a water flow, can be described by the Navier-Stokes equation. Further, for most civil engineering applications, water can assumed to be an incompressible fluid. The Navier-Stokes equation then looks as shown below.

$$\frac{\partial \boldsymbol{v}}{\partial t} + (\boldsymbol{v} \cdot \nabla)\boldsymbol{v} = -\frac{1}{\rho}\nabla p + \nu \nabla^2 \boldsymbol{v} + \mathbf{g} \tag{P.1}$$

in which:

- $\boldsymbol{v} = (u, v, w)$, the (x, y, z)-component of the velocity respectively $[m/s]$
- $\mathbf{g} = (0, 0, -g)$, the gravitational acceleration vector $[m/s^2]$
- $\nu \equiv \frac{\mu_w}{\rho}$, the kinematic viscosity $[m^2/s]$

As can be seen from the formula above, the Navier-Stokes equation actually is a system of three coupled, non-linear, second-order partial differential equations (Van Heijst and Van de Vosse, 2002).

Computational Fluid Dynamics (CFD) models are software tools that can visualize the flow by solving the Navier-Stokes equations. Because the Navier-Stokes equations have more unknowns than equations, some extra assumptions need to be made before they can be solved. This problem is called the **closure problem**.

Every numerical modelling method has its own way of solving the Navier-Stokes equations, which causes the differences in computational time and accuracy between them, as further elaborated in section P.3.1. Within a modelling method, different turbulence models can be assumed. These turbulence models consist of a (set of) equation(s) to deal with the closure problem.

P.3. Modelling the flow

This section contains some information about several modelling methods, turbulence models and CFD-modelling in general.

P.3.1. Modelling methods

In literature varying terminology is used to indicate what in this thesis are called "modelling methods". An attempt is made to pose a clear distinction between the different modelling methods, as in literature no unambiguous definitions can be found. For this thesis, it is important to emphasise to what extent a modelling method is modelling or really resolving the turbulent quantities. Four well-known modelling methods are:

- Reynolds-Averaged Navier Stokes modelling (RANS): Fully modelling all turbulent quantities
- Detached Eddy Simulation (DES): Mix between RANS and LES
- Large Eddy Simulation (LES): Resolving turbulence to grid size scale
- Direct Numerical Simulation (DNS): Turbulent flow fully resolved to Kolmogorov scale

In a RANS model the effect of turbulent fluctuations is fully modelled, as the other three modelling methods are scale-resolving simulations. The above is visualized in the energy density spectrum of figure P.6. An indication is given about the turbulence scales each modelling method is able to resolve. Furthermore, a visualization of the energy cascade, explained earlier in paragraph P.2.1, is added to the figure because this is a useful phenomenon for turbulence modelling.

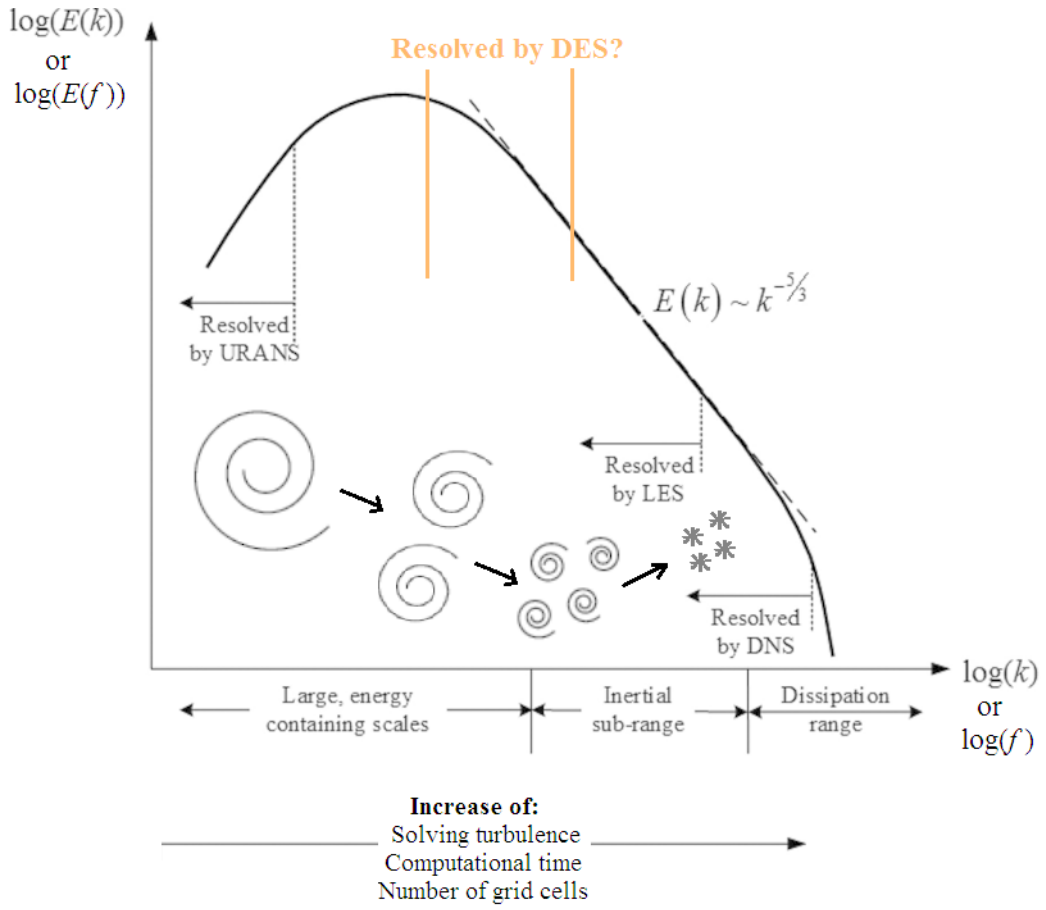

Figure P.6: Energy density spectrum including an indication of the energy cascade and turbulence modelling methods (adjusted from Thompson et al. (2015))

As indicated by the arrows underneath the graph, the required computational power increases as the amount of resolved turbulent length scales are increasing. This is a direct consequence of the grid size needed to resolve an eddy. The larger frequencies f or wave numbers k are representing the smaller eddies. To resolve these smaller eddies, also smaller grid sizes are required. Therefore, as a general rule it can be stated that the more turbulent scales one wants to resolve, the smaller the required grid sizes, the higher the required amount of grid cells and the larger the computational time and costs will be.

It is desired to resolve turbulence to the length scales were the inertial range of the turbulent energy spectrum is reached. The turbulent quantities are then resolved to a level were the eddies became isotropic and their breakdown will follow the slope of $k^{-\frac{5}{3}}$. So the energy cascade is predictable and can therefore be modelled without introducing large uncertainties or inaccuracies. Exploiting this turbulence property by modelling instead of resolving the predictable part of these turbulent quantities can save a significant amount of computational time and effort.

In the end, solving all or almost all turbulent scales results in the most accurate predictions of the real-time flow behaviour, provided that the model set-up is done well. Nevertheless, for many practical problems in hydraulic engineering the available computational power is not yet sufficient to apply DNS or LES as a modelling method. Especially near (rough) boundaries, a very high resolution is needed to accurately simulate the flow characteristics in case of a DNS or LES (Rodi et al., 2013). Fortunately in many cases an important part of the turbulent length scales can be resolved, without resolving the physics inside a boundary layer. This was the basic idea for the development of the DES. Originally DES was developed for separating flows (Spalart, 2009). A LES approach is used at the separation, were the turbulent length scales of interest appear and a RANS approach is used in the rest of the domain. In this way, more accurate results can be obtained compared to a RANS model, but a lot of computational time is saved compared to a full LES. Later on, many modifications are proposed to enlarge the area of applicability for the DES (Spalart, 2009).